U.PORTO

FEUP FACULDADE DE ENGENHARIA
UNIVERSIDADE DO PORTO

Machinability of Maraging Steel Manufactured by Laser Powder Bed Fusion

by

Tiago Emanuel Fraga Silva

Submitted to the Faculty of Engineering

in partial fulfilment of the requirements for the degree of

Doctor in Mechanical Engineering

at the

University of Porto

March 2021

Supervisor
Prof. Dr. Abílio Manuel Pinho de Jesus

Co-Supervisors
Prof. Dr. Pedro Alexandre Rodrigues Carvalho Rosa
Prof. Dra. Ana Rosanete Lourenço Reis

Abstract

The compelling advantages of laser powder bed fusion (LPBF) and its development as a reliable manufacturing process have contributed to the fact that most of the fabricated parts serve as a functional component or be integrated into an assembly. However, the required dimensional tolerances and high surface quality standards are not compatible with the additive process, which impose a need for machining operations, mostly as the finishing of near-net-shapes. This study focuses on the machinability assessment of the 18Ni300 maraging steel obtained through LPBF as well as its comparison with the conventionally manufactured counterpart. Instrumented orthogonal cutting and turning experiments have been developed for that purpose. Timely comparisons with the 316L stainless steel were carried out, allowed by additional research work in some parts of the workplan. The numerical simulation of the metal cutting process is key for predicting the impact that machining operations have on the structural integrity of post-processed additively manufactured alloys, which at this point lack comprehensive characterization in similar conditions to the cutting phenomenon. Moreover, finite element analysis is an advantageous supplement to the machinability assessment, in the way that it allows for a reduction of the relatively time-consuming and expensive machinability tests. With the goal of numerically simulate the metal cutting process, an extensive characterization of the maraging steel of both metallurgical conditions has been performed. The materials' flow stress was assessed through compression tests, for strain rates up to $6000s^{-1}$ and temperatures up to 400°C. Double notched specimens with distinct hole configurations and tensile test with distinct notched geometries were used to estimate pressure-dependent fracture behaviour. Furthermore, an innovative tribological characterization was carried via ring compression tests under representative metal cutting conditions. A joint experimental and numerical approach enabled material modelling in the most important domains of metal cutting (plasticity, damage and friction), allowing for the simulation of the orthogonal cutting process and consequent validation of the identified models through comparison of specific cutting pressures. In addition, the turning operation has been simulated for distinct configurations of cutting parameters. As key conclusions, despite the increased mechanical strength of the maraging steel, when additively manufactured, its machinability is not significantly affected nor additional energy is required in machining operations. In addition, the good performance of the numerical model in portraying industrial cutting operations confirms the characterization approach effectiveness.

Resumo

A tecnologia LPBF permite o fabrico de componentes mecânicos com especificações técnicas adequadas para aplicações estruturais. Não permite atingir o rigor geométrico, dimensional e acabamento superficial necessários para uma montagem mecânica de precisão, pelo que são necessárias operações de pós-processamento com tecnologias de maquinagem de precisão. Este trabalho foca-se no estudo da maquinabilidade do aço maraging 18Ni300 obtido por sinterização laser em cama de pó assim como a sua comparação com a mesma liga produzida de forma convencional. Para tal foram desenvolvidos ensaios experimentais de corte ortogonal e torneamento. A realização de ensaios complementares na liga de aço inoxidável 316L permitiu estabelecer uma referência comparativa para auxiliar a análise compreensiva do estudo. A simulação numérica do processo de corte é uma ferramenta essencial na previsão do impacto causado pelas operações de maquinagem na integridade estrutural de ligas metálicas que, até ao momento, carecem de caracterização em condições representativas do corte metálico. Adicionalmente, a utilização do método dos elemento finitos constitui um importante suplemento no estudo da maquinabilidade uma vez que permite a redução da extensão da caracterização experimental, relativamente morosa e dispendiosa. Com o objetivo de simular numericamente o processo de corte metálico por arranque de apara, foi realizada uma abrangente caracterização do aço maraging nas duas condições metalúrgicas. A lei de escoamento do material foi identificada com recurso a ensaios de compressão para taxas de deformação até 6000^{-1} a temperaturas até 400ºC. Provetes duplamente entalhados com configuração variável dos entalhes circulares assim como ensaios de tração com diferentes geometrias de entalhe possibilitaram estimar a influência da pressão no comportamento à fratura. Uma inovadora abordagem permitiu a caracterização tribológica em condições representativas do corte metálico, através da utilização de provetes anelares. Uma abordagem numérico-experimental possibilitou a modelação do material nos mais importantes domínios do corte (plasticidade, dano e atrito), permitindo a simulação do processo de corte ortogonal e consequente validação dos modelos identificados através da comparação da pressão específica de corte. Foi ainda construído um modelo 3D relativo à simulação da operação de torneamento para diferentes configurações de parâmetros de corte. Em suma, apesar da superior resistência mecânica do aço maraging quando obtido por fabrico aditivo, tal não se expressa na maquinabilidade do material nem foi detetado um aumento da energia necessária às operações de maquinagem. O bom desempenho do modelo numérico em retratar condições de corte industriais permite confirmar a eficácia da abordagem de caracterização.

Acknowledgements

The documented research in this dissertation is the result of comprehensive collaboration. I am deeply grateful to many people, not only for their scientific contribution but also for the honour and privilege of working alongside them.

I would like to express my sincere gratitude to Professor Abílio de Jesus for his continuous and unfailing support, availability, motivation and commitment. The countless debates, guidance, knowledge sharing and problem deconstruction enabled the writing of this document. I am also deeply grateful to Professor Pedro Rosa for his precious help in the experimental component of this work. His immense experience in the metal cutting subject and always pertinent discussion and advice have led this study in the right direction. I am equally obliged to Professor Ana Reis for the opportunity in fulfilling PhD studies while making part of a bigger team, dedicated to all kind of engineering/industrial problem solving. It has been a privilege to learn from my supervisors.

I would like to offer my special thanks to Professor José Xavier and Dr. Filipe Silva for their important support related with digital image correlation technique. I would also like to thank Eng. Afonso Gregório and all IST mechanical workshops staff for their willingness and help in the manufacture of machined specimen geometries.

Renishaw and Erofio are acknowledged for kindly supplying additively manufactured material batches. I am very thankful to PALBIT S.A., for the provided high quality materials (cutting tools and components) and constant availability for experimental testing at their facilities, particularly to Eng. Daniel Figueiredo, Dr. Cristina Fernandes, Eng. Renato Ferreira and Eng. Filipe Ferreira. I am also thankful to COMTES FHT, for the opportunity of an intense one-month apprenticeship of the most varied mechanical testing subjects and chance to perform important experimental tests. A kind word goes to Professor Pavel Konopík, Mrs. Polakova, Martin, Sylvia, Dan, Pedram and Parsa for their help and hospitality.

I would like to acknowledge DEMec mechanical workshops, especially Domingos Carvalho for his precious technical help. I am also thankful to LET laboratory, in

particular the help of Professor Miguel Figueiredo and Rui Silva.

A special acknowledgement goes to Armanda Marques for her dedication and support in optical microscopy and samples preparation.

I wish to thank all my colleagues in INEGI for the direct or indirect support in carrying out this research, especially the closest ones, at UTAF.

A very special appreciation goes to my patient, understanding and loving girlfriend, Helena, who had to put up with the least available version of myself, especially in the last critical (lockdown) months before submission of this document.

Finally, I wish to express my profound gratitude to my friends and family, in particular my brother and parents, for their support and encouragement.

This work has been conducted under the scope of MAMTool (PTDC/EMEEME/31307/2017) and AddStrength (PTDC/EME-EME/31307/2017) projects, funded by Programa Operacional Competitividade e Internacionalização, and Programa Operacional Regional de Lisboa funded by FEDER and National Funds (FCT). The author gratefully acknowledges the financial support of the Portuguese Foundation for Science and Technology (FCT) under the project POCI-01-0145-FEDER-030490 by UE/FEDER through the program COMPETE 2020. The support of TL-Advanced Production of LAETA (UIDB/50022/2020) and SMARTINJECT (POCI-01-0247-FEDER-039920) is also acknowledged.



Contents

1 Introduction **1**

1.1 Motivation and context . . . 1
1.2 Goals . . . 4
1.3 Document structure . . . 5
1.4 Main contributions . . . 6

2 Literature review I: mechanics of metal cutting **7**

2.1 Fundamentals of metal cutting . . . 7
2.1.1 Orthogonal cutting . . . 8
2.1.2 Single shear plane model . . . 9
2.1.3 Primary deformation zone analytical modelling . . . 11
2.1.4 Tool-chip interface analytical modelling . . . 13
2.1.5 Temperature distribution analytical modelling . . . 15
2.1.6 Chip formation mechanisms . . . 16
2.2 Numerical simulation of metal cutting . . . 17
2.2.1 Numerical formulations . . . 17
2.2.2 Material modelling . . . 19
2.2.3 Chip separation modelling . . . 21

3 Literature review II: LPBF-manufactured high strength steels **27**

3.1 Metal additive manufacturing technologies overview . . . 27
3.1.1 Powder bed fusion . . . 29
3.2 Impact of LPBF process on high strength steels . . . 30
3.2.1 Processing parameters . . . 31
3.2.2 Laser scanning strategies . . . 33
3.2.3 Microstructure . . . 34
3.2.4 Residual stress generation and mitigation . . . 36
3.2.5 Feature definition and surface roughness . . . 37
3.3 Mechanical and tribological properties of LPBF high strength steels . . . 38
3.3.1 Flow stress and fracture behaviour . . . 38
3.3.2 Anisotropy and tension-compression asymmetry . . . 46
3.3.3 Transformation induced plasticity effect . . . 47
3.3.4 Tribological properties . . . 48

3.4 Metal cutting of additively manufactured metals . . . 50

4 Experimental procedure and details 53
4.1 Work plan and approach . . . 53
4.2 Metallurgical and physical testing . . . 54
4.2.1 Optical/electron scanning microscopy and chemical analysis . . . 55
4.2.2 Thermal properties identification . . . 56
4.2.3 Surface and hardness inspection . . . 58
4.3 Mechanical and tribological experimental characterisation . . . 59
4.3.1 Uniaxial compression tests . . . 60
4.3.2 Ring compression tests . . . 64
4.3.3 Tensile tests . . . 66
4.3.4 Multiaxial fracture tests . . . 67
4.4 Metal cutting experimental tests . . . 69
4.4.1 Orthogonal cutting tests . . . 69
4.4.2 Turning tests . . . 75

5 Experimental results and discussion 79
5.1 Physical, thermal and metallurgical characteristics . . . 79
5.1.1 Chemical composition . . . 79
5.1.2 Relative density and metallographic analysis . . . 80
5.1.3 Thermal expansion coefficient . . . 82
5.1.4 Specific heat and thermal diffusivity . . . 85
5.1.5 Thermal conductivity . . . 85
5.1.6 Surface roughness . . . 85
5.2 Material and tribological characterization experimental results . . . 87
5.2.1 Uniaxial compression tests results . . . 87
5.2.2 Ring tests results . . . 93
5.2.3 Tensile tests results . . . 95
5.2.4 Multiaxial fracture tests results . . . 98
5.3 Metal cutting experimental results . . . 102
5.3.1 Orthogonal cutting tests results . . . 102
5.3.2 Turning tests results . . . 108

6 Constitutive modelling of materials mechanical behaviour 121
6.1 Frictionless flow stress identification . . . 121
6.2 Tensile tests simulation . . . 124
6.3 Multiaxial fracture tests simulation . . . 126
6.4 Viscous effect modelling . . . 135

7 Metal cutting simulation 139
7.1 Orthogonal cutting simulation . . . 139
7.2 Turning simulation . . . 148

8 Conclusions and future work **151**
8.1 Conclusions 151
8.1.1 Materials characterization 151
8.1.2 Tribological characterization 153
8.1.3 Orthogonal cutting tests 153
8.1.4 Machinability tests 154
8.1.5 Constitutive modelling 155
8.1.6 Numerical simulation 157
8.2 Future work 158

List of Figures

1.1 Application purpose of AM and number of metallic AM systems since 2000 . . . 2

2.1 Most common industrial metal cutting operations 7
2.2 Geometrical description of orthogonal (a) and oblique (b) cutting 8
2.3 Deformation zones in orthogonal cutting 9
2.4 Force diagram in orthogonal cutting 10
2.5 Three different approaches of metal cutting analytical modelling 11
2.6 Normal and frictional stress distribution along the tool rake face 13
2.7 Measured temperature distribution in dry orthogonal cutting of AISI 1045 with carbide tool 16
2.8 Basic chip formation mechanisms 16
2.9 Illustration of ALE formulation with mixed boundary conditions 18
2.10 Conceptual representation of the initial stress states on the η, $\bar{\theta}$ plane. 21
2.11 Typical stress strain curve of a material undergoing damage 22
2.12 Three dimensional asymmetric fracture locus 24
2.13 Implementation of fracture modes I and II on the orthogonal cutting model . . . 25

3.1 Configuration examples of directed energy deposition systems 28
3.2 Schematic illustration of laser powder bed fusion systems 29
3.3 Schematic illustration of melt pool region in laser powder bed fusion systems . . 30
3.4 Relative density for distinct volumetric energy conditions 31
3.5 Porosity trend with changes in the scan speed (for fixed power) 32
3.6 Influence of hatch spacing on the lack-of-fusion defects 32
3.7 Usual laser scanning strategies in LPBF 33
3.8 Effect of G and R on the morphology and size of solidification microstructure. . . 34
3.9 Metallographic image showing laser power influence for equal scan speed on SS316L 35
3.10 Microstructure of most common additively fabricated steels compared with conventional 36
3.12 Tensile properties of LPBF 316L stainless steels 39
3.20 Tensile tests for 17-4PH stainless steel produced by LPBF. 48

4.1 Schematic representation of the experimental work plan. 54
4.2 As-built material samples attached to 316L (a) and 18Ni300 (b) build plates. . . 55

4.3 Metalographic AM 316L sample (a) and its conversion to binary map (b), on a 50x magnification. . . . 56
4.4 Push-rod dilatometer Linesis DIL L75PT (a) and specimen placement detail in quartz holders (b). . . . 57
4.5 Laser flash device Linesis LFA 1000 (a) and specimen placement into carousel (b). 58
4.6 HommelWerke LV-50 stylus contact profilometer (a), Bruker NPFLEX optical surface profilometer (b) and EMCO Test M4U-075 hardness measurement machine (c). . . . 59
4.7 Experimental purpose of each type of printed geometry in schematic build plate of 316L (a) and 18Ni300 (b). . . . 60
4.8 Schematic representation of the compression test 61
4.9 Schematic representation of the specially-designed SHPB 62
4.10 Specially designed SHPB installed at IST, University of Lisbon 63
4.11 Constructive details and application of the specially designed SHPB 63
4.12 Schematic representation of the ring compression test 65
4.13 Tensile specimen geometry in function of notch dimensions. . . . 66
4.14 Tensile specimens and setup 67
4.15 Multiaxial fracture specimens for distinct pressure angle configurations: a) 120°; b) 90° and c) 60°. . . . 68
4.16 Experimental apparatus of the multiaxial fracture tests (a), a detailed perspective of the DIC setup (b), a sample of each tested specimen geometry (c), speckle application on half-specimen (d) and DIC camera capture of the signalled notch region (e). . . . 68
4.17 Schematic representation of the shaping machine orthogonal cutting setup, its kinematics and nomenclature. . . . 70
4.18 Comparison between the distinctly calculated ram speed in function of time for A1 (a) and ram speed in function of its position for B1 and B3 configurations (b). . 72
4.19 Orthogonal cutting experimental setup (a); tool slide lever (b); specimen fixation vise (c); Mitutoyo toolmaker's microscope (d). . . . 72
4.20 Orthogonal specimen wire-EDM cutting (a) and illustration of measurement procedure (b). . . . 73
4.21 Insert geometry used in the orthogonal cutting tests (a) with 5° (b) and 12° (c) rake angles. . . . 74
4.22 Tool rake face (α_r=5°) optical microspopy after sucessive orthogonal cutting tests (t_0 ∼0.1mm): (a) untested rake face; (b) 1 cut; (c) 2 cuts; (d) 3 cuts; (e) 5 cuts and (f) 15 cuts. . . . 74

4.23 Scheme of the turning setup: (a) front view and (b) top view of tool-workpiece relative position; rake surface of the used tools, T-FLAT (c) and T-CB (d). . . . 76
4.24 SEM images of the T-CB cutting tools used in 316L (a) and 18Ni300 (b); T-FLAT cutting tool used in 316L turning (c) with a detailed EDS analysis (d). 77

5.1 Unetched metallographic samples showing void occurrence in AM 316L (a, b) and 18Ni300 (c, d). 81
5.2 Chemically etched metallographic samples of AM 316L in perpendicular (a) and parallel to build direction (b) and electrolytically etched samples of AM 316L (c) in parallel direction to build. Chemically etched samples of CM 316L (d). 81
5.3 Chemically etched metallographic samples of AM 18Ni300 in perpendicular (a) and parallel to build direction (b) and electrolytically etched samples of AM 18Ni300 (c) in parallel direction to build. Chemically etched samples of CM 18Ni300 (d). . 82
5.4 Relative sample length in function of instantaneous temperature for the 316L SS of CM (a) and AM (b) metallurgical conditions. 83
5.5 Relative sample length in function of instantaneous temperature for the 18Ni300 of CM (a) and AM (b) metallurgical conditions. 83
5.6 Slope of the dilatometric curves of both CM (a) and AM (b) 18Ni300 maraging steel, during heating stage. 83
5.7 Heat capacity (green) and thermal diffusivity (red) for 316L (a) and 18Ni300 (b) steels. 85
5.8 Temperature dependent thermal conductivity of each tested steel and each metallurgical condition. 86
5.9 SEM images of as-built 316L (a) and 18Ni300 (b) surfaces showing non-fully melted metallic powder particles. 87
5.10 Influence of metallurgical condition on the stress vs. strain of 316L (a) and 18Ni300 (b) compression behaviour. 88
5.11 Comparison between 18Ni300 CM maraging stress vs. strain compression curves obtained from different laboratories. 88
5.12 Influence of strain rate on the stress vs. strain compression behaviour of 316L AM (a) and CM (b). 89
5.13 Influence of strain rate on the stress vs. strain compression behaviour of 18Ni300 AM (a) and CM (b). 89
5.14 Influence of temperature on the stress vs. strain compression behaviour of 18Ni300 AM (a) and CM (b). 90

5.15 Optical micrographs of the compression specimens' cross-section tested in quasi-static conditions at room temperature showing a nearly-uniform deformation (in its final stage) in AM (a) and CM (b) metallurgical conditions. 91
5.16 Optical micrographs of the compression specimens' cross-section tested at 6000s^{-1} and room temperature showing distinctively non-uniform deformation (in its final stage) in AM (a) and CM (b) metallurgical conditions. 91
5.17 Influence of simultaneous temperature and strain rate on the stress vs. strain compression behaviour of 18Ni300 AM (a) and CM (b). 92
5.18 Optical micrographs of the AM (a) and CM (b) compression specimens' cross-section tested in simultaneous 6000s^{-1} and 370°C, showing distinctively non-uniform deformation (in its final stage). 92
5.19 Influence of simultaneous temperature and strain rate on the stress vs. strain 316L CM compression behaviour. 92
5.20 Temperature and strain rate influence of the estimated friction coefficient of AM 18Ni300 maraging steel. 94
5.21 Temperature and strain rate influence of the estimated friction coefficient of CM 18Ni300 maraging steel. 94
5.22 Influence of notch geometry (stress triaxiality) on the tensile behaviour of AM (a) and CM (b) maraging steels. 95
5.23 Comparison between tension and compression behaviour of AM (a) and CM (b) maraging steel in quasi-static and room temperature conditions. 96
5.24 Engineering stress-strain curve (a) showing quasi-stable flow occurrence (diffuse necking) in both CM (b) and AM (c) maraging steels. 96
5.25 Fracture surfaces of the tensile test specimens 97
5.26 Load vs. displacement curves resultant from the multiaxial fracture tests: compression-shear (a), shear (b), tension-shear (c). 99
5.27 Polished and electrolytically etched micrographs of the CM maraging steel multiaxial specimen MA60 (a), MA90 (b) and MA120 (c) ligaments. 99
5.28 Multiaxial specimens final shape. 100
5.29 Free body diagram showing load decomposition at the ligament of multiaxial specimen with 60° (a), 90° (b) and 120° (c) pressure angles. 101
5.30 Relationship between shear and normal stresses (a) and pressure dependence on equivalent stress (b) at yield, for each multiaxial fracture specimen and metallurgical condition. 102
5.31 Experimental cutting loads for orthogonal cutting with t_0=0.165mm. 103

5.32 Influence of metallurgical condition (a) and rake angle (b) on the cutting force of maraging steel in orthogonal cutting conditions. 103
5.33 Influence of rake angle on the specific cutting pressure of AM 18Ni300 cut in perpendicular direction to BD (a), parallel direction to BD (b) and the CM 18Ni300 (c). Comparison of all K_c results, showing prevailing influence of rake angle (d). 104
5.34 Optical microscopy images of chip morphology of CM maraging steel obtained from orthogonal cutting tests with a 12° (a) and 5° (b) tool rake angle, for distinct uncut chip thickness; detailed measurements of continuous (c) and lamellar/segmented (d) morphology chips. 105
5.35 Optical micrographs showing distinct deformation pattern of melt pool geometries on workpiece and chip (a); etched chip section (b) and a detail (c) showing friction influence on chip deformation. 106
5.36 Friction coefficient results calculated through load ratio of equation 2.8 (a), and chip compression ratio (b), for all metallurgical conditions. 107
5.37 Shear angle predictions using geometrical and Merchant's metal cutting theory. . 107
5.38 Experimental correlation of the thrust force, F_t, and feed force, F_f, with the cutting force, F_c for both CM and AM 316L steels at a rotational speed of 2500 rpm using: (a) T-Flat and (b) T-CB cutting tools. 108
5.39 Experimental correlation of the thrust force, F_t, and feed force, F_f, with the cutting force, F_c for both CM and AM 18Ni300 steels at a rotational speed of 2500 rpm using: (a) T-Flat and (b) T-CB cutting tools. 109
5.40 Experimental evolution of the thrust force, F_t, as a function of the depth of cut, a_p for both CM and AM 18Ni300 and AISI316L steels using: (a) T-Flat and (b) T-CB cutting tools. 110
5.41 Experimental evolution of the feed force, F_t, as a function of the feed per revolution, f for both CM and AM 18Ni300 and AISI316L steels using: (a) T-Flat and (b) T-CB cutting tools. 110
5.42 Experimental evolution of the cutting force, F_c, for both CM and AM 18Ni300 and AISI316L steels using T-CB cutting tools: (a) Cutting force as a function of the feed per revolution, f, for three fixed depths of cut, a_p, of 0.1, 0.3 and 0.5 at a rotational speed of 2500 rpm, and (b) influence of the rotational speed on the vector components of the cutting load (a_p=0.5mm and f=0.2mm/rev). 111

5.43 Specific cutting pressure, K_c, in function of uncut chip section for: (a) CM 316L, (b) AM 316L, (c) CM 18Ni300, and (d) AM 18Ni300. 112
5.44 Specific cutting pressure, K_c, in function of uncut chip section for: (a) 316L and (b) 18Ni300. 112
5.45 Specific cutting pressure, K_c, obtained from orthogonal cutting and turning operation. 114
5.46 Chip types throughout variation of the feed per revolution, f, and depth of cut, a_p, for the AM 316L stainless steel using T-FLAT cutting inserts for different rotational speeds: (a) 2500rpm, and (b) 1800rpm. 114
5.47 Chip types throughout variation of the feed per revolution, f, and depth of cut, a_p, for AM 18Ni300 steel using T-CB cutting inserts for different rotational speeds: (a) 2500 rpm, and (b) 1800 rpm. 115
5.48 SEM images of chips obtained from the turning tests on 316L stainless steel for f=0.2 mm/rev, a_p=0.5 mm and n=2500 rpm; (a) CM 316L using T-CB insert, (b) AM 316L using T-CB insert, and (c) AM 316L using T-Flat insert. 116
5.49 SEM images of chips obtained from the turning tests on 18Ni300 steel for f=0.2 mm/rev, a_p=0.5 mm and n=2500 rpm; (a) CM 18Ni300 using T-CB insert, (b) AM 18Ni300 using T-CB insert, and (c) AM 18Ni300 using T-Flat insert. 116
5.50 Chip types throughout variation of the feed per revolution, f, and cut depth, a_p, for 316L stainless steel using T-CB cutting inserts at a rotational speed of 2500 rpm for (a) AM 316L condition, and (b) CM 316L condition. 117
5.51 Post-machining surface roughness, R_a of 316L (a) and 18Ni300 (b) for each processing condition and used tool insert, as a function of feed rate, for a cut depth, a_p, of 0.3mm, T-CB cutting inserts at a constant rotational velocity of 1800 rpm for a feed per revolution. 117
5.52 SEM images of machined surfaces in AM 316L stainless steel for a cut depth, a_p, of 0.3mm, T-CB cutting inserts at a constant rotational velocity of 1800 rpm for a feed per revolution, f, of (a) 0.2mm/rev, (b) 0.1mm/rev, and (c) 0.05mm/rev. . . 118
5.53 SEM images of machined surfaces in AM 18Ni300 steel for a cut depth, a_p, of 0.3mm, T-CB cutting inserts at a constant rotational velocity of 1800 rpm for a feed per revolution, f, of (a) 0.2mm/rev, (b) 0.1mm/rev, and (c) 0.05mm/rev. . . 118
6.1 Flowchart for frictionless flow stress and friction coefficient estimation, using compression and ring compression specimens. 122

6.2 Non-deformed numerical (axisymmetric) models of the cylindrical (a) and ring (b) compression specimens; deformed cylindrical (c) and ring (d) compression specimens assuming frictionless conditions; deformed cylindrical (e) and ring (f) compression specimens assuming μ=0.577. 123
6.3 Friction calibration curves for compression ring test (a) and stress-strain strain curves (b) of AM maraging steel in quasi-static, room temperature conditions. . . 124
6.4 Boundary conditions on the N-5 specimen geometry (a); Plastic strain (b) and stress triaxiality (c) fields distributions for the notch region (signalled red square); (d) Inverse reproduction of the N-∞ CM specimen experimental load-displacement curves. 125
6.5 Estimated (numerically) stress triaxiality evolution in function of plastic strain for the AM (a) and CM (b) maraging steel. 126
6.6 Multiaxial specimen numerical model scheme with employed boundary conditions (a); equivalent plastic strain (b) and von Mises stress fields (c) of the red-signalled region for a top die displacement of 0.22mm. 127
6.7 Distinct flow stress curves used to simulate the multiaxial specimen for both AM (a) and CM (b) metallurgical conditions. 128
6.8 Load-displacement results obtained from the simulation of the multiaxial fracture specimen without damage consideration: MA60 AM (a) and CM (b); MA90 AM (c) and CM (d); MA120 AM (e) and CM (f). 129
6.9 Comparison between DIC (left) and FEM (right) shear strain fields at an (a) incipient stage, d=0.2mm, and at an (b) intermediate stage of the test (d=0.5mm). 130
6.10 Deformed shape comparison of DIC and FEM results and plotted stress triaxiality and equivalent plastic strain of multiaxial specimen with (a) 60°, (b) 90° and (c) 120° pressure angles. 131
6.11 Stress triaxiality and equivalent plastic strain evolution along crack path for multiaxial specimens with (a) 60°, (b) 90° and (c) 120° pressure angles; identified damage law (d) using both multiaxial and tensile specimens. 132
6.12 Comparison between experimental curves and numerical simulation of the multiaxial specimens (maraging AM) within distinct pressure angles. 133
6.13 Suggested JC damage parameters for the AM and CM maraging steels modelling of fracture. 134
6.14 Identification of B and n parameters of the JC equation for the AM (a) and CM (b) maraging steels. 136

6.15 Identification of C parameters of JC equation for the AM (a) and CM (b) maraging steels. . . . 137
6.16 Viscoplastic flow stress curves, using the identified C parameter on the compression-based hardening curves of AM (a) and CM (b) maraging steels. . . . 137

7.1 Workpiece geometry and parametrized dimensions. . . . 140
7.2 Mass scaling influence on average cutting load and CPU time on the orthogonal cutting model (t_0=0.1mm; L_c=0.5mm). . . . 141
7.3 Strain rate field on the orthogonal cutting model for a t_0=0.1. . . . 142
7.4 Orthogonal cutting chip formation and evolution for α_r=5°, t_0=0.1mm and cutting lengths of 0.15 (a), 0.4 (b), 0.8 (c) and 1.3 mm (d). . . . 143
7.5 Orthogonal cutting chip formation and evolution for α_r=12°, t_0=0.1mm and cutting lengths of 0.15 (a), 0.4 (b), 0.8 (c) and 1.3 mm (d). . . . 143
7.6 Orthogonal cutting chip formation and evolution (using sacrificial layer) for α_r=5°, t_0=0.1mm and cutting lengths of 0.15 (a), 0.4 (b), 0.8 (c) and 1.3 mm (d). . . . 144
7.7 Orthogonal cutting chip formation and evolution (using sacrificial layer) for α_r=12°, t_0=0.1mm and cutting lengths of 0.15 (a), 0.4 (b), 0.8 (c) and 1.3 mm (d). . . . 144
7.8 Comparison between experimental trends and numerical results of chip compression ratio, r_c (a) and shear angle, ϕ_c (b). . . . 145
7.9 Comparison between experimental and numerical specific cutting pressure on the orthogonal cutting with a 5° (a) and 12° (b) rake angle, using the two described chip separation methods. . . . 145
7.10 Temperature dependent flow curves used in the simulation of orthogonal cutting with thermal softening behaviour. . . . 146
7.11 Equivalent plastic strain on the physical (a) and sacrificial (b) numerical approaches of the orthogonal cutting model; temperature field on the physical (a) and sacrificial (b) numerical approaches of the orthogonal cutting model. . . . 147
7.12 Schematic view of the longitudinal turning numerical model (a) and definition of geometrical cutting parameters (b). . . . 148
7.13 Chip geometry, von Mises stress (S) and equivalent plastic strain (PEEQ) for a_p=0.1 mm (a, b); for a_p=0.3 mm (c, d); for a_p=0.5 mm (e, f) and f=0.2 mm. . . . 149
7.14 Comparison between experimental and numerical cutting force, F_c (a) and specific cutting pressure, K_c (b). . . . 150

List of Tables

2.1 Shear angle definition according to different modelling techniques. 12
2.2 Frictional shear stress estimation according to different approaches 14
2.3 Constitutive equations typically used in plasticity material modelling 20
2.4 Approaches towards chip separation modelling 22
2.5 Most common damage models. 23

3.1 Classification, description and most common nomenclatures of MAM processes . 27
3.2 Methods for quantification of processing parameters in LPBF. 30
3.3 Tensile tests results of the four distinct specimen groups (Röttger et al., 2020). . 39
3.4 Calibrated plasticity models available in literature for the LPBF 316L stainless steel. 42
3.5 Calibrated Hosford-Coulomb fracture models available in literature for conventional and LPBF 316L stainless steel. 42
3.6 Comparison of additively manufactured and wrought 18Ni300 mechanical properties. 43
3.7 Calibrated JC plasticity models available in literature for the conventional 18Ni300 maraging steel. 45

4.1 Processing parameters used in the LPBF of 316L and 18Ni300 steels. 54
4.2 Geometry and purpose of each printed geometry. 60
4.3 Tested configurations of strain rate and temperature in the compression experimental setup. 61
4.4 Tested configurations of strain rate, temperature and lubrication in the ring compression experimental setup. 66
4.5 Tested configurations of stress triaxiality according to notch geometry. 66
4.6 Internal components measured dimensions of the L2.03.6 shaping machine. . . . 71
4.7 Different machine speed and stroke configurations of the L2.03.6 shaping machine. 71
4.8 Overview of tested cutting parameters in turning tests. 78

5.1 Tested materials at each characterization stage. 79

5.2 Chemical composition (wt%) of SS316L and 18Ni300 steel alloys with respective reference values. 80
5.3 Thermal expansion coefficient ($10^{-6}°C^{-1}$) in function of temperature, for each tested steel. 84
5.4 Surface roughness average ($\overline{x}$) and standard deviation (σ) values [μm] for as-built condition. 86
5.5 Hardness values of 316L and 18Ni300 steels in both CM and AM ($\perp$ BD) metallurgical conditions. 87
5.6 Summary from the stress analysis on the multiaxial specimens ligament. 101

6.1 Fracture strain and stress triaxiality estimation. 125
6.2 Swift-Voce equation parameters for hardening curves "a" and "b" for each material metallurgical condition. 128
6.3 Fracture strain and stress triaxialities estimations. 133

7.1 Parametrized workpiece, tool and mesh dimensions. 140
7.2 Material properties of AM 18Ni300 used in the built numerical model of orthogonal cutting. 141

Abbreviations

AM	additive manufacturing
ALE	arbritary Lagrangian-Eulerian
BD	build direction
BJ	binder jetting
BUE	built up edge
CD	cutting direction
CDF	computational fluid dinamics
CEL	coupled Lagrangian-Eulerian
CM	conventional manufacturing
DED	directed energy deposition
DIC	digital image correlation
DM	direct manufacturing
DMD	direct metal deposition
DMLS	direct metal laser sintering
EBM	electron beam melting
EDS	energy dispersive spectroscopy
EDM	electrical discharge machining
EPBF	electron powder bed fusion
FDM	fusion deposition modelling
FEM	finite element method/modelling
HT	heat treatment
HRC	hardness (Rockwell C)
HV	hardness (Vickers)
JC	Johnson-Cook
LC	laser cladding
LDW	laser deposition welding
LENS	laser engineered net shaping
LBM	laser beam melting
LMD	laser metal deposition

LPBF	laser powder bed fusion
MAM	metallic additive manufacturing
MTS	mechanical threshold stress
PBF	powder bed fusion
PH	precipitation hardening
PM	powder metallurgy
PSD	particle size distribution
PVD	physical vapor deposition
SEM	scanning electron microscopy
SHPB	split hopkinson pressure bar
SLM	selective laser melting
SLS	selective laser sintering
SPH	smooth particle hydrodynamics
TRIP	transformation induced plasticity
UAM	ultrasonic additive manufacturing
VMR	Vaccum remelting
XRD	X-ray diffraction

Symbols

A	material parameter (hardening laws)
A_l	elongation at break
A_s	shear plane area
B	material parameter (hardening laws)
C	material parameter (viscoplasticity)
D	damage parameter
E	Young's Modulus
E_l	linear energy density
E_s	surface energy density
E_v	volumetric energy density
F_s	shear force
F_n	normal force
F_v	friction force
F_u	normal to friction force
F_c	cutting force
F_f	feed force
G	temperature gradient
G_f	fracture energy
K_c	specific cutting pressure
L	characteristic length
L_c	cutting length
P_L	laser power
Q	Voce law material parameter
R	temperature gradient
R_c	resultant force (cutting)

T	temperature
U_T	toughness
V	volume
V_c	cutting speed
a	thermal diffusivity
b	workpiece in-plane width (orthogonal cutting)
c_p	specific heat
d_s	layer thickness
h_s	hatch spacing
h_m	enthalpy at melting
l_0	initial length
l_c	slinding region
l_p	sticking region
k	von Mises shear strength
k_0	Voce law material parameter
k_R	tool cutting edge angle
m	mass
m_f	friction factor
m_t	temperature modelling material parameter
n	hardening parameter
r_c	chip compression ratio
r_d	laser beam radius
t_0	uncut chip thickness
t_c	chip thickness
v_s	scan speed
v_f	sliding speed

Greek letters

α	Swift-Voce hardening law material parameter
α_r	tool rake angle
α_{inst}	thermal expansion coefficient
β_f	friction angle
β_v	Voce law material parameter
γ_f	tool relief angle
ΔH	specific energy
ε_0	reference strain
ε_T	thermal strain
ε_0^{pl}	plastic strain at the onset of damage
ε_f^{pl}	fracture strain
η	stress triaxiality
η_a	surface absorptivity
λ	thermal conductivity
λ_s	tool cutting edge inclination
μ	friction coefficient
ν	Poisson's ratio
ξ	third deviatoric stress invariant
ρ	density
ρ_m	density at melting
σ_y	yield strength
σ_u	tensile strength
σ_n	normal stress
σ_m	hydrostatic von Mises stress
τ_s	shear stress
ϕ_c	shear angle
θ	Lode angle
$\bar{\theta}$	Lode angle parameter

Chapter 1. Introduction

1.1. Motivation and context

Formerly known as rapid prototyping, additive manufacturing (AM) has shifted its main focus towards industrial applications rather than the development of isolate non-functional prototypes, over the last decade. Originally limited to a group of polymers, it quickly evolved to metal processing. The current range of metallic material options combined with the possibility of attaining intricate geometrical features (some of them impossible, otherwise) has attracted most industrial sectors. Moreover, the fact that no tooling (moulds and dies) is required, facilitates and accelerates the production of small batches. It is also known that standard mechanical properties are not compromised. Sames et al. (2016) and Lewandowski and Seifi (2016) report that the tensile and yield strengths of additively manufactured steel alloys are identical to the ones of conventional manufacture. Nevertheless, a small amount of research focuses on mechanical properties different from uniaxial testing, meaning that for more comprehensive knowledge on the behaviour of additively manufactured metallic alloys, properties as multiaxial testing, impact behaviour, fatigue life and fracture toughness have to be assessed. The lack of research has not, however, hindered the development of specific purposed applications in the most varied fields of industry. Kumar and Nair (2017) highlight the usage of topologically optimized AM parts as well as the replacement of twenty-part assemblies by a single geometrically complex AM component, in the aerospace industry. Meng et al. (2020) indicate some efforts in using additively manufactured parts as reinforcement in automotive structural assemblies. In medical applications, metallic porous parts are used as bone scaffolds (Wang et al., 2016) and dental prostheses are efficiently produced (Gebhardt et al., 2010), with a high degree of customization. Mazur et al. (2016) illustrate the enhanced cooling rates of mould inserts with conformal channel systems in tooling, indicating decreased cycle times and improved life of the tooling system.

The compelling advantages of AM and its development as a manufacturing process have contributed to the fact that most of the fabricated parts will serve as a functional component or be integrated into an assembly. Figure 1.1a displays the most common application purposes of AM, while figure 1.1b shows the substantial increase of metallic additive manufacturing (MAM) portrayed by the number of sold machines over time. It is, however, important to note the need for

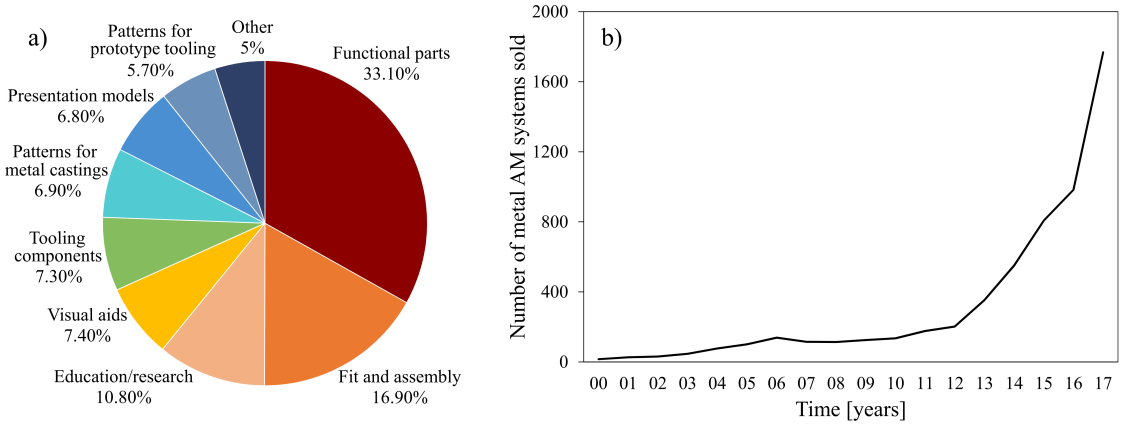


Figure 1.1: Application purpose of AM (a) and number of metallic AM systems since 2000 (b), adapted from Campbell et al. (2018).

post-processing of metallic printed parts. These are fabricated on a build plate, sometimes with support structures, which are required to be removed. Heat treatment for stress relief and hot isostatic pressing (HIP) may also be required for some parts. Moreover, the surface quality of the generated near-net shapes is low, imposing the need for finishing machining operations (Fox et al., 2016). To ensure functionality and allow for assemblage, metallic AM parts require demanding dimensional tolerances and high surface quality, which is not yet compatible with the additive process. Features such as precision and threaded holes as well as reference contact surfaces are exclusive of subtractive processes, which has resulted in the appearance of hybrid manufacturing (Flynn et al., 2016). In conclusion, the added value of AM is highly significant in areas that deal with expensive materials and high complexity parts, where a considerable amount of machining is required (Kamal and Rizza, 2019).

Several aspects of MAM indicate that machining operations on such materials constitute an increased challenge, relatively to the cutting of conventionally fabricated parts. The layer-derived anisotropic behaviour and occurrence of high residual stresses can be pointed out as causes for eventual differences in the machinability of metallic AM parts. Moreover, the stiffness of topologically optimized parts (which are very often fabricated using AM) is reduced, meaning the possibility of machining induced defects or damage due to uncontrolled vibration or improper part fixture (because of complex surfaces). Thorough control of the metal cutting operations is essential to ensure successful post-processing of additively fabricated components, which are too valuable to jeopardize with faulty machining. Therefore, understanding the parameters that contribute to an adequate chip formation is essential. Despite being a challenging task due to all the phenomena involved (high strains, strain-rates, local tool-chip interface temperatures as well as stresses) it has been the subject of investigation on a considerable range of conventional metallic alloys. Even though some research is found, aiming at the characterization of additively manufactured steels, very few

focus on their viscoplastic response at high-temperature and fracture behaviour, which is key for predicting the impact of the cutting process through its numerical modelling.

The scope of this dissertation fits in the original and ambitious MAMtool research project, focusing on the cutting behaviour of metallic powder-based additive manufactured tool components and addressing the need for their post-processing. Maraging steel is commonly used in the additive manufacture of plastic injection mould inserts with conformal cooling channels (Minguella-Canela et al., 2020). Due to physically following the contours of the part to be injected, these tools present enhanced productivity (lower thermal cycles) and, thus, faster cost amortization. Figure 1.2 shows the comparison between conventional drilled linear cooling channels and the conformal geometries, where noticeably lower temperature distributions are developed, resulting in reduced cooling times (up to 100%). The assemblage of moulding tool inserts into the complete injection mould requires very high precision and tight dimensional tolerances. The impact that the post-processing (cutting) parameters have on machined surfaces integrity, cutting loads, chip control are the main expected outcomes of the project, which have direct impact on productivity, energetic efficiency and cutting tools life.

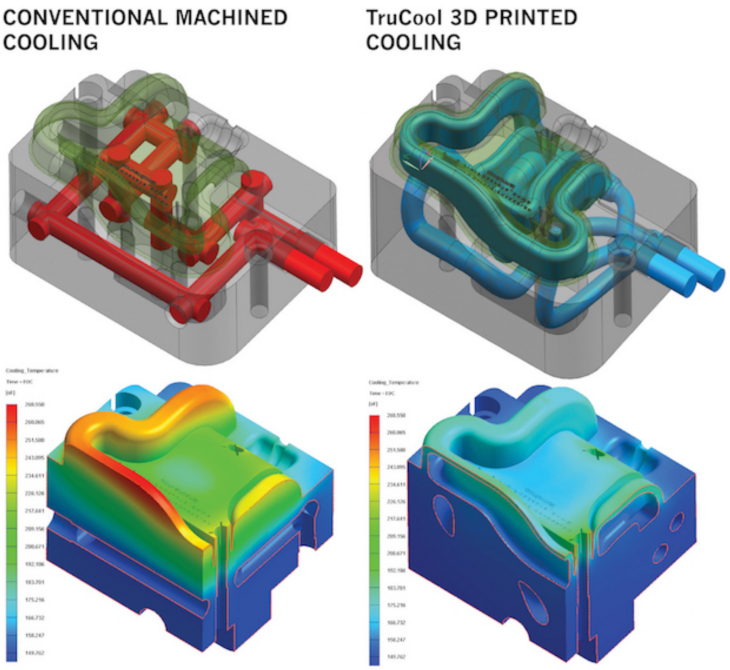


Figure 1.2: Temperature distribution on plastic injection mould insert using conventional drilled cooling channels and additively manufactured conformal cooling channels (Metal AM, 2017).

1.2. Goals

The lack of knowledge regarding the machinability of additively manufactured metals implies that their comprehensive characterization is carried in similar conditions to the cutting phenomenon. Hence, this work focuses on the thorough characterization of AM steel alloys towards machinability assessment and its numerical simulation. To accomplish that, a set of multidisciplinary, ordered goals was established:

G1 Materials selection, manufacturing process characterization and multiple geometries specimen design, for further addressing a wide range of tests;

G2 Metallurgical, mechanical and physical characterization of the obtained materials:

- Microstructural analysis, including phase, grain size, orientation evaluation as well as occurring defects and heterogeneities, through optical microscopy and scanning electron microscopy (SEM);
- Chemical composition analysis, using spark emission spectroscopy and SEM/EDS as well as micro and macroscopic hardness measurement;
- Thermal properties identification, relevant for the metal cutting simulation and distortion evaluation;
- Compression behaviour assessment of the selected steel alloys for multiple conditions of strain rate and temperature;
- Fracture behaviour identification for distinct states of stress, exploring digital image correlation (DIC) techniques;

G3 Experimental cutting testing of the selected steel alloys:

- Instrumented tests of orthogonal cutting and turning operations, allowing for the cutting loads measurement;
- Generated chip morphology assessment and identification of convenient chip removal scenarios;

G4 Identification of constitutive models capable of depicting the flow stress and damage behaviour of the considered alloys:

- Evaluation of suitable constitutive models for the numerical representation of the mechanical behaviour;
- Model parameters identification using a hybrid approach (direct data and inverse approaches);

G5 Numerical simulation of the cutting process, portraying distinct machining operations:

- Validation of the identified constitutive models;

1.3. Document structure

This document is divided into 7 chapters which are very briefly explained in this section for the sake of an overview of this research work.

Chapter 1 presents the research subject, supported by its motivation and taking into account the current academic and industrial scenario. A methodology with specific goals is defined in order to comprehensively characterize the machinability of additively manufactured maraging steel.

Chapter 2 corresponds to a literature review on the theory of metal cutting. The mechanisms of the cutting phenomenon are described and the most common analytical models regarding materials plasticity, damage and friction are reviewed. In addition, a description of numerical techniques towards the simulation of machining operations is led.

Chapter 3 focuses on the particularities of additively manufactured metals. A bigger focus is given to 18Ni300 maraging steel and 316L stainless steel, when possible. The differences of such materials with the conventionally fabricated are also taken into account. The most commonly used MAM methods for the fabrication of functional steel parts are also briefly reviewed. This chapter ends with a review of the (few) studies that regard metal cutting of AM metals.

In chapter 4 the experimental setup of the conducted tests is fully described as well as the used materials. Firstly, some details regarding the inspection of the material batches are given. The purpose and methodology of the conducted mechanical and tribological experimental tests as well as the machinability tests (orthogonal cutting and longitudinal turning) are fully examined.

The results of each characterization procedure described in the previous chapter are discussed in chapter 5. Comparison between the performance of additively and conventionally manufactured steels is conducted for the whole range of experimental tests. Moreover, the machinability assessment of the considered metals is performed. When possible, the results are as well compared with the literature.

Chapter 6 deals with the constitutive modelling of maraging steel. For that, the experimental characterization tests are simulated enabling the direct and inverse calibration of the main effects in the metal cutting simulation (friction, plasticity and damage behaviour).

In chapter 7 the numerical simulation of the cutting process is conducted. Firstly, in order to assess the suitability of the identified material model, the orthogonal cutting operation is simulated. After that, an industrial machining operation (longitudinal turning) is simulated for a representative

amount of practical cutting parameters, using the same material laws identified in the previous characterization stages. The obtained numerical results are compared with the experimental.

1.4. Main contributions

The present section enumerates the main contributions of this research, which are summarized as follows:

- The identification of physical and thermal parameters for 18Ni300 maraging steel and 316L stainless steel in two distinct metallurgical conditions: additively manufactured (LPBF) and conventionally manufactured - vacuum remelted (VMR) cast.
- A thorough mechanical and tribological characterization of the maraging steel of additively manufactured and conventional metallurgical conditions through compression specimens for a wide range of strain rates and temperatures. Innovative compression tests with simultaneous high temperature and high strain rate have been conducted.
- The fracture behaviour of maraging steel (in two metallurgical conditions) is assessed for different stress triaxialities via smooth and notched tensile specimens as well as novel double notched specimens (Abushawashi (2013)), directed towards flow stress and fracture modelling in metal cutting applications.
- An instrumented and controlled orthogonal cutting setup is developed. The additively manufactured and conventional maraging steels are tested in this setup enabling to understand the influence of metallurgical condition and build direction (within AM) on the workpiece machinability.
- Machinability tests are carried out in turning setup for a wide range of finishing parameters using two different tool insert geometries.
- Numerical simulation procedure for experimental tests enabling the identification of plasticity and damage models.
- Orthogonal cutting has been numerically simulated via two distinct numerical approaches which are compared and the obtained results are correlated with the experimental data.
- A numerical model was developed towards the simulation of an industrial machining process (turning).

Chapter 2. Literature review I: mechanics of metal cutting

In this section, a brief analysis of the mechanics of metal cutting and its bridging characteristics to the numerical simulation of the machining processes are reviewed. As noted by Astakhov and Outeiro (2008), the key goal of advanced cutting mechanics is to be able to predict the cutting load and cutting power, through the analysis of the thermomechanical processes involved, which is proven to be challenging due to the extensive non-consensual research. The inclusion of new materials, such as the additively fabricated, demands a step towards wider understanding of the cutting phenomenon, due to the complex behaviour such materials could represent.

2.1. Fundamentals of metal cutting

In contrast to the additive manufacturing processes, metal cutting is defined in DIN8589 (2003) as a mechanical separation of material layers from a workpiece, in the form of chips, by means of a cutting tool (Klocke, 2011). Several operations, consisting on this basic principle, compose the machining domain. Figure 2.1 illustrates the most common and enumerates a few others. Despite the multitude of industrial operations, a simplified version of the cutting process - the orthogonal cutting - is often used in order to analyse the effect of parameters such as cutting speed, feed, tool geometry, material properties, friction as well as force, energy and power requirements (Astakhov, 1998). In other words, orthogonal cutting constitutes an approximation to industrial machining operations and can serve as a good option for the calibration of analytical or numerical models.

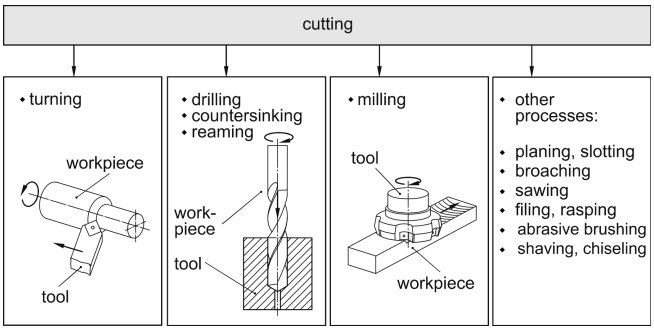


Figure 2.1: Most common industrial metal cutting operations (Toenshoff and Denkena, 2013).

2.1.1. Orthogonal cutting

Portraying a reasonably good approximation of the multi-physical cutting phenomenon, orthogonal cutting is achieved by purposefully removing material from a workpiece, using a cutting edge that is perpendicularly positioned to the tool's motion (orthogonal to cutting speed), as shown in figure 2.2a. Cutting is assumed to be uniform along the cutting edge and very often the orthogonal cutting model can be considered a two-dimensional plane strain deformation process, due to a width of cut significantly larger than uncut chip thickness (zero strain in width direction). It is important to acknowledge the absence of side cutting, which entails that only the main cutting edge is engaged and the two forces exerted by the tool develop in the xy plane. When the tool cutting edge inclination, λ_s is different than 0°, oblique cutting conditions are assumed (refer to figure 2.2b). Tool cutting edge angle, k_R, should also be 90° for orthogonal conditions. Despite often seen as a theoretical configuration, orthogonal cutting can be performed by means of longitudinal face turning or cross cylindrical turning configurations, as long as the enumerated conditions (illustrated in figure 2.2a) are reasonably fulfilled, as stated by Klocke (2011).

The dynamics and deformation geometry of orthogonal cutting as well as its main parameters and nomenclature are illustrated in cross-sectional view of figure 2.3, which schematically shows a stationary stage of chip flow. Three deformation zones can be distinguished. The primary deformation zone relates to the mixed state-of-stress deformation caused by tool penetration into the workpiece. It defines the transition between workpiece material and chip material. The deformed and separated material, now in the form of chip, slides and partially deforms along the tool's rake face, leading to the secondary shear zone, characterized by the severe tool-chip friction conditions. The tertiary zone corresponds as well to a friction region caused by the tool's flank face contact with the newly machined surface. The need for the definition and understanding of the mechanics involved in the metal cutting process arises from the cutting force prediction attempts, quitting trial and error approaches. Throughout last century, many models have been conceived in an attempt to thoroughly describe the metal cutting phenomenon. Despite its limitations, the single shear plane model is still the most popular mainly due to its simplicity.

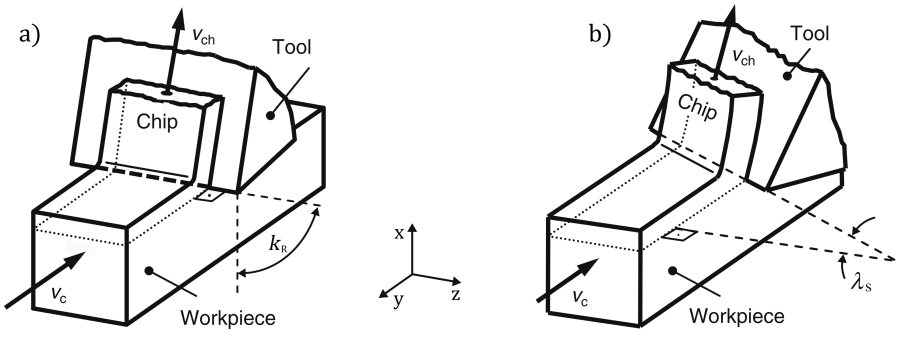


Figure 2.2: Orthogonal (a) and oblique (b) cutting schemes (Klocke, 2011).

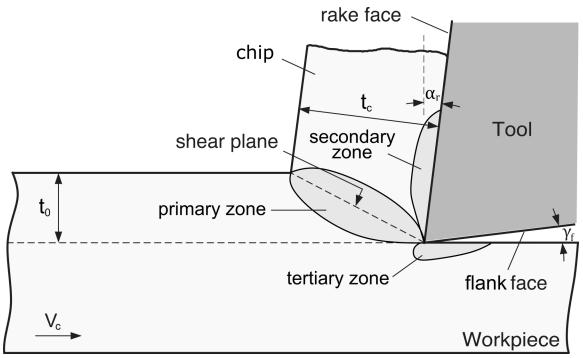


Figure 2.3: Deformation zones in orthogonal cutting, adapted from (Altintas, 2012).

2.1.2. Single shear plane model

The cutting force calculation by application of the Thales theorem on the orthogonal cutting model was the first attempt towards the definition of the force diagram in metal cutting. It was developed by Merchant and Ernst (1941) and it is displayed in figure 2.4. The authors assumed negligible strain hardening, the occurrence of uniformly distributed deformation exclusively at the infinitely thin primary shear zone (shear plane). It is further assumed that the cutting edge is sharp without a chamfer or radius. Also, the shear angle ϕ_c, is defined by minimization of cutting energy criterion. According to the model, all cutting forces are due to shearing process on the primary shear zone (F_s and F_n) or chip–rake face contact (F_v and F_u) on the secondary shear deformation zone. The resultant force, R_c, can therefore be decomposed in the orthogonal directions, leading to the cutting force, F_c and the feed force, F_f, as illustrated in eq. 2.1. Focusing on the primary shear zone, one can geometrically derive the shear force (eq. 2.2) in function of the resultant force, the shear angle, ϕ_c, and friction angle, β_f.

$$R_c = \sqrt{F_c^2 + F_f^2} \tag{2.1}$$

$$F_s = R_c \sin(\phi_c + \beta_f - \alpha_r) \tag{2.2}$$

Moreover, (uniform) shear (τ_s) and normal (σ_n) stress distributions on the shear plane can be calculated as the ratios between the correspondent force component and the shear plane area, A_s, as shown in eqs. 2.3 to 2.5:

$$\tau_s = \frac{F_s}{A_s}, \tag{2.3}$$

$$\sigma_n = \frac{F_n}{A_s}, \tag{2.4}$$

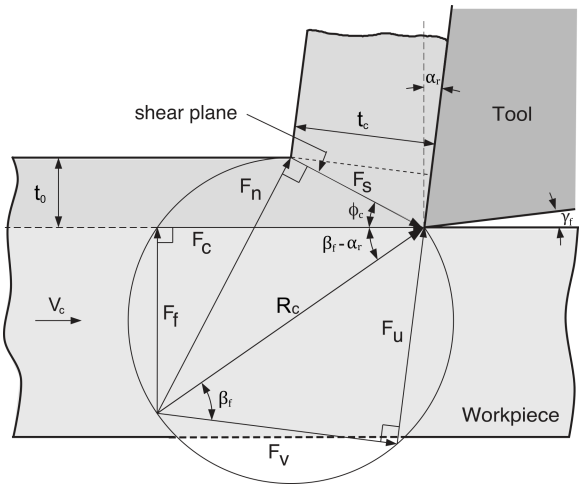


Figure 2.4: Force diagram in orthogonal cutting, adapted from (Altintas, 2012).

$$A_s = b\frac{t_0}{\sin\phi_c}, \tag{2.5}$$

where b corresponds to in-plane workpiece width. The chip compression ratio, r_c, is defined by the ratio between the chip thickness and uncut chip thickness (refer to eq. 2.7) and allows for the geometrical definition of the shear angle:

$$\phi_c = \tan^{-1}\frac{\cos\alpha_r}{r_c - \sin\alpha_r}. \tag{2.6}$$

$$r_c = \frac{t_c}{t_0} \tag{2.7}$$

Furthermore, and relatively to the secondary shear zone, the average friction coefficient (Coulomb model) can be calculated as the ratio between the friction force, F_u, and its normal, F_v, which in function of F_c and F_f, is depicted as follows:

$$\mu = \tan\beta_f = \frac{F_u}{F_v} = \frac{F_c\sin\alpha_r + F_f\cos\alpha_r}{F_c\cos\alpha_r - F_f\sin\alpha_r} = \frac{F_c\tan\alpha_r + F_f}{F_c - F_f\tan\alpha_r}. \tag{2.8}$$

Based on the established force relationships, mechanistic modelling of cutting forces is possible. For instance, knowing that the feed and cutting forces can be geometrically expressed in terms of resultant force as shown in eqs. 2.9 and 2.10:

$$F_c = R_c\cos(\beta_f - \alpha_r), \tag{2.9}$$

$$F_f = R_c\sin(\beta_f - \alpha_r), \tag{2.10}$$

these can be re-written, taking into consideration eqs. 2.2, 2.3 and 2.5 resulting in expressions that depend exclusively on tool geometry, cutting conditions and material terms, as shown in eqs. 2.11 and 2.12.

$$F_c = bt_0\tau_s\left[\frac{\cos(\beta_f - \alpha_r)}{\sin\phi_c\cos(\phi_c + \beta_f + \alpha_r)}\right], \tag{2.11}$$

$$F_f = bt_0\tau_s\left[\frac{\sin(\beta_f - \alpha_r)}{\sin\phi_c\cos(\phi_c + \beta_f + \alpha_r)}\right]. \tag{2.12}$$

The specific cutting pressure can be defined as a material constant often used to estimate the required cutting force.

$$K_c = \frac{F_c}{bt_0} = \tau_s\left[\frac{\sin(\beta_f - \alpha_r)}{\sin\phi_c\cos(\phi_c + \beta_f + \alpha_r)}\right] \tag{2.13}$$

As seen from eq. 2.13, K_c is a function of material's shear stress (τ_s), tool geometry (α_r), tool-chip friction (β_f) and shear angle (ϕ_c). While tool geometry can be inferred beforehand and material's shear stress and tool-chip friction can be accessed through additional testing, shear angle analytical prediction remains unknown, which is why many authors have been focusing on finding analytical predictions of such variable.

2.1.3. Primary deformation zone analytical modelling

The great challenge in understanding and modelling the physical phenomenon of cutting has motivated research into the development of distinct models, which were based on three different approaches: (i) single shear plane; (ii) slip line field and (iii) shear zone. Figure 2.5 illustrates and compares these theories. Despite its simplicity, the single shear plane model envisioned by Piispanen (1937) and explored by Merchant and Ernst (1941) is still the most popular approach. Lee and Shaffer (1951) were the first to propose a slip line field model, which relies on the assumption that deformation occurs at the shear plane, although there is a slip line field stressed up to yield point. In shear zone models, rather than a plane, a shearing region is considered in workpiece deformation, where strain hardening is considered. Among others, Palmer and Oxley (1959) were the pioneers of

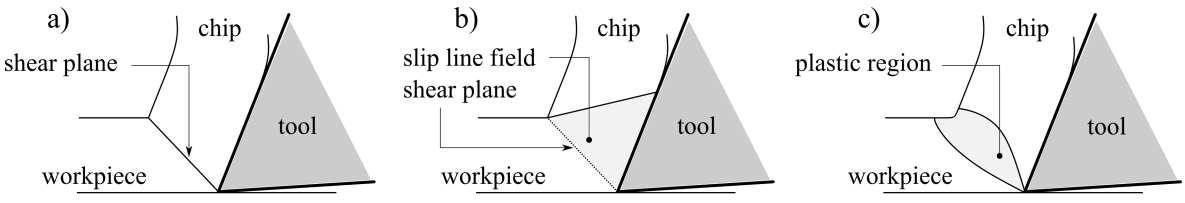


Figure 2.5: Three different approaches of metal cutting analytical modelling: single shear plane (a); slip line field (b); shear zone (c).

such approach. It is important to note that these three approaches (refer to fig. 2.5) rely on the assumption that the metal cutting phenomenon is mostly a plasticity problem. It is also generally acknowledged that friction plays an essential role in the modelling of chip formation, which as been comprehensively studied by Zorev (1966). Despite its flaws, the vast majority of works on metal cutting are supported on Merchant's theory (Dudzinski and Molinari, 1997; Budak et al., 1996), focusing on the proposal of corrections, capable of enhancing the predictability of such model.

More recently, the idea that metal cutting should be seen as purposeful fracture problem (Astakhov, 1998) and that the energy used in the creation of new surfaces should be accounted has resulted in the development of new shear angle predictions, with the contribution of numerical methods, as demonstrated by Atkins (2003) and Rosa et al. (2007b). Table 2.1 presents some of the most relevant analytical models for the prediction of shear angle.

Table 2.1: Shear angle definition according to different modelling techniques.

Model	Shear angle equation	
Merchant and Ernst (1941)	$\phi_c = \frac{\pi}{4} - \frac{1}{2}(\beta_f - \alpha_r)$	(2.14)
Stabler (1951)	$\phi_c = \frac{\pi}{4} - \beta_f + \frac{\alpha_r}{2}$	(2.15)
Lee and Shaffer (1951)	$\phi_c = \frac{\pi}{4} - (\beta_f - \alpha_r)$	(2.16)
Hucks (1951)	$\phi_c = \frac{\pi}{4} - \frac{\arctan(2\mu)}{2} + \alpha_r$	(2.17)
Shaw et al. (1953)	$\phi_c = (\frac{\pi}{4} + \eta')(\beta_f - \alpha_r)$	(2.18)
Sata (1954)	$\phi_c = \frac{\pi}{4} - \alpha_r \pm \frac{\alpha_r - (\pi/12)}{2}$	(2.19)
Zorev (1958)	$\phi_c = \cot K\phi_c - \tan(K\phi_c + \beta_f - \alpha_r) = \cot\phi_c + \tan(\phi_c - \alpha_r)$	(2.20)
Palmer and Oxley (1959)	$\phi_c = \arctan[c - D + \frac{c + (\sigma_B/k_1)}{e^{(1/D)(c+(\sigma_B/k_1)}}]$	(2.21)
Okushima and Hitomi (1961)	$\phi_{lower} = \frac{K_1}{2} - \frac{\beta_f}{2} + \frac{\alpha_r}{2}; \quad \phi_{upper} = \frac{K_2}{2} - \frac{\beta_f}{2} + \frac{\alpha_r}{2}$	(2.22)
Oxley (1961)	$\phi_c = \arctan[1 + \frac{\pi}{2} - 2\phi_c + \frac{\cos 2(\phi_c - \alpha_r)}{\tan\beta_f} - \sin 2(\phi_c - \alpha_r)] - (\beta_f - \alpha_r)$	(2.23)
Sata and Yoshikawa (1963)	$\phi_c = arc\cot[\cot\theta + \frac{\cos\theta}{\sin(\theta + \alpha_r)kL}]$	(2.24)
Atkins (2003)	$\phi_c = [1 - \frac{\sin\beta_f \sin\phi_c}{\cos(\beta_f - \alpha_r)\cos(\phi_c - \alpha_r)}][\frac{1}{\cos^2(\phi_c - \alpha_r)} - \frac{1}{\sin^2\phi_c}]$	(2.25)

2.1.4. Tool-chip interface analytical modelling

Despite the enormously challenging task that is friction estimation in metal cutting, its importance is undeniable. Not only it influences loads and energy consumption but also the cutting performance, such as workpiece surface quality and tool life. Even though there are numerous attempts towards friction modelling (refer to table 2.2), it remains the least understood phenomenon in metal cutting. Due to its simplicity, Coulomb's friction law is widely adopted in the representation of orthogonal cutting model, and can be expressed as the ratio between average shear stress and normal contact pressure of the tool's rake face (eq. 2.26). According to von Mises plasticity, a material's shear yield stress is given by $k = \sigma_y/\sqrt{3}$. This means that Coulomb's friction threshold is $\mu = k/\sigma_y = 1/\sqrt{3} = 0.577$, due to being the transition point between sliding and shearing deformation (absence of sliding). Constant shear friction model (Prandlt's law) circumvents that issue by assuming that shear stress is proportional to shear strength (eq. 2.27), meaning that friction factor, m, (which should not be confused with friction coefficient) can assume values from 0 to 1. The model proposed by Zorev (1963) assumes that tool-chip interface is divided in two regions: sticking (l_p) near the tool edge, and sliding (l_c), beyond sticking region, as illustrated on the tool's rake face of figure 2.6. Due to the very high normal contact pressures, the author defines that along l_p, shear stress equals to the material's shear strength (eq. 2.28), meaning the occurrence of plastic deformation (seizure). In the following region, l_c, Coulomb's model is applied. The usage of constant shear friction model in the sticking region and Coulomb's law in the sliding region, gives rise to the hybrid model (eq. 2.29). Following a similar trend, Shirakashi and Usui (1973) propose a non-linear equation that saturates at shear strength for high contact pressure, being similar to Coulomb's law for low contact pressure. For an improved portrayal of the mean friction stress, Childs and Maekawa (1990) proposed a correction to the previous model. Other contributions relate to the usage of hard-

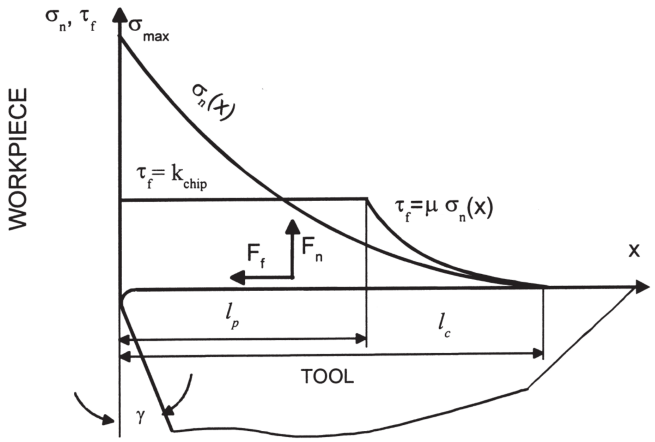


Figure 2.6: Schematic representation of normal and frictional stress distribution along the tool's rake face (Özel and Altan, 2000).

Table 2.2: Frictional shear stress estimation according to different approaches (Markopoulos, 2012; Melkote et al., 2017).

Model	Frictional shear stress formulation	
Amonton-Coulomb (1785)	$\tau_f = \mu\sigma_n$	(2.26)
Prandtl's law	$\tau_f = m_f k$	(2.27)
Zorev (1963)	$\tau_f = \begin{cases} k, & 0 \leq l \leq l_p \\ \mu\sigma_n, & l_p \leq l \leq l_c \end{cases}$	(2.28)
Hybrid model	$\tau_f = \begin{cases} m_f k, & 0 \leq l \leq l_p \\ \mu\sigma_n, & l_p \leq l \leq l_c \end{cases}$	(2.29)
Shirakashi and Usui (1973)	$\tau_f = k\left[1 - \exp\left(-\frac{\mu\sigma_n}{k}\right)\right]$	(2.30)
Iwata et al. (1984)	$\tau_f = \frac{HV}{0.07}\tanh\left(\frac{\mu\sigma_n}{HV/0.07}\right)$	(2.31)
Childs and Maekawa (1990)	$\tau_f = m_f k\left[1 - \exp\left(-\frac{\mu\sigma_n}{m_f k}\right)^n\right]^{1/n}$	(2.32)
Sekhon and Chenot (1993)	$\tau_f = -\alpha K\|\|v_f\|\|^{p-1}v_f$	(2.33)
Yang and Liu (2002)	$\tau_f = \sum_{k=0}^{4}\mu_k {\sigma_n}^k$	(2.34)

ness (eq. 2.31), sliding speed contribution (eq. 2.33) and polynomial approximation of normal and frictional stresses towards friction coefficient estimation (eq. 2.34).

The unsatisfactory results when it comes to friction estimation, has been promoting the benchmarking of existent models as well as its correction with the development of novel approaches. Knowing that friction effect can be divided into its adhesion and mechanical contributions (interlocking and plastic deformation), Grzesik (1999) has estimated the adhesion term, proposing an estimation approach which includes its significant contribution. Regarding slide/stick region models, Arrazola and Özel (2010) points out that the major drawback relates to the uncertainty of the material's shear stress, as it is influenced by cutting conditions. Based on Zorev's approach, Zhou (2014) proposes a novel friction estimation that accounts for the chip stagnation layer. Cristino et al. (2010) found that metal cutting under oxygen atmosphere results in higher friction values, chip compression factors and chip curvature radius as well as lower shear plane values, suggesting that surface films in freshly cut surfaces can influence chip formation. It has been noted by several authors that workpiece material, cutting tool details, lubrication and atmosphere all influence friction coefficient values (Grzesik and Nieslony, 2004; Childs, 2006; Puls et al., 2014; Rosa et al., 2019), suggesting the idea that, much like materials' damage and plastic behaviour, friction should be subject of thorough constitutive modelling. Friction assessment is commonly led through experimental instrumented machining operation (mostly turning, but also milling), through cutting force, chip dimensions and

contact surface measurements. The distinction between sliding and sticking regions is, however, challenging in real cutting conditions. Interrupted tests allied to the usage of surface topography, element mapping and mass spectrometry techniques seem to be a good approach towards a better friction estimation (dos Santos et al., 2017; M'Saoubi and Chandrasekaran, 2005).

2.1.5. Temperature distribution analytical modelling

The cutting temperature fields and heat partition predictions are of extreme difficulty, given the very challenging techniques for temperature measurement in machining operations, hindering the validation of any suggested model. Nonetheless, the topic has been subject of extensive research, as illustrated by the review and pioneering work of Komanduri and Hou (2001). Based on previous analytical models of Hahn (1951) and Chao (1953), the authors have proposed an analytical model that consists of a moving band heat input that is a large fraction of the mechanical work input to predict the temperature field. This approach has been extensively used and enhanced by many researchers, as reviewed by (Arrazola et al., 2013). It is well established that there are three heat sources (generated by mechanical energy) in the metal cutting phenomenon, being (i) at the primary deformation zone, due to chip formation; (ii) at the secondary zone due to tool-chip sliding and (iii) at the tertiary zone, due to tool-workpiece sliding.

In order to understand the relative contribution of each heat source Astakhov (1998) has highlighted that the heat balance, Q_b, is of utmost importance given that practically all of the mechanical energy associated with chip formation ends up as thermal energy and can be expressed as the sum of three components, as shown in eq. 2.35:

$$Q_b = Q_c + Q_w + Q_t \tag{2.35}$$

where Q_c is the thermal energy transported by the chip, Q_w is the thermal energy conducted into the workpiece and Q_t is the thermal energy conducted into the tool. In machining of many ductile materials, heat source of primary deformation zone is the strongest accounting on 65–90% of the total thermal energy generated so that 10–35% of thermal energy is generated due to friction over the secondary and tertiary zones (Astakhov and Outeiro, 2019). The results of actual temperature measurements in orthogonal cutting of conditions (AISI1045 with a carbide tool) has been conducted by Shaw (2005), which illustrate a multitude of results where the workpiece is at much lower temperature than the chip. Heat advection (heat is transported with the chip) explains the relative lower temperatures of workpiece in such proximity to the main heat source (Astakhov, 2012).

The idea that the metal cutting is a (relative) cold-working process is coherent with Zorev (1966), who did not consider temperature a relevant aspect in metal cutting. Through similar thermal energy balance (refer to eq. 2.35) the author estimated that maximum temperatures at the

end of chip formation zone would range 300°C, which accounts negligible reduction of mechanical performance for plain and alloyed steels Abushawashi (2013).

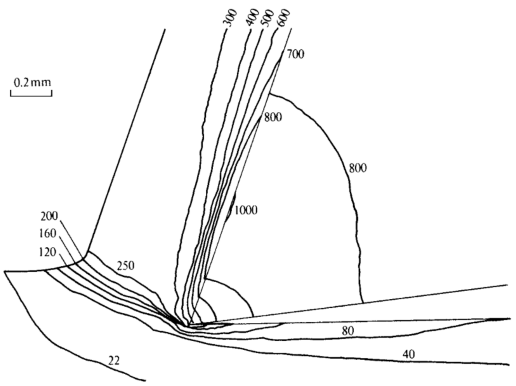


Figure 2.7: Measured temperature distribution in dry orthogonal cutting of AISI 1045 with carbide tool (Shaw, 2005).

2.1.6. Chip formation mechanisms

Unlike most manufacturing processes, metal cutting is generally perceived as purposeful material fracture (Astakhov, 1998). The tool induces severe shearing stress which forces the workpiece material above the cutting edge to plastically flow as a chip. The morphology, sequence and overall deformation of the chip during its flow can be a good measure of the cutting performance and material behaviour. Continuous chip formation (figure 2.8a) relates to an uniformly structured chip that slides along the rake face in a stationary flow, with presumably constant friction conditions. High cutting speeds, low friction coefficient at the tool-chip interface, positive rake angles as well as small uncut chip thickness promote its occurrence. This chip formation mechanism is commonly undesirable due to the enhanced frictional heat (possibly lower tool life) and also chip curling which may undermine surface quality of generated surface. Rake surfaces with chip breaking grooved geometries are commonly employed towards this effect minimization (Kim et al., 2009). Chip adhesion to the tool rake face and cutting edge may occur in this type of chip formation, which is generally undesirable due to promoting excessive tool wear and undermining surface quality, given that

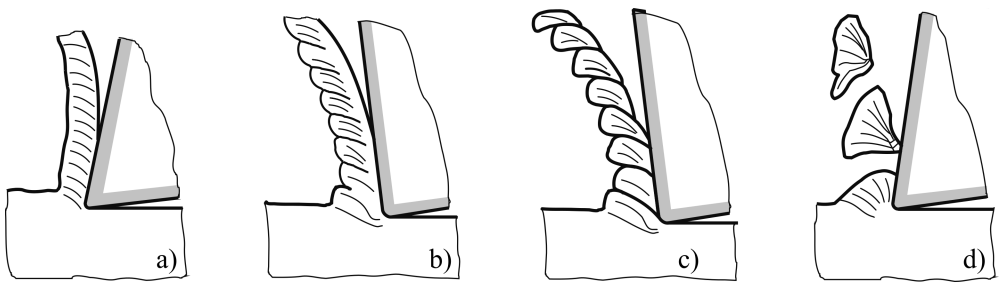


Figure 2.8: Basic chip formation mechanisms (Toenshoff and Denkena, 2013).

cutting edge sharpness is compromised. Although it may still be considered continuous, lamellar chip formation (figure 2.8b) is characterized by is cyclical behaviour due to uneven deformation. Friction variation, namely sticking versus slipping, motivated by vibration is commonly pointed as a reason for its occurrence. Thermomechanical instability can also contribute to such chip formation mechanism. This is the particular case of shear bands. The term has been coined by Zener and Hollomon (1944) and in metal cutting it refers to the cyclical accumulation of plastic flow promoted by material thermal softening due to strain and strain rate localization near primary and secondary cutting zones. The shear bands tend to occur when machining high-strength materials with high ductility (Klocke, 2011). Segmented chip formation (figure 2.8c) can be seen as a particular case where a strong occurrence of this (or similar effects) cause partial chip material detachment and usually arise for bigger uncut chip thickness (Toenshoff and Denkena, 2013). Discontinuous chip formation is a typical mechanism of brittle materials. Excessive uncut chip thickness, low cutting speeds and small rake angles may contribute to its occurrence.

2.2. Numerical simulation of metal cutting

The challenging task that the modelling of real machining operations represents, allied to the appearance of more powerful numerical methods has resulted in an indubitable preference of researchers for finite element modelling (FEM). Moreover, it has enhanced the benchmarking of the already-existent analytical models and promoting the development of more predictive approaches with a smaller degree of abstraction. The predictive potential when it comes to, for instance, loads, surface integrity, tool life, surface roughness and chip evolution is highly appreciated in the development of new cutting tools. In addition it consists of a relatively quicker and cheaper alternative to experimental testing. The need for an thorough definition of material behaviour (plasticity, friction and damage) can be seen as a limitation. Another limitation is the numerical portrayal of the extreme conditions that are characteristic of cutting, such as the large element deformation and friction definition.

2.2.1. Numerical formulations

Two primary fundamental formulations are usually employed in the numerical simulation of metal cutting. The most used is the Lagrangian formulation, in which the mesh deforms in time with the material. Inversely, with the Euler formulation the mesh is fixed in space (as a control volume). The latter formulation is standard for Computational Fluid Dynamics (CFD) and one of its most relevant shortcomings is the need for prior definition of the chip flow geometry (Arrazola et al., 2014). On the other hand, unlike Lagrangian, it easily deals with high deformation and allows

for long duration cutting simulations with less computational cost, which is crucial for predicting, for example, temperature distribution in steady state machining which allow to infer on tool-wear. Remeshing criteria are typically used in Lagrangian formulation in order to minimize element distortion at the cost of an increased CPU time. It is also important to correctly adjust its intensity and frequency to ensure the accuracy of the obtained results, as there is inevitable field data loss in mesh transition (Ducobu et al., 2016). The combination of the advantages of both classical formulations has resulted in hybrid approaches such as the Arbritary Lagrangian-Eulerian (ALE) in which the mesh is allowed to move independently (arbitrarily) from material motion (Adetoro and Wen, 2010) and Coupled Lagragian-Eulerian (CEL) in which the workpiece and tool are described by Eulerian and Lagrangian formulations, respectively (Ducobu et al., 2016). Figure 2.9 illustrates the usage of ALE formulation with distinct combination of boundary conditions. Despite the focus of this dissertation on FEM, it is important to highlight the importance of meshless methods, such as smooth particle hydrodynamics (SPH). Its predictability is, in general, lower than ALE or Lagrangian FEM, which explains its exclusivity to cases with severe deformation and element distortion (Zetterberg, 2014). Regarding the solution methods it is generally accepted that for large plastic deformation

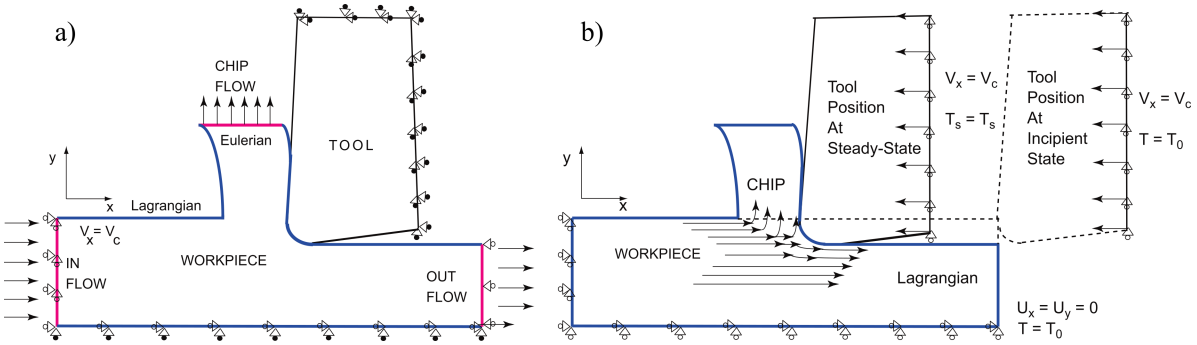


Figure 2.9: Illustration of ALE formulation with mixed boundary conditions (a) and pure Lagrangian boundary conditions (b) (Arrazola and Özel, 2010).

implicit time integration is prevailing. On the other hand, when the simulation includes highly dynamic applications (e.g. cutting, crashworthy simulation), explicit time integration is commonly applied. In this solution method, quantities at the time step $t + \delta t$ are estimated based solely on t, meaning that for a stable process, time step is defined by minimum elastic wave time scale, which in turn is dependent on the sonic velocity, c of the material, that depends on Young's Modulus, E and density, ρ, as depicted in eq. 2.36 for solids (Klocke, 2011). Artificially increasing the materials' density - mass scaling - can be a viable technique towards computing time minimization, through time step increase.

$$c = \sqrt{E/\rho} \tag{2.36}$$

2.2.2. Material modelling

The numerical simulation of most varied manufacturing processes requires a constitutive model definition, since they establish the flow stress in function of strain. Material hardening can be modelled by many popular equations (refer to table 2.3), as is the case of Ludwik-Hollomon, Swift, Voce and the combination of the last two (eqs. 2.37 to 2.40). However, due to the extreme strain, strain rate and temperature conditions of metal cutting, more complete models are used in metal cutting. Johnson and Cook (1985) have proposed an identical hardening to Ludwik (first term), including the viscoplasticity and temperature effects with the second and third term, respectively. The small number of parameters and relatively simple calibration contribute to extensive usage of this model in metal cutting simulation. Despite its popularity, stress values at very high strain rates are inaccurately depicted, as noted by Sima and Özel (2010) who have reviewed and benchmarked distinct modified versions of the Johnson Cook (JC) material model. Most modifications relate to the flow stress softening for higher strains, which enables the portrayal of adiabatic shear bands without considering a damage model. Towards the modelling of H13 tool steel, Umbrello et al. (2008) suggested a modified-JC model with incorporated hardness effect. Maekawa et al. (1983) have proposed an integral term that accounts for the loading history with the coupled effect of strain rate and temperature. Incremental tests are required for the calibration of this model. Silva et al. (2012), through innovative electromagnetic interrupted compression testing techniques, have also developed a loading path dependent model, given the identified significant influence on materials stress response.

Unlike empirical, physically-based constitutive models are based on microstructural aspects that control plastic deformation. Their usage is, however, limited due to the challenging calibration and parameter identification, requiring precisely controlled experiments. Based on dislocation mechanics theory and crystal structure of materials, the model proposed by Zerilli and Armstrong (1987) incorporates the effect of strain hardening, strain rate hardening and thermal softening with reasonable accuracy, being extensively used in metal cutting simulation. Its questionable suitability for very high temperature and low strain regimes (Samantaray et al., 2009) has been promoting its modification by several authors (Abed and Voyiadjis, 2005). Despite the intricate calibration, Follansbee and Kocks (1988) have developed the Mechanical Threshold Stress (MTS) model that accounts for recrystallization and dislocation mechanisms under dynamic loading. Svoboda et al. (2010) have compared this model with the JC model in the numerical simulation of orthogonal cutting of 316L. Despite the good predictability, extrapolation outside the calibration range may give unreliable results (Wedberg et al., 2012).

Recent trends in constitutive modelling aiming machining simulation consider the stress state dependency on both flow stress and damage models. In fact, the thorough review by Melkote et al.

Table 2.3: Constitutive equations typically used in plasticity material modelling Melkote et al. (2017); Silva (2016).

Model	Constitutive equation	
Ludwik (1909)	$\sigma = \sigma_y + K{\varepsilon_p}^n$	(2.37)
Voce (1948)	$\sigma = k_0 - Q(1 - e^{-\beta_v \varepsilon_p})$	(2.38)
Swift (1952)	$\sigma = K(\varepsilon_0 + \varepsilon_p)^n$	(2.39)
Swift-Voce	$\sigma = \alpha\Big[K(\varepsilon_0 + \varepsilon_p)^n\Big] + (1-\alpha)\Big[k_0 - Q(1 - e^{-\beta_v \varepsilon_p})\Big]$	(2.40)
Maekawa et al. (1983)	$\sigma = f(\dot{\varepsilon}, T)\Big(\int_{T,\dot{\varepsilon}} e^{\frac{K}{n}T}\dot{\varepsilon}^{-\frac{m}{n}} d\varepsilon_p\Big)^n$	(2.41)
Johnson and Cook (1985)	$\sigma = (A + B{\varepsilon_p}^n)\Big[1 + Cln\frac{\dot{\varepsilon}}{\dot{\varepsilon_0}}\Big]\Big[1 - \Big(\frac{T - T_0}{T_m - T_0}\Big)^{m_t}\Big]$	(2.42)
Zerilli and Armstrong (1987)	$\sigma = \sigma_a + Be^{-\beta T} + \beta_0 \varepsilon_p^{1/2} e^{-\alpha T}$ $\beta = \beta_0 - \beta_1 ln\dot{\varepsilon}$ $\alpha = \alpha_0 - \alpha_1 ln\dot{\varepsilon}$	(2.43)
MTS Follansbee and Kocks (1988)	$\sigma = \sigma_a + \sigma_{th}$ $\sigma_a = \alpha G b \rho^{1/2}$ $\sigma_{th} = \sigma_0\big[1 - \big(\frac{kT}{g_0 G b^3} ln\frac{\dot{\varepsilon_0}}{\dot{\varepsilon}}\big)^{(1/q)}\big]^{(1/p)}$	(2.44)
Silva et al. (2012)	$\sigma = (A + e^{m\varepsilon_p}{\varepsilon_p}^n)(B + Cln[D + \dot{\varepsilon}])$	(2.45)
Bai and Wierzbicki (2008)	$\sigma = \sigma(\varepsilon_p)[1 - c_\eta(\eta - \eta_0)]\big[{c_\theta}^s + ({c_\theta}^{ax} - {c_\theta}^s)\big(\lambda - \frac{\lambda^{m+1}}{m+1}\big)\big]$	(2.46)
Buchkremer et al. (2014)	$\sigma = [\sigma(\varepsilon_p)\big(c_{\dot{\varepsilon}}^1 ln\dot{\varepsilon} + c_{\dot{\varepsilon}}^2\big) + c_{\dot{\varepsilon}}^3\dot{\varepsilon}][c_T^1 e^{c_T^2 T} + c_T^3]\big[{c_\theta}^s + ({c_\theta}^{ax} - {c_\theta}^s)\big(\lambda - \frac{\lambda^{m+1}}{m+1}\big)\big]$	(2.47)

(2017), points out that the role of stress in plastic yielding and fracture should definitely not be ignored, despite the more challenging multiaxial loading experiments, when compared to the typical uniaxial axisymmetric geometries. Pressure-dependent yield has been initially proposed by Drucker and Prager (1952) towards the modelling of soil and granulate materials and has shown to be applicable to metal cutting (Gain et al., 2019). State-of-stress dependency was firstly proposed by Bai and Wierzbicki (2008) but only recently has started to be explored in machining simulation by Buchkremer et al. (2014) who suggest a Lode angle parameter ($\bar{\theta}$) sensitive model that includes the typical effects of strain, strain rate and temperature on the longitudinal turning of AISI1045 steel. Lode angle, θ, is related to the normalized third deviatoric stress invariant, ξ through eq. 2.48 (Bai and Wierzbicki, 2008). Since Lode angle range is $0 \leq \theta \leq \pi/3$, the range of ξ is $-1 \leq \xi \leq 1$, meaning

that the Lode angle parameter can be normalized by eq. 2.49, resulting in a range of -1$\leq \bar{\theta} \leq$ /1

$$\xi = \left(\frac{r}{q}\right)^3 = \cos(3\theta) \tag{2.48}$$

$$\bar{\theta} = 1 - \frac{6\theta}{\pi} = 1 - \frac{2}{\pi}\arccos\xi \tag{2.49}$$

Similarly, but including stress triaxiality (η) effect, Cheng et al. (2019a) proposes a state-of-stress dependent towards the cutting simulation of Ti6Al4V. Stress triaxiality (η) is defined as the ratio between hydrostatic von Mises stress (σ_m) and the equivalent stress ($\bar{\sigma}$), as shown in eq. 2.50. The usage of different types of specimens with variable grooves enables the characterization of a material's plastic behaviour under distinct state-of-stress, as shown in the conceptual representation of η and $\bar{\theta}$ of figure 2.10.

$$\eta = \frac{\sigma_m}{\bar{\sigma}} \tag{2.50}$$

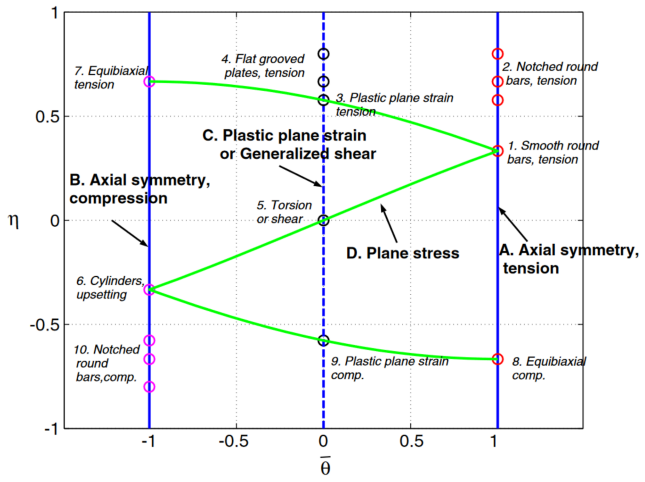


Figure 2.10: Conceptual representation of the initial stress states on the η, $\bar{\theta}$ plane (Bai and Wierzbicki, 2008).

2.2.3. Chip separation modelling

The purposeful fracture in metal cutting imposes the need for the definition of a chip separation criteria. These can be typically divided in two categories (Huang and Black, 1996): physically-based and geometrical. Zetterberg (2014) has thoroughly listed the most used techniques as well as their advantages and disadvantages, as described in table 2.4. Regarding non-physical methods, the predefinition of a line of elements that act as a sacrifice layer (also known as split line), promoting chip separation throughout node split or element deletion on that path is a commonly used approach.

Table 2.4: Approaches towards chip separation modelling Zetterberg (2014).

Chip separation method	Advantages	Disadvantages
Sacrifice layer	Easy to control separation	Non-physical
Remeshing	Absence of non-physical criterion	Computationally costly
Eulerian formulation	Absence of non-physical criterion	Prior chip geometry definition
Meshless method	Absence of non-physical criterion	Less accurate load prediction
Damage model	Physically-based	Mass loss

The separation can be performed based on different criteria, being the most common a threshold value for the distance between the tool and the immediately ahead nodes. Sometimes, node splitting or deletion is based on critical stress, strain or energy threshold values. Remeshing procedure consists on the application of a new mesh when a specific criterion (typically element distortion) is verified. Despite coming at the cost of high computational time, this method enables chip separation without the definition of a damage model. Moreover, the fact that there is no need to use a non-physical criterion as well as the absence of element deletion (which would cause mass loss) can be seen as advantages. Similarly, the Eulerian formulation and the meshless methods do not require the usage of a non physical method. There is, however, important handicaps that relate to the prior definition of chip geometry and less accurate predictions, respectively. Lastly, the usage of a damage model implies its thorough identification and calibration so that the approach can be physically relatable. It is essential to apply very fine mesh sizes when using this approach in order to minimize mass loss, which is seen as the biggest disadvantage.

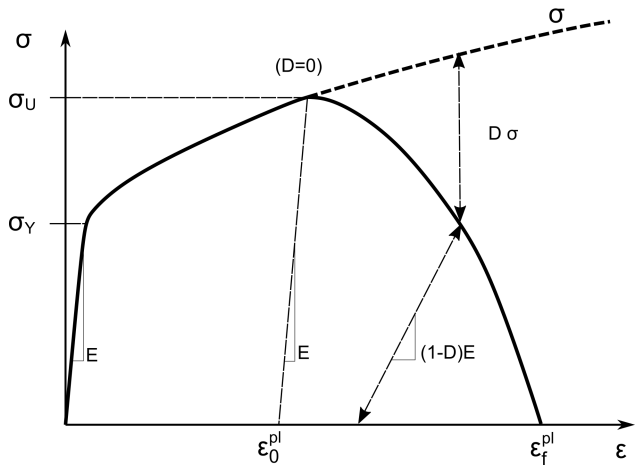


Figure 2.11: Typical stress strain curve of a material undergoing damage (solid line) and undamaged behaviour (dashed line) (Smith, 2009).

Figure 2.11 illustrates the generic stress-strain behaviour of a material undergoing damage (solid line) as well as its undamaged response (dashed line). Within the assumption of an elasto-plastic material with isotropic hardening, damage can be seen as a decrease of elastic properties of the material as well as stress softening. Damage models determine the point of damage initiation (D=0), though the definition of equivalent plastic strain at the onset of damage, ε_0^{pl}, at which the damage variable, D, assumes a positive value. From that point ($0>D\geq1$) the material's stress-strain is modelled by a damage evolution law. Similarly to plastic behaviour of materials, a wide range of damage models is available in literature. It is, nonetheless, important to highlight their rather challenging calibration, given that material's failure a function of strain, strain rate and temperature. The lack of knowledge regarding the influence of those extreme conditions on damage motivates the usage of simple models such as Cockcroft and Latham (1968) and its normalized model, which take into account the maximum principal stress. Based on the void growth and coalescence, Rice and Tracey (1969) and McClintock (1968) have developed a stress triaxiality dependant models that have been largely used due to their simplicity. Johnson and Cook (1985) developed a fracture model that is sensitive to strain, strain rate and temperature. Its simplicity and capability of portraying realistic fracture initiation in conditions of high strain, stress and temperature distributions has motivated its extensive usage. Wilkins et al. (1980) proposed the first fracture model sensitive to

Table 2.5: Most common damage models.

Model	Constitutive equation	
Cockcroft and Latham (1968)	$D=\int_0^{\varepsilon_f}\sigma_1 d\varepsilon$	(2.51)
McClintock (1968)	$D=\int_0^{\varepsilon_f}\left[\frac{2}{\sqrt{3}(1-n)}\sinh\left(\frac{\sqrt{3}(1-n)}{2}\frac{\sigma_1+\sigma_3}{\sigma}\right)+\frac{\sigma_1-\sigma_3}{\sigma}\right]d\varepsilon$	(2.52)
Rice and Tracey (1969)	$D=\int_0^{\varepsilon_f}Ae^{\left(\frac{3\sigma_m}{2\sigma}\right)}$	(2.53)
Wilkins (1978)	$D=\int_0^{\varepsilon_f}w_1w_2d\varepsilon$ $w_1=\frac{1}{1+\alpha\sigma_m}$ $w_2=(2-A_s)^{\beta}$	(2.54)
Johnson and Cook (1985)	$D=\left(d_1+d_2e^{d_3\frac{\sigma_m}{\sigma}}\right)\left[1+d_4ln\frac{\dot{\varepsilon}}{\dot{\varepsilon}_0}\right]\left[1+d_5\left(\frac{T-T_0}{T_m-T_0}\right)\right]$	(2.55)
Bao and Wierzbicki (2004)	$\varepsilon_f=\begin{cases}d_1\left(\eta-\frac{1}{3}\right)^{d_2}, & -1/3<\eta\leq0\\ d_3\eta^2-d_4\eta+d_5, & 0<\eta\leq0.4\\ d_6\eta^{-1}, & 0.4<\eta\leq0.95\end{cases}$	(2.56)
Bai and Wierzbicki (2008)	$\varepsilon_f=\left[\frac{1}{2}(D_1e^{-D_2\eta}+D_5e^{-D_6\eta})-D_3e^{-D_4\eta}\right]\bar{\theta}^2$ $+\frac{1}{2}(D_1e^{-D_2\eta}+D_5e^{-D_6\eta})\bar{\theta}+D_3e^{-D_4\eta}$	(2.57)

the deviatoric stress ratio A_s, which is related to the Lode angle parameter, aiming the simulation of penetration and perforation processes.

Bao and Wierzbicki (2004) suggested an empirical fracture model that takes into account stress triaxiality in the definition of fracture strain, claiming that apart from strain intensity it is the most important factor in ductile fracture. They have also suggested a "cut-off" value in ductile fracture, meaning the absence of damage for $\eta < -1/3$. Their model is, thus, defined into three branches, depending on the η regime. With the realization of Lode angle parameter dependence on the fracture of certain materials, Bai and Wierzbicki (2008) proposed a novel 3D fracture locus that is η and $\bar{\theta}$ dependent. Through the calibration of parameters D_1 to D_6 (eq. 2.57) upper ($\varepsilon_f^{(+)}$), lower ($\varepsilon_f^{(-)}$) and intermediate ($\varepsilon_f^{(\circ)}$) boundary limits (refer to figure 2.12) are defined, establishing the fracture behaviour in specific state-of-stress conditions.

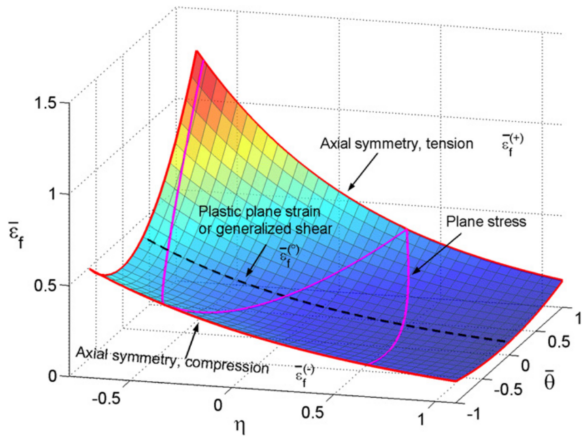


Figure 2.12: Three dimensional asymmetric fracture locus proposed by (Bai and Wierzbicki, 2008).

Liu et al. (2013) have benchmarked the several damage models towards their applicability to metal cutting. They have found the both Johnson-Cook and the empirical Bao-Wierzbicki fracture model (when coupled with a strain-rate sensitive term) result in realistic prediction of the metal cutting phenomenon. The authors have also tested the models proposed by Wilkins et al. (1980) and Cockcroft and Latham (1968) which fail to portray chip formation in its current form (requires proper modification). Moreover, the authors have concluded that the usage of a damage evolution law (fracture energy) provides more reliable results than not using one, which is coherent with Atkins (2003) theory of energy expenditure in the generation of new surfaces. The method proposed by Hillerborg et al. (1976) combines fracture mechanics and finite element analysis and may be regarded as a material parameter capable of expressing the energy absorption relative to crack opening.

$$G_f = \int_{\varepsilon_0^{pl}}^{\varepsilon_f^{pl}} L\sigma_y d\varepsilon^{pl} \tag{2.58}$$

It was firstly used by Mabrouki et al. (2008) in orthogonal cutting simulation and has been continuously employed in metal cutting simulation (Abushawashi, 2013; Cheng et al., 2019b). The fracture energy is depicted in eq. 2.58, where L corresponds to the characteristic length, associated with an integration point. The post damage initiation softening response is characterized by a stress–displacement response rather than a stress–strain response Smith (2009). Based on a fracture mechanics perspective, Mabrouki et al. (2016) has implemented the coexistence of the two fracture modes (I and II) on the orthogonal cutting model, using two different values of fracture energy ($G_{f,I}$ and $G_{f,II}$). Figure 2.13 illustrates fracture modes I and II on the orthogonal cutting model, which correspond to opening normal to the fracture plane and sliding parallel to the fracture plane, respectively.

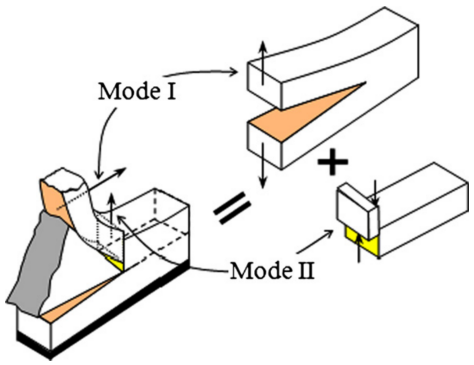


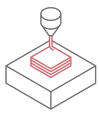
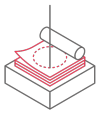
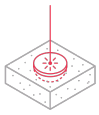
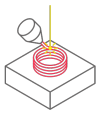
Figure 2.13: Implementation of fracture modes I and II on the orthogonal cutting model (Mabrouki et al., 2016).

Chapter 3. Literature review II: LPBF-manufactured high strength steels

3.1. Metal additive manufacturing technologies overview

In contrast to subtractive manufacturing technologies, AM consists of a material addition process, usually layer upon layer, in order to produce parts from three-dimensional models. The MAM systems are generally characterized according to the state of feedstock material (powder, wire, filament or sheet) and energy source (mainly laser, electron or arc). Despite the multitude of AM processes currently available, the manufacture of metallic parts falls into 5 categories, described in table 3.1, according to the ISO/ASTM52910-17 standard. Some examples of manufacturer-related system nomenclatures are also displayed. It is important to note that 3 of the 5 categories are seen as multi-step processes given that the shape and final material properties are not attained in a single operation.

Table 3.1: Classification, description and most common systems' nomenclatures of MAM processes, adapted from Redwood et al. (2017).

MAM Processes	Material extrusion	Binder jetting	Sheet lamination	Powder bed fusion	Directed energy deposition
					
Description	Material is selectively dispensed through a nozzle or orifice	Liquid bonding agent is selectively deposited to join powder materials	Material sheets with specific contour are bonded to form an object	Thermal energy selectively fuses regions of a powder bed	Thermal energy fuses materials by melting as the material is deposited
Systems	- FDM	- BJ	- UAM	- SLM - DMLS - EBM - LBM - SLS - LMD - LaserCUSING	- DMD - DM - LENS - LC - LDW

Material extrusion and binder jetting require washing and sintering stages. Sheet lamination involves welding mechanisms for consolidation and CNC contour milling for ensuring the parts' shape. Single-step processes allow for manufacturing near fully dense parts, in one single stage,

thorough material (re)melting without the need for further sintering and curing. These processes can be divided in two categories, powder bed fusion (PBF) and directed energy deposition (DED), which constitute the most often used AM process in the manufacture of metal components (Herzog et al., 2016). Due to that fact, and given the similarity in processing conditions between both processes, this literature review focuses on aspects regarding PBF and DED, especially the former, as well as the associated need for post-processing of the as-built parts.

In DED an energy source is used to melt the feedstock material, which is deposited onto the desired location, forming a part's layer. A nozzle is typically attached to the energy source, which is mounted on a multi-axis arm, allowing for its movement around a table that can also be animated, enabling the creation of complex geometries. Additionally to the production of new parts, this technology is well suited for component repair or functionality improvement. Since flat surfaces are not a requirement for starting the process, new (different) material can be deposited on damaged or worn parts. Figure 3.1 displays two examples of powder-fed (a) and wire-fed (b) configurations. These require a fully inert chamber or shielding gas for the protection of the material being deposited. The latter is more adequate for less reactive metals. Despite the large volume of argon or nitrogen, a fully inert chamber may be necessary for the processing of highly reactive alloys. In powder-fed systems, the flow control of powder particles is ensured via a carrying gas (typically helium). Moreover, electron beam systems should be performed in a vacuum to prevent deflection of the electron beam by the air molecules (Zenou and Grainger, 2018).

Directed energy deposition is the fastest of MAM processes. The typical high build rates make it suitable for the fabrication of high-volume parts, with a compromise on precision and detail. For that reason post-processing is imperative, meaning that the attained raw shapes are submitted to a final (often extensive) machining stage for improving surface quality. The fact that the biggest commercial offer of additive/subtractive hybrid systems is based on material deposition technologies (Chong et al., 2018), supports the need for machining in DED. Residual stresses relief through heat treatment is generally also part of a components' post-processing stage.

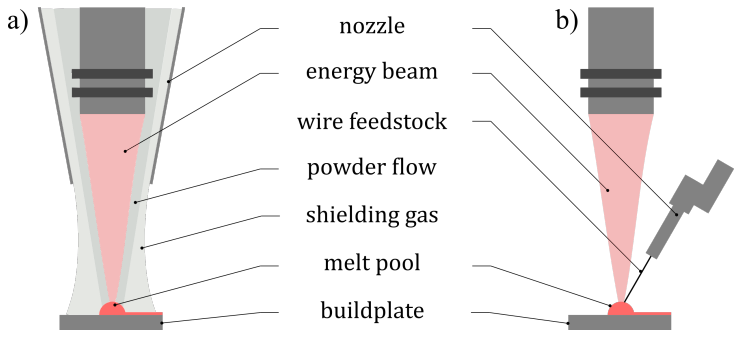


Figure 3.1: Configuration examples of directed energy deposition: powder-fed system with shielding gas (a); wire-fed (laser or electron beam)system (b).

3.1.1. Powder bed fusion

In powder bed systems a heat source fuses thin layers of metal powder according to the desired shape. Three main stages constitute this MAM process (refer to figure 3.2): (i) powder is transferred from the supply container to the build plate, forming a powder layer; (ii) a laser or an electron beam fuse the surface layer (re-melting under-layers) according to the defined scan path; (iii) build plate is lowered (the displacement of a layer thickness) allowing for cycle repetition until the part is completed. Unused powder is commonly sieved and reused. Similarly to the DED, the process is operated under a vacuum or inert gas atmosphere to prevent oxidation of reactive metal powders and to minimize moisture and air exposure. In order to enhance the adhesion of the first layer, build plate is normally heated up to approximately 200°C in laser and 700°C, in electron beam systems. The smaller temperature gradients contribute to a decrease in residual stresses. Build plate material is generally of the same material as the processed metal powder, ensuring metallurgical compatibility as well as identical heat expansion, minimizing residual stresses (Yap et al., 2015). Once the part is completed, it is removed from the powder bed. The attached powder particles are manually or mechanically removed. EDM is typically used for separating the part from build plate (Murr et al., 2012).

The promising outlook of laser powder bed fusion (LPBF) is referenced by Khairallah et al. (2016) and well illustrated by the considerable amount of distinct manufacturers' solutions as well as the wider choice of materials and available data regarding its processing. Hence, it has been selected for building the material samples throughout this research work. The lower build rates (layer thickness between 20 and 200μm), smaller beam diameters and finer powder particle sizes allow for higher geometrical resolution when compared with electron powder bed fusion (EPBF) (Patterson et al., 2017). Solid state lasers (e.g. fibre lasers) with powers ranging between 20W and 1kW are commonly used in metallic processing. Mirrors mounted on galvanometer scanners allow for the deflection of the laser beam (Risse, 2019). Despite limited to those systems inertia, scan speeds can reach values of 15 m/s (Herzog et al., 2016).

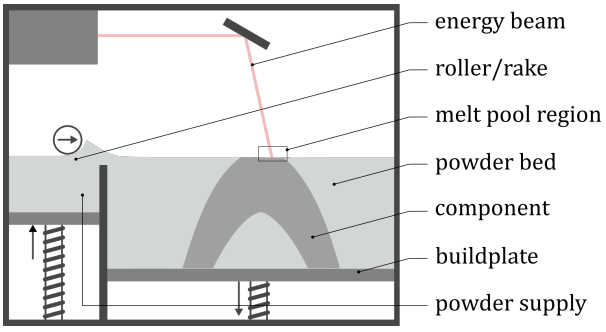


Figure 3.2: Schematic illustration of laser powder bed fusion systems, adapted from Frazier (2014).

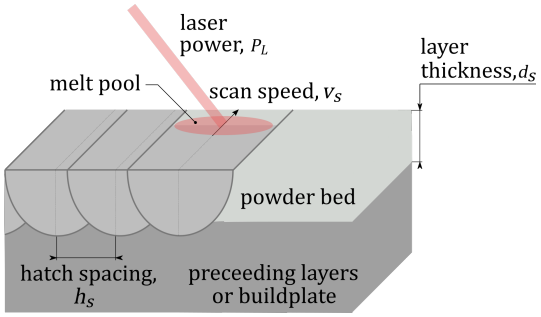


Figure 3.3: Schematic illustration of melt pool region in laser powder bed fusion systems, adapted from Yap et al. (2015).

The usage of adequate processing parameters allows for producing defect-free parts, with identical mechanical properties to wrought metals. Figure 3.3 illustrates the melt pool region in laser powder bed fusion, along with the definition of the main process parameters. The volumetric energy density (E_v) is often regarded an unified parameter capable of quantitatively identify adequate processing conditions and ensuring full part consolidation, through parameters optimization Carter et al. (2016). Table 3.2 shows some of the most applied methods. Due to the more complete characterization when compared to linear and surface methods (refer to eqs. 3.1 and 3.2, respectively), volumetric energy density (refer to eq.3.3) has been extensively used. Nonetheless, Bertoli et al. (2017) have reported its limitations in describing melt pool depth, which leads to the development of more sophisticated methods that rely on the normalised enthalpy values (eq.3.4) and account for laser efficiency and beam size diameter.

Table 3.2: Methods for quantification of processing parameters in LPBF.

Method	Equation	
Linear energy density (Wang et al., 2011)	$E_l = P_L/v_s$	(3.1)
Surface energy density (Kempen, 2015)	$E_s = P_L/(v_s h_s)$	(3.2)
Volumetric energy density (Yap et al., 2015)	$E_v = P_L/(v_s h_s d_s)$	(3.3)
Normalised enthalpy (Wu et al., 2014)	$\Delta H/h_m = \eta_a P_L/(\rho_m H_m \sqrt{\pi a r_d v_s})$	(3.4)

3.2. Impact of LPBF process on high strength steels

Favourable mechanical behaviour and structural integrity may be seriously hindered by the multitude of variables that characterize the LPBF process. Ensuring the smallest amount of defects on fully dense parts, typically with densities greater than 98% (Yap et al., 2015), is usually achieved through optimization of processing parameters and powder particles selection with appropriate attributes (namely shape and size distribution). LPBF steels present a distinctive mechanical behaviour when compared with the conventionally fabricated ones (cast, rolled, laminated, forged). Their peculiar microstructure, which originates the well known layer-based anisotropic behaviour,

as well as the unavoidable residual stresses, suggest particular attention. The impact of the most important LPBF variables is studied in this section, with special relevance to the 316L stainless steel and 18Ni300 maraging steel. The excellent cost-efficient mechanical strength allied to the good processability of 316L stainless steel (Bajaj et al., 2020), makes it one of the most additively manufactured materials. Moreover, when exceptional mechanical strength is required, maraging steels constitute the most viable additively manufacturable solution, especially due to their good weldability, promoted by the lack of carbon (Turk et al., 2019). The extensive usage of these steels contributes to a comprehensive literature regarding the most suitable processing conditions and the influence of the most important parameters.

3.2.1. Processing parameters

The primary concern when selecting processing parameters is ensuring minimum defects. That is commonly achieved through customization of the melt pool geometry, which can be predicted through analytical models (Bajaj et al., 2019). As denoted in the previous section, volumetric energy density, E_v constitutes a unifying parameter in LPBF. Zhang et al. (2017b) have studied its influence on the relative density of parts. For that, specimens with a certain deviation from optimal energy density conditions (E_{v0}) were manufactured through variation of the laser power, and their relative density was inspected via image analysis and Archimedes method. Figure 3.4 contrasts the measured with literature values and displays the metallographic images of each volumetric energy condition. A similar trend to literature can be identified, meaning a gradual decrease in part density until $0.7E_{v0}$ and a drastic drop around $0.5E_{v0}$, supported by the lack-of-fusion defects (irregular voids).

In LPBF, the melt pool depth is typically controlled by heat conduction through the previously deposited layers. Under certain conditions, the melting mechanism can change to keyhole mode

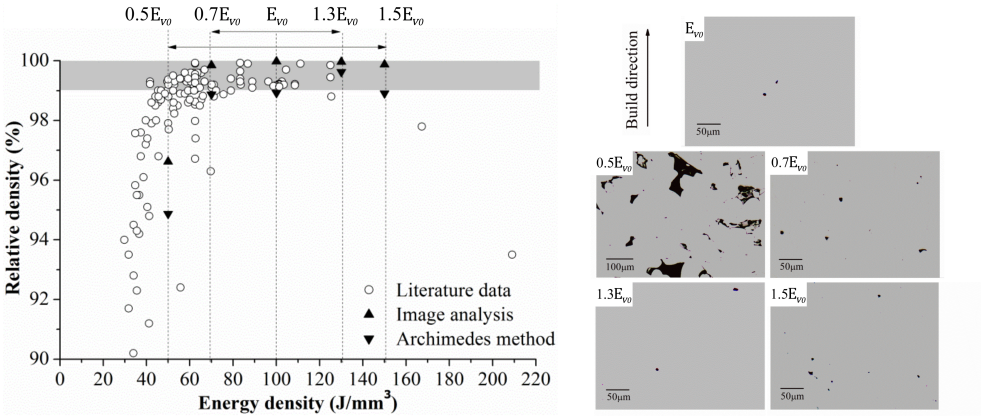


Figure 3.4: Relative density for distinct volumetric energy conditions from optimal conditions (E_{v0}) and respective optical metallographic images, for 316L stainless steel (Zhang et al., 2017b).

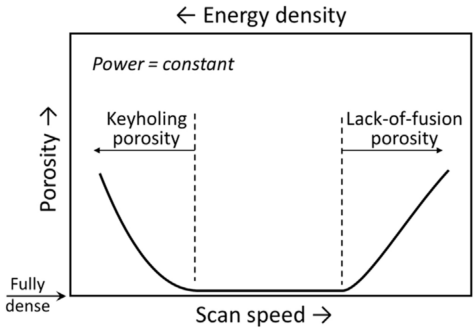


Figure 3.5: Porosity trend with changes in the scan speed (for fixed power) (Tang et al., 2017).

where depth is controlled by metal evaporation (King et al., 2014). Tang et al. (2017) have developed a melt pool geometry-based simulation model capable of predicting relative density. Build from the results of Gong et al. (2014), they report the typical trend in parts porosity (refer to figure 3.5), according to scanning speed settings, showing increased keyhole porosity for high energy density and lack-of-fusion at lower energy density parameters configurations (due to insufficient overlap of successive melt pools).

The identification of suitable parameters is a material-sensitive challenging task. As stated by Mukherjee et al. (2018) a careful selection of hatch spacing can minimize lack-of-fusion defects and distortion for a fixed set of parameters. In order to validate of their own numerical model, they examined the influence of processing parameters on common LPBF-processed alloys. Figure 3.6 shows the effect of hatch spacing and scan speed on the occurrence of lack-of-fusion defects. One can deduce that higher values of hatch spacing hinder appropriate fusion bonding between laser hatches, resulting in increased porosity. Due to exhibiting the smallest melt pools, the two considered alloys (SS316L and IN718) show a clearer sensitivity to the hatch spacing parameter. Concerning hatch spacing, it is also convenient to mention its crucial role in the surface quality of parts. Xia et al. (2016) have studied its influence on the IN718 alloy and noticed that the combined

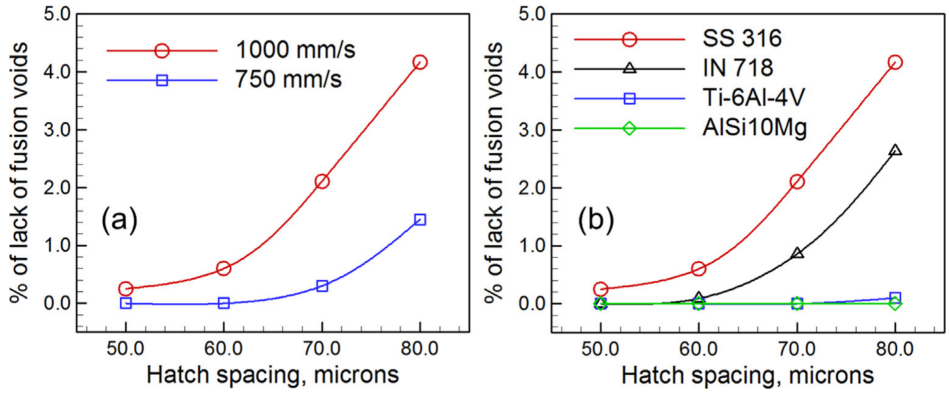


Figure 3.6: Influence of hatch spacing on the lack-of-fusion occurrence for the SS316L and two distinct scan speeds (a) and for 4 distinct alloys at a 1000m/s scan speed (b) (Mukherjee et al., 2018).

effects of the low dynamic viscosity and surface tension of the melt pool contribute to the transfer of molten metal towards previously deposited hatchs. Along with layer thickness, these two parameters have significant influence on surface topography (Lou et al., 2019). In the LPBF process, the latter is normally determined by maximum powder particle size. The minimum feature size is defined by layer thickness along building direction (Z) and by laser spot size (in the XY plane).

3.2.2. Laser scanning strategies

Scan strategy refers to the laser path during the melting process of each layer. While the contour of each layer is typically scanned using a spotted pattern contour (Sames et al., 2016), bulk is scanned according to a specific laser pattern. Some of the most used scan strategies are displayed in figure 3.7. Laser scanning strategy selection enables a more thorough control, quality and repeatability of the manufacturing process. For instance, vector orientation can be incrementally rotated for every layer, allowing for a minimization of residual stresses. Through thermo-mechanical numerical simulation, Parry et al. (2016) have demonstrated that for an isotropic stress field, long scan vectors should be avoided and their direction uniformly distributed. Using a similar analysis, Le et al. (2018) have shown that using a sequential scan strategy (all scan vectors have the same length and direction) results in a non-flat printed surface, contrarily to alternating scan. Bhardwaj and Shukla (2018) have shown distinct grain orientations in the microstructure of 18Ni300 for samples fabricated with and without 90° rotation in every other layer (in an alternating scan strategy). In order to avoid spatter defects (powder particles ejection during laser scan), Khairallah (2019) has developed a strategy that performs a gentle first run in order to promote particle adhesion, minimizing their mobility on a second effective laser scan. Other remelting strategies, such as laser polishing, have been studied by Demir and Previtali (2017) on the 18Ni300 maraging steel. They have concluded that such strategy, which consists of a superficial melting, provides a slightly improved surface quality and relative density. In contrast, due to the remelting, dimensional errors are induced and microstructures are coarser (slower solidification).

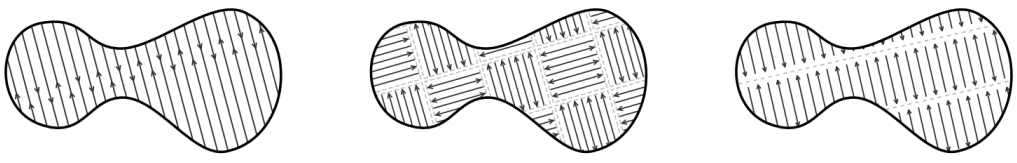


Figure 3.7: Usual laser scanning strategies in LPBF (Parry, 2018).

3.2.3. Microstructure

Due to the heat sources similarity, the structures of MAM may resemble the ones of multi-pass traditional welding processes. The rapid beam scanning of LPBF has, however, enhanced the flexibility of layered manufacturing, allowing for a higher degree of precision and customisation. The microstructure of additively manufactured metals is coined by successive melt pool structures, relative to laser fusion of the powder particles. These solidification structures are highly influenced by the temperature gradient (G) and solidification rate (R) and can be planar, cellular, columnar dendritic or equiaxed dendritic. Figure 3.8 shows the resulting solidification structure according to $G \times R$ and G/R parameters. While the former relates to the morphology of the solidification structure, the latter is associated with its size. Bertoli et al. (2017) have developed a model capable of predicting the solidification parameters (G and R) as a function of laser power and scan speed for the SS316L. Their model was calibrated using specimens manufactured through LPBF, with distinct P_L/v_s ratios. They have shown that, within realistic laser power and scan speed conditions, the resulting microstructure morphology is not affected. The same columnar-cellular microstructure was observed regardless of the processing conditions, despite some differences in its size.

Grain growth, from the boundary towards the centre of the melt pool is typically resultant from LPBF process. The fine columnar structures develop in the direction of maximum heat flow, which is normal to the solid/liquid interface. Choo et al. (2019) have studied the influence of laser power in the microstructure development of SS316L. For higher laser power configuration, flatter and wider melt pools are generated, and a marked vertical alignment of columnar grain formation is noticed (refer to figure 3.9a). Due to resulting in highly anisotropic behaviour, such microstructure is not desirable. Lower laser power can mitigate such effect, promoting radial grain formation (displayed in figure 3.9b), illustrating that tuning of processing parameters can contribute to an improved microstructure, hence increased mechanical strength.

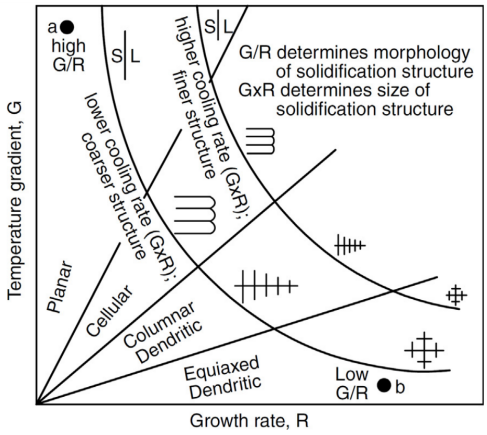


Figure 3.8: Effect of G and R on the morphology and size of solidification microstructure (Kou, 2003; DebRoy et al., 2018).

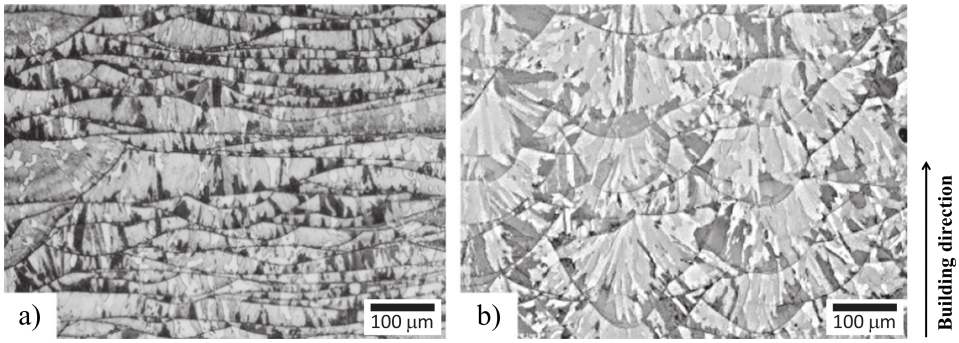


Figure 3.9: Metallographic image showing melt pool and grain formation for laser powers of 380W (a) and 200W (b), for equal scan speed (Choo et al., 2019).

Bajaj et al. (2020) have thoroughly reviewed the microstructure and mechanical properties of most common additively manufactured steels, comparing it with the conventionally fabricated. In figure 3.10 they present an overview of typical microstructures. For LPBF stainless steels, such as the 316L, microstructure is typically fully austenitic. In DED 316L, despite the austenitic dominant phase, a relatively small amount of ferrite "islands" (volume fraction of approximately 10%) tends to form at the boundary of austenite grains (Yadollahi et al., 2015). Regarding the microstructure of maraging steels, namely the 18%Ni, they present cellular/dendritic solidification structure when fabricated through both LPBF and DED. Their microstructure differs greatly form the conventionally manufactured maraging steels (which are fully martensitic) and is composed of of a martensitic matrix with small regions of retained austenite, as confirmed by Kempen et al. (2011) and Takata et al. (2018). That is due to the micro-segregation upon solidification, leading to inhomogeneity and locally differing phase stabilities, as stated by Jägle et al. (2017).

Large volume fraction of austenite in LPBF 316L and maraging steels is generally undesirable due to lowering the overall mechanical strength of the materials. However, the presence of austenite may trigger transformation induced plasticity (TRIP) effect (Jägle et al., 2014). This means that the retained austenite transforms to martensite upon plastic deformation, delaying a significant amount of work hardening, thus improving high strength-ductility ratios (Pereloma et al., 2016). Most literature regarding TRIP effect on maraging steels focuses on the heat treatment optimization towards improved ductility and mechanical strength. For instance, Conde et al. (2019) have studied the effect of different isothermal tempering cycles aiming for martensite to austenite reversion, showing that between 610 and 690°C significant reversion occurs with high thermal stability. Moreover, tempering at 690 °C caused massive and complete austenitization, resulting in low austenite stability upon cooling due to compositional homogenization.

Heat treatment can significantly improve the mechanical strength of LPBF maraging steels. In short, aging heat treatment grants outstanding combination of strength and toughness, due to hardening of the martensitic structure by intermetallic precipitation. Motivated by the fact that most machining stages of a component occur prior to heat treatment (enhanced machinability) the

processed materials in this research were accessed in their as-built condition.

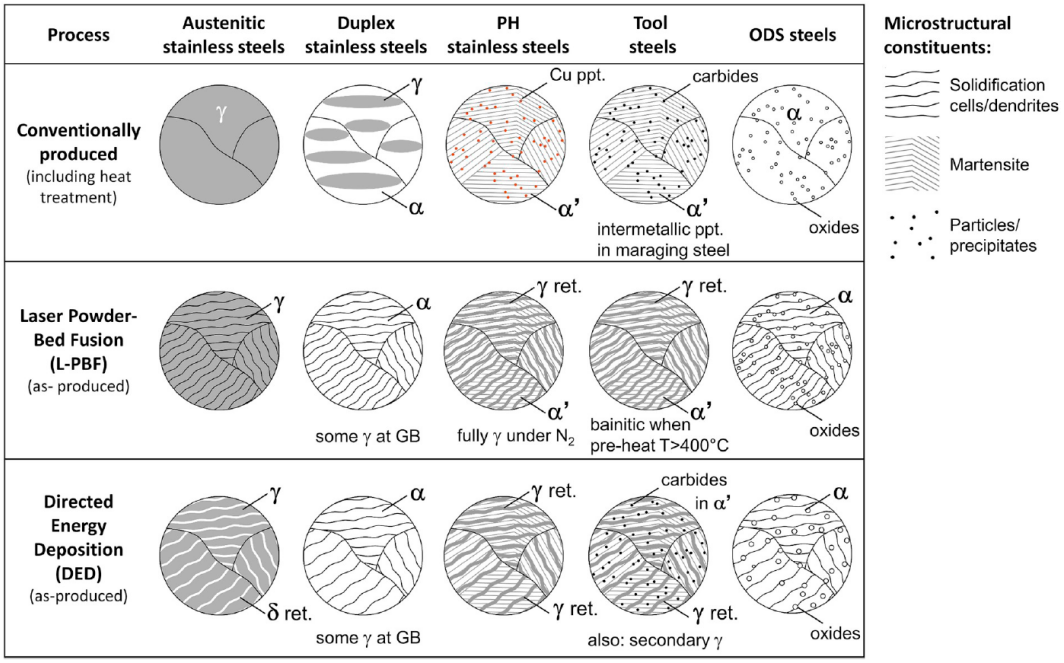


Figure 3.10: Microstructure of most common additively fabricated steels compared with conventional (Bajaj et al., 2020).

3.2.4. Residual stress generation and mitigation

The occurrence of residual stresses is strongly associated with the large thermal gradients inherent to the additive process and two mechanisms can be distinguished. The first results from the rapid heating of the upper surface and rather slow heat conduction, leading to a decrease in the material's strength. The underlying material restricts the expansion of the heated top layer, which develops compressive strains until the material is plastically deformed. In the cooling phase, a second mechanism induces residual stresses due to the shrinking caused by thermal contraction of the top layers which, again, inhibited by the underlying material, lead to tensile stress in the added top layer and compressive stress below, as stated by Mercelis and Kruth (2006). They have additionally concluded that, given the larger stresses in the perpendicular to laser scanning, a finer discretization of the scan strategy results in lower and more equal residual stress values along X and Y directions.

Kempen et al. (2014) have studied the influence of LPBF parameters on the residual stresses of parts and concluded that build plate pre-heating is one of the most important aspects due to allowing for lower thermal gradients, reducing residual stresses. On the other hand, laser power has the least influence on residual stress, when compared to other variables such as scan speed and layer thickness. Heat treatments are often applied aiming for residual stress relief. It is, however, important to

note that finishing machining of additively manufactured parts can eliminate the necessity for heat treatment stages, despite the fact that further research is needed Flynn et al. (2016). In fact, Yaghi et al. (2019) present a residual stress mitigation methodology that involves the experimental measurement of distortion and residual stresses, its validation by means of numerical simulation of the hybrid process (additive and subtractive) and consequent geometrical compensation for residual stress mitigation on newly fabricated components.

3.2.5. Feature definition and surface roughness

Surface quality of additively manufactured parts is quite relevant not only due to the demanding requirements of the current applications using MAM (tooling industry, aerospace/aeronautics) but also due to the need for functionality and assemblage of those parts. As shown by Frazier (2014), feature definition (which is intrinsically related to surface quality) and build rate are inversely correlated (refer to figure 3.11a). The reason for such a contrary effect is that for obtaining small features, a finer discretization of the part is needed in terms of hatch spacing and layer thickness, which reflects on build time. This means that attaining the best AM surface quality compromises productivity, emphasising the convenience of hybrid manufacturing strategies. Moreover, metal cutting as post-processing ensures the mitigation of AM-related unavoidable features, such as the stair-stepping effect, illustrated in figure 3.11b as well as the improvement of structural integrity and mechanical behaviour, specially when it comes to fatigue life. Despite not always possible due to characteristic geometrical complexity of AM parts, there is numerous situation where its application is highly beneficial. It is, however, important to note that due to the possible geometrical complexity of AM parts, conventional machining operations are not always possible

Wüst et al. (2020) have studied the influence of SLM process parameters on the areal surface roughness of 18Ni300 maraging using design of experiments and Taguchi method. It was found that for both vertical and horizontal surfaces, scan speed has the biggest influence on surface roughness. The statistical analysis allowed for the prediction of optimal factor levels that resulted in roughness

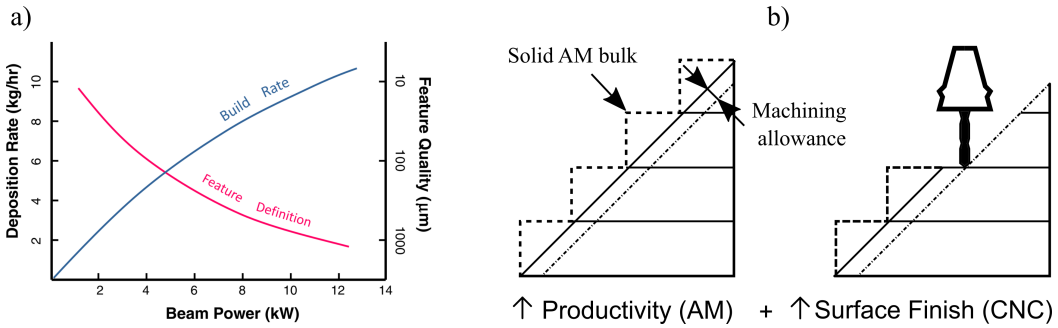


Figure 3.11: Relation between build rate and feature quality (Frazier, 2014) (a) and hybridization through metal cutting (b), adapted from Jones (2016).

reduction of 40% when compared to the manufacturer's processing recommendations. Process-related defects such as spatter particles significantly affect surface roughness. Ali et al. (2019) compared SLM parts printed in different build plate locations, categorized as non-spatter rich region (NSR) and spatter rich region (SR), arriving to the conclusion that an increase of 15% to 28% in surface roughness was identified in the SR, depending on the parts geometry.

3.3. Mechanical and tribological properties of LPBF high strength steels

This section aims at presenting the mechanical behaviour of LPBF high strength steels, in specific the 316L stainless steel and the 18Ni300 maraging steel, which are the focus of this work. Particular attention is given to studies that deal with optimally fabricated AM steels and the comparison with the conventionally manufactured counterparts, rather than the investigation of processing aspects impact on their performance. Getting to know the flow stress of the considered steels under high strain, strain rate and temperature conditions is also the aim of this section, given that those conditions correspond to the ones found in metal cutting. Lastly, a revision of studies that focus on the cutting of LPBF steels is also part of the present chapter.

3.3.1. Flow stress and fracture behaviour

The reliability of high strength steels is based on the principle of a good compromise between strength and ductility. Owing to its excellent corrosion and oxidation resistance, the 316L stainless steel is one of the most popular steels and often submitted to distinct metallurgical routes (such as cold rolling and forging) for yield strength enhancement. Wang et al. (2018) demonstrate the potential of LPBF in obtaining exceptional mechanical strength without compromising ductility. Their results, included in figure 3.12a, show the tensile test curves of two distinctly-processed AM 316L (labelled as "Concept" and "Fraunhofer") compared with cast and wrought conventional counterparts. The higher yield strength, superior ductility and steadier work hardening enables the identification of a novel strength-ductility configuration for the present alloy (refer to figure 3.12b). The higher mechanical strength of LPBF 316L (as well as other steels) is associated to the strong thermal gradients of the AM process, that promote a fine-grain microstructure (Prashanth and Eckert, 2017). In addition, as stated by Liu et al. (2018), the pre-existent dislocation network of such materials smoothly prevent the dislocations' motion while guaranteeing continuous plastic deformation. The authors point out to potential tailoring of mechanical properties according to the input manufacturing parameters. However, the full potential of such concept is hindered by one of LPBF biggest vulnerabilities: the lack of repeatability due to the multitude of process vari-

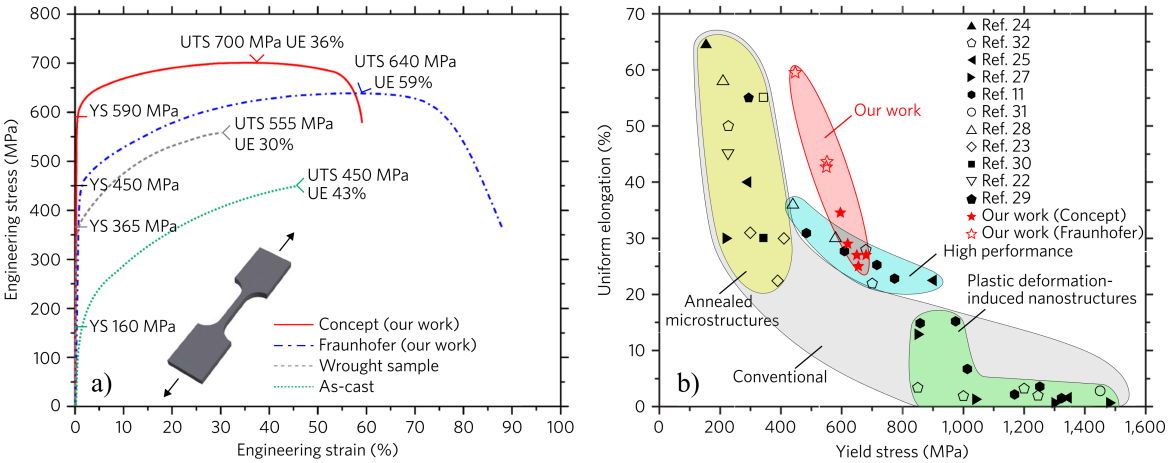


Figure 3.12: Tensile curves of 316L for distinct metallurgical conditions (a) and their strength-ductility configurations (b) (Wang et al., 2018).

ables that affect the mechanical performance of printed metals. Despite the generally-acknowledged higher yield and tensile strengths of AM parts comparatively to conventional, those properties can widely vary, and most studies show a lower ductility of the AM samples. For instance, focusing on the comparison between hot pressed, cast and LPBF 316L, Bartolomeu et al. (2017) confirms the superior mechanical performance (hardness, yield and tensile strengths) of the latter and a higher ductility of the former. In an attempt to illustrate this variability, Röttger et al. (2020) have examined the material properties of 316L samples printed in four distinct AM machines (optimally operated) using the same powder batch. These properties were obtained from uniaxial tensile tests conducted in two distinct directions: perpendicular (XY) and parallel (Z) to build direction, for each of the four samples. Table 3.3 shows the obtained results and demonstrate the wide variations of AM mechanical performance. The differences in yield strength amongst additively manufactured specimens can be of 80 MPa, despite their identical microstructure. In a recent study, Roach et al. (2020) have shown that the mechanical performance of LPBF parts can significantly vary, within the same buidplate, depending on their size. Completing a statistically-representative number of tensile

Table 3.3: Tensile tests results of the four distinct specimen groups (Röttger et al., 2020).

Specimen	σ_y [MPa]	σ_u [MPa]	A_l [%]	Porosity [%]
A_Z	452±9	548±7	56±7	0.028
A_{XY}	503±32	644±7	51±10	0.028
B_Z	438±4	525±15	16±3	0.660
B_{XY}	440±22	573±19	39±4	0.570
C_Z	424±9	528±32	39±4	0.049
C_{XY}	445±23	629±32	46±8	0.107
D_Z	458±14	598±1	63±1	0.073
D_{XY}	469±5	621±7	49±1	0.089
Cast 316L	365±22	563±6	69±9	0

tests for different sized (as built) 316L specimens they have found that yield stress, tensile strength and elastic modulus can be reduced to half, if the specimen's gauge length is scaled down from 25 to 1.6 mm. The unaltered microstructure and hardness of the different-sized specimens indicates that surface roughness effects are responsible for the diminished mechanical performance because of two main factors: a decrease of the resistant section area and increase of stress concentration factor. Moreover, the findings emphasize the importance of ensuring optimal surface conditions in AM parts, in line with the present study.

Very limited data can be found regarding the high temperature and high strain rate behaviour of the LPBF 316L stainless steel. From the small amount of available data, none of it concerns the portrayal of the material's behaviour under cutting conditions. It is, nonetheless, important to highlight relevant studies that may contribute to supporting and benchmarking the results obtained in the current work. For instance, Zhong et al. (2020) have investigated the strain hardening rate and high temperature behaviour of oxide dispersion strengthened (ODS) 316L steels with variable amount of Y_2O_3, fabricated by SLM. They focused on the quantification of significant improvements in the mechanical strength of 316L due to its general use in structural applications (including service temperatures up to 600°C), namely in nuclear reactors. The great potential of AM in the fabrication of ODS parts is exploited, given the great challenge in conventional practice. Figure 3.13a shows the true stress-strain curves as well as strain-hardening rate of SLMed 316L stainless steel (as-built) for room temperature and 400°C. Interestingly, the room temperature results show a very stable recovery of the strain hardening rate, witch goes in line with the improved hardening capability, identified and explained by Wang et al. (2018). Necking is delayed due to the nanoinclusions and cellular dislocation network that allow for deformation twinning and dislocation pinning, according to the authors. Despite the diminished ductility, the trend is similar at elevated temperatures, as is observed for the 400°C curve, where reasonably good mechanical strength is attained.

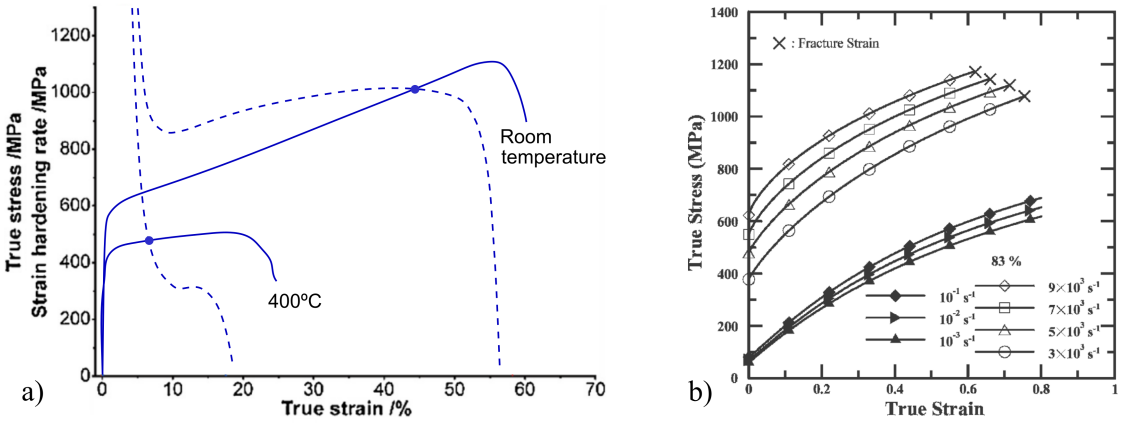


Figure 3.13: True stress-strain and strain hardening rate curves of LPBF 316L at room temperature and 400°C (Zhong et al., 2020) (a) and strain rate effect on the compression behaviour of PM 316L with 83% relative density (Lee and Chiu, 2006) (b).

In order to determine whether additively manufactured 316L parts (as-built) can be used in high strain rate applications, Kneen et al. (2020) have performed compression tests in split-hopkinson pressure bars (SHPB), at strain rates in the order of 10^3 s^{-1}. Two different sets of processing parameters were taken into consideration in order to represent two relative density categories: favourable and unfavourable. Unlike quasi-static and Charpy V-notch impact tests (also conducted in the study) the SHPB test results did not show influence to part density nor print orientation. Despite the similar trend to wrought 316L (mechanical strength increase with strain rate), the authors claim that LPBF 316L is less sensitive to strain rate. Furthermore, they report that at an approximate strain rate of 10^3 s^{-1}, mechanical strength is doubled and close to the maximum values registered by Lee and Chiu (2006), which identically characterized 316L manufactured via powder metallurgy (PM), displayed in figure 3.13b.

In spite of the low strain rates (as compared to those in metal cutting), Li et al. (2020) have comprehensively characterized LPBF 316L stainless steel, in order to model the deformation behaviour of shell-lattice structures. Strain hardening was depicted through a combination of Swift (power) and Voce (exponential) hardening laws, while temperature and strain rate were modelled with the corresponding Johnson-Cook (JC) terms. With respect to the strain rate effect, the authors have noticed a rate independent strain hardening and, similarly to other authors, an increase in yield and tensile strengths, for increasing strain rates (refer to figure 3.14a). Wilson-Heid et al. (2020) have also identified the parameters for the strain hardening of LPBF 316L. Even though the dependence on strain rate and temperature was not modelled, the quasi-static room temperature behaviour is quite similar to the one depicted by Li et al. (2020). Table 3.4 presents the identified parameters of each author regarding the plasticity model.

Using distinct specimen geometries (uniaxial/plane strain tension, notched and un-notched, shear and Nakazima) and numerically validating the conducted tests, Li et al. (2020) have calibrated

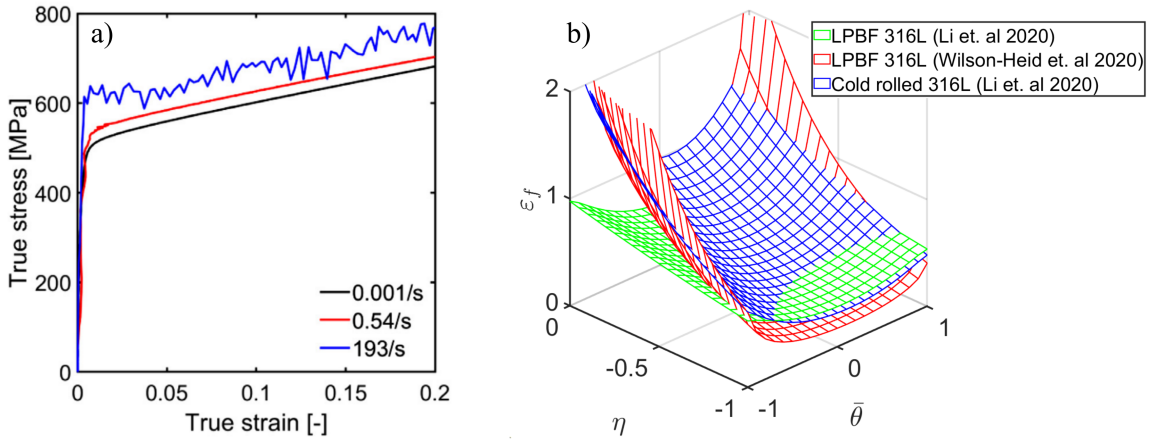


Figure 3.14: Strain rate effect on plastic behaviour by Li et al. (2020) (a) and literature fracture loci (b) of the LPBF 316L.

Table 3.4: Calibrated plasticity models available in literature for the LPBF 316L stainless steel.

Study	A [MPa]	ε_0	n	k_0 [MPa]	Q [MPa]	β_v	α	C	m_t
Li et al. (2020)	857.1	0.61	0.99	503.6	838.7	1.35	0.85	0.0124	0.91
Wilson-Heid et al. (2020)	1289	0.206	0.516	-	-	-	-	-	-

Table 3.5: Calibrated Hosford-Coulomb fracture models available in literature for conventional and LPBF 316L stainless steel.

Study	a	b	c	n
LPBF316L Li et al. (2020)	1.45	0.720	0.023	0.100
Cold rolled 316L Li et al. (2020)	1.30	1.05	0.065	0.100
LPBF316L Wilson-Heid et al. (2020)	0.694	1.30	0.244	0.199

the stress triaxiality (η) and lode angle parameter ($\bar{\theta}$) dependent Hosford-Coulomb (H-C) fracture model, for both cold-rolled 316L and LPBF316L. Also focusing on the multiaxial plasticity and fracture behaviour of LPBF 316L, Wilson-Heid et al. (2020) have experimentally determined the fracture locus, using data from plane strain/uniaxial tension, shear and combined shear/tension loading tests. Through numerical validation of the tests, a plasticity (Swift) and fracture model (H-C) were calibrated. The identified model parameters are described in table 3.5. The correspondent fracture loci, for quasi-static conditions, are displayed in figure 3.14b. This figure shows that, according to Li et al. (2020), the fracture behaviour of the LPBF 316L is less sensitive to the state of stress than the conventional material. Interestingly, the fracture behaviour suggested by Wilson-Heid et al. (2020) supports the trend that Lode angle parameter and stress triaxiality have similar influence on the fracture strain in both conventional and additively manufactured 316L. The inconsistencies found in literature reveal that further investigation is essential. The identified models are, nonetheless, of extreme relevance since they allow for further comparison/benchmarking with the identified constitutive models, in the current study. The mentioned constitutive equations (for plasticity and fracture) are presented in tables 2.3 and 2.5, where a detailed review of the most suitable models for metal cutting is conducted.

When increased performance in terms of yield strength is required, typical of very demanding structural applications, maraging steel is usually considered due to its excellent combination of strength and ductility. The combination of such mechanical properties with the advantages of additive manufacturing has contributed to a recent focus on the 18Ni300 maraging steel. Apart from the AM process-related customization (through microstructure control), heat treatment can effectively improve mechanical strength, allowing for additional adjustment of the materials' attributes. It is important to take into consideration the disparity in mechanical properties of the aged and non-aged conditions. Figure 3.15 exhibits the two distinct strength-ductility configurations, for both additively manufactured and wrought metallurgical conditions. It is noticed that, within the AM samples, a wide range of ductility values can be attained. Despite the fact that, in general, ad-

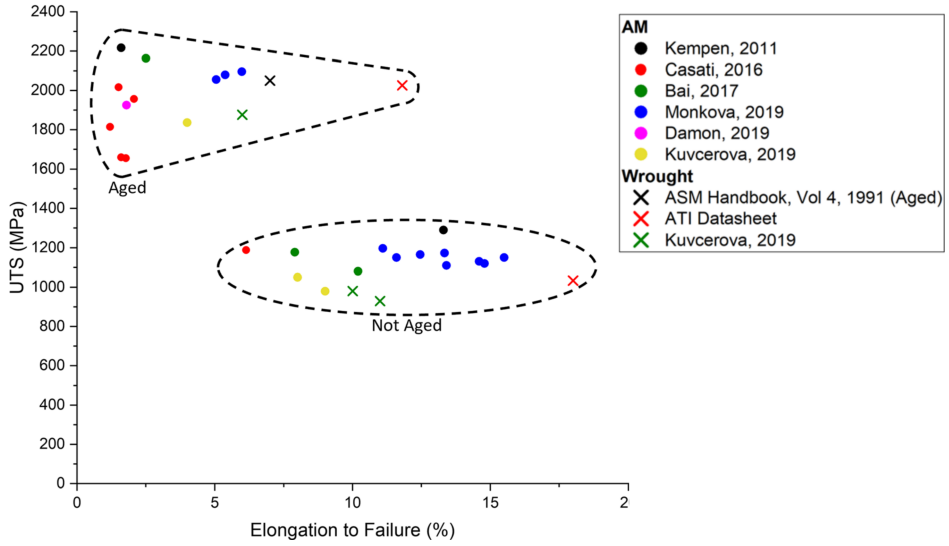


Figure 3.15: Strength-ductility configurations of aged and non-aged 18Ni300 maraging steel (Haghdadi et al., 2021).

Table 3.6: Comparison of additively manufactured and wrought 18Ni300 mechanical properties.

Study	σ_y [MPa]	σ_U [MPa]	A_l [%]	HRC
Tan et al. (2018) (as-built)	915±7	1085±19	11.3±0.3	35.7±1.1
Yasa et al. (2010) (as-built)	-	1290±112	13.3±1.86	40
Marvac (2009) (wrought)	760-895	1000-1070	6-15	35

ditively manufactured samples are less ductile than wrought, the opposite is also possible. Tan et al. (2018) and Yasa et al. (2010) have managed to manufacture 18Ni300 maraging steel with superior ductility to the conventional, as is displayed in table 3.6. Similarly to what was observed for the 316L stainless steel, and as expected for the additively manufactured steels, the yield and tensile strength of 18Ni300 are typically higher than the conventional counterparts, which is also noticed in the cited studies. Still referring to figure 3.15, it is important to note that as-built and annealed conditions are included within the "not aged" samples. Moreover, Monkova et al. (2019) (labelled as blue circle), have tested those two conditions and noticed a higher ductility that for the annealed samples. In their aged condition, a bigger dispersion in the tensile strength is noticed, which may be explained by the different ageing conditions. In fact, a great amount of the conducted research deals with obtaining the best mechanical properties in function of ageing time and temperature, as is the focus of, for instance, Yin et al. (2018) and Casati et al. (2016). They have shown that ageing treatment can modify phase composition and with increasing ageing temperature and time, more reversed austenite and intermetallic precipitation occurs. Moreover, optimal ageing temperature and time were identified (490°C for 3h period). In this review, however, a bigger emphasis is given to as-built state, since it was the reference processed condition in the experimental work of this research.

When it comes to the high temperature and high strain rate behaviour of additively manufactured 18Ni300, more comprehensive studies are lacking in the current literature. Taylor et al. (2020) focus on the development of a SHPB for dynamic tensile testing, claiming that both conventional and AM maraging steels were successfully analysed. However, no data is presented regarding their mechanical behaviour. Schmidova et al. (2019), through the analysis of dynamic tensile tests, report that the LPBF 18Ni300 reveals significant hardening capacity for increased strain rates. The authors state an almost 25% increase in tensile strength at 700s^{-1} and 38% at 1400s^{-1}, comparatively to the quasi-static scenario. Church et al. (2018) have compared the tensile behaviour of LPBF and wrought 18Ni300 maraging steels, in their aged condition, for different strain rates and temperatures. The authors present, as well, a calibrated plasticity model (modified Zerilli-Armstrong) for both additively manufactured and wrought steels. It is, however, important to note that the tests were carried at a maximum strain rate of 1s^{-1}, which may be relevant in order to investigate optimal hot workability but insufficient to model this material under impact applications or simulate the cutting phenomenon.

Similarly to the additively manufactured, the literature focusing on the strain rate effect of the conventional 18Ni300 maraging steel mostly concerns its hot workability, not contemplating high strain rates. This is the case of the works by Kendall (1972), Mazhar et al. (1988) and, more recently, Chakravarthi et al. (2018) who have fully characterized the maraging steel in the 900°C - 1200°C temperature range and in the 0.001s^{-1} - 100s^{-1} strain rate range. Still, a limited number of studies focuses on the high strain rate behaviour of conventional 18Ni300. Song et al. (2015) have characterized conventional 18Ni300 and 18Ni250 maraging steels using the SHPB. They state that dynamic yield strength is 40-45% higher than quasi-static, despite the insignificant difference between 1000s^{-1} and 3000s^{-1}. Figure 3.16a shows the dynamic stress-strain results in which, right after yield, a stress decrease for increasing strain is noticed, indicating the formation of early necking. In order

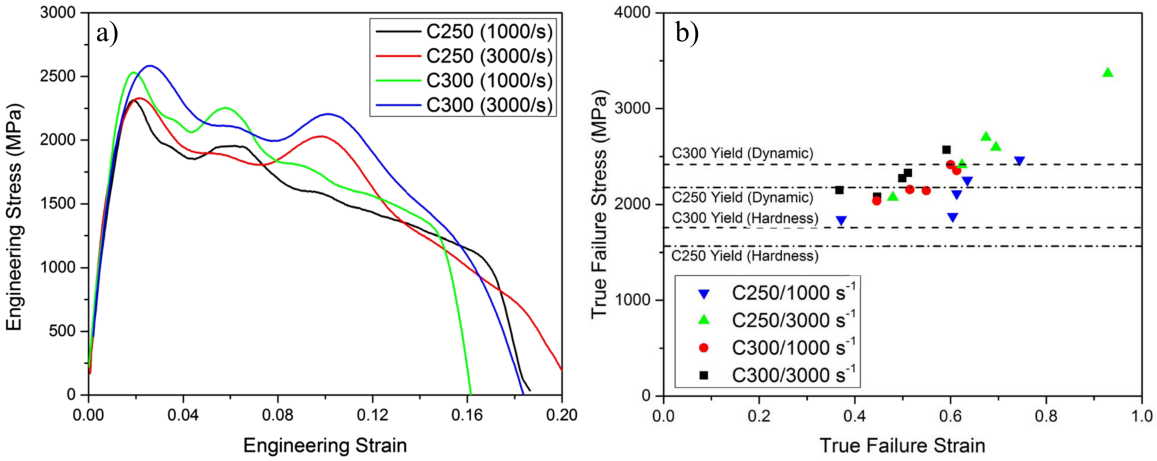


Figure 3.16: Engineering tensile stress–strain curves (a) and true failure stresses and strains (b) for the 18Ni250 and 18Ni300 maraging steels at 1000s^{-1} and 3000s^{-1} strain rates (Song et al., 2015).

Table 3.7: Calibrated JC plasticity models available in literature for the conventional 18Ni300 maraging steel.

Study	A [MPa]	B [MPa]	n	C	m
Cinnamon et al. (2006)	2170	940	1.175	0.0046	0.78
Polyzois (2010)	758	172	0.2258	0.0522	0.78

to calculate the true stress-strain response at failure (refer to figure 3.16b), Bridgman correction (Bridgman, 1952) was applied, showing a superior ductility of the 18Ni250 grade maraging steel. Dealing with the identification of a constitutive material model for the 18Ni300 maraging steel, Cinnamon et al. (2006) and Polyzois (2010) propose sets of JC plasticity model parameters, described in table 3.7, determined using SHPB.

Despite not focusing on the exact same maraging steel, Fu et al. (2020a) have comprehensively identified the temperature and strain rate influence in the flow stress of iron–nickel based ultra-high strength steel (wt. 18 to 20% Ni). The authors point out that due to the low conductivity of the alloy (caused by the high Ni content), thermal softening effect may overcome the strain-hardening effect. Figure 3.17a shows the compression test stress-strain curves at 300°C, where it is noticeable a lower strength for the test conducted at $10000s^{-1}$. The authors also highlight the effect that dynamic recrystallization has in work hardening at higher temperatures (600°C), when thermal softening is less pronounced. Figure 3.17b shows the increasingly negative strain hardening as the rate of deformation is increased. In sum, they state that the dynamic response of the tested alloy is a combination of rate hardening, thermal softening and strain hardening which, according to the temperature and speed test configurations, can be expressed differently.

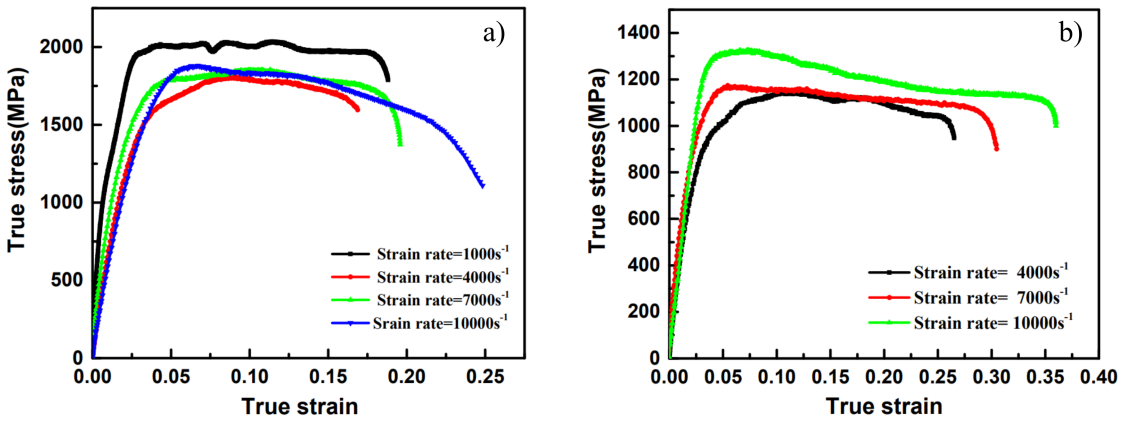


Figure 3.17: Dynamic mechanical response of ultra-high strength steel (18-20%Ni) under high temperature conditions: a) 300°C b) 600°C (Fu et al., 2020a).

3.3.2. Anisotropy and tension-compression asymmetry

It is well known that the LPBF process induces differentiated mechanical strength, depending on the tested direction and that microstructural features or defects are responsible for such effect (Kok et al., 2018). Jeon et al. (2019) have assessed the LPBF 316L stainless steel anisotropic behaviour, through compression and tensile tests at different orientations. Interestingly, the authors report distinct anisotropy levels according to the loading. Figure 3.18a shows the significantly lower yield and tensile strengths as well as strain hardening under tensile loading for the Z direction, comparatively to the X direction. Grain morphology is generally acknowledged as the main cause for anisotropy in additively manufactured steels. The columnar grain formation, elongated along build direction, means a higher density of grain boundaries perpendicularly to build direction leading to a higher number of dislocations barriers, thus, an higher mechanical strength. In sum, and as stated by Yu et al. (2017), the mechanical strength of LPBF steels follows the Hall-Petch relation (Hall, 1951) given that, due to their columnar geometry, distinct effective grain size is noticed in each direction. In addition, the authors point out pore orientation effect (strain concentration around pores leading to crack propagation and failure) as an additional reason to such pronounced anisotropy in the tensile behaviour. Regarding the compression tests (figure 3.18b), authors report a less significant anisotropy due to the fact that compressive loading promotes pore closure.

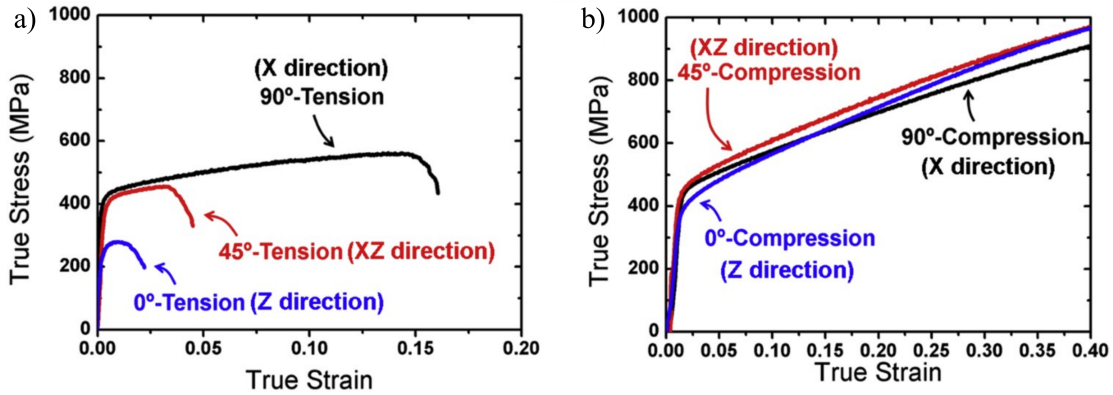


Figure 3.18: Tensile (a) and compressive (b) stress-strain curves for different loading orientation (Jeon et al., 2019).

Cyr et al. (2018) have performed tensile and compression tests on the DMLS 18Ni300 maraging steel. Figure 3.19 presents those results and additionally show the influence of build direction on tensile behaviour. They have shown a similar anisotropy trend in the tensile tests (an higher mechanical strength when loaded perpendicularly to build direction). Supported by DIC measurements, the authors report that geometric softening (necking) is responsible for the strong tension-compression asymmetry. They state, however, an identical hardening in the additively manufactured maraging steel in both tension and compression, which goes in line with the previous work conducted by Spitzig et al. (1976) in conventional (wrought) maraging steel.

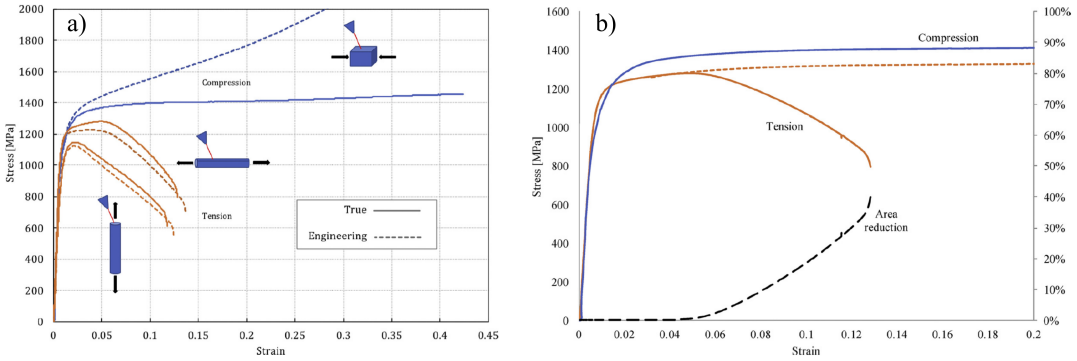


Figure 3.19: Stress-strain curves obtained from both tensile and compression tests on the AM 18Ni300 maraging steel (a) and predicted hardening without influence of geometrical softening (b) (Cyr et al., 2018).

3.3.3. Transformation induced plasticity effect

The transformation induced plasticity (TRIP) effect can be noticed in the additively manufactured metals, namely precipitation hardening (PH) and maraging steels (Bajaj et al., 2020). Due to promoting strain hardening and, therefore, enhancing the materials' ductility, the combination of this effect with, for instance, the martensite ageing is seen as a way to obtain steels with outstanding strength-ductility ratios (Raabe et al., 2009). TRIP effect is specially relevant in the characterization of materials towards machining operations due to the high deformations attained.

On their investigation of TRIP effect on Ti-free grade 300 LPBF maraging steel, Kannan and Nandwana (2020) have shown that its existence at room temperature enhances the mechanical strength of the steel without compromising ductility. Moreover, their results suggest that the rapid cooling rates, finer microstructure and solutes segregation characteristic of LPBF can promote the mechanical performance at room temperature. Shamsdini et al. (2021) have studied the strain-induced phase transformation on the 18Ni300 LPBF maraging steel. They have found that the TRIP effect leads to a variation of the strain-hardening rate, in the obtained results of tensile tests. Despite referring to a different group of LPBF steels, Rafi et al. (2014) have, as well, identified differences in the strain-hardening rate, which were attributed to the strain-induced phase transformation. Figure 3.20 illustrates the effect on the tensile behaviour of 17-4 PH stainless steel. The authors performed tensile tests for the following conditions: as-built (no HT), solubilized (2h at 650°C), solubilized and aged (2h at 788°C + 1h at 482°C), and directly aged (2h at 788°C). The absence of heat treatment seems to result in the highest amount of retained austenite, which in turn leads to a more pronounced effect of two distinct strain-hardening rates. The fact that a fully martensitic structure is formed when direct aging is applied is consistent with the absence of TRIP effect for that specific condition. In their comprehensive study on microstructural evolution and nanoprecipitation of the SLM grade 300 maraging, Tan et al. (2017) have concluded that due to the intrisic heat treatment of SLM samples and fast solidification, nanoprecipitates were generated which, coupled with the TRIP

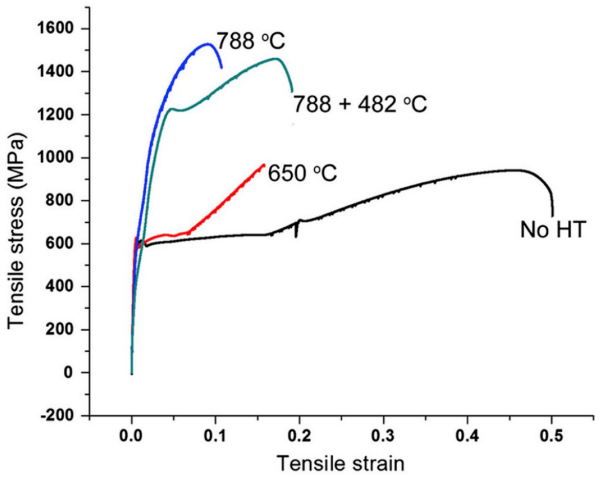


Figure 3.20: Tensile tests for 17-4PH stainless steel produced by LPBF (Rafi et al., 2014).

effect, accounted for precipitation strengthening.

3.3.4. Tribological properties

The tribological properties of the studied materials are of utmost importance when it comes to their characterization towards metal cutting, namely the tool-chip and tool-workpiece interface. Whereas friction mechanisms have been discussed in section 2.1.4, a review of some material properties for the 316L stainless steel and grade 300 maraging steel is carried in the present section. Bartolomeu et al. (2017) have compared the wear behaviour of cast, hot pressing and SLM 316L stainless steel. They have found that the wear resistance of SLM steel was 28% higher than its cast counterpart due to the finer grain size, inherent to the AM process, as illustrated in figure 3.21b. Moreover, they present the measured friction coefficient (ball-on-plate) where a distinction between the conventional and additively manufactured steels is highly noticeable (refer to figure 3.21a). Yang et al. (2019) have investigated the tribological behaviour of SLM 316L. They have concluded that despite showing prominent anisotropic wear behaviour for low loads, such effect is not significant

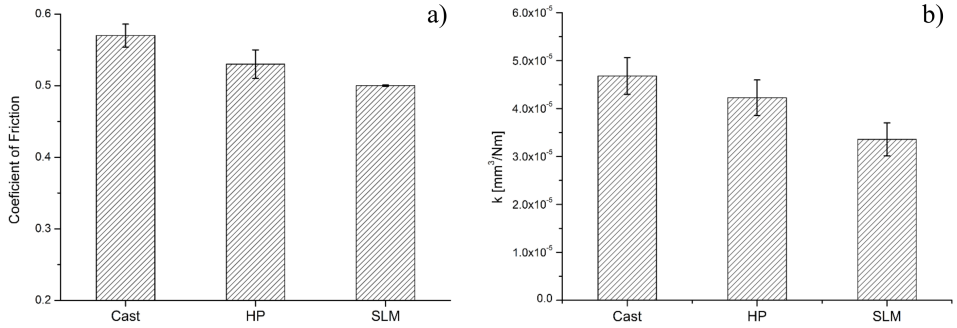


Figure 3.21: Friction coefficient (a) and specific wear rate (b) for the distinct tested specimens of 316L steel (Bartolomeu et al., 2017).

under high loads, meaning an isotropic wear resistance.

Focusing on the identification of heat treatment parameters for optimized mechanical strength, Yin et al. (2018) have concluded that best wear properties of SLM 18Ni300 maraging steel can be obtained for 3h at 490°C of ageing, as shown in figure 3.22b. Phase composition and microstructure significantly influence the mechanical and tribological properties of the alloy. The conducted tribological tests (pin on disk) show an higher measured friction coefficient in as-built state (refer to figure 3.22a) and allowed for concluding that the wear mechanism of the SLM maraging steel changes from abrasion wear in the as-fabricated condition to adhesion tribofilm in the optimally aged condition. The tribological behaviour of 18Ni300 has also been subject of study by Sun et al. (2020), who have conducted high-speed dry sliding tribological tests on a pin-on-disc setup. The authors state that friction coefficient decreases with increasing sliding speed and load (refer to figure 3.23). Temperature increase at the pairs interface is pointed as the main reason for such effect. The very little available data on the tribological characterization of additively manufactured 18Ni300 maraging steel shows substantial discrepancy (friction coefficient from 0.09 to 0.62), suggesting the need for further research on this topic.

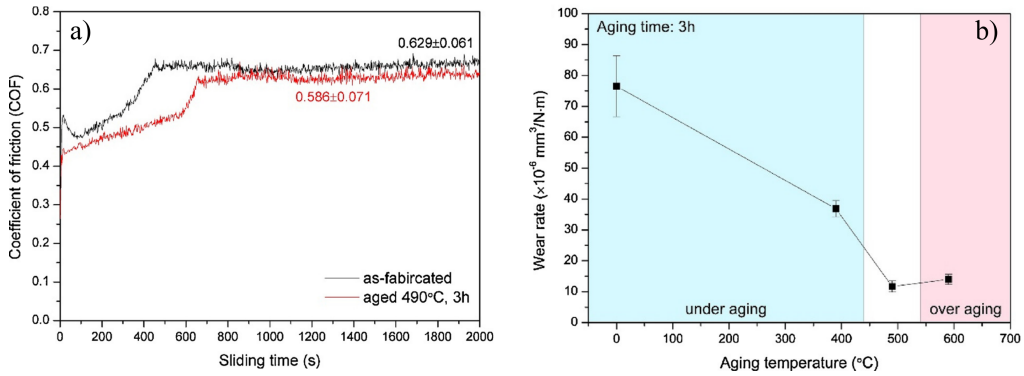


Figure 3.22: Measured friction coefficient of as-built and heat treated SLM 18Ni300 maraging steel (a) and wear resistance in function of ageing temperature (b) Yin et al. (2018).

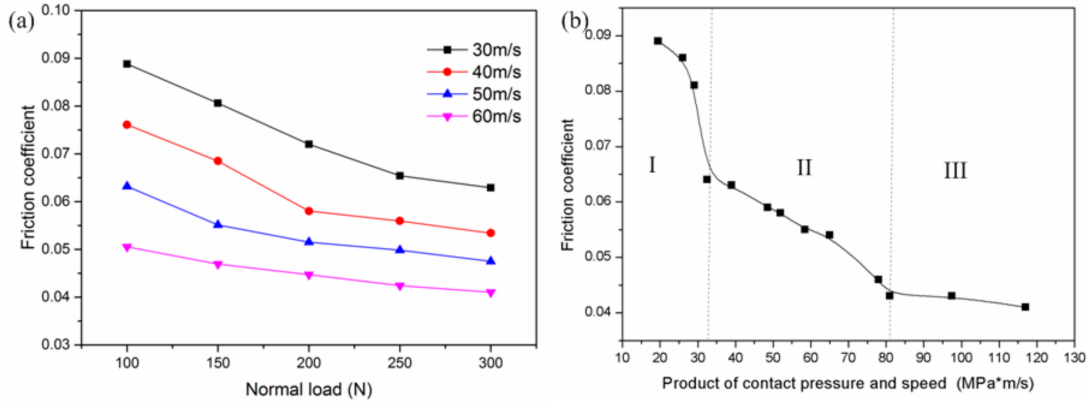


Figure 3.23: Measured friction coefficient in function of load (a) and the product between speed and contact pressure (b) for 18Ni300 Sun et al. (2020).

3.4. Metal cutting of additively manufactured metals

The bound post-processing stages of additively manufactured parts imposes the investigation of their machinability. Difficulty in machining such materials with standard tools and cutting parameters has been reported, for instance, by Marbury (2017) in milling operations on the 316L (tool breakage). Despite understudied, a review of the available research on additively manufactured metals is the aim of this section. Kaynak and Kitay (2019) have examined the surface integrity of as-built and machined surfaces of SLM SS316L alloy. The study points out the necessity for finishing in additively manufactured alloys and compares the surface quality, roughness, hardness and microstructure of distinctly post-processing methods: turning, vibratory surface finishing and drag finishing. Despite the better results in terms of surface quality promoted by turning operations, the authors suggest drag finishing as the most promising technique given the difficulty in the application of single-point cutting on complex surfaces. Guo et al. (2017) have analysed the microstructure, mechanical properties and machinability of the AM 316L stainless steel in two different directions, and verified that higher loads are generated when milling perpendicularly to build direction, which also explained the higher surface roughness and tool wear. Focusing on the same alloy, Struzikiewicz et al. (2019) have determined the influence of cutting parameters on the cutting force, surface finish and temperature of SLM SS316L, conducting an analysis of variance. Undesirable chip formation was obtained for all combinations of tested cutting parameters. Leça et al. (2020), focusing on the machinability of LPBF 316L through longitudinal turning operations, has shown that porosity directly influences the cutting loads and report a relationship between chip fragmentation and porosity.

Fortunato et al. (2018) have performed face milling operations in order to identify suitable cutting conditions for distinctly heat treated 18Ni300 samples. Very low roughness (Ra$<0.45\mu$m) can be achieved in all material/cutting parameters configurations. Oliveira et al. (2020) have studied the effect of distinct cutting parameters on the surface roughness and residual stresses of milled 18Ni300 maraging steel, manufactured by LPBF. The authors claim that melt pools, layer construction, and porosity can affect the chip formation. Moreover, it was found that an increase in cutting speed promotes the generation of compressive residual stresses (refer to figure 3.24), which can also be achieved with specific combinations of feed per tooth and (lower) cutting speed. Such aspect shows the importance an accurate selection of cutting parameters in milling operations of AM maraging steel parts. Bai et al. (2020) have compared the machinability of the AM ASTM A131 steel with its conventional counterpart, focusing on the effect of cutting speed. The authors state that the microstructure differences between AM and CM materials is directly reflected in chip morphology (continuous for the AM), cutting forces and tool (higher for the AM). Calleja et al. (2018) have studied the machinability of both AM and CM Inconel 718 superalloy, using turning and milling

setups. The heat treated AM material presented the highest cutting loads. On the other hand, the as-built AM material showed higher machinability than the conventional, which according to the authors, facilitates process industrialization decisions on whether applying HT before of after machining. With regards to a similar alloy (Inconel 625), Yang et al. (2020) report that surface topography and integrity is affected by relative orientation of cutting direction to the LPBF build direction and scan strategy orientation. Montevecchi et al. (2016) report significant differences in the machinability of AM H13 tool steel, when compared to its conventional counterpart. The lubrication cutting conditions in turning operations have also been subject of research by Bertolini et al. (2019), focusing on its influence on microstructure, hardness and surface integrity of both AM and CM Ti6Al4V alloy. Distinct machinability is identified according to the metallurgical condition (lower for the AM alloy). The authors also point out the need for further research towards cutting parameters optimization of AM metals. Zimmermann et al. (2021) have analysed the dependence of LPBF manufacturing parameters on the chip and surface morphology as well as burr formation and milling forces of the AlSi10Mg. The results are compared with the conventional (cast) material and evidence distinct chip morphology, cutting load, surface quality, and burr formation. In sum, the machinability studies of additively manufactured alloys are a very recent research trend (starting from 2017), promoted by the uncertainty of the behaviour of this novel metallurgical condition when submitted to conventional material removal processes. As reported, the dissimilarities between AM and CM metals keep the growing number of publications on the field.

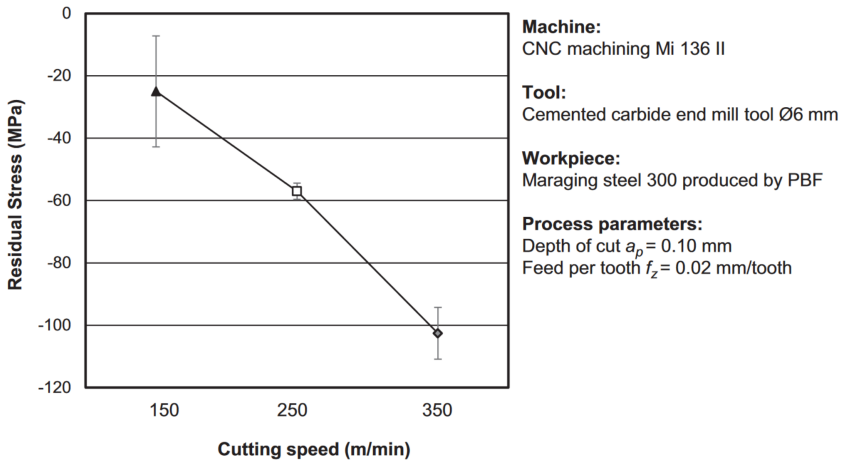


Figure 3.24: Residual stresses on the 18Ni300 maraging steel milled surfaces for distinct cutting speeds (Oliveira et al., 2020).

Chapter 4. Experimental procedure and details

This chapter focuses on describing the extensive experimental characterization program conducted on selected materials, which includes the determination of their physical, metallurgical, tribological and mechanical behaviours. Ultimately the procedure towards the assessment of the materials' machinability is presented. With regards to the manufacturing processes of the selected materials, the most important parameters are summarized. A special emphasis is given to the additively manufactured material samples when it comes to its condition inspection. This particular attention given to the AM as-built metal samples is motivated by the verified wide variability of these materials performance, depending on processing parameters (as found in literature review). This approach aims at better understanding the actual printing quality and enables the comparison with conventional materials, which constitutes and ideal starting point towards the core activity that is mechanical and technological characterization.

4.1. Work plan and approach

The selection of suitable additively manufactured steels, which the current study will take into account, constituted the first stage of the experimental procedure. Two distinct alloys were chosen for the sake of completeness of this study: a high-performance oriented maraging steel (18Ni300), often used in plastic injection mould applications and a general-application stainless steel in the MAM outline (316L). It is important to highlight that the 316L stainless steel was not as extensively and diversely tested as the maraging steel. Rather than comprehensively testing two materials, the goal of including the 316L was to occasionally examine the behaviour of a relatively well known material, particularly given the extreme characterization conditions. It allowed for valuable comparisons as well as experimental setups validation at the initial stage of this research. The 18Ni300 maraging steel was selected to specifically address the lack of research regarding its mechanical and machinability characterization, in particularly in the additively manufactured form. Its selection for this research work is associated with the characteristic high strength and convenient good weldability, which makes it the suitable candidate towards high-performance tool design (from the limited available spectrum of AM engineering materials). It is important to note that the same materials of conventional metallurgic condition (vacuum remelted cast) were subject of the same analysis as the additively

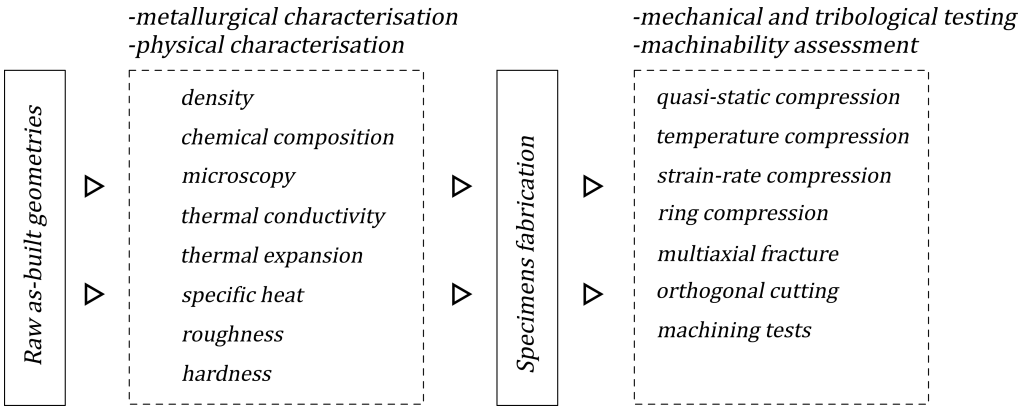


Figure 4.1: Schematic representation of the experimental work plan.

manufactured.

The experimental procedure can be divided in two main stages, as displayed in figure 4.1. The first deals with the materials inspection and analysis. For that, small samples extracted from each material batch were subjected to porosity and microstructure analyses, thermal parameters identification, chemical composition verification as well as surface roughness and hardness measurements. After this initial stage, specimens were fabricated (machined) and consequently tested to compression under distinct temperature, strain rate, triaxiality and tribological conditions. For validation of the built cutting numerical models, orthogonal cutting and machining tests were also conducted.

4.2. Metallurgical and physical testing

In order to address the characterization requirements for each additively manufactured alloy, two material batches (316L and 18Ni300) were built, through laser powder bed fusion. An ytterbium laser with a spot size of 70 μm was used for processing the material samples. Parts were built according to the manufacturers' recommendation for optimal printing conditions and overall quality. A more detailed description of the printing parameters can be found in table 4.1. As reported in the literature review in chapter 3, additively manufactured parts may present a considerably different mechanical performance, depending on a multitude of aspects in their manufacture. In order to fully understand the materials' as-built condition, a comprehensive analysis regarding physical, metallurgical and mechanical properties was carried, which is described in the following sections. Figure 4.2 displays both 316L and 18Ni300 build plates, where different groups of specimens (randomly distributed) can

Table 4.1: Processing parameters used in the LPBF of 316L and 18Ni300 steels.

Material	P_L [W]	v_s [m/s]	h_s [μm]	d_s [μm]	PSD(d_{10}/d_{90})
316L	300	1.00	110	50	15/45
18Ni300	400	0.86	95	40	15/45

be seen. The number and part geometry does not differ among them. Their purpose and geometry is related to specific sets of testing methodologies, which are further discussed in section 4.3.

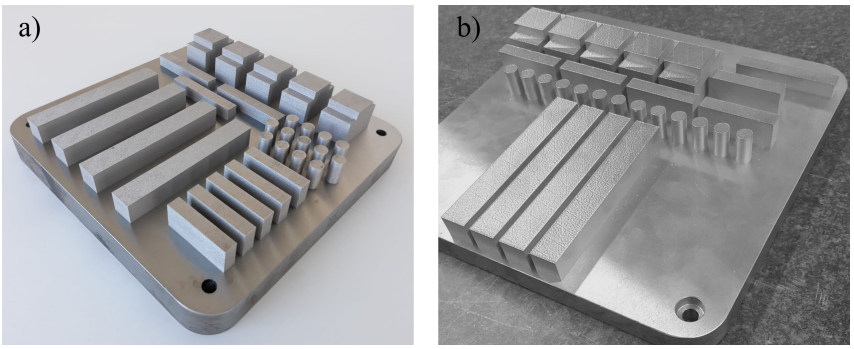


Figure 4.2: As-built material samples attached to 316L (a) and 18Ni300 (b) build plates.

4.2.1. Optical/electron scanning microscopy and chemical analysis

According to Slotwinski et al. (2014), the porosity amount in additively manufactured parts is one of the biggest aspects of interest. Despite its purposefulness for specific applications such as osseointegration with biological tissues (Lowther et al., 2019), high porosity is generally unfavourable due to increasing mechanical failure possibility during service life of parts. The micrograph cross-section method for porosity measurement was adopted in this study. In this technique, AM samples were cut in two distinct directions (perpendicular and parallel to the build direction), embedded in resin (through compression mount). Manual and semi-automatic grinding using sandpaper, followed by polishing of the cut cross-sections (Struers Pedemax-2, INEGI), allowed for its optical microscope observation (Olympus PMG3 and Zeiss Axiophot). Etchant is not used in these samples, given that the goal is to simply reveal the absence of material (pores) in a polished surface. In order to estimate relative density, metallographic samples were post-processed in ImageJ software for generating binary maps that more easily allow for porosity accounting. Figure 4.3 displays an example of a binary map generation from a metallographic sample (AM 316L), where black and white correspond to metallic material and its absence, respectively. It is important to have a correct porosity representation, meaning that the higher number of micrographs analysed, the more accurate the estimate of the spacial distribution would be.

Spierings et al. (2011) have compared the most popular porosity measurement techniques in MAM. They have arrived to the conclusion that the significant differences between previous technique and the Arquimedes method are approximately 1% for relative densities higher than 98% and using 4 distinct micrograph samples with 40% magnification. Moreover, this method has the advantage of revealing porosity shape and its distribution in the cross-section, which may enable the identification of process-related flaws (for instance, porosity alignment due to excessive scan speed).

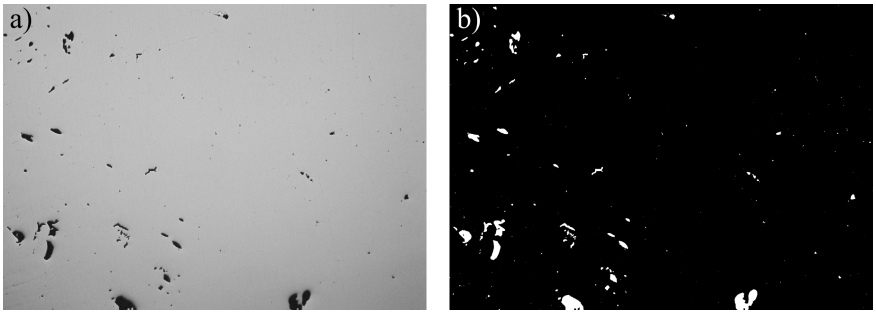


Figure 4.3: Metalographic AM 316L sample (a) and its conversion to binary map (b), on a 50x magnification.

Another approach for defects inspection in the AM samples, as denoted in the literature review section 3.2.3, is the microstructure analysis of each material sample, which was carried in this study by the same optical equipment used in the porosity analysis and, additionally, by means of scanning electron microscopy (FEI Quanta 400FEG, at CEMUP). For such task, material samples had to be etched in order to show the melt pool baths as well as the grain morphology. Samples were chemically etched with different reagents, according to the observation purpose. Aqua regia, super picral solution (20g picric acid + 100 HCL) and nital (2%) solutions were used for chemical etching whilst oxalic acid was used for electrolytical etching (6V DC for 50 seconds). While grain morphology can easily be observed with chemical etching, melt pool geometry and AM-related microscopic features, such as laser trace, require electrolytical etching.

Chemical composition analysis of the considered materials in this study was performed using spark emission spectroscopy (SPECTROMAXx, at INEGI). Knowing the chemical composition of each considered alloy, enables the comparison/verification compliance with material standards, for each alloying element.

4.2.2. Thermal properties identification

Metal cutting can be considered a complex multi-physics problem where, among others, the thermal effects play a significant role. It is not by chance that Astakhov and Outeiro (2019) adverted to the importance of temperature in metal cutting, and more specifically, the need for developing numerical models that closely portray the materials' behaviour under cutting conditions. For that reason, experimental tests for the determination of the most important thermal variables in the numerical simulation of metal cutting have been contemplated in this study.

Thermal expansion measurements were performed with a push-rod dilatometer (Linseis DIL L75PT, at COMTES FHT), shown in figure 4.4a for both considered steels (316L and 18Ni300) in both metallurgical conditions (AM and conventional). Two ⌀5x40mm specimens for each material were heated and cooled at 1°C/min in resistance furnace under nitrogen protective gas from room

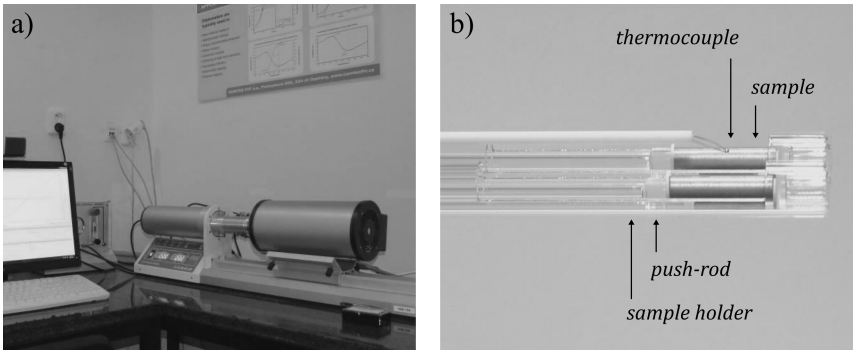


Figure 4.4: Push-rod dilatometer Linesis DIL L75PT (a) and specimen placement detail in quartz holders (b).

temperature (25°C) to 1000°C and back to 25°C (refer to figure 4.4b). The dilatometer system has a horizontal arrangement with two quartz push rods (contact force of 0.3 N) and LVDT expansion measurement. Additionally, thermal expansion measurements of polycrystalline alumina specimens were conducted, following the same heating procedure. Those serve as reference, allowing for the subtraction of the instrument parts thermal expansion influence. The specimens thermal strain in function of temperature is calculated as described in equation 4.1, as an average of both specimens. That enables the determination of the instant thermal expansion coefficient (α_{inst}), displayed in equation 4.2, which corresponds to the derivative of the thermal strain function at the temperature of interest.

$$\varepsilon_T = \frac{\Delta l}{l_0} \tag{4.1}$$

$$\alpha_{inst} = \frac{d\varepsilon_T}{dT} \tag{4.2}$$

Thermal conductivity is calculated according to the formula in equation 4.3, where a is thermal diffusivity, ρ is the density and c_p the specific heat, at a given temperature. Theoretical density values were calculated through the gravimetric method for room temperature (refer to equation 4.4), relying on the mass measurements of precision-machined samples. Density values in function of temperature were calculated based on dilatometry tests, according to the relationship described in equation 4.5.

$$\lambda = \rho \cdot a \cdot c_p \tag{4.3}$$

$$\rho_{rt} = \frac{m}{V} \tag{4.4}$$

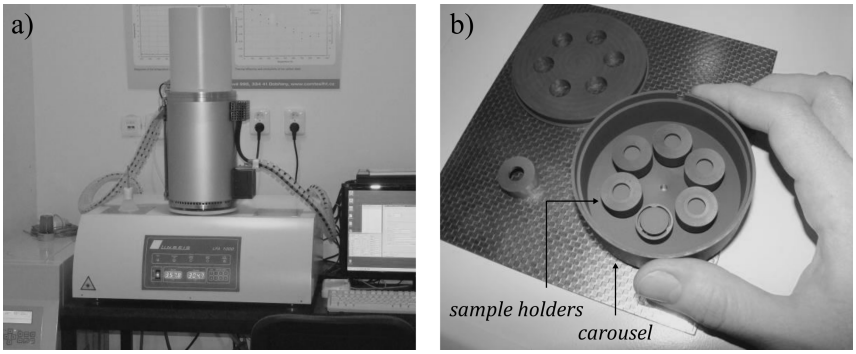


Figure 4.5: Laser flash device Linesis LFA 1000 (a) and specimen placement into carousel (b).

$$\rho(T) = \frac{\rho_{rt}}{(1 + \varepsilon_T(T))^3} \tag{4.5}$$

Laser flash analysis was used for determining thermal diffusivity and specific heat (Linesis LFA1000, at COMTES FHT, refer to figure 4.5). A coin-shaped specimen is heated from one side by a short energy pulse (laser), resulting in a time dependent temperature rise on the opposite side, which is measured by an infra-red sensor. Thermal diffusivity is calculated from that temperature rise as described in equation 4.6, where d is the specimen thickness and $t_{0.5}$ is the time at 50% temperature increase. Specific heat of the samples, c_{ps}, was determined according to the formula in equation 4.7, where c_{pr} is the heat capacity of a reference sample (pure molybdenum) and ΔT the temperature increase induced by laser pulse, for the sample and reference.

$$a = 0.1388 \frac{d^2}{t_{0.5}} \tag{4.6}$$

$$c_{ps} = c_{pr} \frac{\Delta T_s}{\Delta T_r} \tag{4.7}$$

4.2.3. Surface and hardness inspection

Roughness of as-built AM surfaces was measured by means of a stylus profilometer (Hommel-Werke LV-50, at CETRIB) with a TKL300 probe, as stated in DIN4768 standard. The two relevant surface orientations, parallel and perpendicular to build direction, were analysed. The significant magnitude of the as-built samples surface roughness hinders the usage of optical methods for its measurement. Still, for the analysis of machined samples an optical non-contact surface profilometer (Bruker NPFLEX, CETRIB) was used. Figures 4.6a and 4.6b display the mentioned apparatus. Hardness measurements were conducted for both 316L and 18Ni300 steels (in both metallurgical conditions) according to standards ISO6507 and ISO6508. In addition, on the maraging steel, hardness was measured on machined surfaces. Three repetitions were performed on each sample. Figure 4.6c shows the EMCO Test M4U-075 hardness measurement machine.

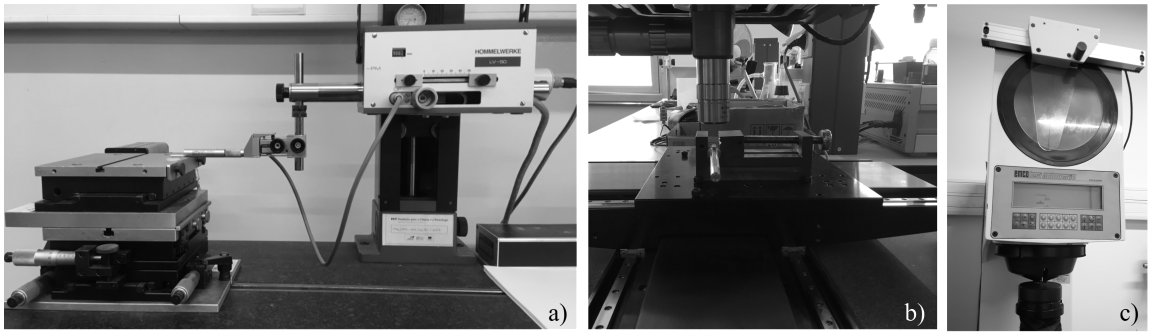


Figure 4.6: HommelWerke LV-50 stylus contact profilometer (a), Bruker NPFLEX optical surface profilometer (b) and EMCO Test M4U-075 hardness measurement machine (c).

4.3. Mechanical and tribological experimental characterisation

The relative illiteracy regarding the mechanical behaviour of additively manufactured materials, when compared with conventional manufactured ones, imposes an increased effort towards their characterization. As previously reported in the literature review chapter in 3, there is a significant difference between mechanical strength of additively manufactured and conventionally fabricated materials, which is why the experimental testing procedure of this study was conducted for both metallurgic conditions. Envisioning the various mechanical and technological characterization stages, different groups of AM raw shapes were designed. Figure 4.7 presents a schematic top view of each material build plate and points out the different printed geometries and their purpose, which can be compression, tensile, orthogonal cutting, pressure-dependent fracture and machining tests. Table 4.2 presents the dimensions of each printed geometry type as well as the intended specimens. It is important to mention that from the remaining material of machinability tests, tensile specimens and ring compression specimens were manufactured, ensuring maximum material utilization.

Compression tests in close conditions to the cutting phenomena (high temperature and high strain rates) are the basis of experimental procedure. Vertical cylinders and horizontal bars were printed in order to prepare specimens for uniaxial compression in two distinct orientations: perpendicular and parallel-to-build directions. Hat-shaped geometries were printed in order to identify the fracture behaviour of the considered materials, under distinct pressure conditions. In order to manufacture the final specimens, different hole configurations are conceived on the raw shape, which when submitted to compression can result in mixed stress states. Further details regarding the experimental setup of such tests can be found in subsection 4.3.4. In order to extend the pressure range in which fracture is characterised, smooth and notched tensile tests were prepared from the raw-shaped horizontal bars. Due to representing the elemental operation of the cutting phenomenon, orthogonal cutting tests were conducted in order to enable a preliminary validation of the developed numerical cutting model. Small prismatic raw shapes were contemplated, which can be easily sliced

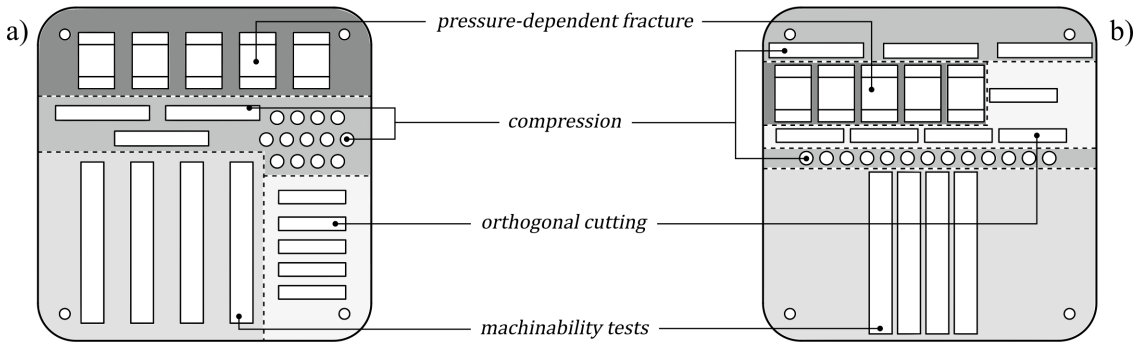


Figure 4.7: Experimental purpose of each type of printed geometry in schematic build plate of 316L (a) and 18Ni300 (b).

Table 4.2: Geometry and purpose of each printed geometry.

Printed geometry purpose	Raw shape(s)
Compression	⌀10x20mm and □10x70mm*
Pressure-dependent fracture	Hat-shaped prisms (refer to 4.3.4)
Orthogonal cutting	10x20x50mm
Machinability	□16x120mm

* for parallel and perpendicular to build direction compression testing, respectively.

into thin rectangular specimens. Similarly to the compression tests, the influence of build direction on the cutting loads was investigated. Ultimately, rectangular bars were printed for use in typical industrial machining operations, such as turning in the case of this research.

4.3.1. Uniaxial compression tests

In order to identify the flow stress of the 316L and 18Ni300 steels (for both metallurgical conditions), uniaxial compression tests were selected. Despite not as representative as the actual tool-chip interaction, these are still much commonly used for the plastic behaviour definition towards metal cutting simulation (Zhang et al., 2021; Rosa et al., 2007a), given the relative simplicity in obtaining the stress-strain material response and allowing for a direct (rather than inverse engineering) characterization. Experiments were designed in order to determine the influence of different loading rates and temperatures, for a closer portrayal of metal cutting conditions.

The compression test involves placing the specimen between two flat parallel plates (dies), and reducing its height by compression, as illustrated in figure 4.8a. Under ideal frictionless conditions, the specimen experiences homogeneous deformation and the absolute values of strain and strain rate can be estimated based on the specimen height evolution in time from the initial dimension h_0 to the compressed final height h. Effective values can be approximated by taking into consideration volume conservation during deformation and the fact that the specimen's diameter (or instantaneous

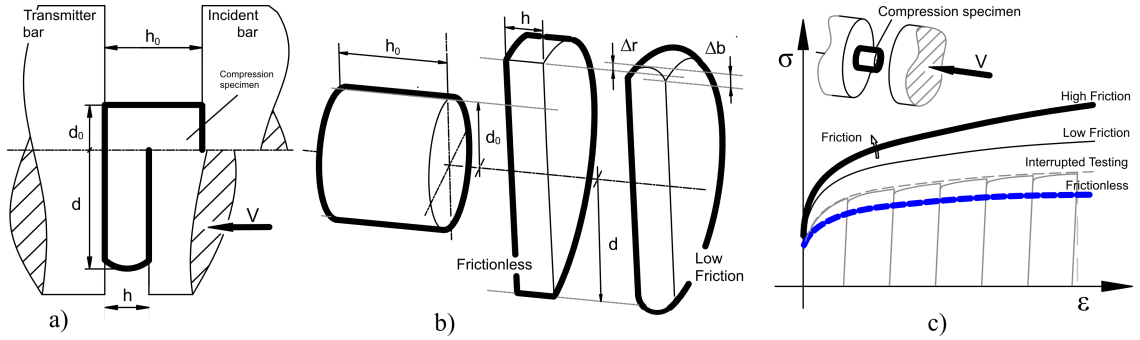


Figure 4.8: Schematic representation of the compression test kinematics (a); friction influence on the deformed cylinder morphology, shown in cross-section (b); and typical flow curves according to the applied tribological and mechanical conditions (c).

Table 4.3: Tested configurations of strain rate and temperature in the compression experimental setup.

Tested configurations:	C1	C2	C3	C4	C5	C6	C7	C8	C9	C10
Strain rate (s^{-1})	QS	300	2000	6000	QS	QS	300	6000	300	6000
Temperature (°C)	RT	RT	RT	RT	200	370	200	200	370	370

QS:Quasi-static; RT:Room temperature

specimen's area, A_i) increases during the compression test. Hence, the effective stress is given by $\sigma \sim F/A_i$, the effective strain by $\varepsilon \sim \ln(h_0/h)$ and the strain rate by $\dot{\varepsilon} \sim v_i/h$, where v_i is the instantaneous compression velocity. This experimental methodology overcomes the limitations of the tensile and bending tests in the absence of plastic instability allowing the typical high strain levels of metal cutting. Buckling, which can happen for slender specimens, is also responsible, in addition to friction, for a deviation from the ideal homogeneous uniaxial stress state. Appropriate height-to-diameter ratio was selected based on typical literature values (ASM International, 2000; Li et al., 2009) for quasi-static and dynamic loading, meaning that the printed raw shapes were machined to ⌀4x4 specimens ($h_0/h = 1$). A thin film of graphite grease was used to lubricate the compression plates towards friction minimization.

Table 4.3 lists the tested levels and configurations of temperature and strain rate. Several tests were performed for each strain rate condition to detect possible gaps in the experimental results that could be attributed to problems of homogeneity during the AM material production and specimens manufacturing. At least 3 specimens were utilised for each test condition. Despite all care taken, no homogeneous deformation can be attained due to the impossibility of eliminating the frictional shear on both contact interfaces between compression plates and the test specimens. This undesired contribution promotes a barrel distortion effect and a significant increase of the flow curve. The ideal mechanical response, frictionless flow curve, can be only attained by eliminating the friction contribution using post-processing techniques on the experimental data.

4.3.1.1. Uniaxial compression apparatus

When it comes to the experimental apparatus, compression tests were carried out in a specially-designed Split Hopkinson Pressure Bar, SHPB, (IST, Lisbon) that provides a wide range of strain rate conditions and temperatures. This setup enables the elimination of relative calibration errors attributed to the usage of multiple load cells, meaning that both low and high strain rate tests have been performed with the same load cell. Figure 4.9 presents an overall view of the compressive SHPB in its default configuration and details on how compression specimens are placed between the incident and transmitter bars. The specially-designed SHPB is composed by four main groups: (i) impact bench, (ii) pneumatic gun, (iii) electromagnetic gun and (iv) hydraulic ram cylinder. The impact bench comprises basic structural parts, two compression plates, a load cell and two displacement transducers, which are independent of the operation conditions. Although the load cell is a typical Wheatstone bridge widely used in traditional SHPB, the distance between the compression plates is calculated by the differential value between two linear transducers on each of the split Hopkinson bars (figure 4.9b). Depending on the desired strain rate range an adequate actuator was mounted. The quasi-static and low strain rate compression tests (less than $1s^{-1}$) were carried out using the hydraulic ram cylinder (figure 4.10b) the medium strain rate tests ($100s^{-1}$ to $1000s^{-1}$) were carried out using the electromagnetic gun (figure 4.10a), while the high strain rate tests (above $1000s^{-1}$) were carried out using the pneumatic gun (figure 4.10c). The electromagnetic actuator consists of electrical circuits for charging and firing the banks of energy-storage capacitors and a series of coils that generate the pressure to accelerate the striker bar against the incident bar. The pneumatic gun comprises several components such as a pressure vessel, an air pressure regulator, a pneumatic trigger valve, a launcher tube and a striker bar. The air pressure in the vessel allows to precisely control the amount of energy released during compression. The mass of the striker bar limits the impact velocity, converting pneumatic energy into kinetic energy. The strain rate signature depends on the specimen's ability to dissipate the kinetic energy for a given impact velocity. Despite these basic fundamentals, it is difficult to achieve an adequate signal noise ratio due to the abrupt pressure

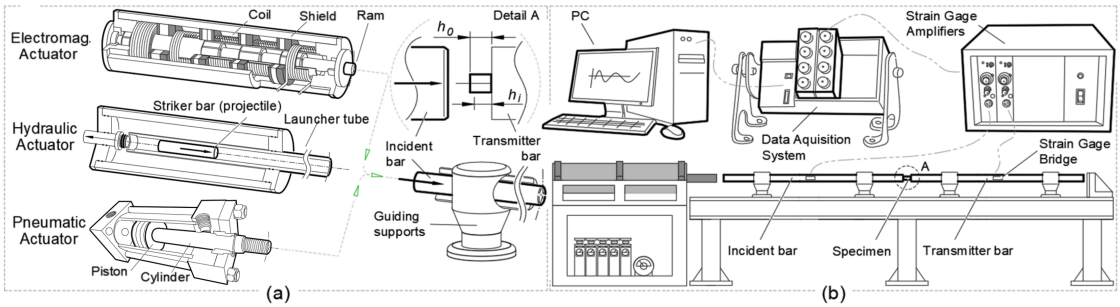


Figure 4.9: Schematic representation of the specially-designed SHPB with its distinct replaceable actuators (a), assembled on the same platform as the downstream data acquisition elements (b).

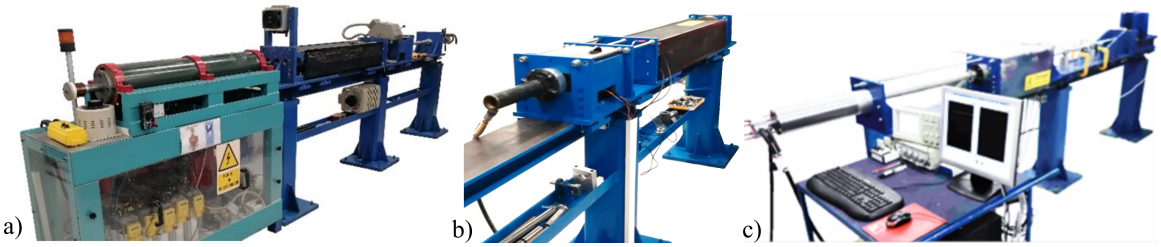


Figure 4.10: Customized SHPB in its electromagnetic actuation default configuration (a), quasi-static hydraulic ram cylinder mount (b) and high strain rate configuration using the pneumatic gun (c).

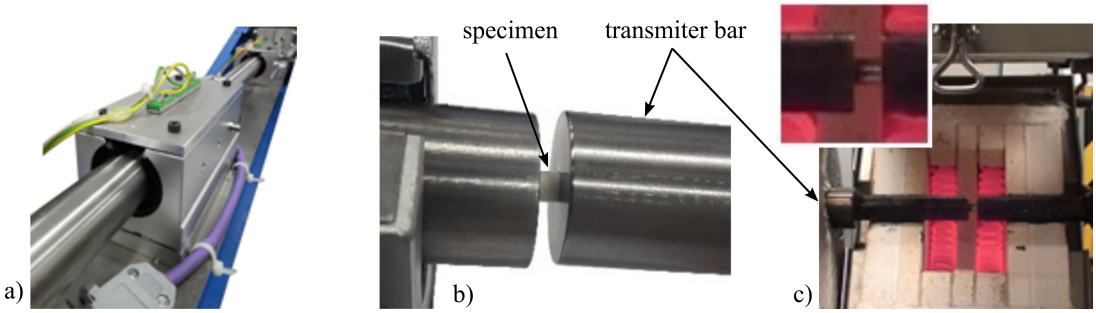


Figure 4.11: Constructive details of the displacement transducers assembly between the linear guides and the impact bars (a); specimen positioning between the incident and transmitter bars (b); and specimen and transmitted bar detail in heating muffle (c).

impact and wave propagating through the SHPB during test monitorization. Thus, a consumable thin nylon sheet of 1 mm was placed between the strike bar and the incident bar to increased loading control. With regards to the hydraulic actuator, an electrical pump supplies the required fluid at the flow rates and pressures necessary for the quasi-static and low strain rate compression tests. A heating muffle was placed at the ends of transmitter and incident bars to achieve high temperature testing (refer to figure 4.11c).

Particular attention should be given to the compression plates (refer to figure 4.11b), as these should maintain their structural integrity despite the adverse conditions. Provided by Palbit S.A., these were made from a powder metallurgy (PM) composite material consisting of tungsten carbide particles and a cobalt metallic binder (WC–15 wt% Co). The high cobalt content provides the required compromise between hardness and toughness to better withstand the shock and vibration of the impact tests. The WC-Co matrix also provides a non-deformable substrate capable of ensuring surface flatness and geometrical profile of the compression plates under high temperatures and extreme compressive loads. Its modulus of elasticity is about three times that of high strength steel allowing to minimize the formation of elastic concavities on the contact interface between the small cylindrical specimens and the compression plates, which could hinder radial expansion of the specimen material. The control of surface roughness is also important to promote uniform material expansion and homogeneous plastic deformation during the uniaxial compression test. For very smooth surfaces ($Ra < 0.1\mu m$) the contribution of the asperity interlocking to the interfacial

friction could be neglected. Thus, the compression plates have been grounded and polished in order to achieve the desired texture and roughness of the flat surfaces. The polishing procedure combines the utilization of abrasive nano-diamond paste and polishing cloths with the rotation of the compression plate in order to ensure predominant circular patterns and average values of surface roughness bellow 0.04 μm. These values were measured by means of an Atomic Force Microscope (AFM), having shown average roughness values (Ra) in the range 0.009 to 0.032 μm along the radial direction of the compression plates. The minimization of chemical adhesion is only possible through the application of adequate coating to the compression plates. For that reason, after the polishing procedures, the WC-Co plates has been covered by a TiAlSiN film of a thickness of not less than 2.5 μm using a PVD HiPIMS procedure. A last polishing of the coated plates surfaces has been carried out to ensure the quality of the surface finish. The combined contribution of the interlocking between asperities and chemical adhesion between material significantly influence the mechanical response of the plates and material flow during the uniaxial compression test.

4.3.2. Ring compression tests

The ring test consists in the uniaxial compression of a ring specimen between two flat parallel plates. The specimen is centred between the plates and compression is performed to several predetermined height reductions. Friction can be estimated by the correlation between the experimental evolution of the inner diameter during compression and friction calibration curves generated in advance by numerical procedures. As the ring height is reduced, the outer diameter expands radially outward and the change in dimensions depends on the amount of compression in the axial direction and on the interfacial friction between ring and compression plates. If friction is small, both the inner and the outer diameter expand. However, due to friction hindering of the radial expansion of the specimen material, the inner diameter can actually become smaller than the original diameter, for higher values of friction (Sofuoglu and Rasty, 1999). In this research, the ring test specimens were made from 18Ni300 steel and the dimensions utilized in the study were 7, 3.5 and 2.5 mm (ratio aprox. 6:3:2) in outside diameter, inside diameter and height, respectively. The end faces of the rings were prepared in order to guarantee an initial surface roughness smaller than 0.1 μm. A lower surface roughness allows for better contact in the first compressive increment and consequently a more accurate measurement of the inner diameter evolution as a function of the specimen height. A lower surface roughness is also important to minimize contaminants (i.e. oxygen gas), nested in the depths of valleys between asperities, that can compromise the overall results. The same experimental apparatus as the compression test was used. Two different lubrication conditions have been used, (i) lubricated contact, graphite grease was used to lubricate the compression plates in order to reproduce the tribological conditions of the uniaxial compressions tests, and (ii) dry contact, to

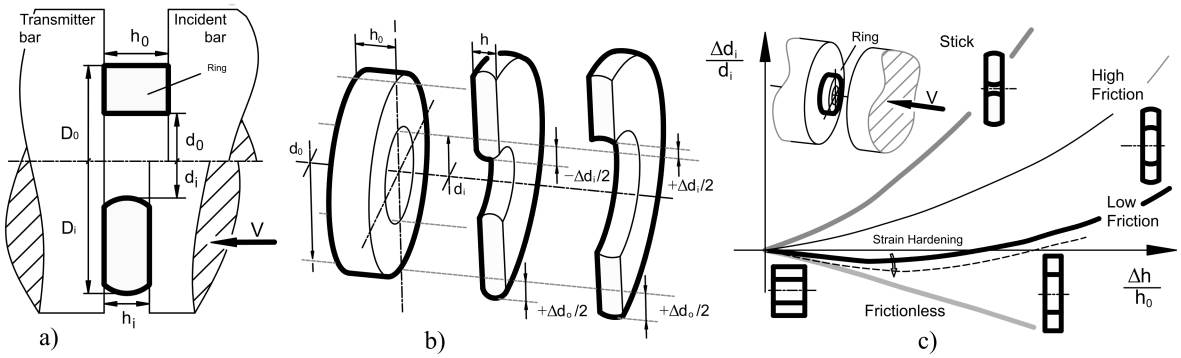


Figure 4.12: Schematic representation of the ring compression test kinematics (a); friction influence on the deformed ring morphology, shown in cross-section (c); and schematical plot of friction calibration curves, obtained by numerical simulation.

study the effect of temperature and loading rate on the interfacial friction under simulative conditions of metal cutting processes. While for quasi-static conditions it is possible to perform interrupted tests and plan to perform various compression stages, in high-speed tests it is not possible to apply such a practice due to the high kinetic energy of the incident bar and only single stages were carried out. At the end of each compression stage, the values of its inner diameter and height were measured and recorded before and after the tests. Also, the plates were cleaned using sandpaper in order to avoid deposition of the testing material on the plates and degreased with ethanol to remove contaminants. The original surface roughness and texture were not affected by the cleaning procedures since sandpaper has an intermediate hardness between 18Ni300 and WC-Co and ethanol evaporates. In case of lubricated contact testing, a thin film of graphite grease was reapplied on the plates surface after the cleaning procedures.

The calibration curves were obtained by means of finite element based simulations using Abaqus program. The compression plates were considered rigid, whereas the bottom plate was considered static and the upper plates moving with a compatible velocity to the experimental tests. The mechanical behaviour of the materials was determined by means of the compression tests (as shown in previous section 4.3.1). Further details on the numerical modelling of ring test will be discussed in chapter 6.1. The calibration curves for quasi-static conditions are exemplified in figure 4.12c, showing that low values of friction give rise to an increase in the inner diameter of the specimens during deformation whereas high values lead to a decrease. The evaluation of the coefficient of friction is performed by overlapping the experimental values on the calibration curves. At least 3 specimens were utilised for each test condition considering possible influence of the texture, shrinkage, porosity, among other issues, of the additively manufactured materials on the tests accuracy and repeatability. Due to material shortage in the same batch, specimens were manufactured from the remainder material of machinability tests. This explains the higher number of ring compression tests performed on the conventional maraging. Table 4.4 shows the conducted experimental workplan. Intermediate strain rate level ($300s^{-1}$) was not tested for the AM material. The presented results and methodology

Table 4.4: Tested configurations of strain rate, temperature and lubrication in the ring compression experimental setup.

Tested configurations:	R1	R2*	R3	R4	R5*	R6	R7	R8*	R9
Strain rate (s^{-1})	QS	300	6000	QS	300	6000	QS	300	6000
Temperature (°C)	RT	RT	RT	200	200	200	370	370	370
Lubrication (°C)	D+L	D	D	D	D	D	D+L	D	D+L

QS:Quasi-static; RT:Room temperature; D:Dry; L:Lubricated(graphite); D+L:both conditions tested.

*configuration tested only in the CM material.

regarding the tribological characterization of the maraging steels was performed in collaboration with IST Lisbon and are, as well, an outcome of the MSc work by Coelho (2021), which is equally integrated in the MAMTool project.

4.3.3. Tensile tests

Tensile tests are often conducted towards flow stress identification of metals. Despite providing a more direct measure of a material's strength relatively to compression setup (due to the absence of friction), the amount of withstand plastic deformation is typically much lower than in compression testing, given the positive pressure conditions. Moreover, their useful range is often limited to the onset of necking, since the material deforms non-homogeneously from that point, hindering a reliable assessment of the effective strain values. In this study, the plastic behaviour has been determined by compression tests, as depicted in section 4.3.1. It is, however, widely acknowledged that metal cutting is not governed solely by plasticity, as fracture also occurs, establishing the need for a damage behaviour identification. The complex state-of-stress that is characteristic of the primary deformation zone imposes a thorough fracture strain characterization which due to being typically

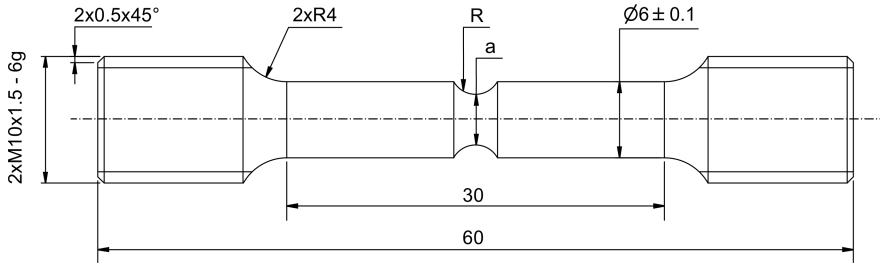


Figure 4.13: Tensile specimen geometry in function of notch dimensions.

Table 4.5: Tested configurations of stress triaxiality according to notch geometry.

Tested configurations:	N-∞ (smooth)	N-5 (notched)	N-2 (notched)
a (refer to fig. 4.13)	6	4	4
R (refer to fig. 4.13)	∞	5	2
$\eta_{Bridgman} = \frac{1}{3} + \ln(1 + \frac{a}{4R})$	0.33	0.52	0.74

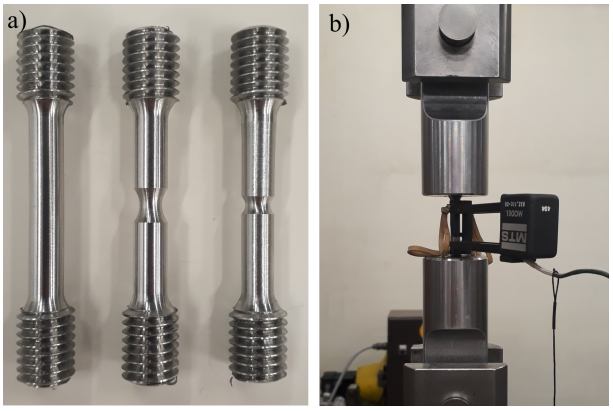


Figure 4.14: Tensile specimens (a) and testing setup on servo-hydraulic machine with placed strain gauge on specimen (b).

sensitive to pressure (Bridgman, 1952) should be calibrated for distinct states of stress. Tensile tests were therefore conducted in order to depict the fracture behaviour of the considered materials under positive stress triaxialities. Three cylindrical geometries were tested: two notched and one smooth (see figure 4.13 and table 4.5). The analytical predictions proposed by Bridgman (1952) were used in order to estimate initial stress triaxialities in function of notch geometry. Threaded grips enabled the fixation of both specimen ends to the testing machine (see figure 4.14). Quasi-static conditions were ensured through the application of a 1mm/min pulling speed to the machine crosshead. Load and displacement were measured for each sample, which were then plotted in terms of true stress and true strain. The usage of numerical modelling towards the identification of fracture initiation is a widely used methodology in order to circumvent plastic instabilities that hinder their direct estimation (Wierzbicki et al., 2005). Such methodology enabled the identification of a damage behaviour in function of the distinct pressure conditions, forced by the applied notches. Figure 4.13 presents the tensile specimen general geometry, while table 4.5 specifies the geometry of each. The tests were performed under quasi-static conditions in a servo-hydraulic MTS testing machine (LET, DEMec, Porto). An extensometer with 25mm gauge length was used (MTS 632.12C-20) in order to measure local displacements (refer to figure 4.14b).

4.3.4. Multiaxial fracture tests

For the identification of the pressure-dependent fracture behaviour, the plane strain specimen specially designed by Abushawashi (2013), who was supervised by professor Astakhov, has been employed due to its ability to cover an intermediate range of stress triaxialities, challenging to attain trough the usage of conventional specimens. These specimens consists of a symmetric double notched geometry, with a nominal gauge length of 2 mm, as shown in figure 4.15. By variation of the pressure angle of the specimen (defined by the center of the two holes), the notch configuration

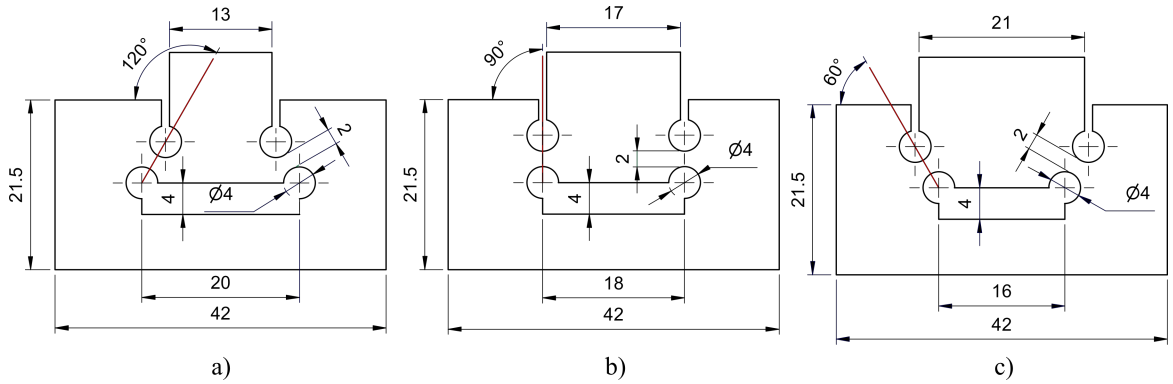


Figure 4.15: Multiaxial fracture specimens for distinct pressure angle configurations: a) 120°; b) 90° and c) 60°.

is altered, allowing for different stress triaxialities. Even though the specimens can be loaded in both tensile or compressive loading conditions, the latter was preferred due to setup simplification. The tests were carried at an Instron 5900R testing machine (INEGI, Porto) making use of a 100kN load cell. A quasi-static compression speed of 1mm/min was imposed on the machine cross-head and two repetitions were conducted in order to ensure experimental repeatability. Due to specimen symmetry, it was important to ensure not only that the compression plates were parallel among each other (top and bottom), but also perpendicular to crosshead displacement direction. Regardless of load condition, for a pressure angle of 90° (refer to fig. 4.15b), no lateral stress is developed, meaning minimum stress triaxiality and theoretically pure shear conditions. Increasing the pressure angle, (e.g. fig. 4.15a) results in a combination of a tensile and shear state-of-stress, yielding intermediate positive stress triaxialities. By decreasing the pressure angle (see fig. 4.15c) a mixture of compression/shear is attained, developing intermediate negative stress triaxialities.

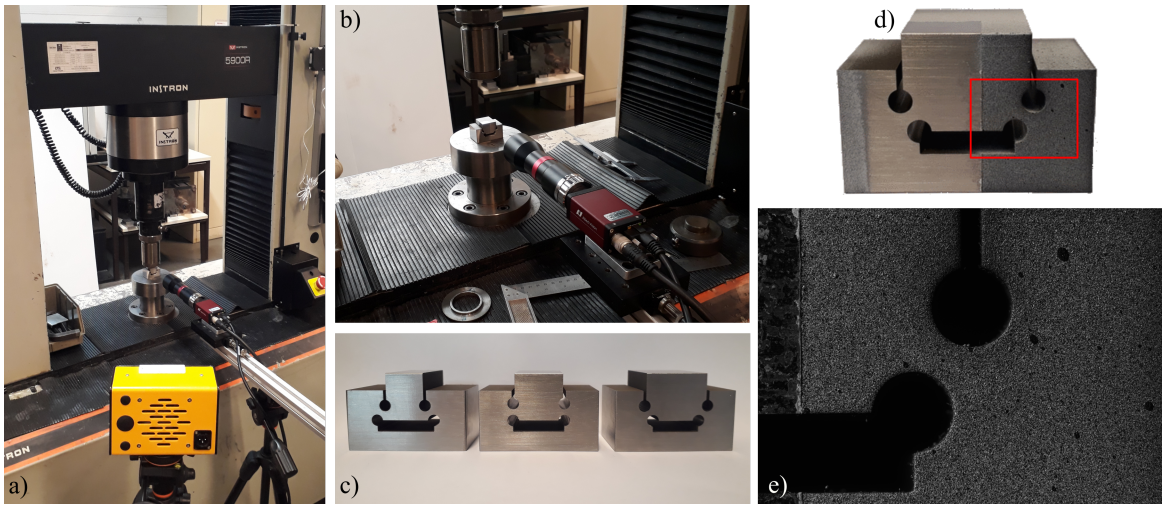


Figure 4.16: Experimental apparatus of the multiaxial fracture tests (a), a detailed perspective of the DIC setup (b), a sample of each tested specimen geometry (c), speckle application on half-specimen (d) and DIC camera capture of the signalled notch region (e).

The identification of the pressure dependent damage behaviour is, similarly to the tensile tests, through a combined experimental/numerical approach. For such, a valid flow stress is applied, allowing for its validation. In order to ensure the correct representation of the build numerical models, digital image correlation (DIC) was used (see figure 4.16). Not only it enables a comparison of the strain fields, but also a more clear insight of the onset damage location, which due to the expected materials' fracture sensitivity to stress triaxiality, might depend on the specimen's pressure angle. DIC is a full-field optical technique that provides the displacement field of a target object by correlating pairs of textured images acquired before and after the application of a given deformation. Specimens texture was achieved through the application of a preliminary white paint (in order to homogenize all surfaces and provide required contrast) followed by a speckle pattern. For that, a IWATA Custom Micron CM-B airbrush (and an air compressor) with black ink was used. Speckle was applied on approximately half of each specimen, as shown in figure 4.16d, given that only one of the notches was monitored through DIC. In this study, a charged-coupled device (CCD) Manta G235 digital camera (9 bits, 1936x1216 pixels) coupled to a telecentric lens and a lighting device were used, as illustrated in figure 4.16. The Vic2D commercial software was used for image processing and computation of the logarithmic strain fields. The setting parameters were selected based on a quantitative evaluation. Subset size was calculated to ensure a optimal match confidence of 0.01 pixel for a given assumed noise level. A subset size of 97 and a step size of 10 pixels were used.

4.4. Metal cutting experimental tests

4.4.1. Orthogonal cutting tests

Orthogonal cutting tests are often used to portray more intricate real machining operations such as turning or milling. It is important to note that this setup is closer to an experimental methodology for characterizing materials towards metal cutting operations (more representative than, for example, compression tests) rather than an actual industrial machining operation. In the present thesis, orthogonal cutting tests were performed with the aim of measuring cutting loads and infer on its eventual difference among the distinctly manufactured maraging steels. In the AM samples, two distinct cutting directions were contemplated: parallel and perpendicular to build direction. Friction at the tool-chip interface in orthogonal cutting conditions are subject of study, in these tests. The influence of tool geometry influence (namely rake angle) has also been a studied parameter in the present experimental procedure. Ultimately, the numerical simulation of the process will allow the validation of the identified material constitutive models.

There are multiple possible setups for performing orthogonal cutting tests. Facing turning operations of a tubular workpiece (Markopoulos et al., 2016) and cutting off of a pre-machined

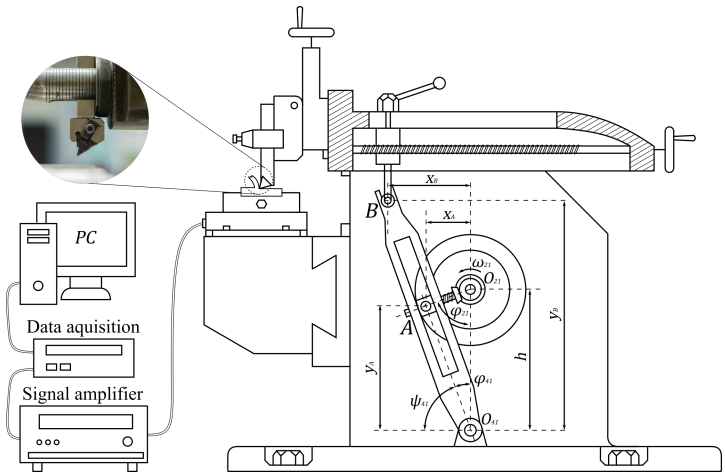


Figure 4.17: Schematic representation of the shaping machine orthogonal cutting setup, its kinematics and nomenclature.

workpiece with ribs/disk (Outeiro et al., 2013) are the most common setups on a lathe. Similar configurations have been developed in milling setups (Daoud et al., 2015; Wang et al., 2015). In this study, orthogonal cutting instrumented experiments were performed on a mechanical shaping machine (L2.03.6, at FEUP). Despite being industrially outdated, this type of machine tool is quite relevant towards the experimental representation of the orthogonal cutting phenomenon due to its robustness and high rigidity that translates into the capability of sustaining high cutting loads in close speed conditions to cutting. In addition, it presents some advantages when compared to the turning and milling setups for orthogonal cutting due to the simplified kinematics. Figure 4.17 illustrates the mechanical shaping machine which is, essentially, a quick-return mechanism. The bull gear is electrically driven (actuation not illustrated) and pushes the ram on a linear cyclical movement (forward and backward). One of the first tasks in the setup preparation was to estimate the effective cutting speed of the ram. Two distinct approaches were carried for such purpose: the first consisted of measuring the mechanical components and calculating speed through the kinematic analysis of the quick-return mechanism. The second was through video recording and derivation of the determined position in function of time. With regards to the first approach, the x-coordinate of point B can be written as a function of ψ_{41} as depicted in equation 4.8. Knowing the relationship between ψ_{41} and φ_{41} (refer to eq. 4.9) one can arrive to equation 4.10. Moreover, $\tan\varphi_{41}$ can be depicted in terms of the radius, r, the crank angle, φ_{21}, and the bull gear heigh relatively to the slotted link fixation point, h, as shown in equation 4.11.

$$x_B = \frac{y_B}{\tan\psi_{41}} \tag{4.8}$$

$$\psi_{41} = 90^\circ - \varphi_{41} \tag{4.9}$$

$$x_B = \frac{y_B}{\cot \varphi_{41}} = \frac{y_B}{1/\tan \varphi_{41}} = y_B \tan \varphi_{41} \tag{4.10}$$

$$\tan \varphi_{41} = \frac{x_A}{y_A} = \frac{r \sin \varphi_{21}}{h - r\varphi_{21}} \tag{4.11}$$

Knowing that the angle φ_{21} is a function of time and can be expressed relatively to ω_{21} as φ_{21}=$\omega_{21}t$, and combining equations 4.10 and 4.11 the x coordinate of point B can be written in function of the constant angular velocity, ω_{21}, as expressed in equation 4.12. Differentiating equation 4.12 in relation to time, the velocity of point B can be defined in equation 4.13. The maximum stroke and maximum forward speed were calculated, based on the measured dimensions of the mechanical components, for the distinct angular speed available configurations, using equations 4.12 and 4.13.

$$x_B = y_B \frac{r \sin(\omega_{21} t)}{h - r \cos(\omega_{21} t)} \tag{4.12}$$

$$\dot{x}_B = y_B \frac{r\omega_{21}[h \cos(\omega_{21} t) - r]}{[h - r \cos(\omega_{21} t)]^2} \tag{4.13}$$

Table 4.6 presents the measured values of machine components and maximum stroke, while table 4.7 displays all speed and stroke possible configurations. Bull gear radius was only measured for maximum stroke configuration (A1). It showed to be in agreement with the theoretical value of stroke (less than 1% of error), which is why r values for the remaining configurations were numerically adjusted towards a match between theoretical and calculated strokes. In order to support the kinematic analysis, the tool position and velocity were video-monitored and the results were compared to the analytical kinematic analysis. A measuring scale was positioned under the tool

Table 4.6: Internal components measured dimensions of the L2.03.6 shaping machine.

Variable (refer to figure 4.17)	Measured value [mm]
r (for maximum stroke)	95.5
h	425
y_B	725
maximum stroke	337

Table 4.7: Different machine speed and stroke configurations of the L2.03.6 shaping machine.

Configurations:	A1	A2	A3	B1	B2	B3
Angular speed [rpm]	25	35	45	60	85	115
Theoretical stroke [mm]	337	250	200	150	100	75
Radius, r [mm]	0.0955*	0.0720	0.0580	0.0440	0.0293	0.0225
Calculated stroke [mm]	334.3	249.1	199.65	150.9	100.1	75.9
Stroke error [%]	0.94	-	-	-	-	-
Maximum forward speed	21.0	22.8	24.6	25.8	25.2	25.8

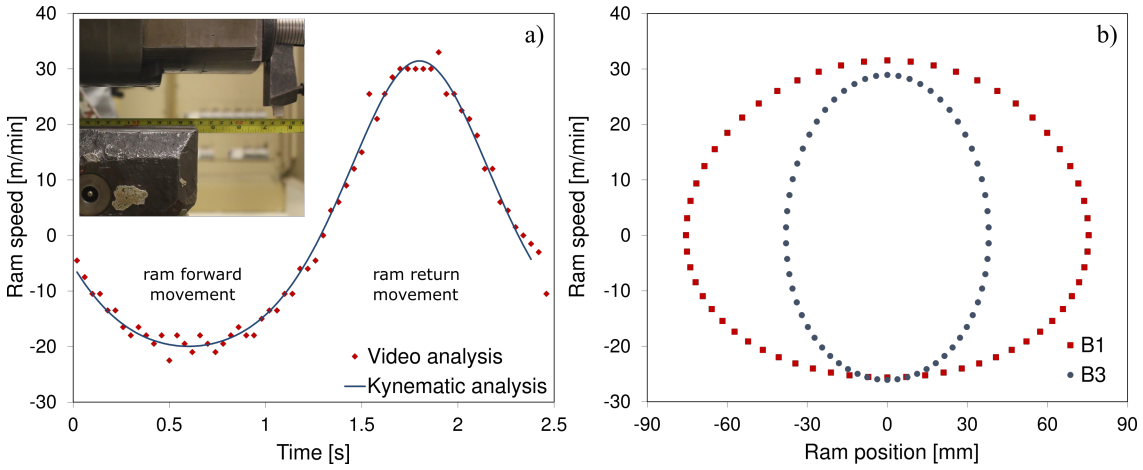


Figure 4.18: Comparison between the distinctly calculated ram speed in function of time for A1 (a) and ram speed in function of its position for B1 and B3 configurations (b).

path allowing for the calculation of its position in function of time. The graph in figure 4.18a shows the comparison between these two approaches as well as a video-frame example. It is observed that B3 and B1 configuration result in maximum forward speed. The latter was selected due to the longer stroke length, meaning that the ram is close to a constant (maximum) speed for a longer length. The ram speeds in function of its position for B1 and B3 configurations are presented in figure 4.18b. It is important to note that the specimen was placed at the middle of the forward stroke length, meaning that tests will be conducted at a near-constant cutting speed of 25.8 m/min.

Load measurement was performed through a three-component piezoelectric dynamometer (Kistler 9257B). A charge amplifier (Kistler 5070A) and a data acquisition system (Advantech 4711A) enabled signal conversion and data collection, which was further analysed using typical processing software. The printed raw geometries intended for orthogonal cutting tests were cut through wire-EDM in their longitudinal and transverse directions. This way, a single printed geometry results

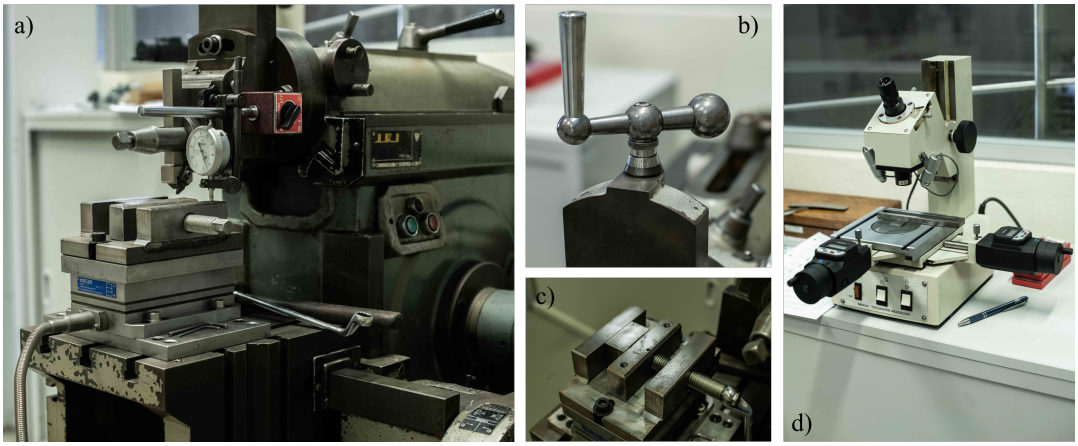


Figure 4.19: Orthogonal cutting experimental setup (a); tool slide lever (b); specimen fixation vise (c); Mitutoyo toolmaker's microscope (d).

in eight orthogonal cutting specimens. All final specimens were ground to 1 mm thickness. Two cutting directions were tested: perpendicular to build direction (with a cutting length of 24 mm) and parallel to build direction (cutting length of 19 mm). Identical specimens were prepared for the CM maraging steel. Figure 4.20a shows the initial printed raw geometry and the 8 final specimens.

A clamping vise was built for specimen fixation (refer to figure 4.19c) and tightened to the dynamometer, which in turn was bolted to the shaping machine table, as shown in figure 4.19a. All components were aligned with the ram movement. The shaping machine tool slide (refer to fig. 4.19b) allows for the definition of the uncut chip thickness, t_0, through its vertical displacement. Given that its scale resolution (0.1mm) is not appropriate for a thorough control of the t_0, a Mitutoyo dial indicator with a 0.005 mm resolution was clamped to the tool slide for improved t_0 definition. The dial indicator probe had the vise surface (fig. 4.19) has a reference, which was ground for better accuracy. Despite all efforts, the definition of a truly accurate t_0 value before each cutting test revealed to be very challenging. Such has led to a verification methodology of the amount of removed material from the workpiece for each cut. This methodology, illustrated in figure 4.20b, starts with the positioning and levelling of the specimen on the clamping vise, followed by an initial cut to ensure parallelism between the specimen top surface and the ram path. After that, the specimen is unclamped and placed on a profile projector for its height measurement (h_i). Successive measurements (in 1 mm intervals) are performed, in order be able to calculate the effective t_0 along the cutting length. A Mitutoyo toolmaker's microscope with a 2x magnification lens (fig. 4.19d) was used for measuring the linear height distances along the specimens' cutting length. Due to being zones of transient cutting, due to chip formation evolution and its cutting end, the specimen extremities were excluded from the measurement stage. Once measured, the specimen is re-clamped on the vise, using a gauge block to guarantee its horizontal alignment and the experimental cutting

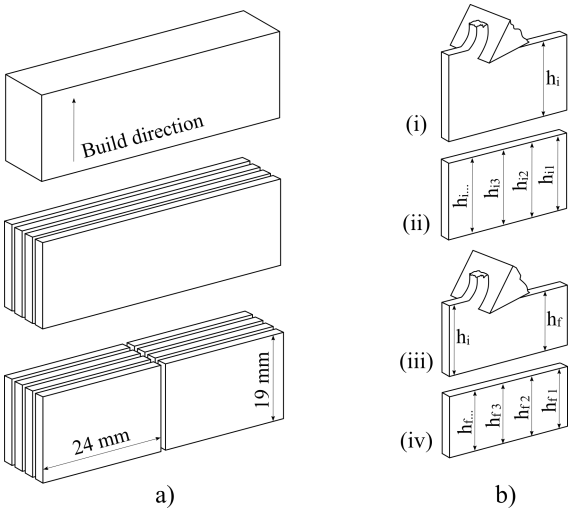


Figure 4.20: Orthogonal specimen wire-EDM cutting (a) and illustration of measurement procedure (b).

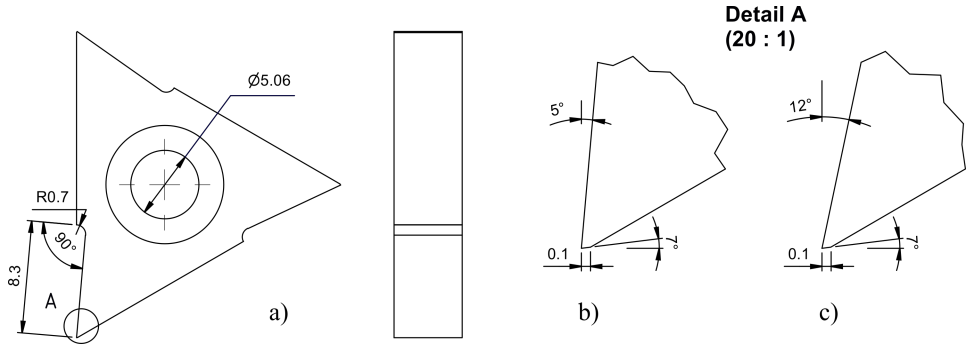


Figure 4.21: Insert geometry used in the orthogonal cutting tests (a) with 5° (b) and 12° (c) rake angles.

test takes place with the advance of the cutting tool (c) and the formation of a chip that is collected. Lastly, a final measurement is led for the same successive 1mm intervals, enabling the calculation of the effective t_0 by subtracting each corresponding final height to the initial value (h_i-h_f).

Specially-designed inserts with three available cutting edges of 4 mm in length were used in the orthogonal cutting tests, manufactured by Palbit S.A. The inserts were mounted on a tool holder with a V pocket with their inverse geometry (ensuring rigidity), which in turn was fixed to the shaping machine ram. Figure 4.21 illustrates the two tested tool geometries, which differ solely

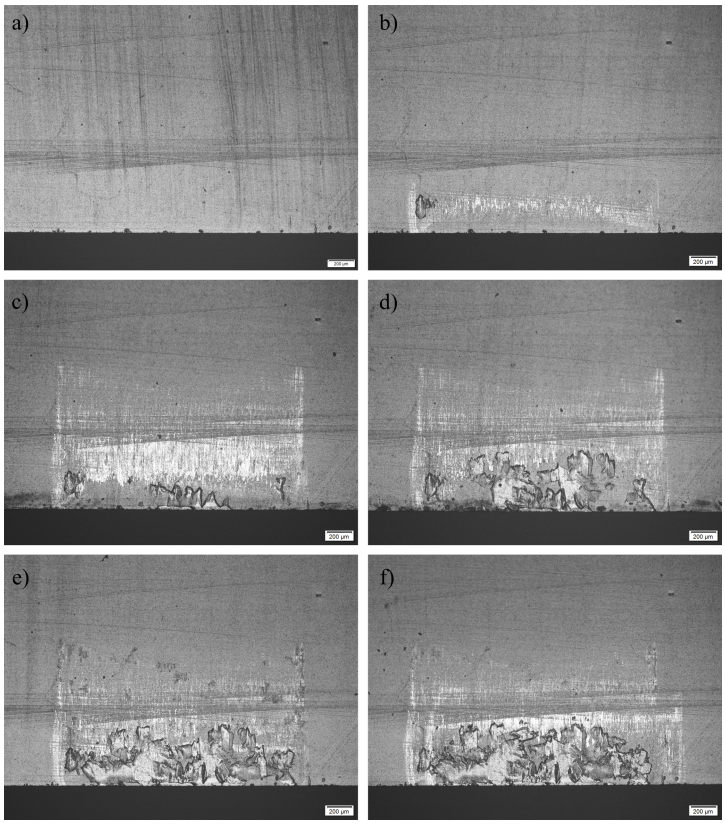


Figure 4.22: Tool rake face (α_r=5°) optical microspopy after sucessive orthogonal cutting tests (t_0 ~0.1mm): (a) untested rake face; (b) 1 cut; (c) 2 cuts; (d) 3 cuts; (e) 5 cuts and (f) 15 cuts.

in rake angle. A physical vapour deposition (PVD) AlTiN layer was applied as coating (PH7920 grade), as it improves tool life, workpiece surface finish and decreases cutting loads when compared to uncoated carbides, mostly due to the enhanced friction conditions at the tool-workpiece interface (Varghese et al., 2019; Endrino et al., 2006).

In order to ensure the suitability of the orthogonal cutting tools, preliminary tests were performed to check the integrity of the cutting edge, rake angle and overall structural strength. For that, an optical microscopy inspection of the tool after each successive test was conducted. No changes in the geometry were observed, especially the cutting edge that remains without any wear signals. Build-up edge, as shown in figure 4.22 seems to accumulate on the rake face after the first cut. In order to avoid the influence of build up material on the tool's rake face, an unused rake surface was employed for every test.

4.4.2. Turning tests

The experimental tests in longitudinal turning setup may provide a more accurate measure of a real-life machining operation, thus providing a good measure of the materials' machinability. The controlled conditions and simplified kinematics of orthogonal cutting (relatively to real machining operations) may contribute to a better understanding of the underlying physics in cutting and facilitate the comparison with numerical models. It is, however, necessary to understand how compatible these cutting operations are and if the same machinability tendencies are identified. For that, the materials machinability was assessed by means of longitudinal turning tests carried out on a universal lathe EFI DU20 with 5.9 kW power (DEMec workshops, FEUP) under dry conditions. Additively manufactured components are often very close to their final geometry and machining operations are conducted in order to attain a better surface quality or to ensure dimensional tolerances for specific applications. Because of such aspect, the current tests focused on finishing operations. Cutting load is significant as an indicator of the operation stability and energy requirements of the machining process. Combined with chip morphology characterization, it allows the identification of favourable cutting scenarios in the post processing stage, envisioning an increase of the production rate and quality of the finished product. Additionally, it allows the determination of the specific cutting power value, which, due to being sensitive to material's imperfections (Stepan et al., 2011), can help to understand if the typical materials defects and heterogeneities compromise the machinability of high strength additively manufactured steels. When it comes to load measurement and acquisition, the same equipment employed in the orthogonal cutting tests was used (5 kHz data sampling rate). The load cell was mounted on the lathe's tool carriage and levelled in order to ensure the alignment of the cutting tool with the centre of rotation of the fixation chuck. Figure 4.23 shows a schematic representation and the related nomenclature of the experimental apparatus. An ISO DCMW

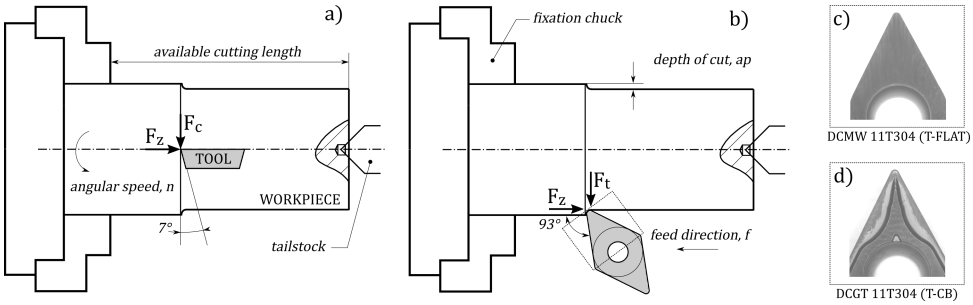


Figure 4.23: Scheme of the turning setup: (a) front view and (b) top view of tool-workpiece relative position; rake surface of the used tools, T-FLAT (c) and T-CB (d).

11T304 cutting insert with a flat top chip-breaker and an alumina (Al2O3), Titanium CarboNitride (Ti(C,N)) CVD coating (herein referred to as T-FLAT) supplied by Palbit S.A. was selected as a control tool geometry. Additionally, an ISO DCGT-11T304-FS with chip-breaker and the same coating as the orthogonal cutting inserts, TiAlN PVD coating, (herein referred to as T-CB) was selected to provide a more representative cutting insert to the industrial turning operations. Both cutting inserts have a similar 0.4 mm nose radius and were mounted on a tool holder providing a -3° side cutting edge angle, 0° cutting edge inclination and 7° back relief angle. These two different insert geometries served also to assess the chip-breaker efficiency applied to AM materials processing. Given the slenderness of the turning specimens, tail stock was used to minimize chatter due to vibration. This also contributed to the best rational use of the available material, allowing for a smaller chuck fixation length. The available cutting length (100 mm) was divided into 4 segments, each one for a different combination between the feed rate and depth of cut while maintaining a constant rotational speed. Two specimens were used for each material, enabling one repetition for each. An unused cutting tool was selected for each segment in order to ensure equal conditions. Regarding the operative parameters, a full factorial combination of two rotational speeds (1800 and 2500 rpm), three feeds (0.05, 0.1 and 0.2 mm/rev) and three depths of cut (0.1, 0.2 and 0.3 mm) were explored. Each specimen is subjected to various cutting passes so the starting point for each cut is an already machined surface. Since the tests were performed under constant rotational speeds, the cutting speeds have evolved along the successive cutting passes due to the diameter reduction. The 2500 rpm resulted into cutting speeds between 118 and 77 m/min; the 1800 rpm resulted into cutting speeds between 85 and 55 m/min, as shown in table 4.8. The resulting cutting speeds are considered in a low range, but could be considered acceptable for more aggressive dry cutting conditions adopted in the current research. Regarding the depth of cut and feed values, the values were selected to represent finishing conditions. It is interesting to note that for finishing processes it is often recommended a depth of cut not lower that 1/3 of the tool nose radius, which was respected in this research.

Exploratory cutting tests were carried out to identify an appropriate range of cutting para-

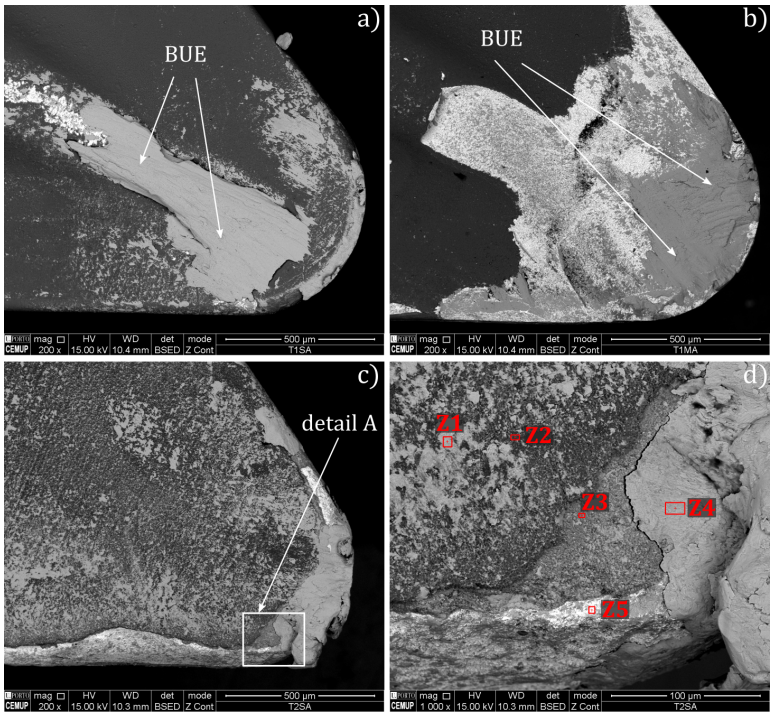


Figure 4.24: SEM images of the T-CB cutting tools used in 316L (a) and 18Ni300 (b); T-FLAT cutting tool used in 316L turning (c) with a detailed EDS analysis (d).

meters to investigate the machinability of additively manufactured steels. These preliminary tests revealed that workpiece material is one of the most important process parameters affecting the cutting tool performance. According to the visual observation and Scanning Electron Microscopy (SEM) two types of wear occurred: flank wear and central crater wear at the rake face of the tested cutting inserts. After dry cutting AM 316L for 5 minutes, no significant changes were visually identified, whereas for AM 18Ni300 a significant deterioration of the overall geometrical and coating wear were clearly observed. A close observation using Energy-Dispersive X-ray Spectroscopy (EDS) also revealed changes taking place in the rake face induced by AM 316L. In figure 4.24c a T-FLAT insert used on additively manufactured 316L is shown, while in figure 4.24d a magnification of detail A is presented. The chemical composition of the 5 regions (Z1 to Z5) was determined. The fact that Z5 corresponds to the tool substrate material, indicates the detachment of the coating layer as a consequence of the abrasion between the workpiece material on the cutting edge region. Regarding the surface region, it is noticed that coating has also suffered erosion/detachment given that not only the external layer, Al2O3, but also the internal layer, Ti(C,N), were identified (Z2 and Z3, respectively) on the EDS analysis. Moreover, the chemical composition of Z1 and Z4 indicates adhesion of the workpiece material on the tool rake surface forming the so-called BUE. This indicates a drastic reduction of the tool life in AM 18Ni300 and to a lesser extent in AM 316L processing that need further investigation based on long-term cutting tests using a significant amount of material. For this reason, short-term cutting tests have been chosen for the present investigation to ensure that

insert geometry and tribological condition remain constant during experiments. Short-term cutting tests have also allowed to minimize the formation of BUE. Figures 4.24a and 4.24b show evidences of an adherent boundary layer on the T-CB tool surface after cutting 316L and 18Ni300, respectively.

Table 4.8: Overview of tested cutting parameters in turning tests.

n [rpm]	f [mm/rev]	a_p [mm]	⌀ [mm]	v_c [m/min]
2500	0.2	0.5	15	118
		0.3	14	110
		0.1	13.4	105
	0.1	0.5	13.2	104
		0.3	12.2	96
		0.1	11.6	91
	0.05	0.5	11.4	90
		0.3	10.4	82
		0.1	9.8	77
1800	0.2	0.5	15	85
		0.3	14	79
		0.1	13.4	76
	0.1	0.5	13.2	75
		0.3	12.2	69
		0.1	11.6	66
	0.05	0.5	11.4	64
		0.3	10.4	59
		0.1	9.8	55

Chapter 5. Experimental results and discussion

The present chapter shows the obtained results from the previously described experimental tests. A special emphasis is given to their comparison with regards to the distinct metallurgical conditions of the materials. Moreover, when possible, the results are compared with the literature, contributing to their thorough discussion and analysis. Table 5.1 shows an overview of the used tested materials in each specific characterization.

Table 5.1: Tested materials at each characterization stage.

Material:	CM 316L	AM 316L	CM 18Ni300	AM 18Ni300
Physical thermal and metallurgical characteristics	x	x	x	x
Quasi-static compression	x	x	x	x
Dynamic compression	x	x	x	x
High temperature compression			x	x
High temperature + dynamic compression	x		x	x
Ring compression			x	x
Tensile			x	x
Multiaxial fracture			x	x
Orthogonal cutting			x	x
Machinability (longitudinal turning)	x	x	x	x

5.1. Physical, thermal and metallurgical characteristics

5.1.1. Chemical composition

The chemical composition of each material, depending on its metallurgical condition, is depicted in table 5.2. Despite some differences in chemical composition of AM versus CM steels, both metallurgical conditions are in accordance with the respective standards. The low carbon content of both materials is highlighted. In austenitic stainless steels, local heating and subsequent cooling (such as welding or AM) can significantly affect corrosion resistance due to carbide precipitation Stull et al. (2018). Lowering the carbon content of the alloy can minimize such effect, which is why 316L is preferentially used in the AM field. On the maraging steel, the lack of carbon enhances weldability,

which in turn makes such alloys a good choice for AM (Lang and Kenyon, 1971; Król et al., 2020), when increased mechanical strength is a requirement for components. Rather than the typical high carbon content, the martensitic microstructure of 18Ni300 steel is achieved by nickel addition, which is the main element. Also interesting to note, is the significantly lower weight percentage of the Mn alloying element in the AM LPBF. This is potentially related with the low melting point of such element, which may volatilize during powder (re)fusion processes.

Table 5.2: Chemical composition (wt%) of SS316L and 18Ni300 steel alloys with respective reference values.

			Ni	Co	Cr	Mo	Ti	Si	Mn	C	P	S
SS316L	ASTM-A276 (2017)	min	10.0	-	16.0	2.00	-	-	-	-	-	-
		max	14	-	18.0	3.00	-	1.00	2.00	0.03	0.045	0.030
	AM material		13.45	-	16.67	2.26	-	0.424	0.53	0.027	0.017	<0.001
	CM material		11.14	-	16.49	2.07	-	0.29	1.84	0.03	<0.001	0.02
18Ni300	MIL-S-46850D (1986)	min	18.0	8.5	-	4.6	0.5	-	-	-	-	-
		max	19.0	9.5	-	5.2	0.8	0.10	0.10	0.03	0.01	0.01
	AM material		18.80	8.84	-	5.15	0.65	0.05	0.03	0.02	<0.001	<0.001
	CM material		18.93	8.92	-	4.88	0.77	0.02	0.03	0.01	<0.001	<0.001

5.1.2. Relative density and metallographic analysis

Figure 5.1 presents two metallographic image samples (one for each direction of interest) for each considered AM material. Voids seem to occur in higher number and larger size for the 316L sample, when compared to maraging steel. While the relative porosity values of the maraging steel (99.7%) is identical to the manufacturer's specification (99,8%), the same is not valid for the stainless steel (97.1%). Despite its lower density, which is an outcome of the used processing parameters, the samples can still be considered a dense part. Moreover, the observed porosity voids did not show an identifiable process-related pattern.

The microstructure of the additively manufactured 316L chemically etched samples is presented in figures 5.2a and 5.2b for perpendicular and parallel directions to build direction, respectively. Grain continuity through melt pools is observed and signalled in figure 5.2b. These results are very much in line with the metallographic samples found in literature for identical steels (refer to figure 3.9). Figures 5.3a and 5.3b show the etched samples of the maraging steel. A similar microstructure is observed in the two directions, characterized by an uneven distribution of lath and plate martensite among austenite. It is important to note that while chemical etching seems to emphasize grain morphology, electrolytical etching highlights the typical macrostructure of AM, such as the melt pools and laser tracks. For instance, figures 5.2c and 5.3c show electrolytical etched samples of 316L and 18Ni300, respectively, where melt pool geometry is evidenced. It is noticed

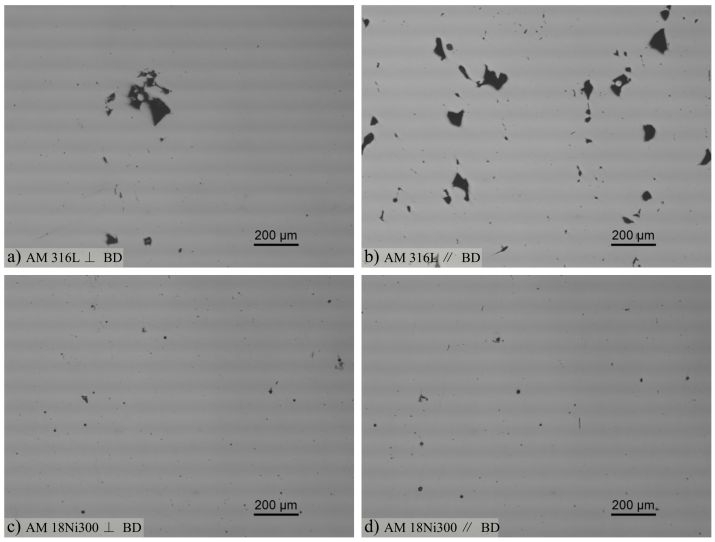


Figure 5.1: Unetched metallographic samples showing void occurrence in AM 316L (a, b) and 18Ni300 (c, d).

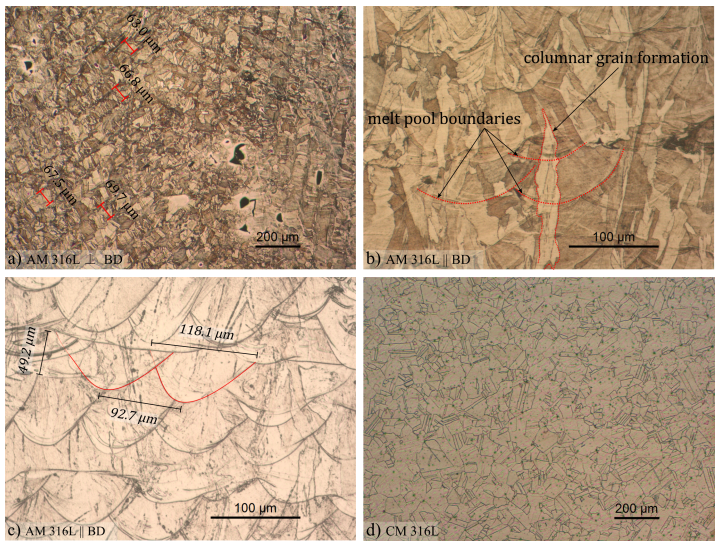


Figure 5.2: Chemically etched metallographic samples of AM 316L in perpendicular (a) and parallel to build direction (b) and electrolytically etched samples of AM 316L (c) in parallel direction to build. Chemically etched samples of CM 316L (d).

that the selected parameters for the processing of 316L stainless steel yield flatter and less wide melt pools, in contrast with the deeper melt pools that are observed in 18Ni300. Making use of the reviewed energy density parameter (refer to equation 3.3), a relation between the melt pools and the processing parameters has been established. The calculated values of E_v were of 55 and 122 [J/mm^3] for 316L and 18Ni300, respectively, which is in accordance with the smaller melt pool area of 316L relatively to 18Ni300. The typical equiaxial crystal geometry of CM annealed stainless steel 316L is observed in figure 5.2d, while in figure 5.3d, plate-like martensitic structure is noticed as well as the absence of thin-lath martensitic structures. The reduced ductility and susceptibility

to microcrack formation in plate martensite when compared to lath morphology (Yokota and Lai, 1974; Kelly and Nutting, 1961) may contribute to the distinct mechanical behaviour between the conventional and additively manufactured maraging steels.

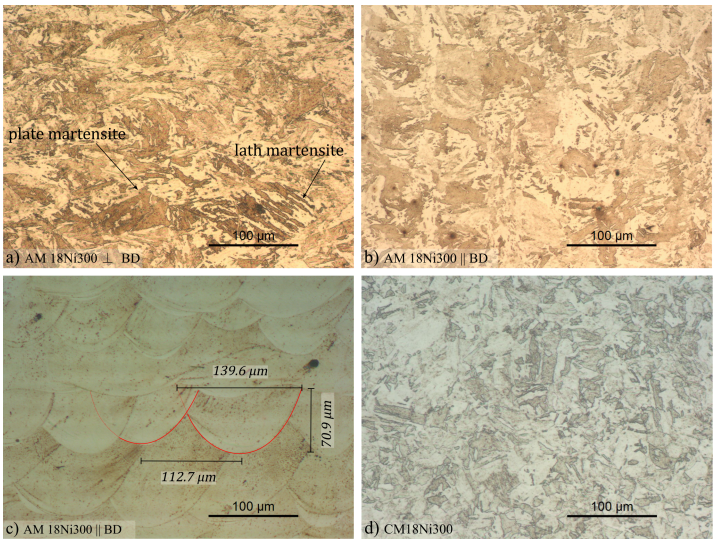


Figure 5.3: Chemically etched metallographic samples of AM 18Ni300 in perpendicular (a) and parallel to build direction (b) and electrolytically etched samples of AM 18Ni300 (c) in parallel direction to build. Chemically etched samples of CM 18Ni300 (d).

5.1.3. Thermal expansion coefficient

Figures 5.4 and 5.5 display the dilatometric curves (changes in sample length in function of temperature) for each material and metallurgical condition. It is observed that the 316L SS shows linear thermal expansion in its AM and CM conditions. On the other hand, the non-uniform expansion of the 18Ni300 maraging steel reveals the occurrence of phase changes. According to de Carvalho et al. (2013), three phase transformations may be noticed in the maraging steels: precipitation, reversion to austenite and martensitic transformation.

Despite being more pronounced on the conventionally manufactured maraging steel, the three phase changes can be identified and are signalled in figure 5.5. In order to accurately point those phase transformations, figure 5.6 shows the slope variation of the dilatometric curves. The slope variations for temperatures bellow 200°C should be disregarded due to being a consequence of variable heating rate which was only ensured constant (1°C/min) starting from that temperature (no phase changes are expected at such low temperatures). The first material contraction corresponds to the precipitation of intermetallic compounds which starts around 550°C. Higher precipitation seems to occur in the conventionally manufactured maraging steel, which might be related with the (marginally) higher Ti and Co content (Schmidt and Rohrbach, 1991). In addition, it has been reported that for higher heating rates, the time available for precipitation decreases, diminishing its occurrence

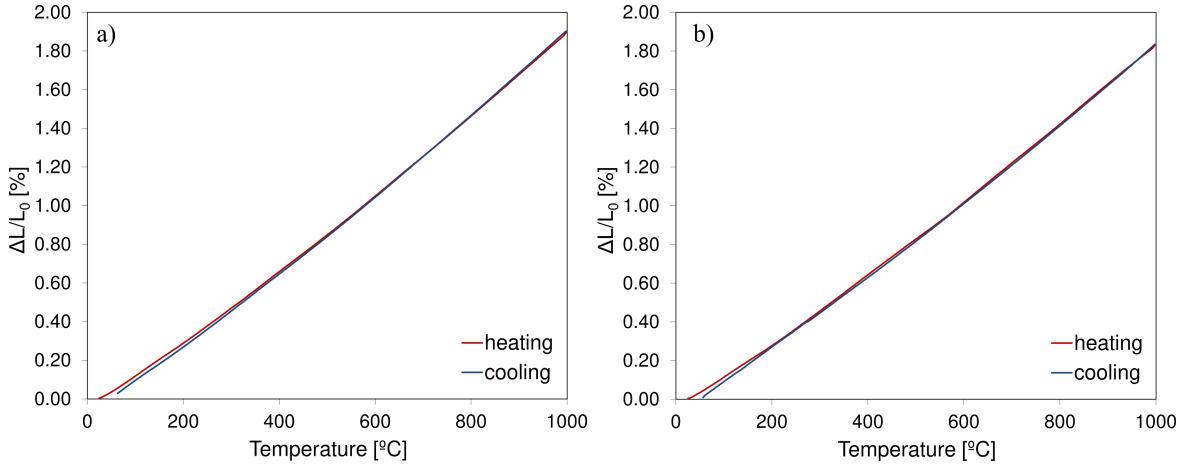


Figure 5.4: Relative sample length in function of instantaneous temperature for the 316L SS of CM (a) and AM (b) metallurgical conditions.

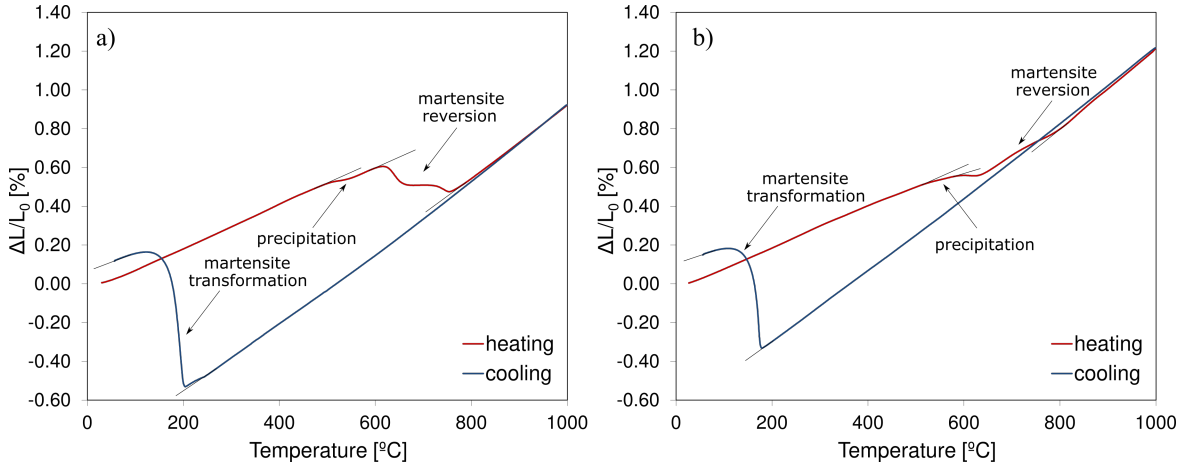


Figure 5.5: Relative sample length in function of instantaneous temperature for the 18Ni300 of CM (a) and AM (b) metallurgical conditions.

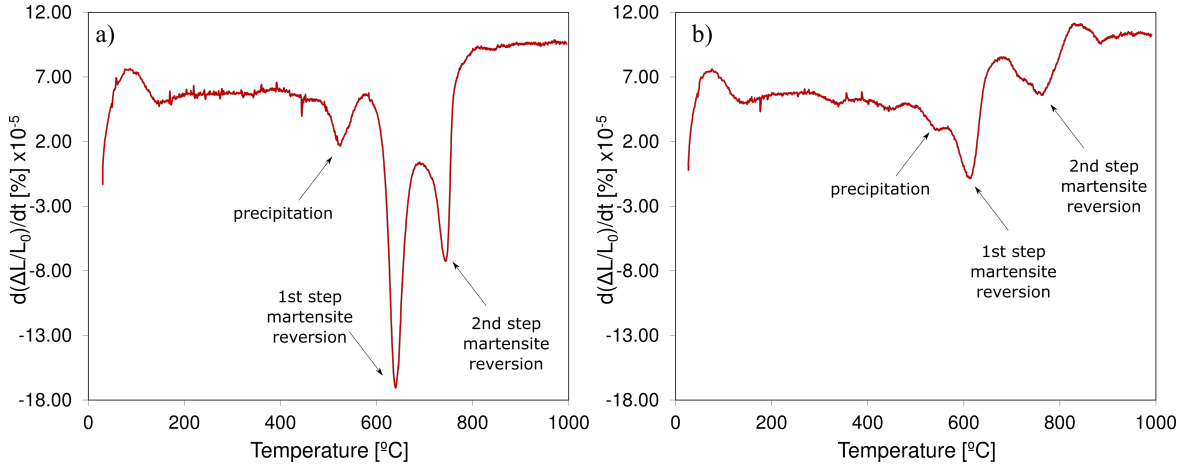


Figure 5.6: Slope of the dilatometric curves of both CM (a) and AM (b) 18Ni300 maraging steel, during heating stage.

Table 5.3: Thermal expansion coefficient ($10^{-6}°C^{-1}$) in function of temperature, for each tested steel.

Material:	CM 316L	AM 316L	CM 18Ni300	AM 18Ni300
25°C	16.01	16.14	10.78	11.25
100°C	16.63	16.14	10.89	11.07
200°C	17.45	17.04	11.05	10.83
300°C	18.28	15.46	11.20	10.59
400°C	19.10	18.85	11.36	10.36
500°C	19.93	19.75	11.51	10.12

(Kapoor et al., 2003), possibly meaning the absence of such effect in very high heating rates such as those occurring in metal cutting. Precipitation is followed by another (larger) contraction, which is related with the start of austenite formation (martensite reversion). That phase transformation happens in two distinct phases, the first by diffusion and the second by shear mechanisms (Król et al., 2020). During cooling, the large material expansion that starts around 200°C (refer to fig. 5.5) sets the start of austenite to martensite transformation.

While in the CM material precipitation and 1st step martensite reversion are markedly separate, these two effects seem to take place almost simultaneously in the AM maraging steel. Also important to note is the magnitude of both 1st and 2nd martensite reversion stages, which is higher for the conventionally manufactured maraging steel. This is in total agreement with the identified (distinct) microstructures of CM and AM tool steels by Bajaj et al. (2020) shown in figure 3.10. The existence of a significant amount of retained austenite (6-11%) in the microstructure of as-built LPBF maraging steel means that less martensite is transformed into austenite through diffusion and shear, which in turn explains the smaller material contraction of the additively manufactured maraging steel. Moreover, the same author indicates that due to the high cooling rates very little or no precipitates are found in the microstructure of as-built LPBF maraging steel, which supports the smaller precipitation-related contraction of AM material. Summing up, and in order to posteriorly use those values in the numerical simulation of metal cutting, table 5.3 displays the thermal expansion coefficient of the tested materials. Those values were calculated up to 500°C, given that beyond that temperature, phase changes occur in the maraging steel. The thermal expansion is critical in dry machining, due to promoting geometrical deviation (tolerancing errors) of the machined part, given the increase in temperature Klocke et al. (2013). A lower thermal expansion is noticed for the maraging steel, when compared to the 316L, meaning the likelihood of smaller thermal deformation allowing for increased dimensional accuracy, which is highly required in the tools and mould industry.

5.1.4. Specific heat and thermal diffusivity

The results for specific heat and thermal diffusivity are shown in figure 5.7 for 316L and 18Ni300 steels. For the maraging steel, monotonic trends can be observed up until 600°C. The identified phase changes starting around that temperature hinder further calculation of c_p and a. Very little differences are noticed with regards to the metallurgical condition of each steel. Despite the lack of substantial results for literature comparison purposes on the maraging steel, it is found that the obtained results for the 316L are in close agreement with literature (Yakout et al., 2020; Van der Aa, 2002), validating the applied methodology.

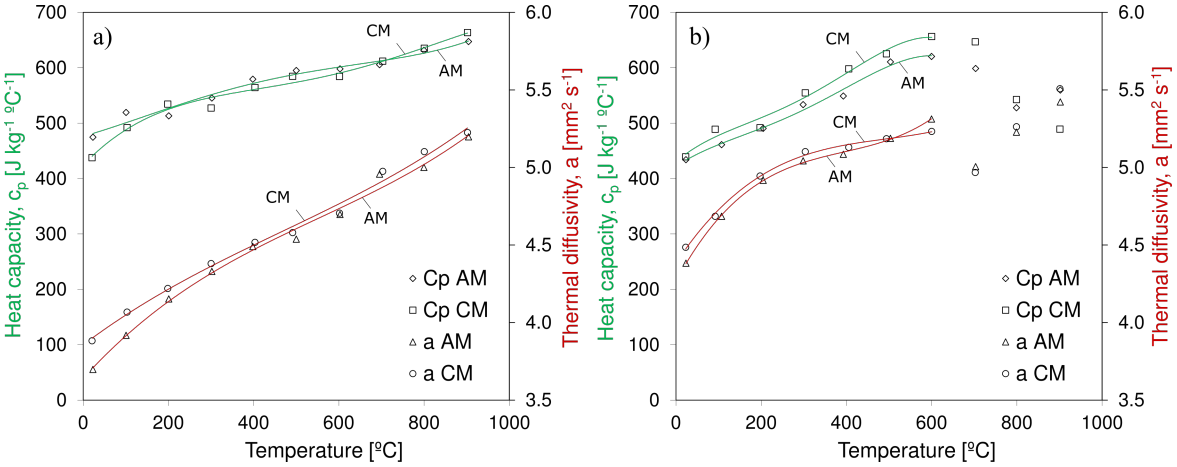


Figure 5.7: Heat capacity (green) and thermal diffusivity (red) for 316L (a) and 18Ni300 (b) steels.

5.1.5. Thermal conductivity

The thermal conductivity of the considered materials is shown in figure 5.8, in function of temperature for all tested materials. An almost linear trend is found for both materials and metallurgical conditions. As expected, the 18Ni300 maraging steel presents a higher thermal conductivity than the stainless steel. The influence of metallurgical condition on the thermal conductivity seems to be different in each steel. While in the 316L steel there is almost no difference between AM and CM, for the 18Ni300, the conventionally manufactured shows a higher conductivity, presenting an almost perfect upper bound offset relatively to the AM.

5.1.6. Surface roughness

The obtained results show that surface roughness resultant from additively manufacturing 316L and 18Ni300 (in time-wise feasible processing conditions) is notoriously high, as depicted from table 5.4. Moreover, it is significantly higher on the surfaces that are perpendicular ($\perp$) to build direction

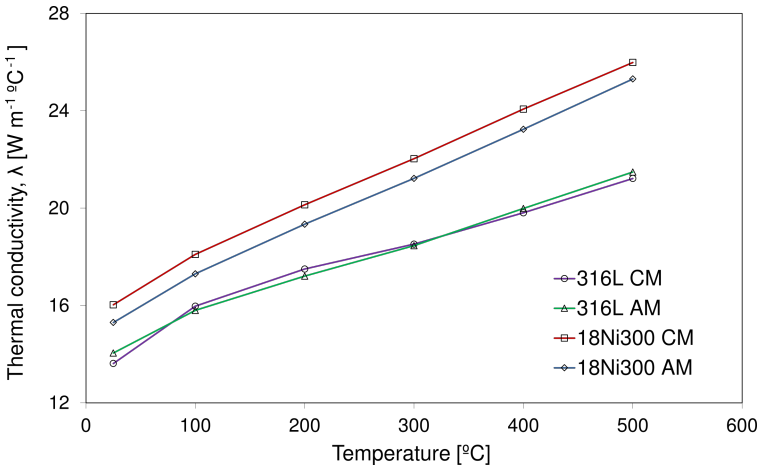


Figure 5.8: Temperature dependent thermal conductivity of each tested steel and each metallurgical condition.

(top surfaces). It is also relevant to note the distinct surface roughness among materials, which is higher for the 316L stainless steel. One of the possible reasons is the higher occurrence of surface defects. Figure 5.9 shows the as-built AM surfaces of 316L (a) and 18Ni300 (b). A noticeable higher number of non-fully melted metal powder particles can be seen in the 316L surface. In addition, particles seem to show larger size in the latter steel. The occurrence of such surface roughness undermining effects is in accordance with literature, as reviewed in section 3.2.5 and is pointed out as one of the main reasons for the poor surface roughness of additively manufactured metals.

Table 5.4: Surface roughness average ($\overline{x}$) and standard deviation (σ) values [μm] for as-built condition.

Material		Ra		Rz		Rmax	
		$\overline{x}$	σ	$\overline{x}$	σ	$\overline{x}$	σ
SS316L	$\parallel$ BD	8.99	0.60	49.68	1.54	63.54	4.82
	$\perp$ BD	11.06	1.04	55.64	4.21	73.52	4.65
18Ni300	$\parallel$ BD	5.35	1.30	29.88	7.84	38.56	5.89
	$\perp$ BD	5.52	0.59	34.50	3.52	47.59	4.49

Regarding the materials' hardness, table 5.5 shows the measured values for both materials in both metallurgical conditions. It is relevant to highlight that hardness was measured in Vickers scale for the 316L and in Rockwell C for the 18Ni300. Besides the expected higher hardness values of the maraging steel, it is seen that for both materials, the additively manufactured condition presents higher average hardness. Knowing that materials' hardness is an indirect measure of yield strength, the results seem to be coherent with the reviewed literature, since increased mechanical strength of AM metals (when compared to CM counterparts) is expected due to a finer microstructure. In fact, according to the correlation between hardness and yield strength of ASTM-A370 (2020) (for ferritic and martensitic steels), values of 930 and 1140 MPa are expected for the CM and AM 18Ni300

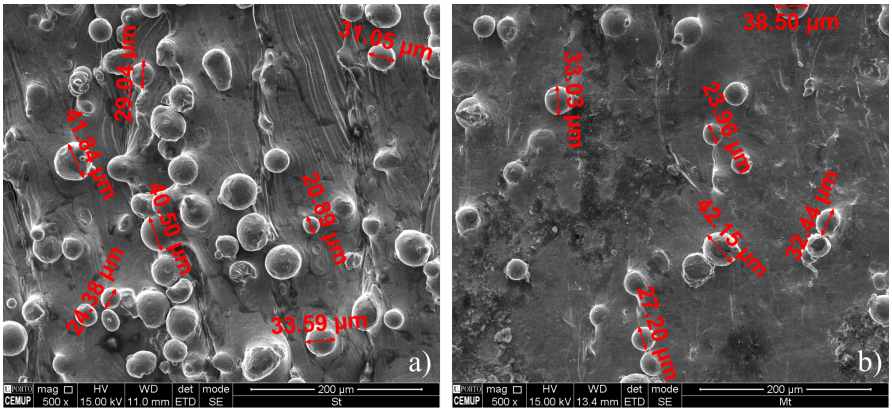


Figure 5.9: SEM images of as-built 316L (a) and 18Ni300 (b) surfaces showing non-fully melted metallic powder particles.

maraging steels, which is supported by compression (refer to figure 5.10b) and tensile tests (refer to figure 5.23) which will be further analysed. Hardness measurements on the machined samples show an approximate 10% increase, which may be attributed to the material's work hardening.

Table 5.5: Hardness values of 316L and 18Ni300 steels in both CM and AM ($\perp$ BD) metallurgical conditions.

Measurement:	1	2	3	$\overline{x}$
316L (CM)	200	194	182	192
316L (AM)	203	217	197	206
18Ni300 (CM)	29	29	29.5	29.2 (272*)
18Ni300 (AM)	33	33	34	33.3 (305*)

*HV value converted from HRC.

5.2. Material and tribological characterization experimental results

5.2.1. Uniaxial compression tests results

The obtained results from the instrumented compression tests in quasi-static and room temperature conditions are displayed in figure 5.10 for both materials. The influence of metallurgical condition and build direction are evidenced on the stress-strain response. The higher mechanical strength of the AM steels is consistent with the typically finer microstructure of these alloys, already identified in the literature review (i.e. figure 3.12 and table 3.6). Despite its approximately 45% lower yield strength, the 316L CM steel presents greater work hardening than its AM counterpart and, thus, similar maximum flow stresses for higher strains (>0.4). On the other hand, with regards to metallurgical condition, the 18Ni300 maraging steel presents identical work hardening and a smaller yield stress difference (CM is approximately 10% lower than AM). A slight anisotropic behaviour

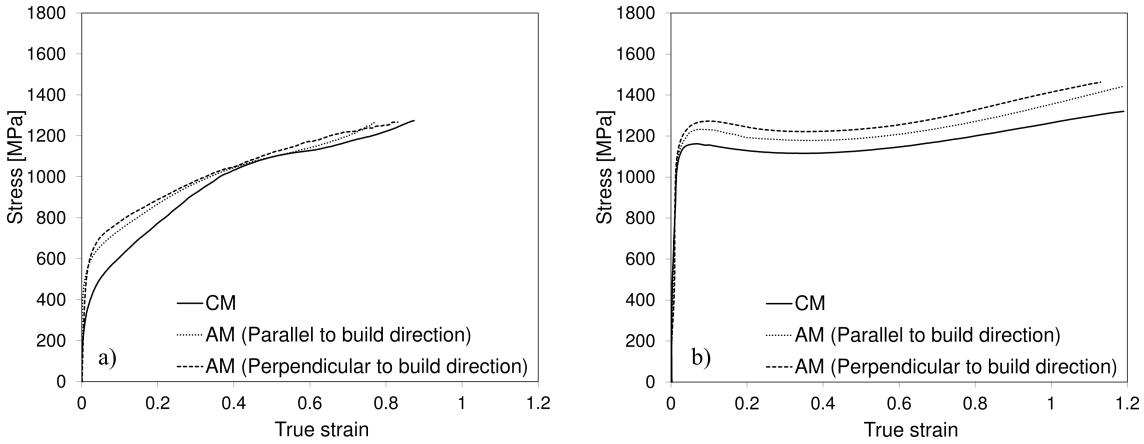


Figure 5.10: Influence of metallurgical condition on the stress vs. strain of 316L (a) and 18Ni300 (b) compression behaviour.

is also noticeable in both AM steels. The highest mechanical strength occurs, in both AM steels, for compression in perpendicular direction to build, which can be explained by the higher grain boundary density which act as barriers to plastic deformation, in that specific loading path, as found in literature review for similar alloys (i.e. figure 3.18) and confirmed in the conducted metallographic analysis of the analysed material samples. The reliability of the specially built experimental setup for compression tests is additionally confirmed through the comparison of three distinct compression curves obtained from different laboratories (refer to figure 5.11), conducted on the same 18Ni300 CM material batch. A slightly distinct work hardening (steeper curve) is noticed for the FEUP tests (Couto, 2019), which may be related with the bigger specimens' aspect ratio (⌀6x6mm). According to Gunasekera et al. (1982), specimen size can promote stress overestimation due to a more pronounced barrelling effect. This is consistent with the fact that for lower strains (lower influence of friction) higher repeatability among the curves is noticed. Moreover, it points out the importance

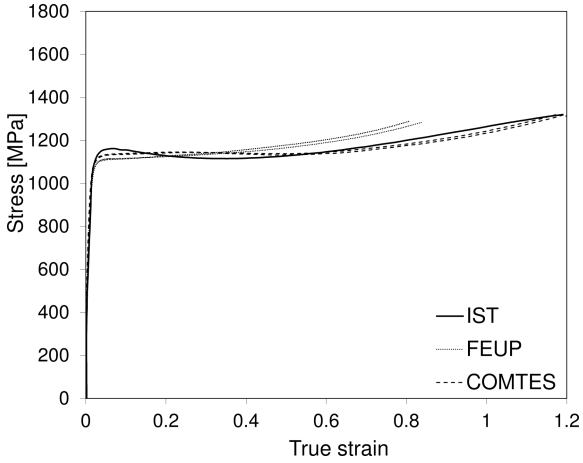


Figure 5.11: Comparison between 18Ni300 CM maraging stress vs. strain compression curves obtained from different laboratories.

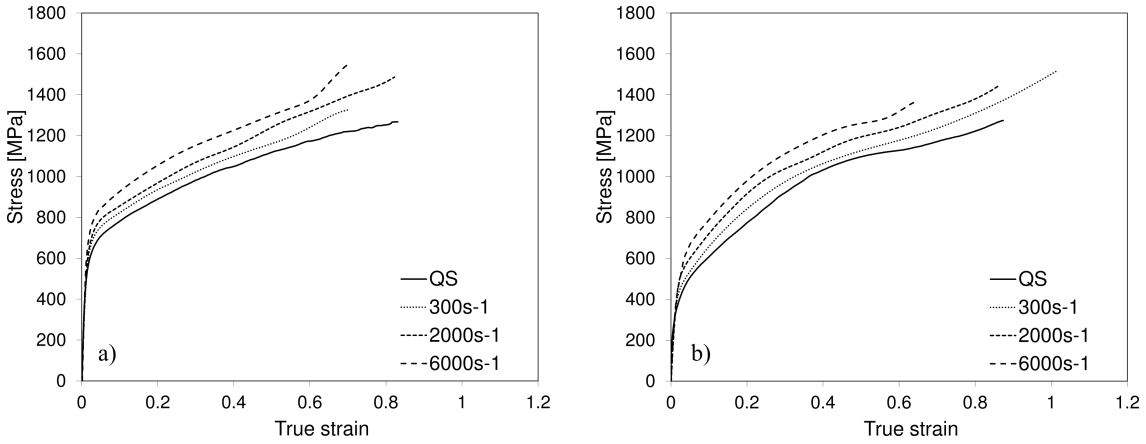


Figure 5.12: Influence of strain rate on the stress vs. strain compression behaviour of 316L AM (a) and CM (b).

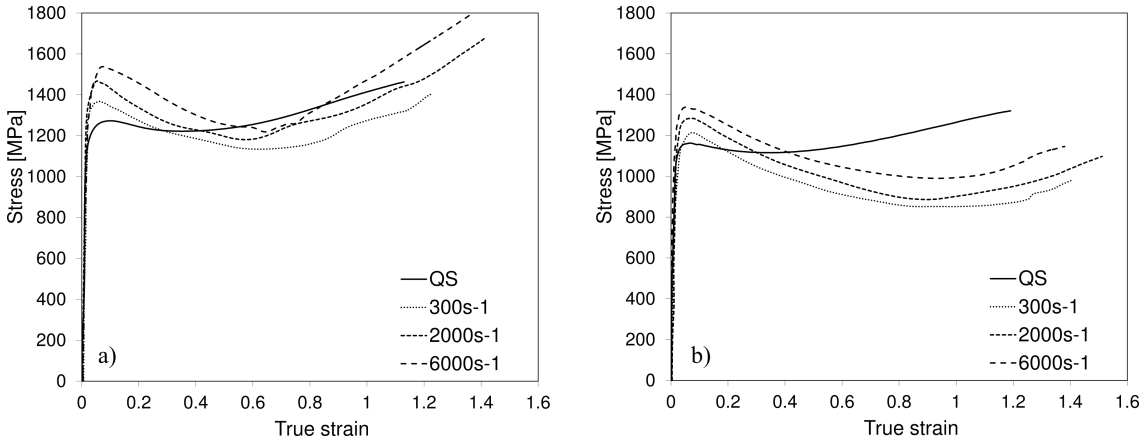


Figure 5.13: Influence of strain rate on the stress vs. strain compression behaviour of 18Ni300 AM (a) and CM (b).

of friction minimization in flow stress identification. Still, maximum stress differences are less than 10% and, if considering same size specimens, less than 3%.

The strain rate influence on the compression behaviour of both AM and CM 316L is shown in figure 5.12. As expected, a strengthening tendency is observed with an increase in strain rate. This tendency and strength values are, again, consistent with the ones found in literature for the 316L steel, which allows for a validation of the experimental setup developed for the high strain rate compression testing of engineering materials. Figure 5.13 presents the strain rate influence on the compression behaviour of AM and CM 18Ni300 steels. Despite exhibiting typical strengthening with increasing strain-rate for incipient deformation, the maraging steels show a sudden softening behaviour from strain values of approximately 0.1. As pointed out in literature review (i.e. fig. 3.17), such effect might be related with the high Ni content, which is responsible for the low conductivity of the maraging alloys, and thus promoting a thermal softening that may surpass the strain-rate strengthening mechanism. Still regarding incipient deformation, it is noticed that strain rate has a

more pronounced strengthening effect on the AM maraging steel. While for the latter an increase of 20% in maximum strength is observed (from QS to 6000s^{-1}), an increase of 15% is registered for the conventional counterpart. Moreover, in the AM maraging steel, the high strain and strain-rate behaviour tends to similar stress values of the quasi-static compression (refer to fig. 5.13a). Interestingly, in the CM maraging steel (see fig. 5.13b), the pronounced softening results in a peculiar reverse strain rate behaviour, meaning lower strength than quasi-static for high strain and strain-rate loading. Also noteworthy is that the softening effect ceases at approximate strain values of 0.7 to 0.8, giving rise to additional strengthening. Transformation induced plasticity (austenite to martensite) as well as deformation-assisted intermetallic precipitation tend to occur in maraging steels. Even though tests were conducted in tensile loading, Rafi et al. (2014) have noticed identical strengthening of the flow curve of 17-4PH additively manufactured tool steel in as-built condition, which was attributed to the strain-induced phase transformation and intermetallic precipitation. This hypothesis is compatible with the more noticeable strengthening in additively manufactured steels, since (as derived from the dilatometric tests) its microstructure contained higher amount of austenite, relatively to its conventional counterpart, where this strengthening effect at intermediate/high strain values is less pronounced. Figure 5.14 shows the quasi-static high temperature behaviour of the maraging steel. Given the considerations of Zorev (1966), Astakhov (1998) and Shaw (2005) regarding the relative low temperatures of the workpiece material when submitted to cutting and the phase transformations of the maraging steel starting at T≈450°C (refer to figure 5.5 and figure 5.6) the maximum tested temperature was of 370°C. Apart from the already identified hardening behaviour, the stress-strain response of the materials seem to present typical softening for increasing temperature in both AM and CM metallurgical conditions. In an attempt to better understand the atypical softening preceded of hardening, a selection of the compressed material specimens (after testing) were cut and its cross section was polished and chemically etched

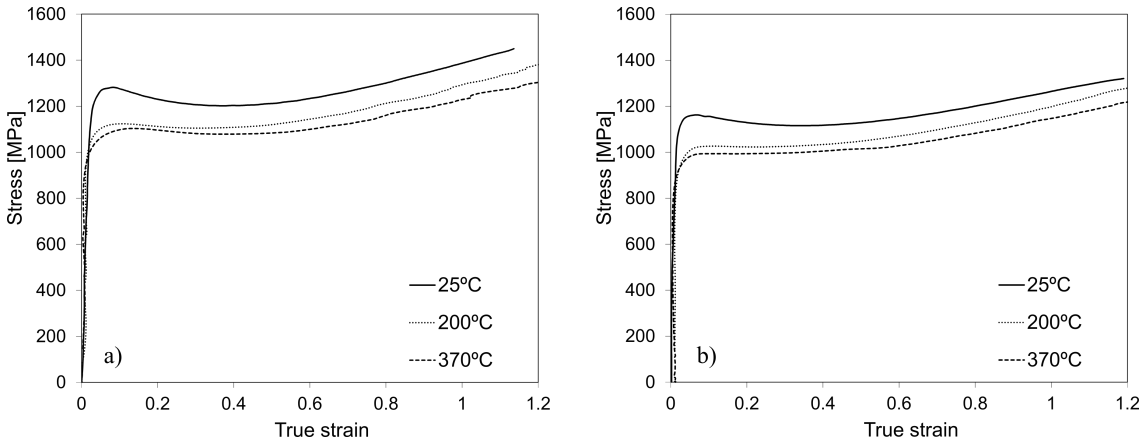


Figure 5.14: Influence of temperature on the stress vs. strain compression behaviour of 18Ni300 AM (a) and CM (b).

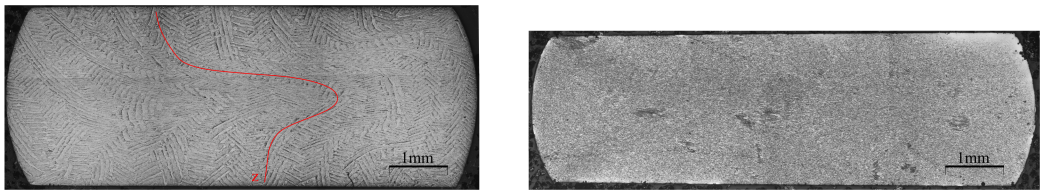


Figure 5.15: Optical micrographs of the compression specimens' cross-section tested in quasi-static conditions at room temperature showing a nearly-uniform deformation (in its final stage) in AM (a) and CM (b) metallurgical conditions.

for optical microscope observation. Figure 5.15 shows the cross section of two specimens, compressed at quasi-static conditions. A clear distinction between the CM and AM is noticed due to the visible laser paths in the latter. In fact, the laser paths allow to infer on the specimen deformation. A group of successive laser paths is signalled with a red line (z). The curved geometry of the line clearly indicates the non-uniform deformation of the specimens due to friction (line would be straight in ideal friction conditions). The observed higher deformation in the centre is compatible with the optical micrographs presented by Gunasekera et al. (1982) and the finite element simulation of the compression test (Wang et al., 2017).

With regards to the specimens' cross section submitted to dynamic loading (refer to figure 5.16) a completely distinct deformation behaviour is noticed, when compared to the quasi-static. Melt pool geometry is still recognizable (seemingly not deformed) for a significant area of the specimens cross section. On the other hand, the occurrence of highly localized material flow is observed. This effect is most probably caused by the low conductivity of the maraging material allied to the high speed of the test (adiabatic conditions). The increase in temperature resultant from plastic deformation

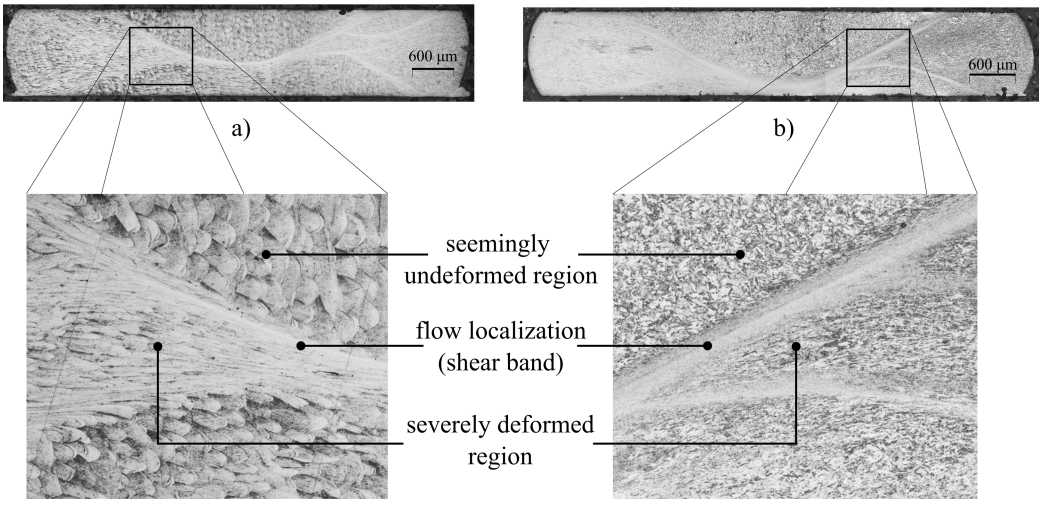


Figure 5.16: Optical micrographs of the compression specimens' cross-section tested at 6000s^{-1} and room temperature showing distinctively non-uniform deformation (in its final stage) in AM (a) and CM (b) metallurgical conditions.

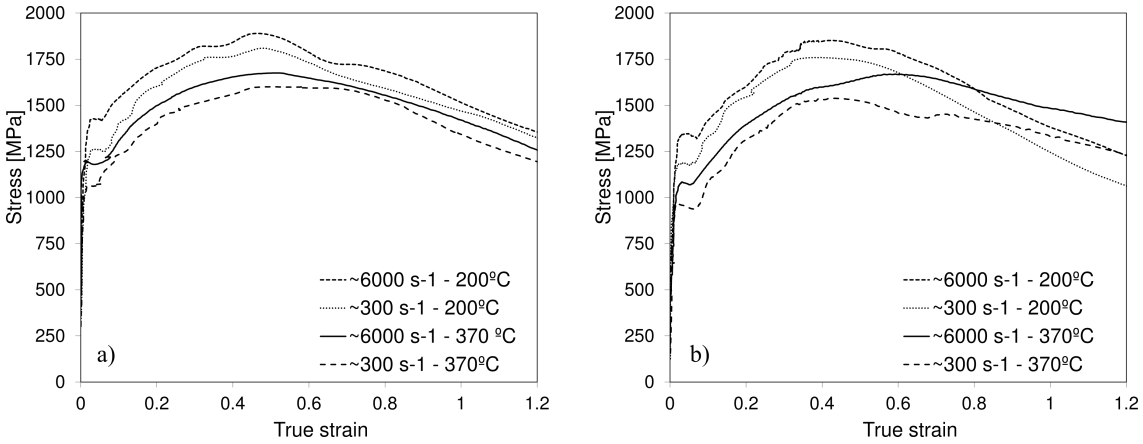


Figure 5.17: Influence of simultaneous temperature and strain rate on the stress vs. strain compression behaviour of 18Ni300 AM (a) and CM (b).



a) b)

Figure 5.18: Optical micrographs of the AM (a) and CM (b) compression specimens' cross-section tested in simultaneous 6000s^{-1} and 370°C, showing distinctively non-uniform deformation (in its final stage).

promotes the softening in the specimen region with highest strain localization. This may indicate that, from the moment adiabatic shear bands start taking place, the validity of the compression stress-strain curve may be questionable, given that an uniform deformation is no longer ensured.

Images of the specimens cross-section in quasi-static high temperature conditions do not exhibit localized material flow. This seems to be in accordance with previous results, given that for quasi-static conditions there is improved dissipation of the heat generated by plastic deformation. Stress-strain results obtained from compression tests in conditions of simultaneous high strain rate and high temperature are shown in figure 5.17 for the maraging steel. For small strains (>0.06), the

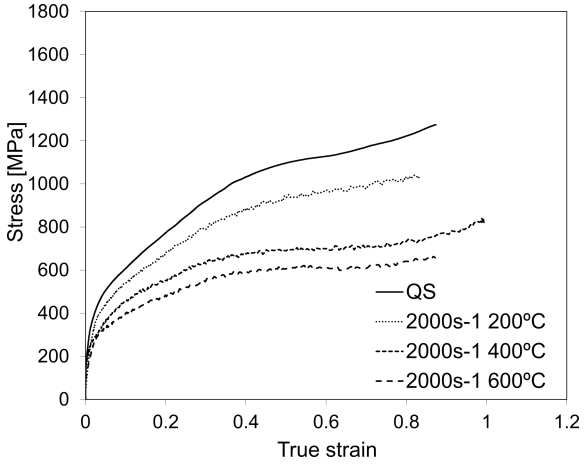


Figure 5.19: Influence of simultaneous temperature and strain rate on the stress vs. strain 316L CM compression behaviour.

observed stress-strain behaviour presents a very similar tendency to the compression results in high temperature and high strain rate isolated conditions. However, a sudden hardening behaviour is visible for strains bigger than 0.06. A maximum strength of nearly 2000 MPa is noticed, regardless of metallurgical condition. This may be explained by hypothetical deformation-induced mechanisms such as intermetallic precipitation and TRIP effect at the localized adiabatic shearing zones. Those specimens' cross-section (refer to figure 5.18) show, similarly to the "isothermal" high strain rate compression tests (figure 5.16), the existence of localized adiabatic shear bands. The coupled temperature and high strain rate conditions seem to intensify the localized flow, which is in accordance with the proposed theory of adiabatic shear band formation in high speed compression tests of the maraging steel.

For verification purposes compression tests of conventionally manufactured 316L in similar conditions (simultaneous temperature and strain rate) were performed (refer to figure 5.19). The results show the expected thermal softening and strain rate hardening, matching literature values, which allow discarding the possibility of faulty setup measurements, given its novelty and the extreme testing conditions.

5.2.2. Ring tests results

The relevance of tribological characterization is highlighted by purposeful contact between surfaces in manufacturing processes (Hutchings and Shipway, 2017). More specifically, the high normal pressures at tool-workpiece interface in the metal cutting phenomenon emphasize the need for an accurate and comprehensive friction estimation, as pointed out by Melkote et al. (2017) in their thorough review of friction in metal cutting processes. As previously reviewed, friction mechanisms can be subdivided into adhesion and mechanical (such as interlocking). It is generally acknowledged that the adhesion friction mechanism is the most dominant (Melkote et al., 2017; Abushawashi, 2013), which is the reason this study mainly focuses on its contribution. Ring compression tests are universally accepted as perfectly valid method towards a simple, effective and reliable determination of friction adhesion in a plastic deformation process (Martín et al., 2015). The possibility of performing such tests in identical conditions to the flow stress characterization compression tests opens the way for the most recent trends of friction modelling (Childs, 2019) which state their integration with flow stress.

The friction estimations of figures 5.20 and 5.21 result from an experimental/numerical identification approach. Due to the numerical nature of that methodology, it will be further described in section 6.1, where a technique towards frictionless flow stress estimation is also presented. The figures show the influence of temperature, strain rate, lubrication and metallurgical condition on the

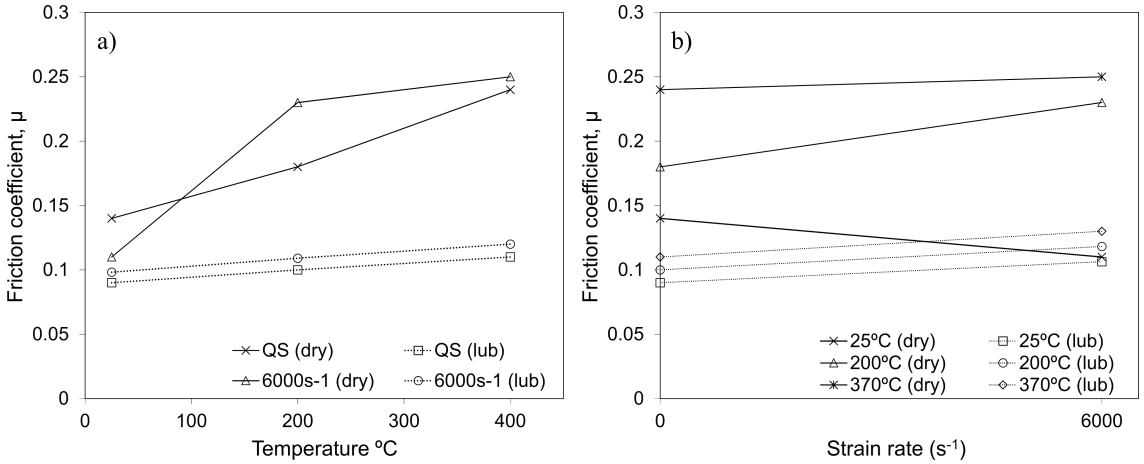


Figure 5.20: Temperature (a) and strain rate (b) influence of the estimated friction coefficient of AM 18Ni300 maraging steel.

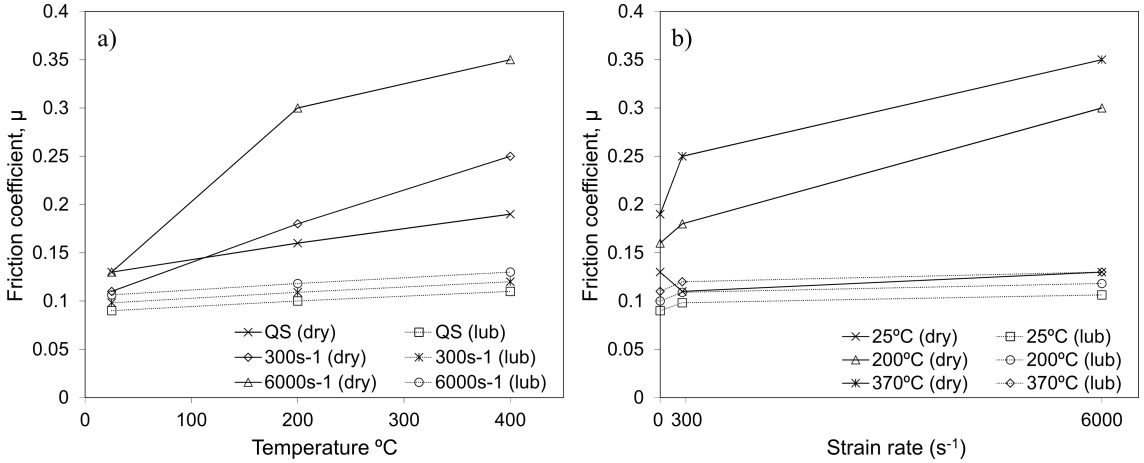


Figure 5.21: Temperature (a) and strain rate (b) influence of the estimated friction coefficient of CM 18Ni300 maraging steel.

friction coefficient between the tool-workpiece materials interface for AM and CM 18Ni300 materials. With regards to lubricated conditions, a very consistent (yet modest) increasing trend is found for rising temperatures and strain rates. On the other hand, for dry conditions, friction coefficient tends to double when the temperature rises from room temperature to approximately 400°C. Such findings are of extreme relevance given that most of the generated heat in the primary deformation zone (due to plastic deformation) flows to the chip (Shaw, 2005), which in turn is sliding against the tool at the secondary deformation zone, where friction is most substantial. Similarly to temperature, strain rate seems to increase friction coefficient. For tests in dry conditions, this tendency is only observed in high temperature regimes and is more evident for the conventionally manufactured maraging steel. The usage of graphite lubricant significantly decreases friction adhesion phenomenon for the materials' interface in all tested conditions. Despite the small number of experiments, these tests seem to provide evidence of the friction dependence on cutting condition. In addition, no significant changes were found in the friction tendency according to temperature and strain rate conditions

with respect to metallurgical conditions. In terms of friction coefficient values, the obtained results are within the wide range of values found in literature for the same material. However, unlike stated by Yin et al. (2018), the material's microstructure did not seem to have significant influence on the results. The identified temperature and friction speed tendencies are opposite to the ones proposed by Sun et al. (2020).

5.2.3. Tensile tests results

The tensile tests results allowed to understand the ductility gap between AM and CM maraging steel. It is well known from literature that despite an higher mechanical strength, the additively manufactured steels typically present diminished ductility (e.g. figure 3.15). Given that the tests were conducted for distinct notch geometries, it is also possible to access the stress triaxiality influence on ductility. Figure 5.22a presents the load-displacement results of the AM maraging steel. Not only it is clear that there is a significant ductility decrease comparatively to the CM (refer to fig 5.22b) but also a much lower repeatability within the AM results. As studied by Kim et al. (2020) and Leça et al. (2020), the existence of internal defects in the additively manufactured steels can compromise their mechanical behaviour, especially their ductility. Also important to take into consideration is the relative size-effect of those defects when analysing small material samples, as might be the case for the tested tensile geometries. In sum, the expected ductility variability of additively manufactured parts is noticeable in the maraging steel printed for the current study.

With regards to notch geometry, the results are in accordance with the predicted stress triaxialities in table 4.5. Even though numerical simulation is required to estimate the actual values (which is further conducted in section 6.2), a ductility decrease tendency is noticed for stress triaxiality increase. In addition, the tension and compression behaviour of both maraging steels have

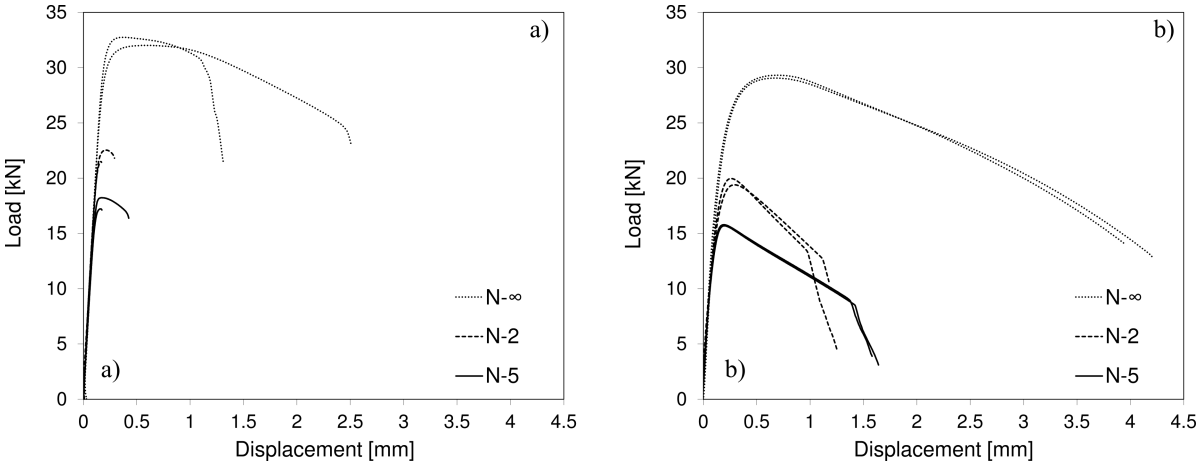


Figure 5.22: Influence of notch geometry (stress triaxiality) on the tensile behaviour of AM (a) and CM (b) maraging steels.

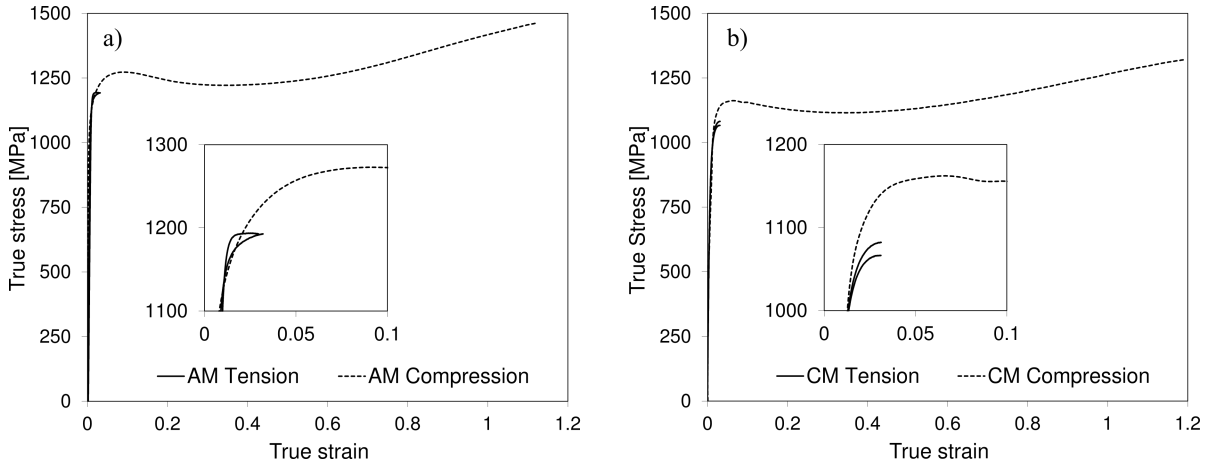


Figure 5.23: Comparison between tension and compression behaviour of AM (a) and CM (b) maraging steel in quasi-static and room temperature conditions.

been compared, as shown in figure 5.23. Given that area reduction was not measured, the tension curves are shown up to load decrease (geometrical necking). The results seem to be compatible with the results of figure 3.19, obtained by Cyr et al. (2018). According to the author, despite the small differences in yield strength between tension and compression (which in the present study are smaller than 10%), if area reduction is accounted both loading conditions should present identical hardening.

Necking can be geometrically classified as diffuse or localized (Semiatin and Jonas, 1984; Hwang, 2020). While in diffuse necking the flow is quasi-stable due to gradual strain redistribution, in localized necking flow is unstable, leading to fracture. The fact that diffuse necking seems to occur in maraging steels (Sakaki et al., 1986) may additionally contribute to the differences in tension and compression stress values. Moreover, and as seen in figure 5.24a, which presents the engineering stress-strain curves, diffuse necking seems to occur at an early stage and for significant elongation.

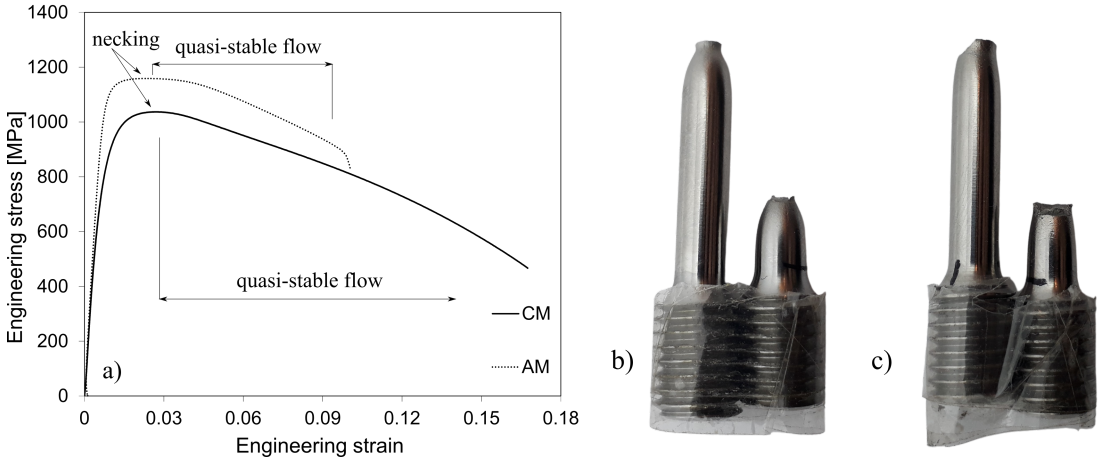


Figure 5.24: Engineering stress-strain curve (a) showing quasi-stable flow occurrence (diffuse necking) in both CM (b) and AM (c) maraging steels.

This is consistent with the very high cross-section area reduction (approximately 80%) in tensile loading, as specified by the manufacturer in the CM metallurgical condition (Voestalpine, 2021). The specimens' final geometry (as seen in figures 5.24b and 5.24c, for the CM and AM material) illustrate the necking behaviour on the smooth tensile samples. A much smaller diameter section can be seen in the CM material, confirming an higher ductility and thus, higher deformation localization (localized necking) at fracture than its additively manufactured counterpart. In addition, the typical cup and cone fracture surfaces can be identified for the tested smooth conventional material specimens (as shown in figure 5.25a and 5.25b), confirming its ductile behaviour. These are formed due to the widely known mechanisms of ductile fracture: void nucleation and growth in the central region; shear-dominated separation in the outer region, usually referred to as "shear lips" (Bluhm and Morrissey, 1966). The less pronounced cup and cone fracture geometry in AM samples seems to show that material fails (abruptly) while flowing in a diffuse necking regime, due to material defects (mostly porosity). In fact, coalesced porosity is visible randomly distributed over the two distinguishable regions of AM fracture surfaces of figures 5.25c and 5.25d. Regarding the fracture surfaces of notched tensile specimens (N5) failure initiation localization is visible for the conventional material (figure

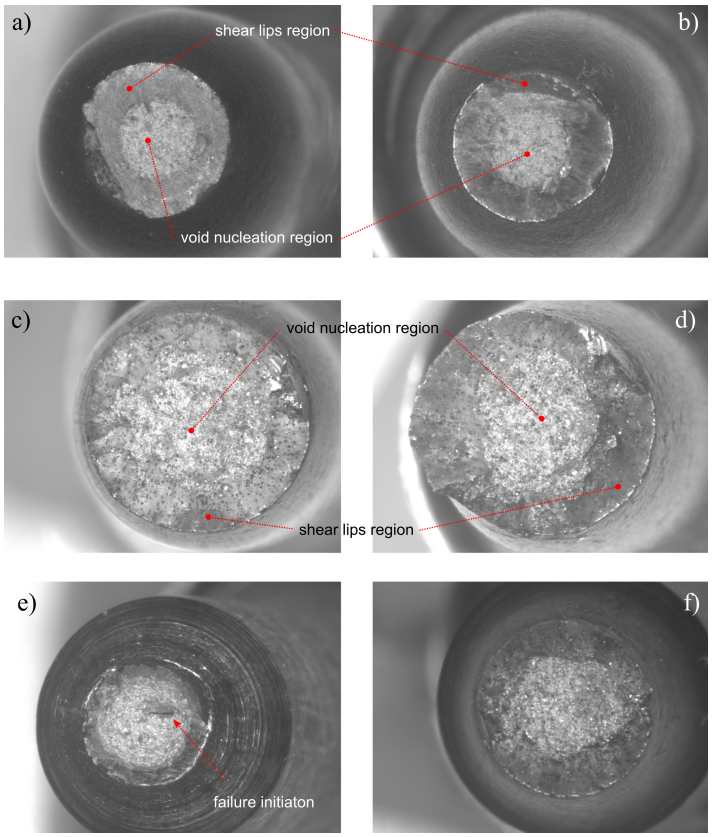


Figure 5.25: Fracture surfaces of the tensile test specimens: cup (a) and cone (b) fracture geometry of CM maraging steel; cup (c) and cone (d) fracture geometry of AM maraging steel; notched specimens of CM (e) and AM (f) metallurgical conditions.

5.25e), unlike for the AM (figure 5.25f), emphasizing their distinct ductility/fracture behaviours. The materials' toughness, U_T, or their ability to absorb energy up to fracture was calculated for both additively and conventionally manufactured maraging steels. As illustrated in eq. 5.1 it can be determined through the integration of the tensile stress-strain curve.

$$U_T = \int_0^{\varepsilon_f} \sigma d\varepsilon \tag{5.1}$$

The obtained results show a U_T in the range of 151 to 173 mJ/mm^3 for the conventional maraging steel, whereas for the additively manufactured, the higher dispersion leads to a broader range of 95-207 mJ/mm^3. Considering that toughness is a direct measure of the strength-ductility ratio, the similar results are coherent with the lower ductility but higher strength of the additively manufactured maraging steel, with regards to its conventional counterpart.

5.2.4. Multiaxial fracture tests results

The load-displacement results of the multiaxial fracture tests are displayed in figure 5.26 for each pressure angle. Figure 5.26d shows all the results for AM and CM metallurgical conditions. The distinct strength-ductility ratios of AM and CM maraging steels are once more in evidence, with the latter showing lower mechanical strength and higher ductility. It is important to note that for the AM maraging steel all specimens have fractured. However, due to the higher ductility of the CM maraging steel, only the specimen with a 90° pressure angle has fractured. Figure 5.28 shows the crack morphology or, in absence of fracture, the last recorded deformed shape of the specimen for each specimen geometry and metallurgical condition. Higher deformation is noticed in the CM specimens, based on their shape. Moreover, and as pointed out in the presentation of tensile test results (section 5.2.3), a marked tendency towards a quasi-stable necking is noticed in the maraging steel, especially in the CM metallurgical condition. This is highlighted in figures 5.28b, 5.28d and 5.28f, where the excessive material deformation leads to a deviation from the intended state of stress at failure.

Figure 5.28d shows an interesting feature that may compromise the validity of DIC analysis in the conventional material. Fracture seems to occur in different locations depending on "in-plane" dimension which may evidence material flow in normal to surface direction. With regards to the AM specimens, it is observed that in low stress triaxiality, fracture tends to occur in a more controlled way, which may be related to the higher expected fracture strength in such regime. Such effect is noticed by the visible crack propagation in the specimens with 60° pressure angle (refer to figure 5.28a) in contrast with the abrupt failure of specimens with 90° and 120° pressure angles (figures 5.28c and 5.28e).

The unfractured ligaments of the CM multiaxial specimens have been polished and etched in

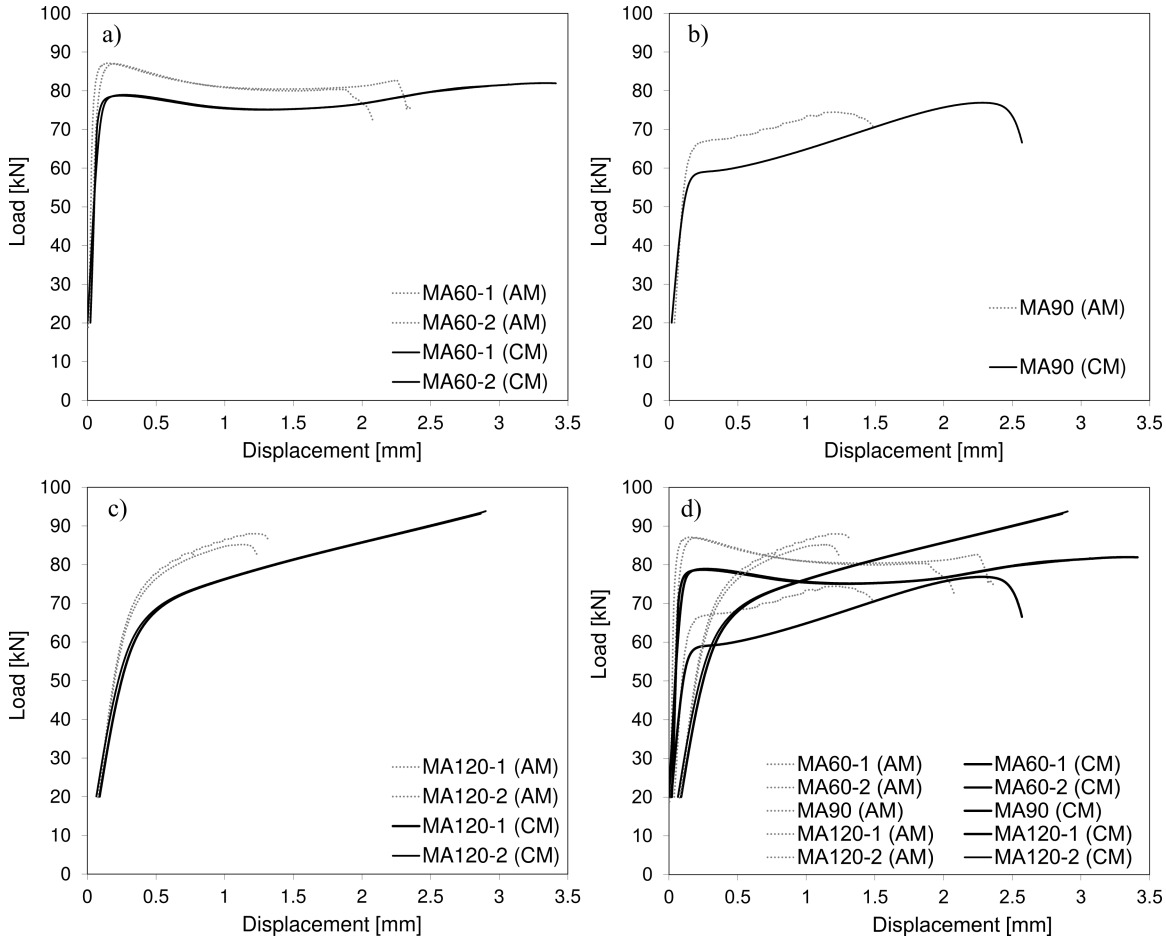
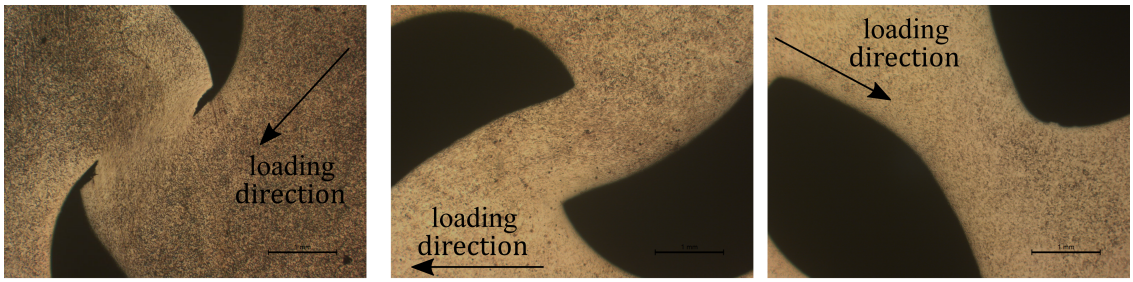


Figure 5.26: Load vs. displacement curves resultant from the multiaxial fracture tests: compression-shear (a), shear (b), tension-shear (c).

order to allow grain morphology observation at the final stage of the test (refer to figure 5.27). No signal of isothermal shearing seems to be taking place in any of the pressure angle configuration. The absence of visible gradients in the microstructure of the ligaments suggests that deformation seems to be evenly distributed, with the exception of the multiaxial specimen MA60 (figure 5.27a), where severe necking is observed.



a) b) b)

Figure 5.27: Polished and electrolytically etched micrographs of the CM maraging steel multiaxial specimen MA60 (a), MA90 (b) and MA120 (c) ligaments.

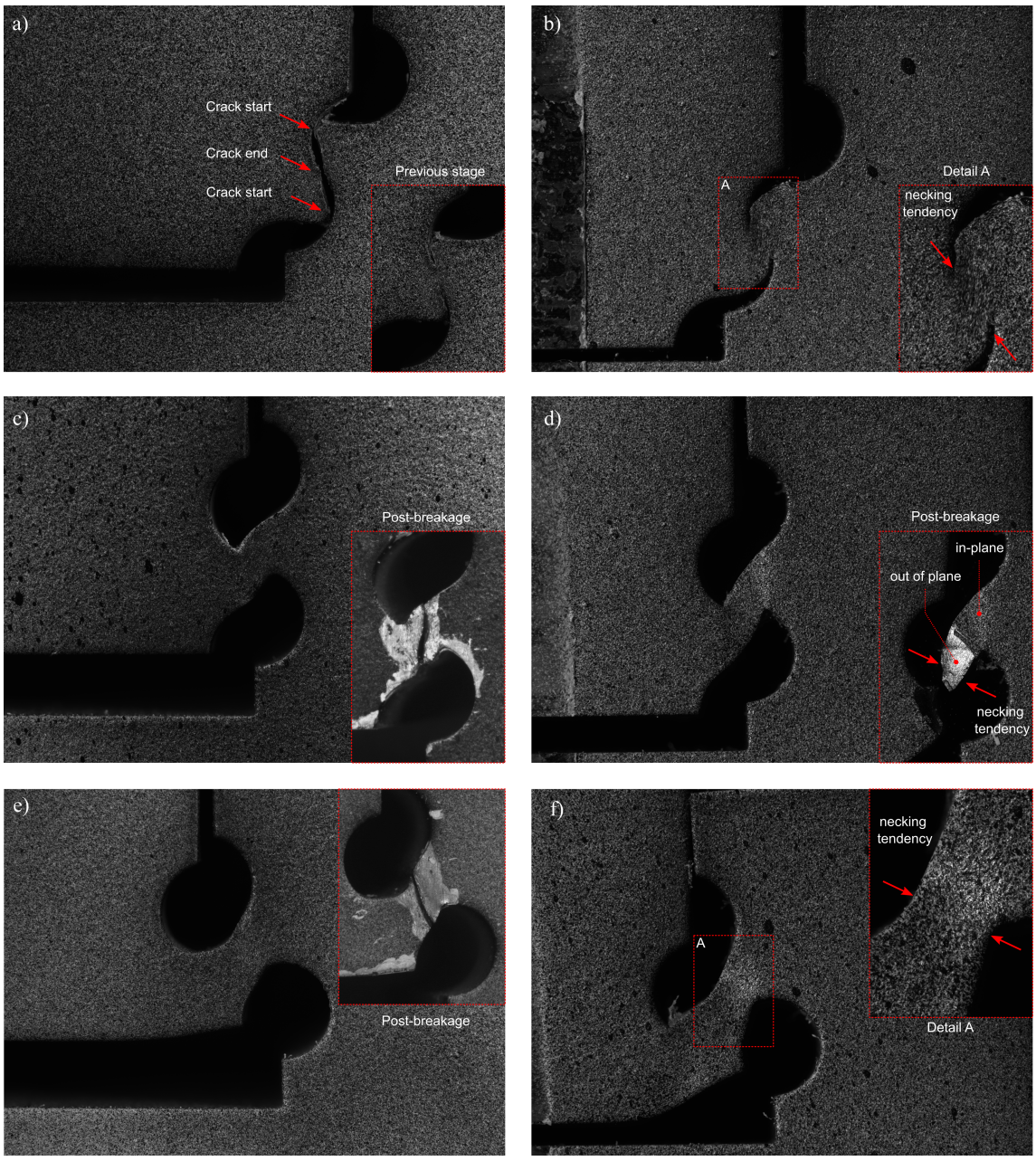


Figure 5.28: Final shape of the multiaxial 18Ni300 specimens: a) AM 60° showing crack evolution from surface to ligament centre; b) CM 60° showing necking tendency; c) AM 90° showing crack path; d) CM 90° showing necking tendency; e) AM 120° showing crack path; f) CM 120° showing necking tendency.

In order to estimate the average loads at each specimens' ligament, load (P) decomposition in its normal (N) and shear (V) forces was performed, as shown in the free body diagrams of figure 5.29. For pressure <90° (figure 5.29a), a combination of compressive and shear stresses are verified; for pressure angles >90° (figure 5.29c), a combination of tensile and shear stresses are verified and for a pressure angle of 90° (figure 5.29b) only shear is verified. Referring to figure 5.26, where load-displacement results are illustrated, the load at yield point was obtained by drawing a secant

line through the origin, with a slope of 5% less than the slope of the elastic linear part of each experimental curve. Those loads and corresponding shear and normal stresses at the ligament of each specimen are presented in table 5.6. It is important to emphasize this is a preliminary approach to FEM and that the stresses were calculated neglecting non-linear geometrical effects and stress concentration led by the double notches. In addition, and according to eq. 5.2 and eq. 5.3, the von Mises equivalent stress ε_{eq} and hydrostatic pressure (p) have been computed, assuming plane strain conditions, and presented in the same table.

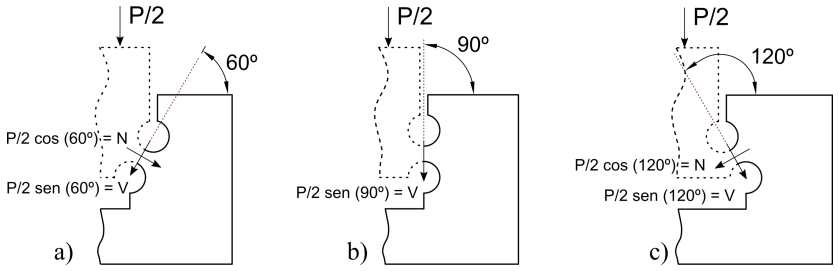


Figure 5.29: Free body diagram showing load decomposition at the ligament of multiaxial specimen with 60° (a), 90° (b) and 120° (c) pressure angles.

$$\begin{aligned} \sigma_{1,2} &= \frac{\sigma}{2} \pm \sqrt{\frac{\sigma^2}{4} + \tau^2} \\ \sigma_3 &= \nu(\sigma_1 + \sigma_2) \end{aligned} \tag{5.2}$$

$$\begin{aligned} \sigma_{eq} &= \sqrt{\frac{(\sigma_1 - \sigma_3)^2 + (\sigma_1 - \sigma_2)^2 + (\sigma_2 - \sigma_3)^2}{2}} \\ p &= \frac{\sigma_1 + \sigma_2 + \sigma_3}{3} \end{aligned} \tag{5.3}$$

Table 5.6: Summary from the stress analysis on the multiaxial specimens ligament.

Specimen	P [kN]	Disp. [mm]	τ_s [MPa]	σ_n [MPa]	σ_1 [MPa]	σ_2 [MPa]	σ_3 [MPa]	σ_{eq} [MPa]	p [MPa]
MA60 1 (AM)	72.05	0.063	624.0	-360.3	469.3	-829.6	-118.9	1126.5	-120.1
MA60 2 (AM)	69.61	0.035	602.8	-348.1	453.4	-801.5	-114.9	1088.4	-116.0
MA60 1 (CM)	69.00	0.067	597.6	-345.0	449.5	-794.5	-113.9	1078.9	-115.0
MA60 2 (CM)	62.38	0.085	540.2	-311.9	406.3	-718.2	-102.9	975.3	-104.0
MA90 (AM)	56.47	0.105	564.7	0	564.7	-564.7	0	978.1	0
MA90 (CM)	48.13	0.091	418.3	0	418.3	-418.3	0	833.6	0
MA120 1 (AM)	55.26	0.204	478.6	276.3	636.3	-360.0	91.2	864.0	92.1
MA120 2 (AM)	53.94	0.205	467.1	269.7	621.1	-351.4	89.0	843.4	89.9
MA120 1 (CM)	48.27	0.224	418.0	241.4	555.8	-314.4	79.6	754.7	80.5
MA120 2 (CM)	46.44	0.192	402.2	232.2	534.7	-302.5	76.6	726.1	77.4

Figure 5.30a shows a seemingly linear relation between normal and shear stresses at the yield. Regarding figure 5.30b, which presents the evolution of equivalent stress at initial yield, a linear pressure dependence seems to be displayed. The decreasing tendency of equivalent stresses at yield, for increasing pressure is somewhat compatible with the differences in flow stress obtained from compression and tensile tests, illustrated in figure 5.23. Sill, the identified pressure dependency should be regarded as "apparent", given the simplified analytical approach towards the obtention of these results, which may be why the pressure dependence magnitudes differ when considering compression/tension and multiaxial specimens.

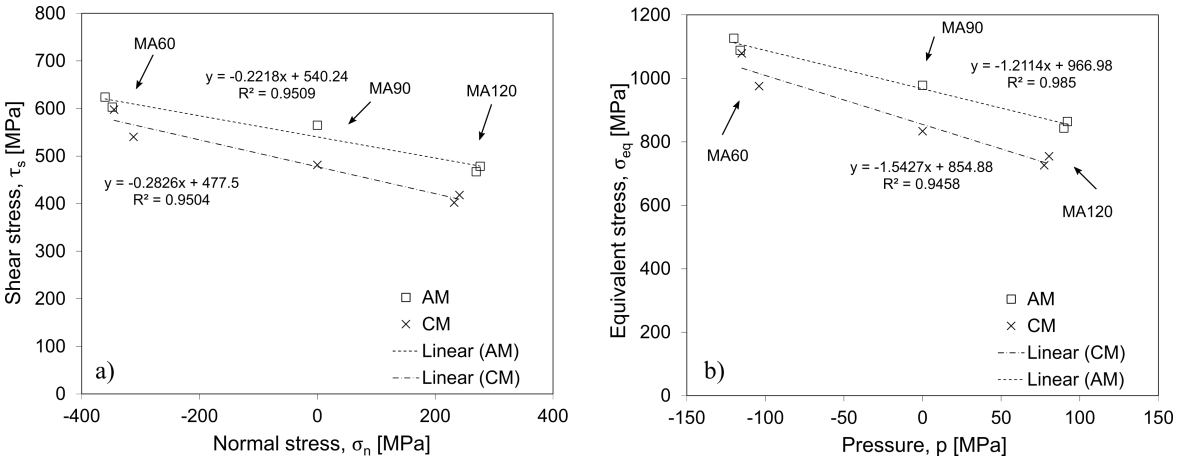


Figure 5.30: Relationship between shear and normal stresses (a) and pressure dependence on equivalent stress (b) at yield, for each multiaxial fracture specimen and metallurgical condition.

5.3. Metal cutting experimental results

5.3.1. Orthogonal cutting tests results

The developed experimental setup successfully enabled orthogonal cutting conditions for a wide range of uncut chip thicknesses. Figure 5.31 shows an example of the obtained cutting loads of an orthogonal cutting test for an average uncut chip thickness of 0.165 mm. Both transient beginning of chip formation (for cutting length <5 mm) and steady-state metal cutting conditions can be clearly identified. The latter was used for the analysis of cutting load on the distinct maraging steel samples. Figure 5.32a shows the experimental measurements of cutting force (F_c), using a 5° rake angle cutting tool. A markedly linear increase of the cutting force with the increase of uncut chip thickness is found, regardless of the metallurgical conditions or cutting direction (CD). Differences in cutting force can be found (distinct slopes in cutting trends), depending on the cutting direction, relatively to build direction. Despite its higher significance for bigger uncut chip thicknesses, the orthogonal cutting tests performed with the tool movement perpendicular to build direction resulted

in bigger cutting forces. In contrast, lower loads seem to result from the orthogonal cutting tests performed in conventionally manufactured maraging steel. The cutting force magnitude, depending on the processed material, shows a strong correlation with its mechanical strength. In addition, the influence of tool geometry on the measured cutting loads (illustrated in figure 5.32b for the AM maraging steel) is in accordance with the expected higher loads for smaller rake angles (Günay et al., 2004). The results show that, within tested conditions, tool geometry has a greater influence on the cutting force, given that regardless of build direction (BD) loads were always higher for a α_r=5° cutting tool. Such aspect highlights the small influence of build direction on the cutting behaviour of additively manufactured components.

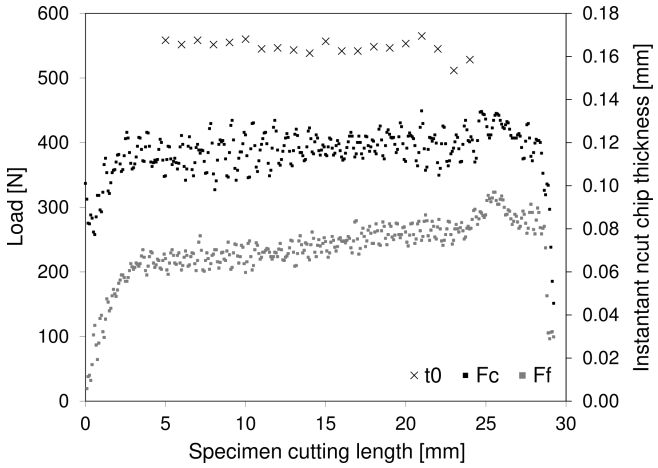


Figure 5.31: Experimental cutting loads for orthogonal cutting with t_0=0.165mm.

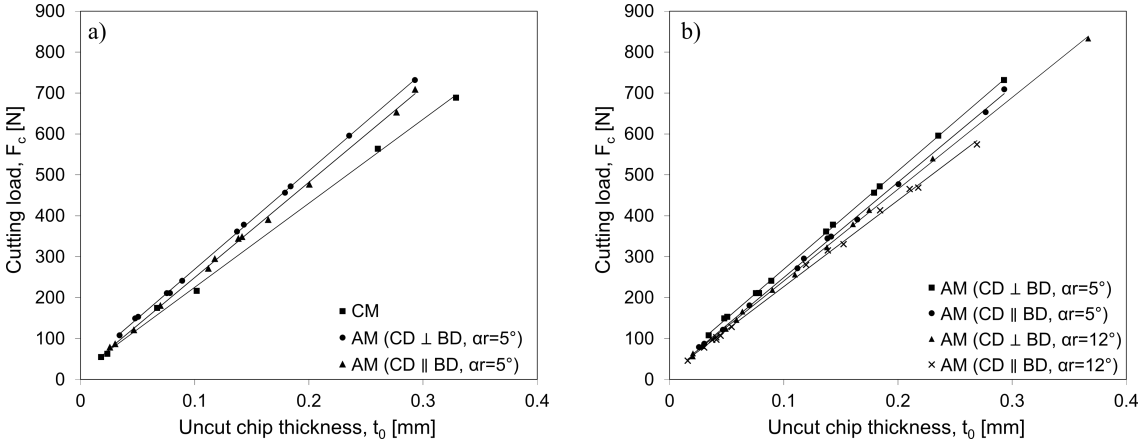


Figure 5.32: Influence of metallurgical condition (a) and rake angle (b) on the cutting force of maraging steel in orthogonal cutting conditions.

As discussed in literature review, specific cutting pressure (K_c) is commonly used for load estimation purposes, according to the selected cutting parameters, and these curves are usually obtained from experimental procedures. It can be seen as a characterization of the offered cutting resistance by a workpiece material, just as the tensile stress characterizes mechanical strength.

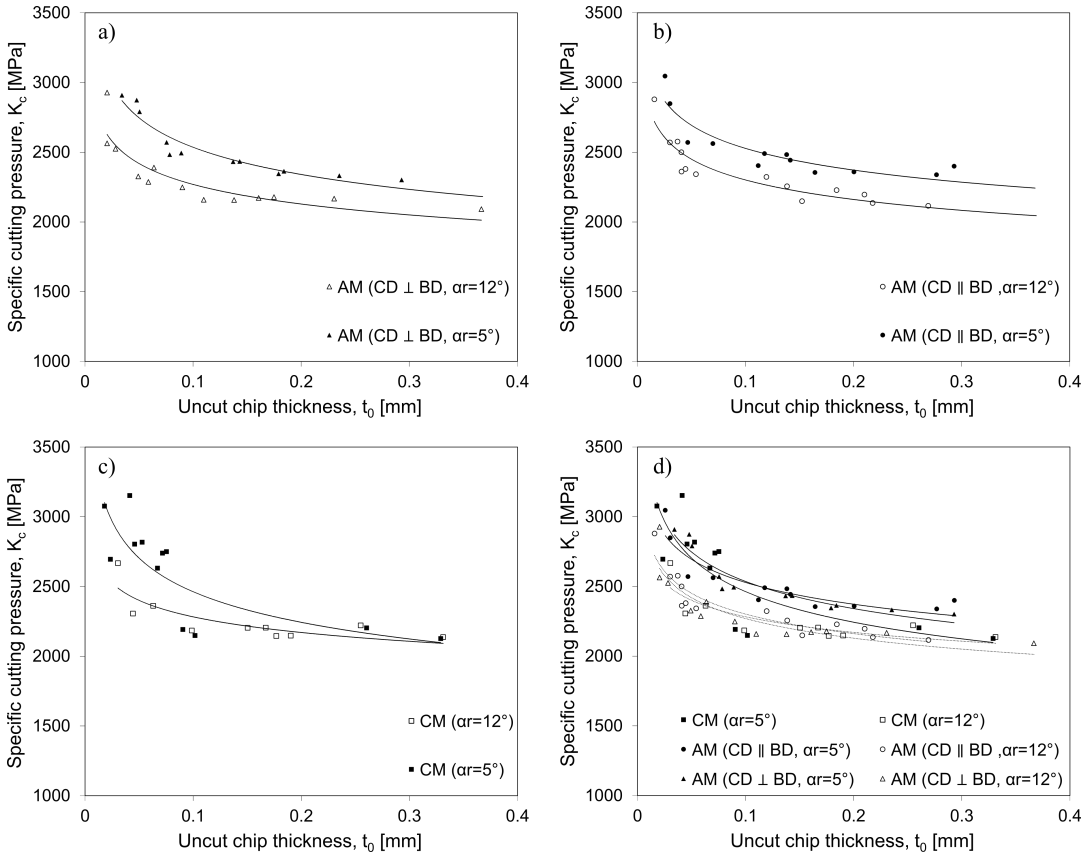


Figure 5.33: Influence of rake angle on the specific cutting pressure of AM 18Ni300 cut in perpendicular direction to BD (a), parallel direction to BD (b) and the CM 18Ni300 (c). Comparison of all K_c results, showing prevailing influence of rake angle (d).

Figure 5.33 presents the K_c curves obtained from orthogonal cutting experiments. The results show a significant increase in K_c for smaller chip section and K_c stabilization for t_0 increase. This typical trends are associated with the size effect in metal cutting. The occurrence of defects in metals (e.g. grain boundaries and missing atoms) is generally acknowledged and the chance of encountering those stress-reducing defects decreases for smaller sizes of removed material (Shaw, 2003). Taniguchi (1993) has conducted a series of experimental tests for increasing size of cut (or deformed) material, finding that the value of K_c tends, in fact, to the materials' mechanical strength, typically obtained through tensile testing. There is however, in practice, a typical mismatch between K_c and the materials' strength, as the former is commonly overestimated (Soares, 2016).

Similarly to literature, the K_c results in this research work are higher than the materials yield strength. It is generally accepted that the formation of new surfaces (and, thus, the required energy for such phenomenon) account for the higher values of K_c, when compared to the materials mechanical strength obtained from tensile or compression tests (where the formation of new surfaces does not supposedly occur). Moreover, K_c values seem to be very similar whether the material is additively or conventionally manufactured, as illustrated in figure 5.33d , which is consistent with

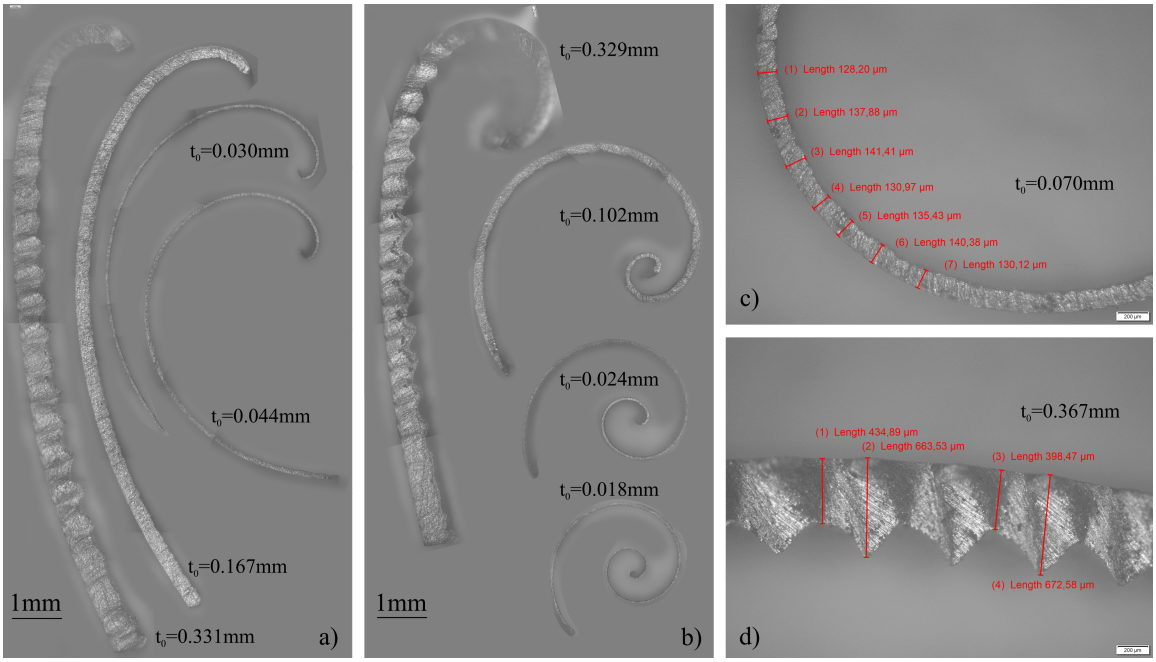


Figure 5.34: Optical microscopy images of chip morphology of CM maraging steel obtained from orthogonal cutting tests with a 12° (a) and 5° (b) tool rake angle, for distinct uncut chip thickness; detailed measurements of continuous (c) and lamellar/segmented (d) morphology chips.

their also identical toughness (U_T). No obvious distinction can be identified for different cutting directions relatively to build direction. A more notorious distinction is inferred from rake angle variation. Tool geometry shows a significant influence on the specific cutting pressure of all tested maraging steel conditions, as depicted from figures 5.33a to 5.33c.

With regards to chip morphology, no substantial differences were found for the distinctly manufactured maraging steels. On the other hand, a smaller tool rake angle seems to promote a higher chip curvature (smaller chip radius), which goes in line with literature (Devotta et al., 2015). Moreover, increasing uncut chip thickness also promotes an increase of chip curvature radius. It has been observed that for increasing t_0 chip gradually transitions from continuous to lamellar/segmented morphology (t_0 ~0.3mm), probably due to a localized shearing zone promoted by the high strains, strain rates, temperature and, mostly, the low thermal conductivity of maraging steel, since for smaller t_0 there is higher heat diffusion. Figures 5.34a and 5.34b show chips obtained from conventional material for a broad range of t_0 for tool rake angles of 12° and 5°, respectively. Figures 5.34c and 5.34d illustrate the average chip thickness (t_c) measurement in chips of additively manufactured maraging steel, which enable the calculation of chip compression ratio, r_c.

Polished and etched chip samples of AM metallurgical condition were observed at the optical microscope. The melt pool geometries, characteristic of additively manufactured samples, enabled inferring on the deformation behaviour of the chips, due to the creation of a recognizable pattern. This is illustrated by the chip of figure 5.35a, more specifically its end, figure 5.35b. Due to reaching

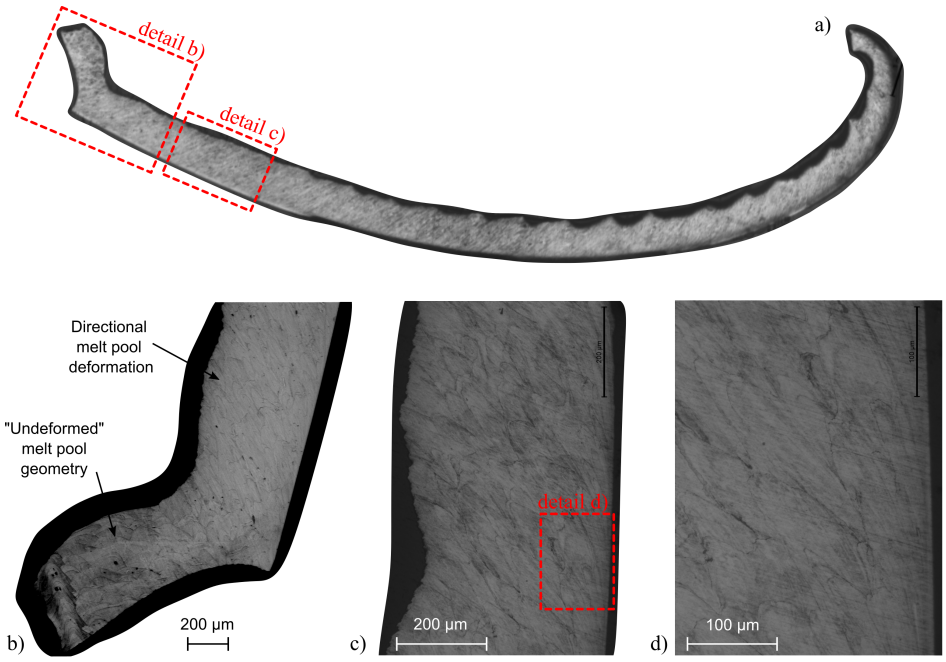


Figure 5.35: Optical micrographs showing distinct deformation pattern of melt pool geometries on workpiece and chip (a); etched chip section (b) and a detail (c) showing friction influence on chip deformation.

the final cutting length of the orthogonal cutting specimen, the material portion relative to uncut chip thickness has been fractured instead of cut, showing seemingly undeformed material at the base, besides the highly deformed chip. Moreover, in figures 5.35c and 5.35d one can distinguish a higher severity of deformation at chip underside (which was in contact with the tool), revealing important friction influence. Unlike in the etched cross section of dynamic compression tests, no evidence of shear bands is noticed, meaning that the atypical hardening for intermediate strains may not occur (as intensively) in the chip formation mechanism, within the tested configuration of cutting parameters.

Friction coefficient was calculated through equation 2.8 for all types of maraging steel. Results show a slight tendency for higher friction coefficient as t_0 decreases (refer to figure 5.36a). A possible reason for such effect might be a progressive change of the friction mechanism, for smaller t_0. It is well known from literature that, in the metal cutting process, there are three basic components of sliding friction: adhesion, ploughing and plastic deformation (Melkote et al., 2017). For smaller t_0 the relative size of the cutting edge becomes more significant, which may result in an increased contribution of that friction component, thus increasing the overall friction values. It is also important to emphasize the very high friction values (higher than the μ=0.577 theoretical limiting value) obtained from cutting force measurement methods. Despite decades of research, friction in metal cutting is still a controversial topic, and though its apparently correct theoretical calculation through the measured cutting loads, the experimental values keep raising challenging questions to

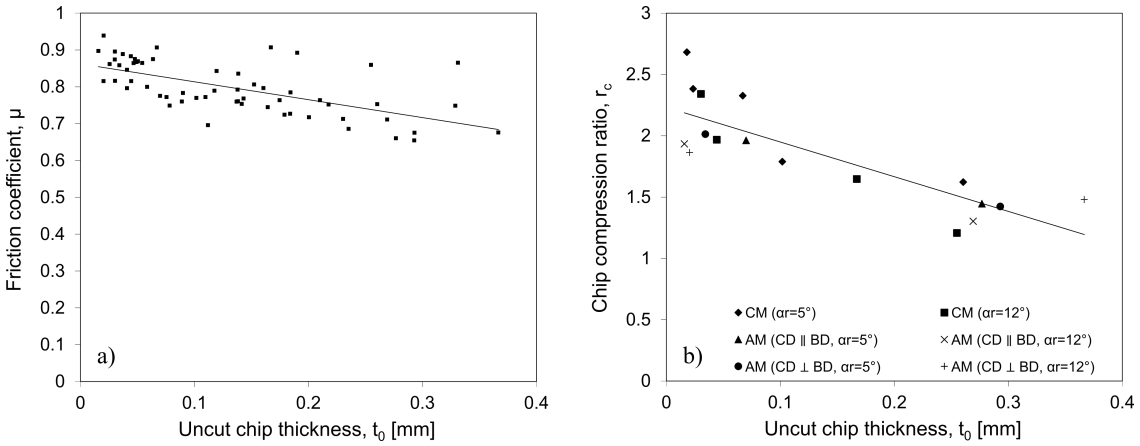


Figure 5.36: Friction coefficient results calculated through load ratio of equation 2.8 (a), and chip compression ratio (b), for all metallurgical conditions.

researchers. The obtained friction results from ring compression tests (≈0.3 in similar strain rate and temperature conditions to cutting) show a higher coherence with the theoretical von Mises limiting value. Similarly to friction results, chip compression ratio presents a linear decreasing trend with uncut chip thickness, as depicted in figure 5.36b. This is in accordance with the theory that a more intense plastic deformation and ploughing effect develop in such t_0 conditions, meaning that the measured chip thickness is potentially influenced by those effects. In addition, the resulting values of chip compression ratio show consistency with other steels in literature (Agmell et al., 2013; Astakhov and Xiao, 2008; Abushawashi, 2013).

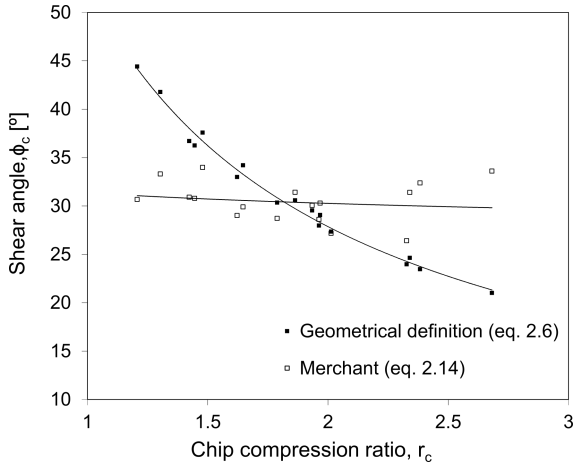


Figure 5.37: Shear angle predictions using geometrical and Merchant's metal cutting theory.

Shear angle was calculated through the geometrical description of metal cutting (depicted in equation 2.6) and Merchant's metal cutting theory (equation 2.14). Results are illustrated in figure 5.37. Shear angle evolution is rather distinct, depending on the calculation method. The geometrical definition shows a clear trend of smaller shear angle for increasing chip compression ratio, which is coherent with similar research by Davim (2007). Knowing that the highest values of r_c correspond

to the smaller t_0, it can be derived that for smaller uncut chip thickness, smaller shear angles are developed. Merchant's model seems to underestimate ϕ_c values for realistic chip compression ratios. Despite the popularity of the model, the mismatch of Merchant's theory has been noticed by several authors (Uhlmann et al., 2013).

5.3.2. Turning tests results

Dynamic load component due to the shear angle oscillation, the crack formation and propagation, and the system chatter stability was found in the experimental measurements. Yet, attention was directed to the static component of cutting load as the main parameter influencing the power required by the cutting process (Monroy Vazquez et al., 2014). The vector components of the cutting load quickly become stationary due to the low strain hardening and high strength of both CM and AM 18Ni300 steels. AM AISI316L presented a similar behaviour. Figure 5.38 shows the experimental correlation between different vector components of the cutting load, namely the feed (F_f) and thrust force (F_t) components with the cutting force (F_c) for both CM and AM 316L stainless steels. Figure 5.38a shows the experimental measurements for the turning tests carried out using cutting inserts with a flat rake face (T-FLAT), while figure 5.38b shows comparable results using cutting inserts with a chip-breaker (T-CB). The vectorial components F_t and F_f increase monotonically with the cutting force. These findings corroborate the geometric relationship between the vector components of the cutting load and the operational parameters of the machining process. Such correlation additionally allows to simplify the presentation and discussion of results, even if there may be a slight deviation for lower cutting forces. Figure 5.39 shows a similar analysis for both CM and AM 18Ni300 maraging steels. In the analysis of thrust force, a notorious tool influence is observed. The values of F_t for T-FLAT inserts are higher with average values of approximately 30% and 15%

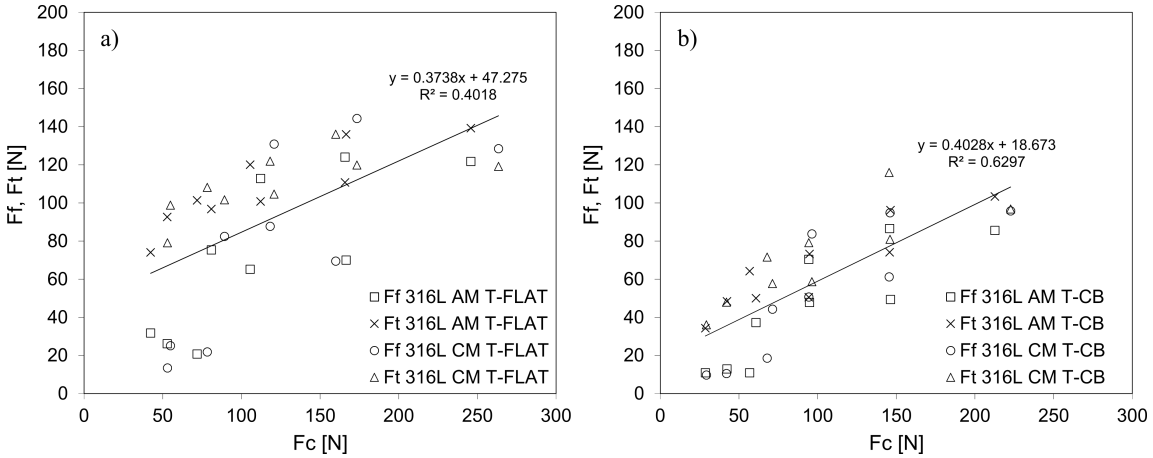


Figure 5.38: Experimental correlation of the thrust force, F_t, and feed force, F_f, with the cutting force, F_c for both CM and AM 316L steels at a rotational speed of 2500 rpm using: (a) T-Flat and (b) T-CB cutting tools.

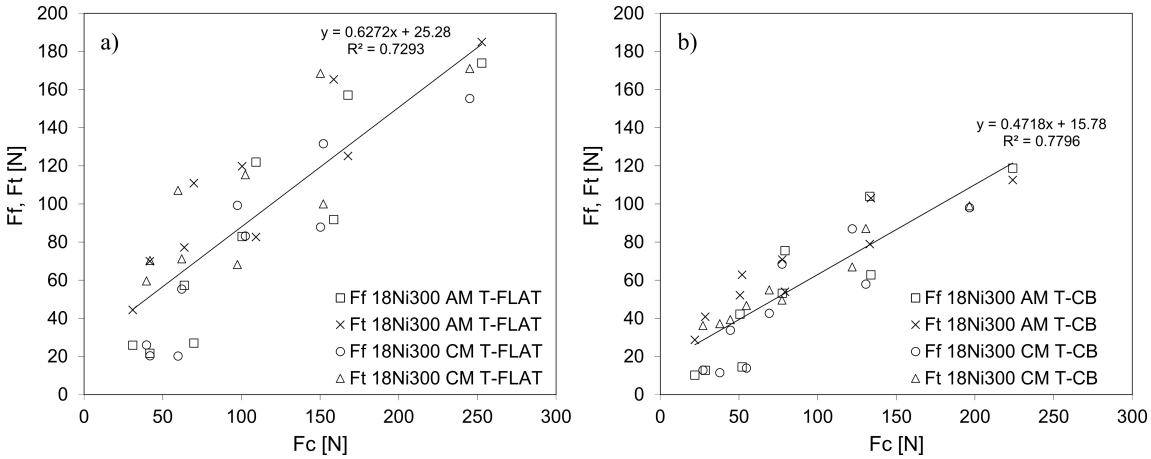


Figure 5.39: Experimental correlation of the thrust force, F_t, and feed force, F_f, with the cutting force, F_c for both CM and AM 18Ni300 steels at a rotational speed of 2500 rpm using: (a) T-Flat and (b) T-CB cutting tools.

for 316L and 18Ni300, respectively. This difference tends to increase for 316L as the cutting load decreases, reaching an average difference of approximately 100%. Although both cutting inserts are designed for finishing operations, the T-CB insert allows for a better performance due to its improved chip breaker geometry, capable of more efficient chip control and lower cutting loads. It should also be noted that the monotonic response shown above does not seem to change with the materials processing condition (AM or CM), thus being valid to the entire range of cutting conditions for each specific combination between the workpiece material and chip breaker geometry. The vector components of the cutting load are significantly correlated, as previously observed in figures 5.38 and 5.39. Even so, the physics of metal cutting indicate a direct relationship between each vector component and the operative parameter in that specific direction. Hence, figure 5.40 shows the influence of the depth of cut, a_p on the F_t component, while figure 5.41 displays the influence of the feed per revolution on the F_f for different combinations between the workpiece material and the turning insert geometry. In general, thrust force and feed force increase monotonically with feed per revolution. The dispersive results in figures 5.40a and 5.41a are due to the intermittent interface contact between the chip and an extensive rake surface promoted by the top flat insert (T-FLAT), as well as a higher sliding force needed to overcome a higher friction. The benefits of using cutting inserts with a chip-breaker are clearly demonstrated in figures 5.40b and 5.41b by a significant reduction of both thrust and feed forces, while its dependence on the feed parameter has also been reduced. Nevertheless, even if the chip breaker effect is considered, the thrust force will be consistently higher for turning tests conducted at a higher depth of cut, differing more than 100% on average. Another relevant aspect shown in figure 5.41 is the fact that the evolution of the feed force as a function of feed does not pass through the origin, which is a result of the size effect mechanisms. Interceptions obtained experimentally are usually explained by rubbing

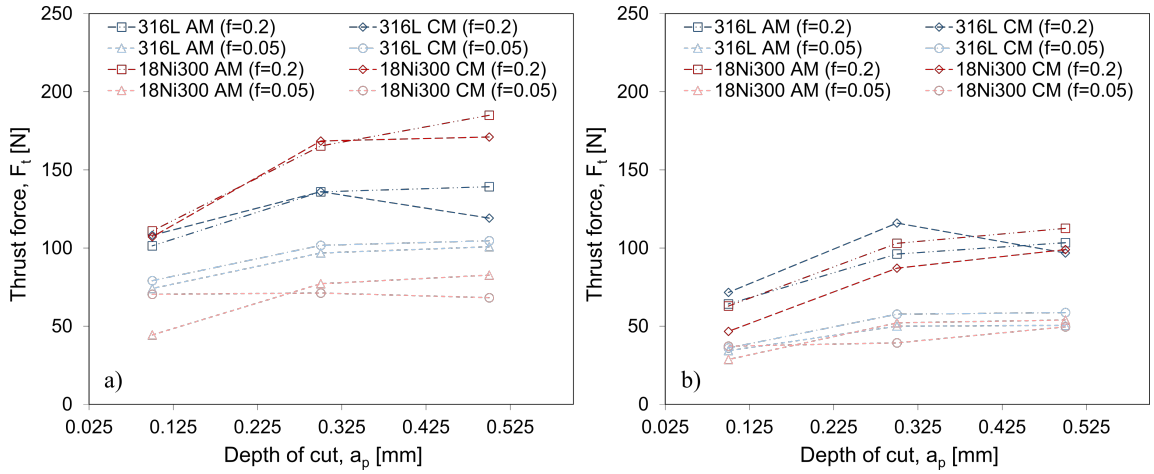


Figure 5.40: Experimental evolution of the thrust force, F_t, as a function of the depth of cut, a_p for both CM and AM 18Ni300 and AISI316L steels using: (a) T-Flat and (b) T-CB cutting tools.

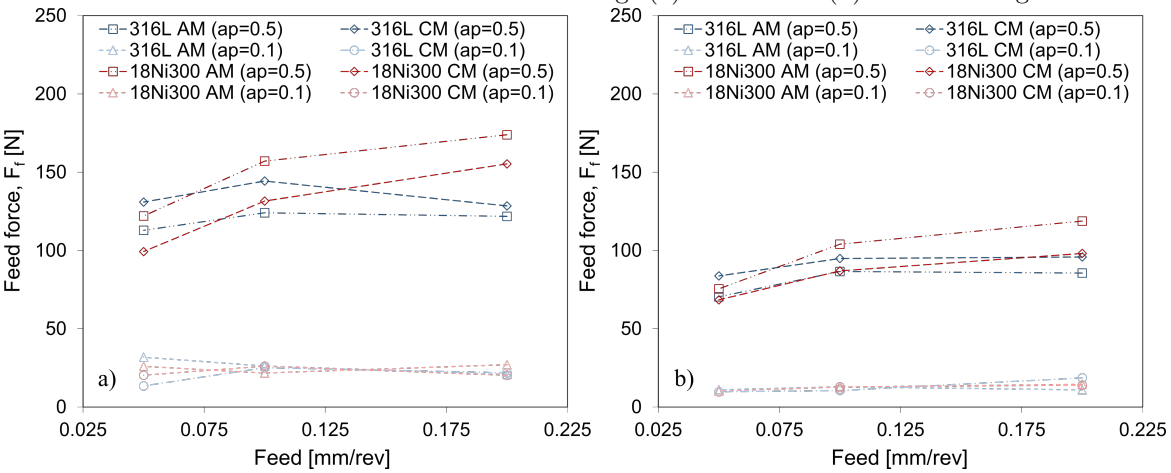


Figure 5.41: Experimental evolution of the feed force, F_t, as a function of the feed per revolution, f for both CM and AM 18Ni300 and AISI316L steels using: (a) T-Flat and (b) T-CB cutting tools.

on the clearance face of the tool, tool bluntness and oblique-chip formation mechanics, among others (Monroy Vazquez et al., 2014). But this positive force interception does not disappear, even for experiments with the sharpest tools and orthochip formation mechanics, whose contribution results from ductile fracture phenomena (Rosa et al., 2007b). Despite the turning tests performed are scarce to obtain an adequate fracture toughness estimative for the CM and AM workpieces, the experimental trend that passes through the origin shows a similar positive interception under comparable cutting conditions, and independent from the metallurgical condition of the workpiece material. Thus, the fracture work involved in the formation of new surfaces seems to remain constant, no matter the CM or AM materials processing procedure. Regarding thrust and feed forces at higher levels of feed per revolution, the AM materials present consistently higher values when compared to the CM materials, differing more than 10% on average. Consequently, the plastic deformation work involved in the chip flow throughout the shear plane seems to increase with the material strength.

Figure 5.42 shows the evolution of static component of cutting force, F_c as a function of the main

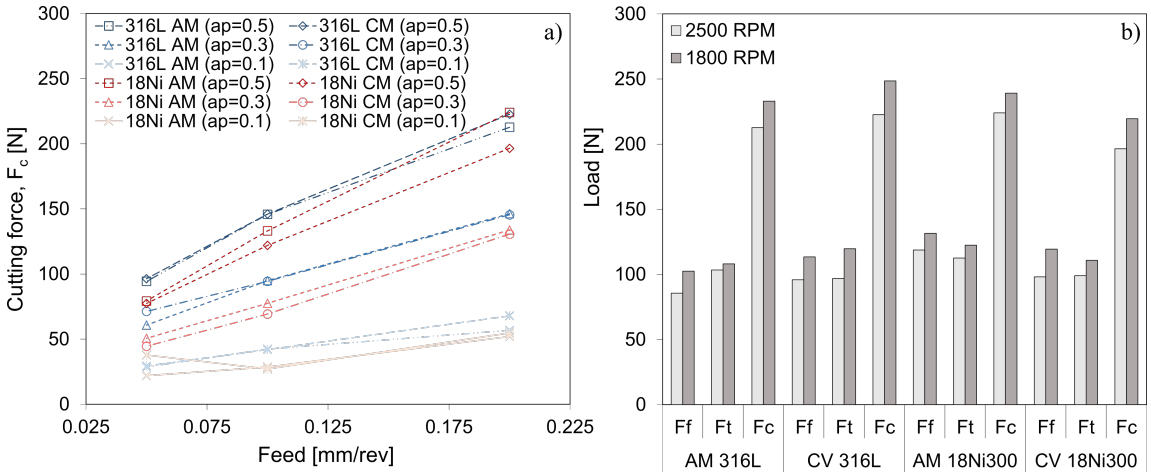


Figure 5.42: Experimental evolution of the cutting force, F_c, for both CM and AM 18Ni300 and AISI316L steels using T-CB cutting tools: (a) Cutting force as a function of the feed per revolution, f, for three fixed depths of cut, a_p, of 0.1, 0.3 and 0.5 at a rotational speed of 2500 rpm, and (b) influence of the rotational speed on the vector components of the cutting load (a_p=0.5mm and f=0.2mm/rev).

operative parameters (a_p, f and rotational speed) for the 18Ni300 and 316L steels, using a cutting insert with a chip-breaker. Through the analysis of the cutting force, a slight tendency for higher loads in the AM materials can be observed. This result reflects a higher mechanical strength of the AM materials, which is in accordance to the uniaxial compression tests presented previously. It is, however, important to take into account that the differences between the cutting forces is not as visible as the differences observed in the mechanical tests performed on AM and CM materials. This phenomenon occurs due to the stress triaxiality and lode angle along the plastic deformation region caused by the nose radius effect and the oblique-chip formation mechanics (Zhang et al., 2017a; Cheng et al., 2019b). The cutting force values are mainly controlled by the uncut chip cross section that is determined by the depth of cut and feed per revolution. Cutting force also decreases with the rotational speed and differs on average less than 10%. However, an increase is usually expected because the deformation of metals is, to a certain extent, time-dependent. This finding suggests the need for further studies to elucidate the influence of the applied loading rate (strain rate effects) and temperature on the flow stress curve. Competing thermal softening and viscous hardening phenomena may be present and seems that the thermal softening is dominating. Additionally, these findings are in accordance with other publications on the 316L stainless steel under identical cutting conditions (Struzikiewicz et al., 2019).

Figure 5.43 shows the evolution of the specific cutting pressure, K_c, as a function of the cross-sectional area of the uncut chip, S, conducted for two distinct cutting inserts under a wide range of operative conditions. The use of a cutting insert without rake surface discontinuities (T-FLAT) is a common technique to obtain reference values for the specific cutting pressure. Thus, the benefits of chip control (T-CB) to the cutting process can be fully evaluated. The tool insert with a chip

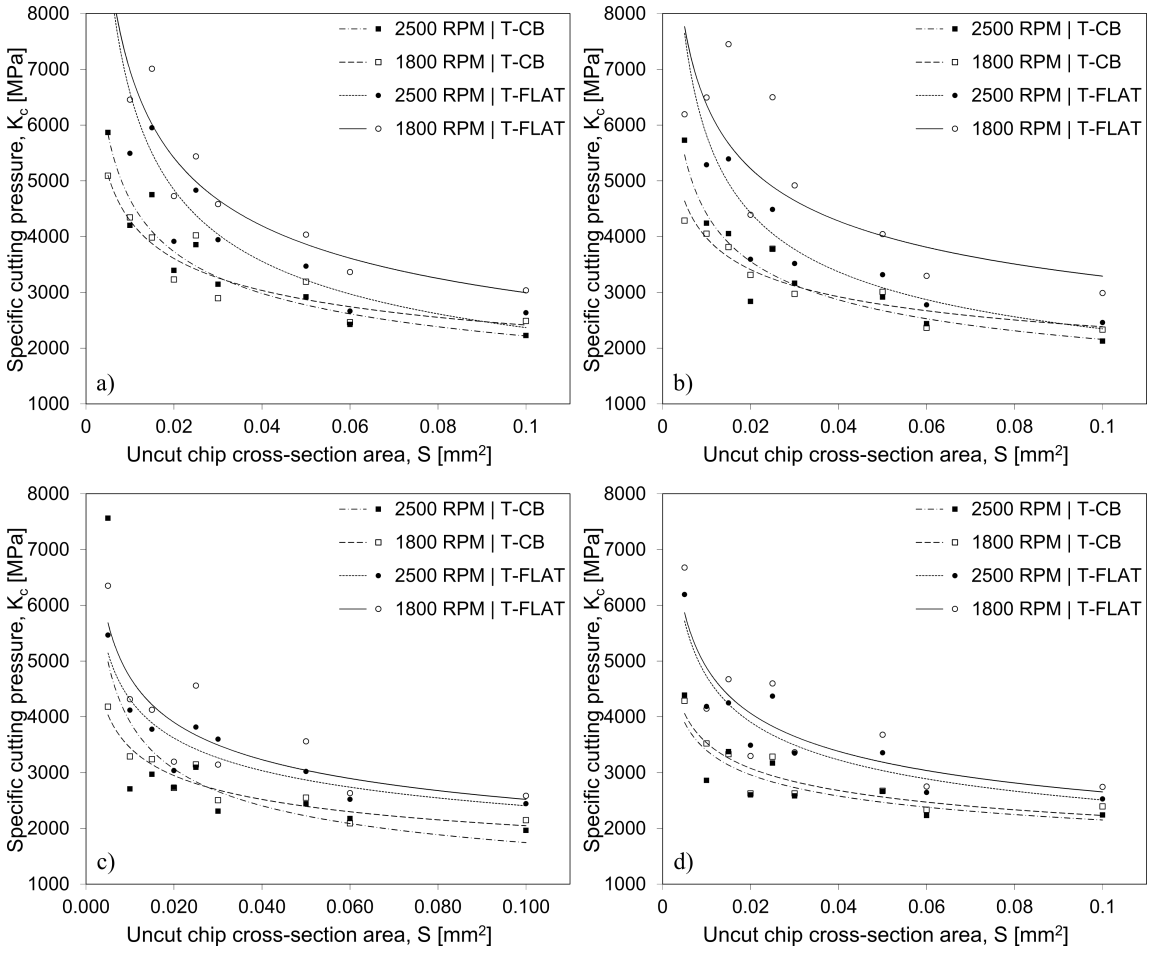


Figure 5.43: Specific cutting pressure, K_c, in function of uncut chip section for: (a) CM 316L, (b) AM 316L, (c) CM 18Ni300, and (d) AM 18Ni300.

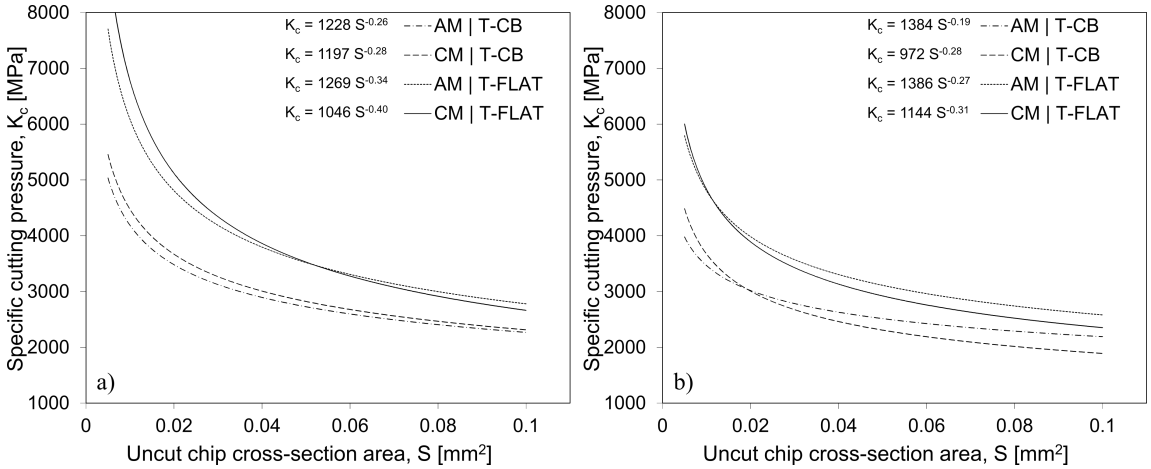


Figure 5.44: Specific cutting pressure, K_c, in function of uncut chip section for: (a) 316L and (b) 18Ni300.

breaker yielded lower cutting specific pressure, representing an energy-wise more favourable scenario in processing both AM and CM materials. When it comes to the distinction between AM and CM steels, no substantial difference was found regarding K_c for the tested conditions. The results show that despite the observed higher flow stresses of additively manufactured steels, no additional energy requirements are needed. Among the curves obtained using the T-FLAT tool insert (for both AM and CM materials), it is verified that the influence of rotational frequency is much less prominent in 18Ni300 than in 316L, which may represent a higher strain rate sensitivity of the latter. Moreover, a tendency for specific cutting pressure to become constant at higher feed-rates and cut depths was noticed. Such evolution is well known and is in accordance with literature (Pérez et al., 2007; Zhang et al., 2016). Additionally, the obtained values are similar to what is known for high strength steels Mitsubishi (2020). The fact that the highest K_c values correspond to reduced chip section areas highlights the importance of studying the behaviour of high-strength steels when submitted to finishing operations. Particularly in AM steels, given the lack of data to predict the cutting load in contrast to the need for surface improvement towards functionality enhancement.

Figure 5.44 highlights the low K_c variation due to material processing condition (AM or CM) for 316L stainless steel (fig. 5.44a) and 18Ni300 maraging steel (fig. 5.44b), using both insert geometries. Given the low influence of cutting speed on the measured loads, the curves include both tested rotational speeds (1800 and 2500 rpm), representing cutting speeds in the range between 55 and 118 m/min. For each material, processing condition and used tool, K_c is proposed as a power function of the chip section area. It is possible to observe that 316L stainless steel, regardless of the processing condition, presents higher K_c than the 18Ni300 maraging steel, for lower cross-section chips. Also in this region, the differences between cutting tools are more expressive. For higher chips cross-sections the differences between tools performance fade as well as the differences between steel grades. This latter result may be related with the fact that, despite its initial lower flow stress, the 316L stainless steel exhibits a marked strain-hardening attaining similar flow stress values to the maraging steel, which in contrast presents almost negligible stain-hardening (refer to figure 5.10). At higher chip cross-sections, the differences between metallurgical conditions of the steels (AM vs. CM) are almost negligible for the 316L steel; nevertheless for the 18Ni300 steel one can realize a higher specific cutting pressure for the AM material. This fact is in agreement with the detected differences in the flow stresses of the alloys: whereas the strength levels of each 316L alloy (AM and CM) tend to converge to an unique response for higher strains, regardless of metallurgical condition (refer to figure 5.10a); for the 18Ni300 alloys the differences between AM and CM flow stresses are independent of the strain level (refer to figure 5.10b).

In figure 5.45 the K_c results obtained from orthogonal cutting experiments are compared with the ones obtained from turning. Despite the smaller chip areas in longitudinal turning operations ($\leqslant$ 0.1 mm^2) there is a noticeable continuity and coherence of the curves plateau for higher chip areas in

orthogonal cutting configuration. The tool geometry influence on the K_c magnitude seems to have a larger influence on the turning experiments which may be explained by the increased complexity of the three-dimensional cutting with regards to orthogonal cutting. Nonetheless the continuity between the simpler tool geometries of each operation (T-FLAT and α_r=5°) is highlighted.

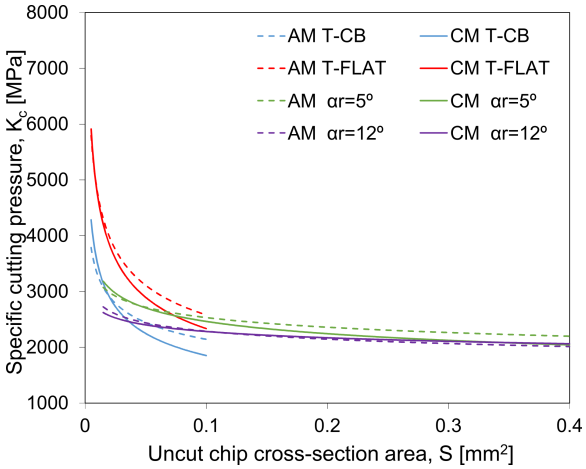


Figure 5.45: Specific cutting pressure, K_c, obtained from orthogonal cutting and turning operation.

Figure 5.46 presents the evolution of the chip morphology throughout the different cutting conditions tested for AM 316L stainless steel using T-FLAT cutting inserts. A more effective chip segmentation, enabling the formation of short shaped chips, occurs for lower uncut chip cross-sectional area and higher cutting speeds. For lower cutting speeds, the chip breaking aptitude significantly decreases and no chip breaking with T-FLAT cutting inserts occurs. When cutting the specimen with a flat rake faced tool, chip tends to assume a helical shape, which slightly changes to conical when using the considered chip-breaking geometry, due to chip flow direction.

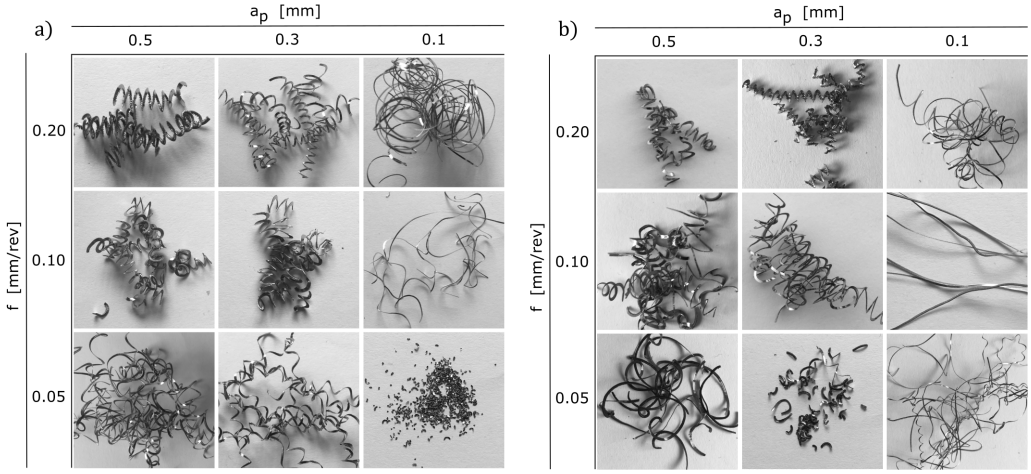


Figure 5.46: Chip types throughout variation of the feed per revolution, f, and depth of cut, a_p, for the AM 316L stainless steel using T-FLAT cutting inserts for different rotational speeds: (a) 2500rpm, and (b) 1800rpm.

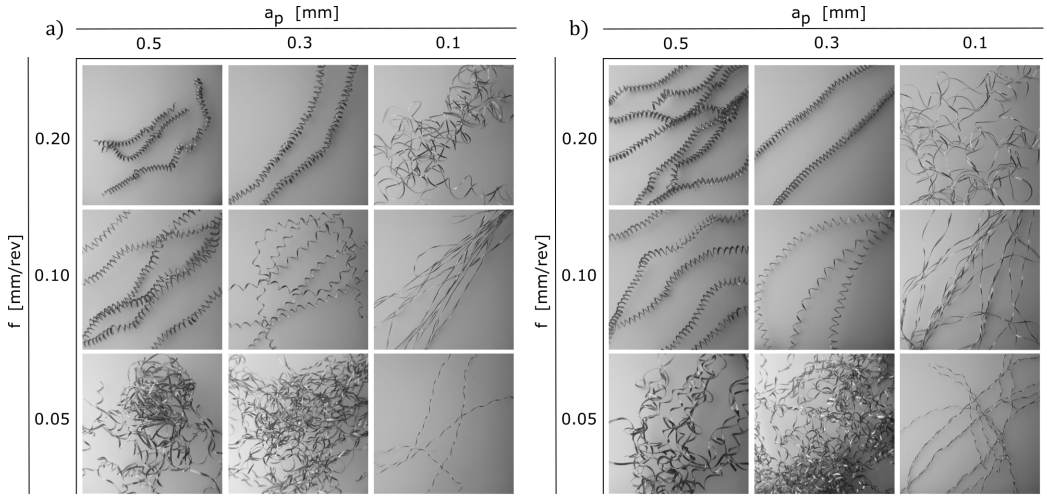


Figure 5.47: Chip types throughout variation of the feed per revolution, f, and depth of cut, a_p, for AM 18Ni300 steel using T-CB cutting inserts for different rotational speeds: (a) 2500 rpm, and (b) 1800 rpm.

Figure 5.47 presents the evolution of the chip morphology throughout the different cutting conditions tested for AM 18Ni300 steel using T-CB cutting inserts. Despite the fact that only commercial T-CB cutting inserts have been used, continuous and helical chips were still obtained. Such results may be explained by the low porosity and high ductility of the AM 18Ni300 steel, and by the scale-down effect in metal cutting. This fact goes against the common sense associated with the high strength and fragile mechanical behaviour of AM materials. Similar results were found for CM 18Ni300 steel. It can also be noticed that T-CB inserts show a more adequate chip control for 316L stainless steel than for the 18Ni300 steel under the typical cutting conditions of a finishing turning operation. Still, regarding the 316L stainless steel, it can be seen that the biggest occurrence of unfavourable chip formation is the appearance of snarled shape chips (long chips that entangle), contrarily to the 18Ni300 maraging steel, where long chips typically remain untangled.

SEM images of chips (figures 5.48 and 5.49) allow for the potential identification of the influence of workpiece material and tool insert on the chip morphology. Serrated chip formation is noticed on both materials. This saw-tooth appearance typically occurs in high-strength materials with low heat conductivity (Wu and To, 2015). As previously mentioned in literature review, this phenomenon arises from excessive deformation of a narrow band of material in the primary shear zone, where heat conduction is negligible due to the larger thermal softening of the material in that region, while the surrounding material is only slightly deformed (Prieto et al., 2018). The fact that more pronounced valleys are observed in the serrated chips of 316L stainless steel than in the 18Ni300 steel is in accordance with the lower thermal conductivity of the material, which in turn contributes to a lower resistant chip section, promoting its breakage. It should also be noted that the above linear response does not seem to change with the materials processing condition (AM or CM), thus being valid to

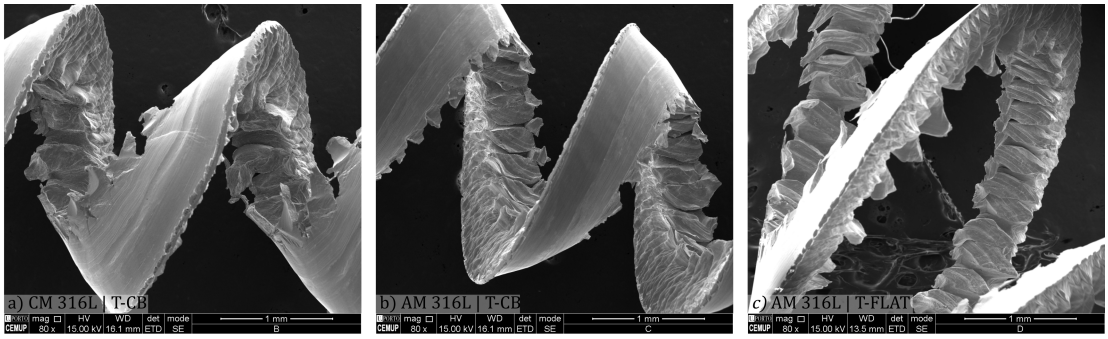


Figure 5.48: SEM images of chips obtained from the turning tests on 316L stainless steel for f=0.2 mm/rev, a_p=0.5 mm and n=2500 rpm; (a) CM 316L using T-CB insert, (b) AM 316L using T-CB insert, and (c) AM 316L using T-Flat insert.

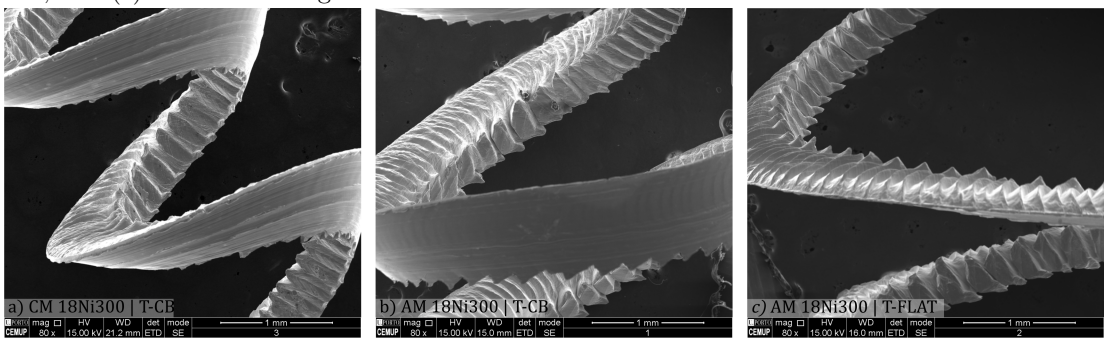


Figure 5.49: SEM images of chips obtained from the turning tests on 18Ni300 steel for f=0.2 mm/rev, a_p=0.5 mm and n=2500 rpm; (a) CM 18Ni300 using T-CB insert, (b) AM 18Ni300 using T-CB insert, and (c) AM 18Ni300 using T-Flat insert.

the entire range of cutting conditions for each specific combination of workpiece material and chip breaker geometry.

Chip collection allowed an association between chip macro-geometry and specific cutting condition for each workpiece material - cutting insert combination. Controlling the cutting parameters in order to generate favourable chip formation is essential for avoiding machined surface damage, especially in finishing operations. Figure 5.50 presents the evolution of the chip morphology obtained on different cutting conditions for 316L stainless steel using T-CB cutting inserts. Despite the usage of commercial T-CB cutting inserts for a better chip control, the typical generated chip geometry did not vary significantly, and the most frequent obtained shape was helical/conical long. Similar results were observed on CM 316L machining. Moreover, the differences between the chip geometries obtained from the CM and AM materials were not statistically significant. Figure 5.50 shows that tool geometry does not seem to have a major impact on chip breakage, since it occurred equally for both tool inserts used. Such aspect may be explained by the high ductility of the considered 316L steels, which promotes a continuous chip formation. Even so, the usage of a chip breaking geometry (T-CB) is still justifiable, as cutting loads were significantly lower.

Surface roughness measurements and SEM visualization were performed in order to assess the integrity of the machined surface. Figure 5.51 displays both experimental measurements and the-

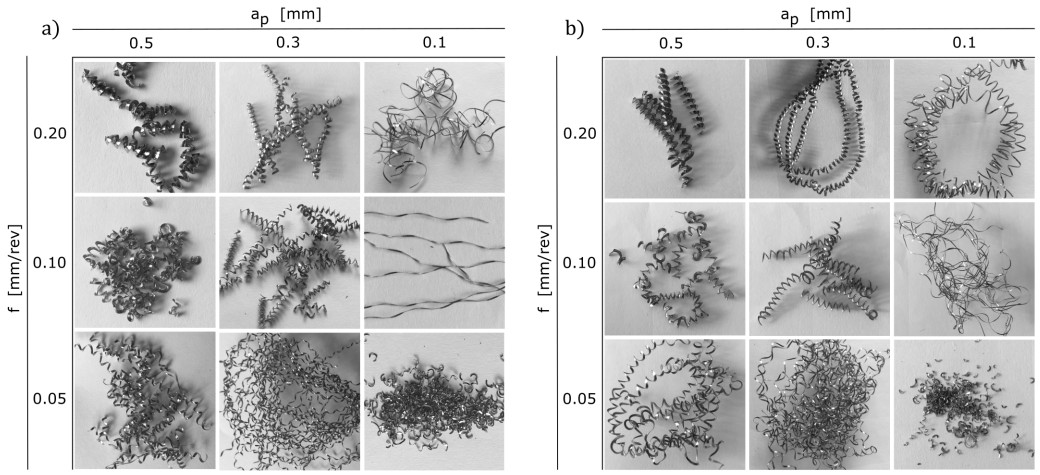


Figure 5.50: Chip types throughout variation of the feed per revolution, f, and cut depth, a_p, for 316L stainless steel using T-CB cutting inserts at a rotational speed of 2500 rpm for (a) AM 316L condition, and (b) CM 316L condition.

oretical estimates for the surface roughness, R_a, along the longitudinal direction of the machined rods. Theoretical estimates were derived from traditional and widely used equations, well described in literature, which accounts solely for geometric factors, namely tool insert nose radius, r_e, and feed per revolution, f (Groover, 2010; Tönshoff and Denkena, 2013).

$$R_a = \frac{f^2}{32 r_e} \tag{5.4}$$

As expected, both experimental values and theoretical estimates increase with the feed per revolution for all tested conditions. However, a more pronounced growth on the theoretical estimates reveals missing contributions that have not been accounted.

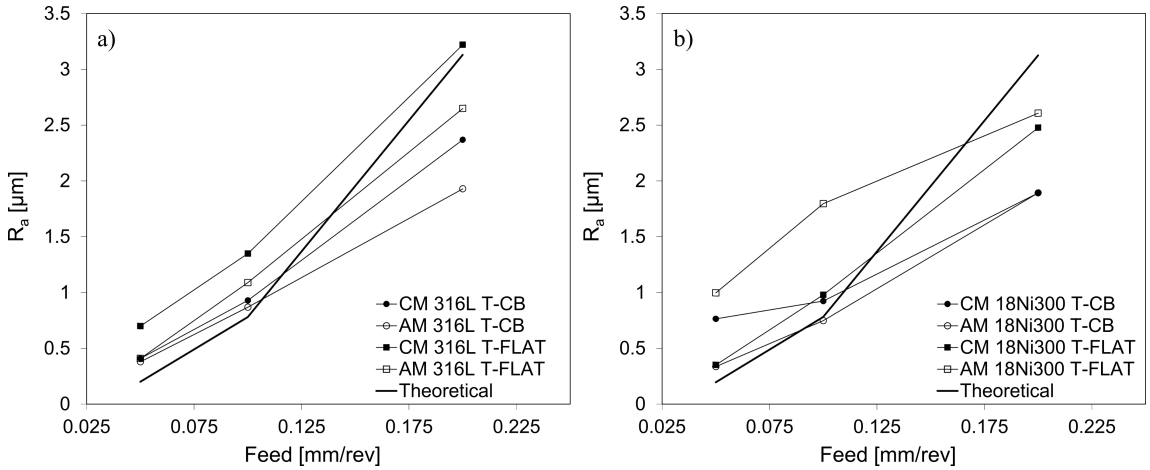


Figure 5.51: Post-machining surface roughness, R_a of 316L (a) and 18Ni300 (b) for each processing condition and used tool insert, as a function of feed rate, for a cut depth, a_p, of 0.3mm, T-CB cutting inserts at a constant rotational velocity of 1800 rpm for a feed per revolution.

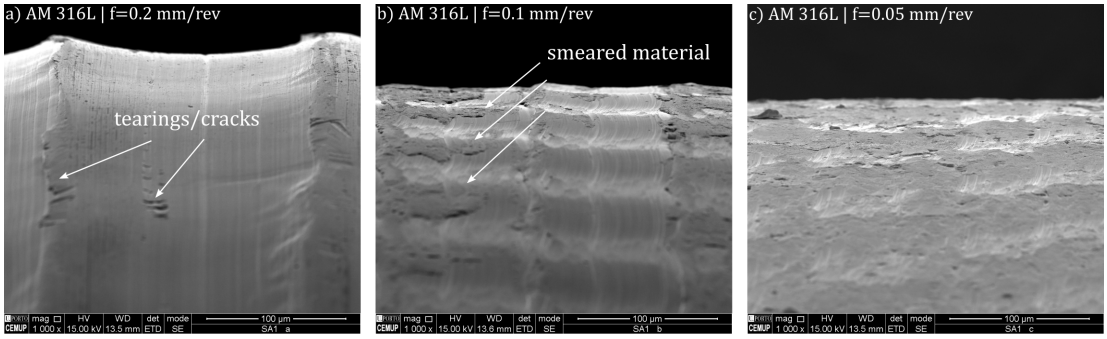


Figure 5.52: SEM images of machined surfaces in AM 316L stainless steel for a cut depth, a_p, of 0.3mm, T-CB cutting inserts at a constant rotational velocity of 1800 rpm for a feed per revolution, f, of (a) 0.2mm/rev, (b) 0.1mm/rev, and (c) 0.05mm/rev.

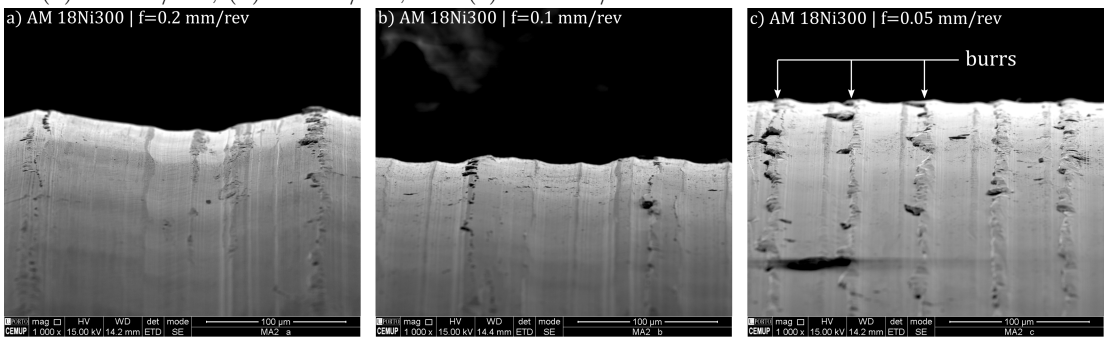


Figure 5.53: SEM images of machined surfaces in AM 18Ni300 steel for a cut depth, a_p, of 0.3mm, T-CB cutting inserts at a constant rotational velocity of 1800 rpm for a feed per revolution, f, of (a) 0.2mm/rev, (b) 0.1mm/rev, and (c) 0.05mm/rev.

Figure 5.52 and 5.53 present the micro-geometry of the machined surfaces revealing a wavy surface. Formation of continuous burrs can also be seen along the peaks crest. While peak-to-valley height decreases in line with the feed, burrs size remained virtually unchanged. This size effect involves simultaneously the interaction between workpiece and cutting insert, and the material performance during and after deformation. In short, higher cutting forces of the T-Flat inserts combined with higher strain hardening of the CM 316L and AM 18Ni300 promotes the burrs dimension, limiting the surface finish of the machined surface. In the 316L stainless steel (refer to figure 5.52a), for operations with the same cutting tool, the average surface roughness of AM samples was consistently lower (approximately 23%). Moreover, the existence of certain surface defects, as the tears/cracks and smeared material, indicate the occurrence of tool or chip adhesion probably due to BUE and have an influence on the measured surface roughness. The fact that these defects (typical of dry cutting) occur often for high feed rates may also explain the slight deviation from theoretical estimates. As size effect phenomena and material performance are not accounted for in the traditional theoretical estimates, practical surface roughness is underestimated for finishing cutting conditions (i.e. 0.05 mm/rev) and overestimated for higher values of the feed per revolution, as illustrated by figure 5.51. From figure 5.51b is possible to infer a similar trend for 18Ni300 maraging steel where the chip-breaking tool (T-CB) shows to be effective in controlling surface roughness. Indeed, lower

cutting forces of the T-CB inserts also allow to minimize chatter due to vibration. However, a higher R_a value can be noticed in the CM samples machined with T-CB tool (for f=0.05mm/rev) and AM samples machined with T-Flat tool, which may have happened due to BUE on the cutting tool and given the significant tool wear with little machining time.

Chapter 6. Constitutive modelling of materials mechanical behaviour

The current chapter deals with the determination of the materials constitutive behaviour which, due to being supported by inverse approaches, requires the numerical simulation of the experimental characterization tests. The chapter focuses only on maraging steels, from both metallurgical conditions. A numerical/experimental analysis on the ring compression tests enables friction estimation and the obtention of frictionless flow stress curves. The simulation of tensile tests allows for the determination of fracture strain under distinct stress triaxiality conditions. The obtained flow stresses are used in the simulation of the multiaxial fracture tests, which enables not only the determination of fracture strain for lower stress triaxialities than the tensile tests, but also allows to improve the plasticity response towards metal cutting simulation.

6.1. Frictionless flow stress identification

As previously mentioned in the experimental procedure (see section 4.3.2), ring compression tests were used in order to characterize friction in similar temperature and strain rate conditions to the compression tests and also common in cutting. These tests consist of an excellent method for assessing friction conditions due to the setup simplicity. By merely tracking the specimen dimensions it is possible to estimate friction (no test instrumentation is required) through immediate comparison with calibration curves, making it very attractive to industrial practice of lubricant benchmark, for instance (Rao and Sivaram, 1993). The integration of ring compression tests with numerical simulation, enables the determination of friction coefficient. However, a prior knowledge of the material's mechanical response is required, which in this study has been done by means of compression tests. Even though friction results were previously presented in section 5.2.2, their identification involves a combination of experimental and numerical techniques and is, thus, presented in detail in the current section. Figure 6.1 shows a flowchart which describes the adopted methodology towards friction coefficient estimation. The first step corresponds to the experimental compression tests and ring compression tests, in same lubricated conditions, for multiple levels of strain rate and temperature. The usage of lubricated friction conditions will allow a faster convergence towards the frictionless flow

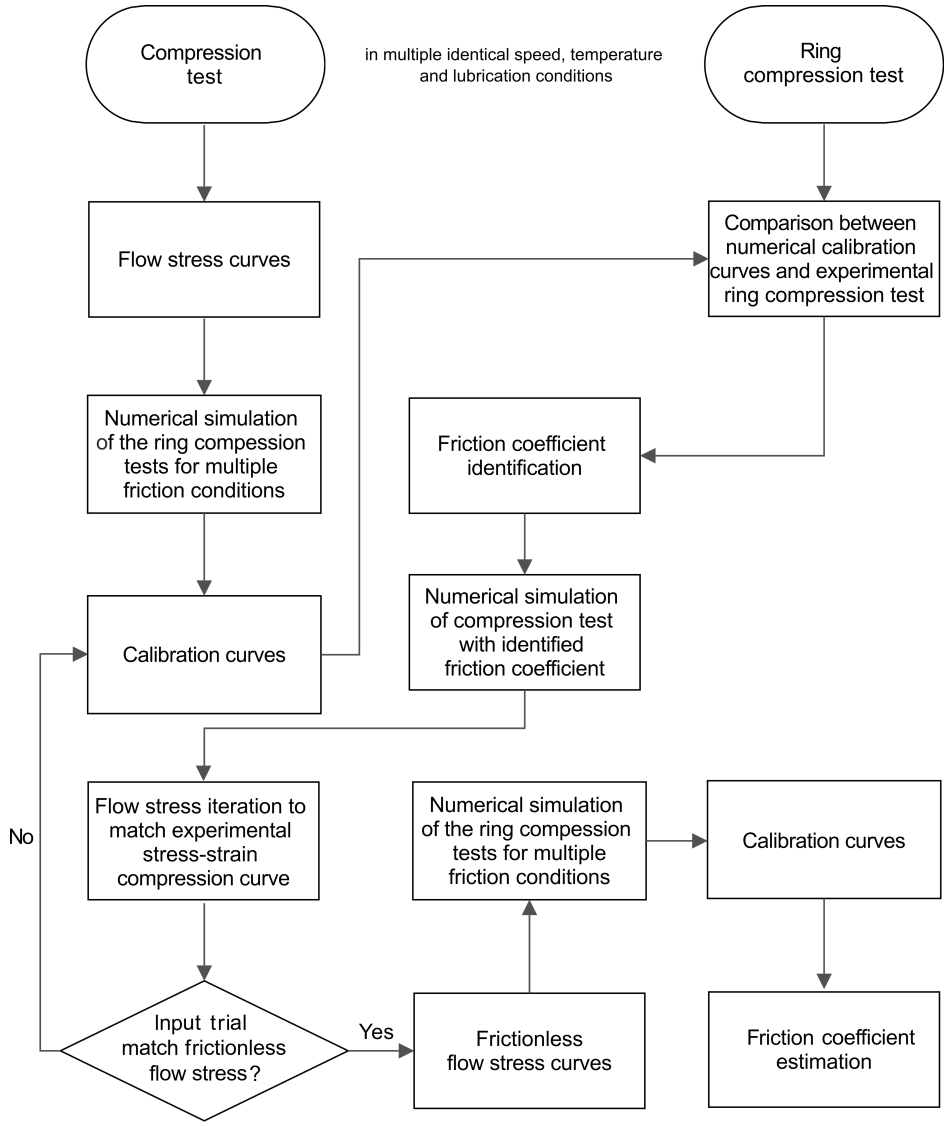


Figure 6.1: Flowchart for frictionless flow stress and friction coefficient estimation, using compression and ring compression specimens.

stress curves. The compression tests enable the estimation of trial flow stress curves that are used to simulate the corresponding ring compression tests for multiple friction conditions. The comparison of the actual experimental values of the ring compression tests with the numerical calibration curves allows for friction estimation. Despite using graphite as lubricant in order to minimize friction, the obtained strain-stress curve is not frictionless. In order to exclude the friction contribution from the trial flow stress, an iterative process is applied. This process consists on the simulation of the compression test using the preliminary flow stress data as material input as well as the estimated friction coefficient. The obtained stress-strain response will be an over estimation of the trial flow stress and by subtracting their difference to the trial curve, a frictionless flow stress is obtained. With the corrected frictionless flow stress new ring compression calibration curves are simulated,

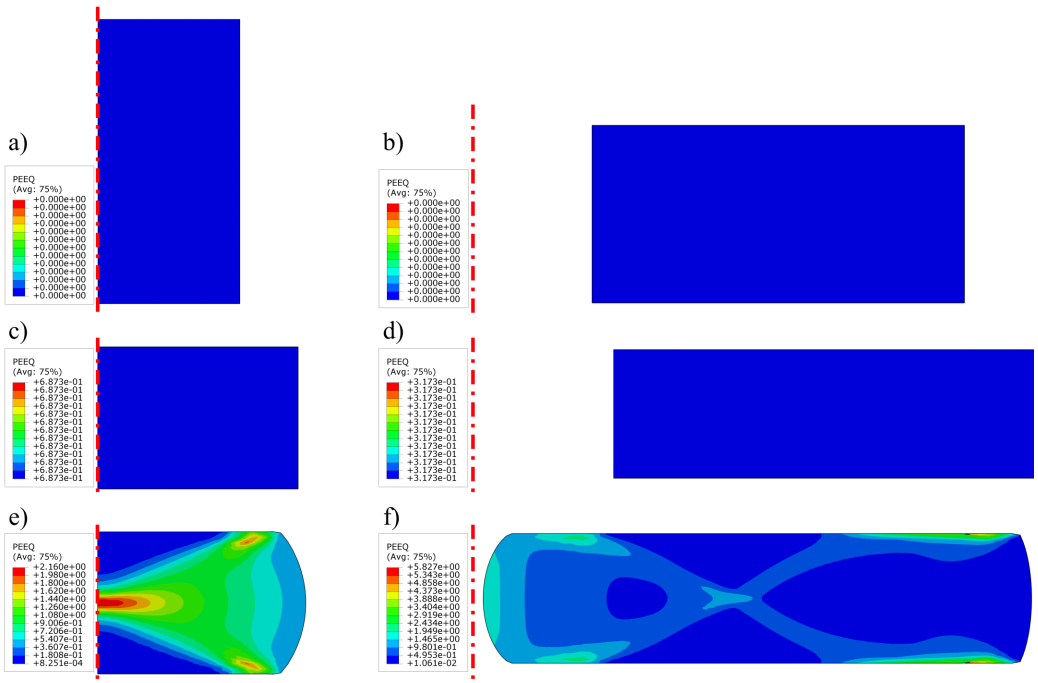


Figure 6.2: Non-deformed numerical (axisymmetric) models of the cylindrical (a) and ring (b) compression specimens; deformed cylindrical (c) and ring (d) compression specimens assuming frictionless conditions; deformed cylindrical (e) and ring (f) compression specimens assuming μ=0.577.

allowing for the final identification of the friction coefficient (for distinct temperatures and strain rates). Both compression and ring compression tests were simulated through axisymmetric models on Abaqus/Standard, which allows for representation of only half of the specimens. Four-noded axissymmetric elements with reduced integration (CAX4R) were employed to mesh the specimens with an element size of 0.1 mm. Contact interaction was defined between the specimen and both top and bottom analytical rigid bodies. The bottom rigid body was encastred (restrained displacement and rotation of all nodes) and the top rigid body animated with downward displacement. Figure 6.2 shows both cylinder compression and ring compression models. Besides the undeformed specimen, it is possible to observe two friction conditions: frictionless and μ=0.577. For frictionless conditions no barreling occurs and, in the ring compression specimen, the inner diameter expands. In contrast, when defining the maximum (von Mises admissible) friction coefficient, barreling is noticed for both kinds of specimens and in the ring geometry, the inner diameter becomes smaller.

An example of calibration curves is shown in figure 6.3a, where the ring inner diameter variation ($\Delta d_i/d_i$) is plotted over ring height variation ($\Delta h/h_0$). The comparison of these curves with the experimental results allow the estimation of a friction coefficient μ=0.09. The resulting stress-strain curve obtained through numerical simulation of the compression test using the estimated friction coefficient is labelled as "output" in figure 6.3b, whereas "input" corresponds to the flow stress as-obtained from compression tests. By subtracting the friction overestimation, one can derive the

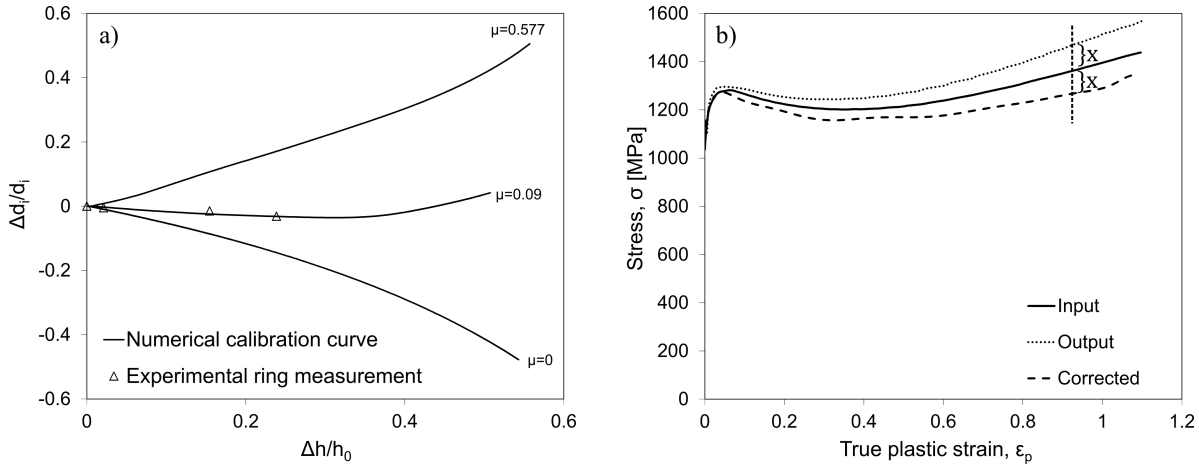


Figure 6.3: Friction calibration curves for compression ring test (a) and stress-strain strain curves (b) of AM maraging steel in quasi-static, room temperature conditions.

corrected frictionless material response. It is relevant to highlight the increasing contribution of friction, for increasing strain, which in turn emphasises the importance of frictionless flow stress estimation in machining simulation (high strains).

6.2. Tensile tests simulation

The numerical simulation of the quasi-static tensile tests enables the prediction of pressure dependent fracture strain and, thus, the identification of damage onset behaviour for the high stress triaxiality range (≥ 0.33). As depicted from the obtained experimental results, the maraging steel shows sensitivity to this parameter, regardless of its metallurgical condition (see fig. 5.22). Numerical models of the tensile tests were built in Abaqus/Standard, using an elastoplastic approach with a von Mises (J2) yield criterion with isotropic hardening. In order to numerically portray an accurate strain-stress behaviour of the material, the flow stress was defined based on tensile tests. Since the experimental tensile true stresses and strains are not known after geometrical necking, an approximation from compression tests hardening was contemplated. The validity of such flow stress is illustrated in figure 6.4 for the smooth CM specimen, where a good correlation between experimental and numerical load-displacement curves is displayed. Four-noded axissymmetric elements with reduced integration (CAX4R) were employed to mesh the specimens with an element size of 0.1 mm. Figure 6.4a illustrates the adopted boundary conditions which include (apart from axissymmetry) zero yy displacement in the bottom nodes and a vertical displacement on the top nodes. The numerical models were built for the L_0 extensometer length, which was of 25mm. Figures 6.4b and 6.4c show the field distributions of equivalent plastic strain and stress triaxiality of a notched specimen (AM N-5). It is observed that both are localized in the centre region of the specimen, where will be maximum. That location has, therefore, been selected for data retrieval as regards

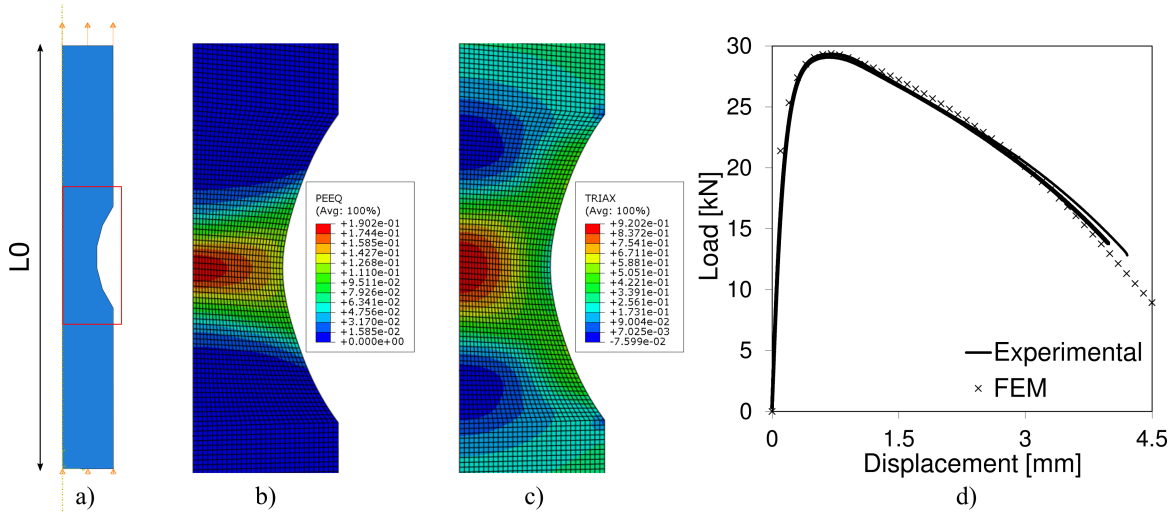


Figure 6.4: Boundary conditions on the N-5 specimen geometry (a); Plastic strain (b) and stress triaxiality (c) fields distributions for the notch region (signalled red square); (d) Inverse reproduction of the N-∞ CM specimen experimental load-displacement curves.

the failure strains and respective stress triaxialities.

The analytical stress triaxiality proposed by Bridgman (1952) relies on the assumption of rigid perfect plastic flow. Despite being convenient for specimen notch design, that assumption should be corrected by taking into consideration a more realistic constitutive behaviour, resulting in a more accurate representation of the stress triaxiality at the onset of damage. Figure 6.5 shows the simulated stress triaxiality evolution in function of plastic deformation for both metallurgical conditions of the maraging steel. Despite the accurate analytical prediction for very small strains, significant evolution of stress triaxiality is noticed which is due to incipient geometrical softening (necking) of the specimen. The procedure for fracture strain estimation consisted in matching the load-displacement numerical curves fracture location with experimental load-displacement curves. That correlation is shown in figure 6.7 for both AM and CM maraging steels. Once there is good correlation, the equivalent plastic strain at the onset of damage was selected as the fracture strain. The estimated values are presented in table 6.1 and in conjunction with the obtained values from the multiaxial fracture specimens to be presented in section 6.3, will enable the identification of

Table 6.1: Fracture strain and stress triaxiality estimation.

Specimen	ε_f	η_{FEM}	$\eta_{Bridgman}$
N-∞ (CM)	1.60	1.07	0.33
N-5 (CM)	1.04	1.10	0.52
N-2 (CM)	0.77	1.25	0.74
N-∞ (AM)	0.53	0.66	0.33
N-5 (AM)	0.19	0.92	0.52
N-2 (AM)	0.10	1.17	0.74

a damage onset model. In table 6.1 are also displayed the Bridgman (1952) predictions of stress triaxiality for the initial specimen geometry. The very significant deviation between η_{FEM} and $\eta_{Bridgman}$ highlight the considerable specimen deformation.

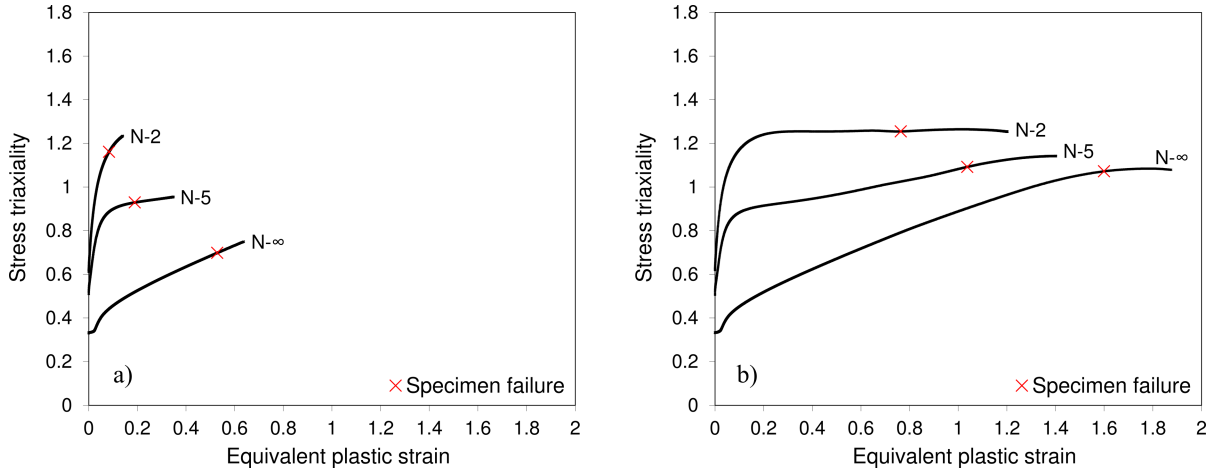


Figure 6.5: Estimated (numerically) stress triaxiality evolution in function of plastic strain for the AM (a) and CM (b) maraging steel.

6.3. Multiaxial fracture tests simulation

The suitability of the multiaxial fracture specimens towards the definition of damage models for cutting has been pointed out by Abushawashi (2013), a co-worker of Astakhov, due to the attained range of low and intermediate stress triaxiality levels, which are not covered by classical tensile notched specimens. Also important to note, is the fact that the plastic behaviour is, likewise, determined based on these specimens, by the referred authors. This was performed through a reverse strategy optimization routine. The author was able to identify a hardening rule, starting from yield, by incrementally estimating the stress and strain values of the flow curve. For each new estimated "plasticity point" a FEM simulation of the test would be led up until such plastic state. According to the over or underestimation of simulated load value (with respect to the experimental), the guessed stress value of the flow curve would be reduced or increased, respectively. Apart from accurately depicting the loads of multiaxial specimens with distinct pressure angles, the plastic model identified by Abushawashi (2013), in conjunction with damage model, correctly predicted cutting loads in the simulation of the orthogonal cutting model. This brings to focus the enormous potential of these specimens towards plasticity validation and definition of the hardening model, especially under such large and heterogeneous deformation, typical of metal cutting (combined pressure and shear loading).

A 2D plane strain approach was used in this research for the simulation of the multiaxial fracture specimens. Their symmetry enabled the modelling of half-specimen. Four-noded elements with reduced integration (CPE4R) and an element size mesh of 0.05 mm were used. The model, illustrated

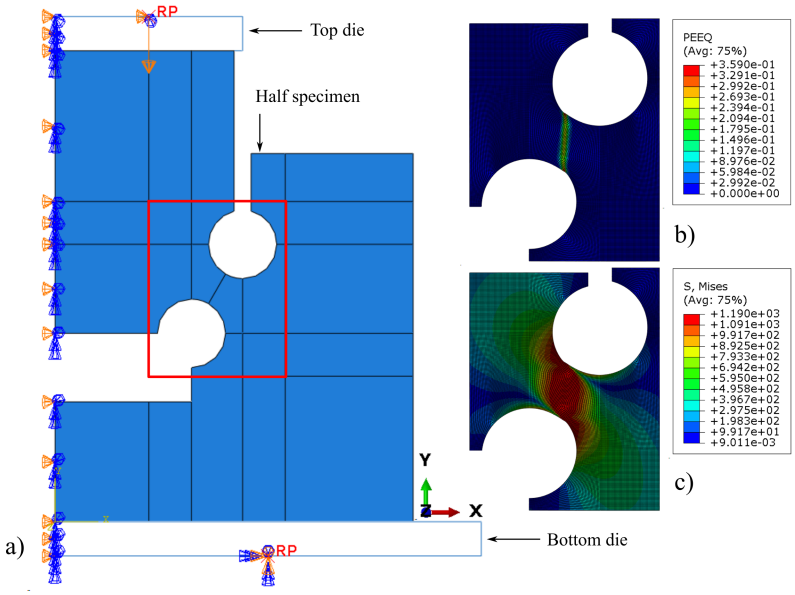


Figure 6.6: Multiaxial specimen numerical model scheme with employed boundary conditions (a); equivalent plastic strain (b) and von Mises stress fields (c) of the red-signalled region for a top die displacement of 0.22mm.

in figure 6.6, consists of a top die (with one degree of freedom in y direction) that compresses the specimen onto a bottom die (encastred). Both dies were modelled as rigid bodies and interface friction was set to 0.2. Figures 6.6b and 6.6c show the stress and strain localization at the notch, for an incipient stage of the numerical simulation. As previously shown in the experimental results section (refer to figure 5.23), a slight variation of the flow stress could be observed according to the direction of uniaxial testing (compression or tension). Moreover, within uniaxial compression tests obtained from different labs, slightly different results were obtained, especially at low strain values (<0.2) as previously shown in figure 5.11. In order to find the most appropriate hardening rule, the multiaxial specimens have been simulated using slightly distinct flow stresses based on the conducted characterization tests. Figure 6.7 shows the tested flow curves for each metallurgical condition of the maraging steel. As generally acknowledged in literature (Rosa et al., 2004), uniaxial compression is the commonly used mechanical test when it is intended to evaluate the mechanical response of materials to severe plastic deformation conditions. On the other hand, the tensile test might portray more reliable results for incipient deformation (due to the absence of friction). The idea that a hybrid (tensile and compression) characterization procedure might be suitable to accurately represent the flow stress has resulted in the flow curves labelled as "a". These curves capture the tensile materials' response for low strain values and assume linear hardening that is tangent to the minimum stress values obtained by compression testing. It is worth mentioning that according to this approach, curve "a" can assume either a negative (AM) or positive (CM) strain-hardening. For completeness purposes, another set of curves (labelled as "b") has been selected to understand the sensitivity of strain-hardening on the modelling of multiaxial fracture specimens. Curves labelled as "b-AM"

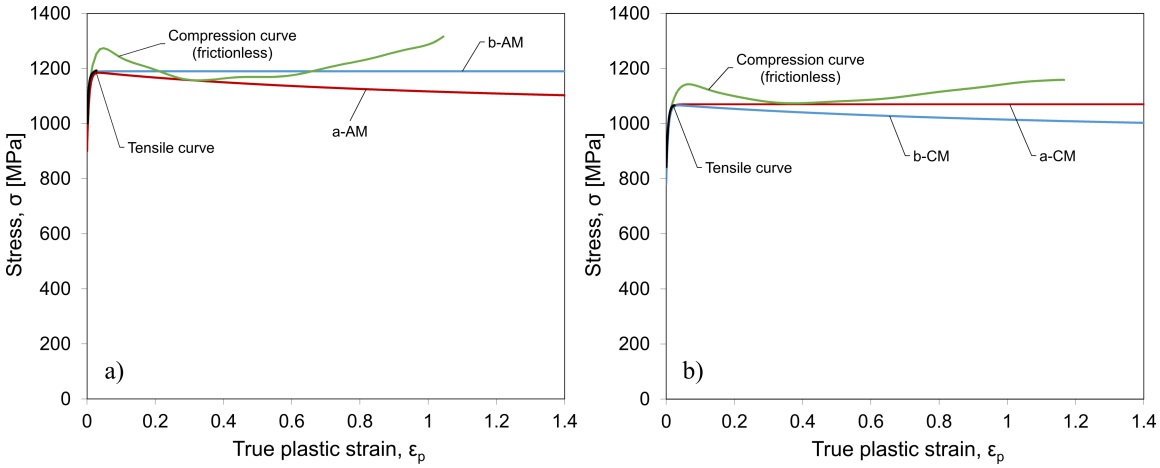


Figure 6.7: Distinct flow stress curves used to simulate the multiaxial specimen for both AM (a) and CM (b) metallurgical conditions.

Table 6.2: Swift-Voce equation parameters for hardening curves "a" and "b" for each material metallurgical condition.

Curve	K [MPa]	ε_0	n	k_0 [MPa]	Q [MPa]	β_v	α
a-AM	950	1	-0.7	887.5	362.5	170	0.2
a-CM	950	1	0	887.5	362.5	170	0.2
b-AM	950	1	0	737.5	362.5	170	0.2
b-CM	950	1	-0.5	737.5	362.5	170	0.2

and "b-CM" correspond to perfect plasticity and a negative hardening rule, respectively. The third curve corresponds to the flow stress identified by means of compression testing, free from friction contribution. Due to allowing for an initial hardening and its saturation (or even softening) the combined Swift-Voce model (refer to eq.2.40) has been used to build the mentioned curves ("a" and "b") and their parameters are shown in table 6.2.

The load-displacement results obtained from the simulation of the multiaxial specimens are shown in figure 6.8 for each metallurgical condition and inputted flow stress. It is important to note that a damage model was not included at this stage, given the initial focus was on the assessment of plastic behaviour. Interestingly, the specimen with a pressure angle of 60° presents higher sensitivity to the hardening curve, most probably due to the more heterogeneous strain field. Also convenient to note is the fact that for very high displacement values, softening of the numerical predictions is noticed for the CM MA90 specimen (figure 6.8d). Such effect is due to high mesh distortion. When it comes to the comparison of numerical and experimental results, and focusing solely on small displacement values (d<0.5mm), it is observed that the flow stress obtained from compression testing (green curve) slightly overestimates the experimental loads for all metallurgical conditions and specimen pressure angles. On the other hand, the hybrid approach (curve "a") results in a accurate prediction of incipient load results, demonstrating, as previously mentioned, an higher

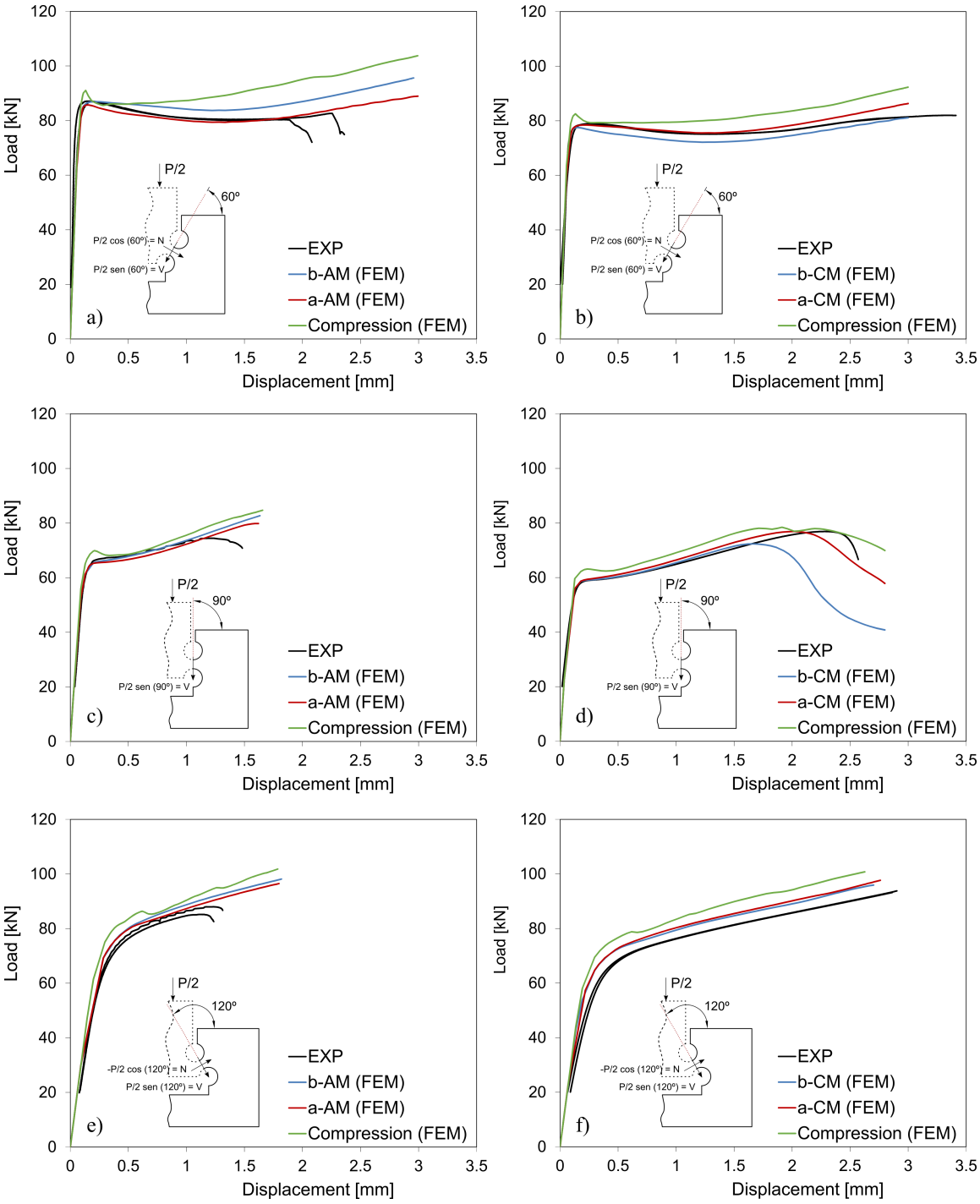
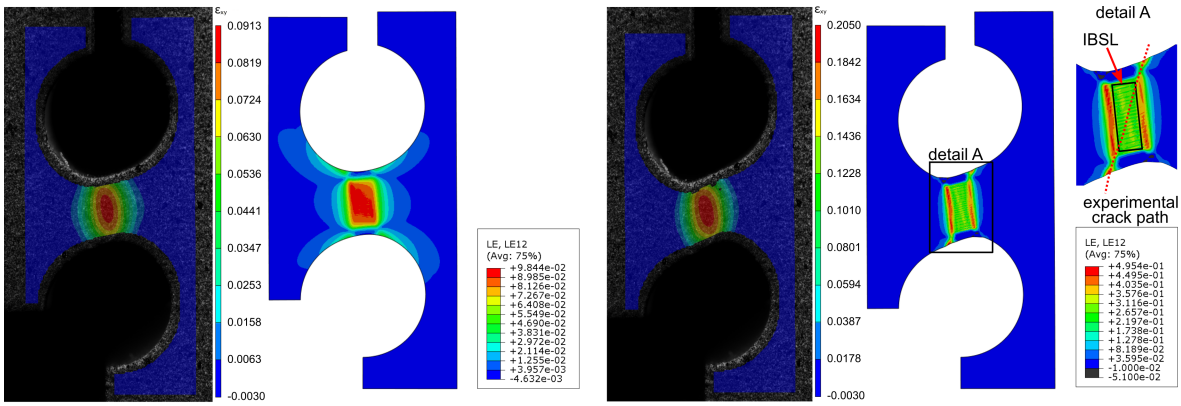


Figure 6.8: Load-displacement results obtained from the simulation of the multiaxial fracture specimen without damage consideration: MA60 AM (a) and CM (b); MA90 AM (c) and CM (d); MA120 AM (e) and CM (f).



a) b)

Figure 6.9: Comparison between DIC (left) and FEM (right) shear strain fields at an (a) incipient stage, d=0.2mm, and at an (b) intermediate stage of the test (d=0.5mm).

reliability of the tensile curve for small strain values.

Despite the well known higher accuracy of compression tests towards the identification of stress-strain behaviour for high strains, it is noticed that a positive strain-hardening does not seem to represent the materials' flow stress, as it presents the biggest deviation from the experimental results. This is observed in all specimens and highly evidenced in figures 6.8a and 6.8b. A possible explanation is that the occurrence of an early diffuse necking behaviour (as mentioned in section 5.2.3) allied to an high ductility of the material may promote a neutral or even negative effective strain-hardening. Shamsdini et al. (2021) have studied the plastic deformation of additively manufactured maraging steels, stating that strain induced phase transformation under uniaxial tensile loading can also promote strain-hardening variation. The authors claim that within the progress of martensitic transformation there is a tendency for strain-hardening to reach null values, which after load peak are negative, due to geometric softening. Such theory is coherent with the fact that non-positive strain-hardening curves, such as "a" and "b", seem to more appropriately represent the materials flow stress. In fact, the presented hybrid definition of flow stress (curves a-AM and a-CM) results in a maximum deviation of 5% in load prediction, which is why that have been selected to depict the materials' flow stress.

The materials' high strength, ductility and tendency towards geometric softening (out of plane movement) hindered data retrieval from digital image correlation. Figure 6.9 shows the shear strain fields comparison (between DIC and FEM) of the AM multiaxial specimen with a pressure angle of 90°. In figure 6.9a, which reflects an incipient stage of the test (d=0.2mm), one can observe a satisfactory correlation not only in the shear strain values but also its localization in the centre of the specimens' ligament. For a more advanced stage (d=0.5mm), a highly heterogeneous shear strain field is developed in the numerical model, as seen in the FEM model of figure 6.9b. Maximum shear strain seems to localize in two vertical bands. Moreover, the specific location where strain

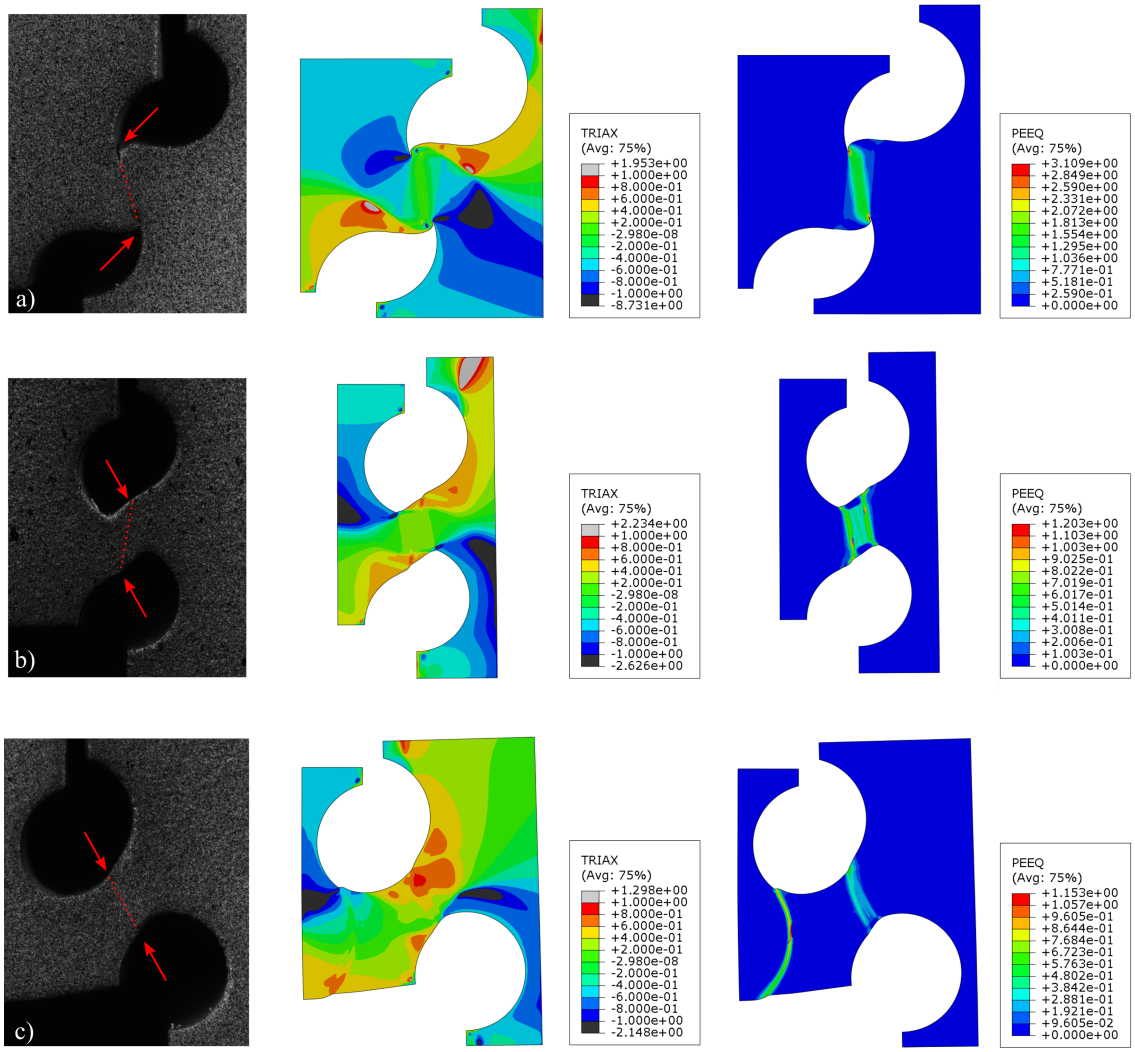


Figure 6.10: Deformed shape comparison of DIC and FEM results and plotted stress triaxiality and equivalent plastic strain of multiaxial specimen with (a) 60°, (b) 90° and (c) 120° pressure angles.

is maximum at the contour of the holes seems to realistically portray the crack path, as shown by the red dashed line in "detail A" of figure 6.9b. Despite the inability of DIC to capture the highly heterogeneous strain field, results show that the DIC predicted values in the centre region of the ligament is somewhat consistent with the average FEM values of the region in between the strain localization (average ε_{xy}=0.278), signalled as "IBSL" in solid black rectangle line of the detail of figure 6.9b. Also, important to highlight is that the experimental deformed shapes of the specimens (obtained by DIC) were coherent with the one obtained by FEM (refer to figure 6.10), allowing for further validation of the built numerical models and determined constitutive flow rule.

Towards the determination of the damage behaviour, the displacement at the onset of damage, d_f has been determined for AM each specimen, through the comparison between experimental and FEM curves (without considering a damage model). It is important to highlight that such

procedure was only possible to conduct for the additively manufactured samples, given that the conventional multiaxial fracture specimens did not fracture, with the exception of one specimen. The fracture displacement was defined as the displacement at which the FEM plastic prediction and the experimental curve diverge. That enabled the determination of the stress triaxiality, η and the equivalent plastic strain, ε_p^{eq}, field distributions at damage initiation, which are shown in figure 6.10. On the same figure, the crack path is signalled (red dashed straight lines) on the experimental deformed geometries, according to the actual crack location and configuration, as shown in figure 5.28. Experimental crack location is in accordance with the maximum ε_p^{ep} at the hole contour surfaces. Such has promoted the propagation of the crack from the surface to the centre of the ligament. Moreover, regarding stress triaxiality, crack seems to occur for maximum positive η in the specimens with 90° (b) and 120° (c) pressure angles. However, due to the prevailing compression/shear loading it occurs for maximum negative η, in the specimen with a 60° pressure angle, enabling fracture locus determination for distinct stress states. Figures 6.11a, 6.11b and 6.11c

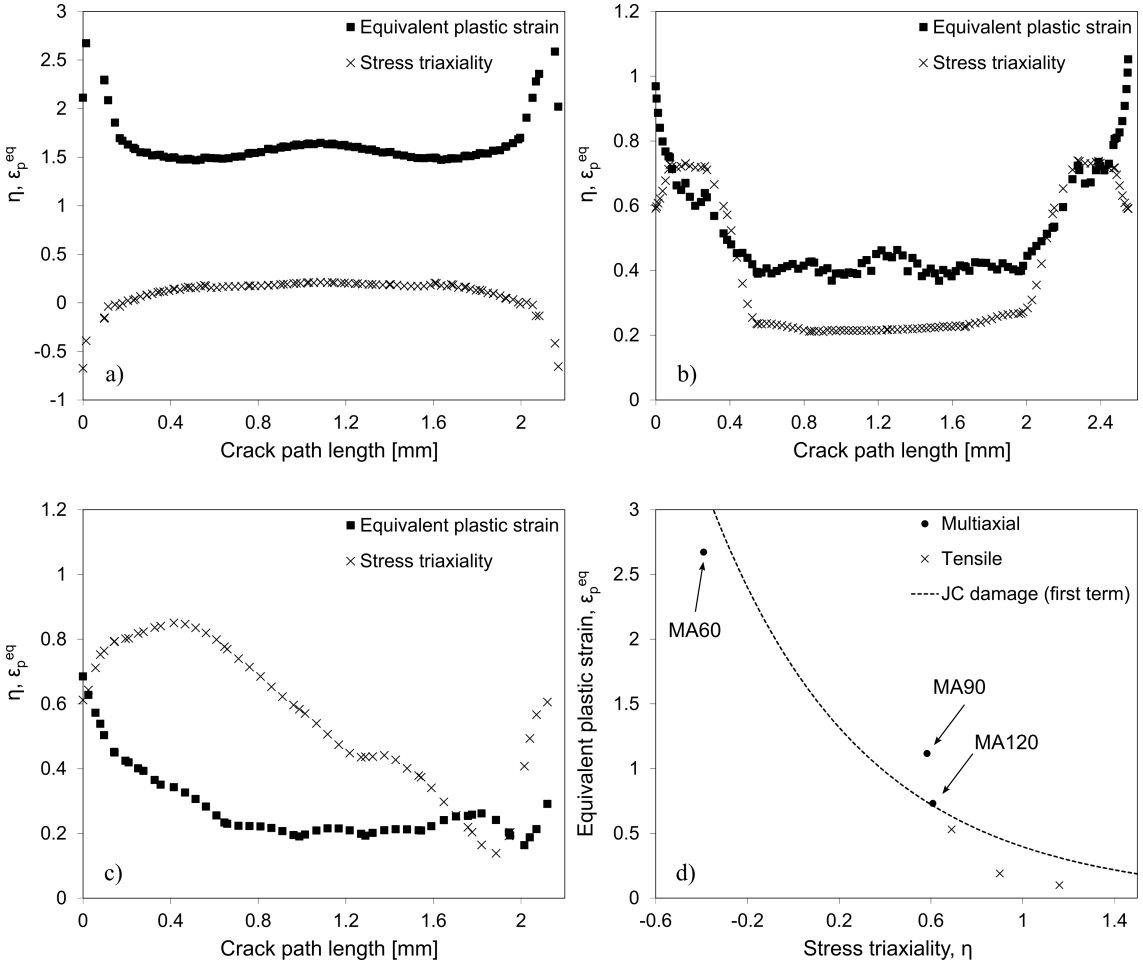


Figure 6.11: Stress triaxiality and equivalent plastic strain evolution along crack path for multiaxial specimens with (a) 60°, (b) 90° and (c) 120° pressure angles; identified damage law (d) using both multiaxial and tensile specimens.

Table 6.3: Fracture strain and stress triaxialities estimations.

Specimens	d_f [mm]	Load [kN]	ε_f	η_f
MA60 (AM)	2.11	82.7	2.67	-0.39
MA90 (AM)	1.03	73.6	1.12	0.58
MA120 (AM)	1.19	87.3	0.73	0.61

show the η and ε_p^{eq} evolution along the that crack path at the onset of damage for specimens with 60°, 90° and 120° pressure angles, respectively. Despite allowing for a relatively easy change on the state-of-stress with a simple modification of notch configuration, the considered multiaxial specimen geometry seems to result in a rather heterogeneous strain field, which makes damage calibration challenging. This has been shown previously in the "detail A" of figure 6.9 and is now confirmed by the significant evolution of η and ε_p^{eq} along the crack path. Knowing that crack propagation occurred from the surface to the centre of the ligament, fracture strain, ε_f and stress triaxiality at fracture, η_f, were obtained for crack lengths near zero and were plotted in figure 6.11d, which in addition to the ε_f obtained from tensile specimens, presents the materials' fracture locus. The stress triaxiality and fracture strain values for the multiaxial specimens are shown in table 6.3. Although it was expected that the multiaxial specimens would allow for fracture locus identification for intermediate pressures, the high ductility allied to the geometrical softening of the current material seemed to delay fracture up to a point where the specimen geometry no longer corresponds to the theorized state-of-stress. Still, the results obtained from multiaxial specimens show compatibility with the ones obtained from tensile testing, as higher relative stress triaxialities were expected for the latter. The reduced JC damage law (eq. 2.55) was fitted to the identified exponential decrease in fracture strain, ε_f, for increasing η. With regards to material damage evolution, element degradation was defined through fracture energy dissipation, as previously presented in eq. 2.58. Fracture energy has

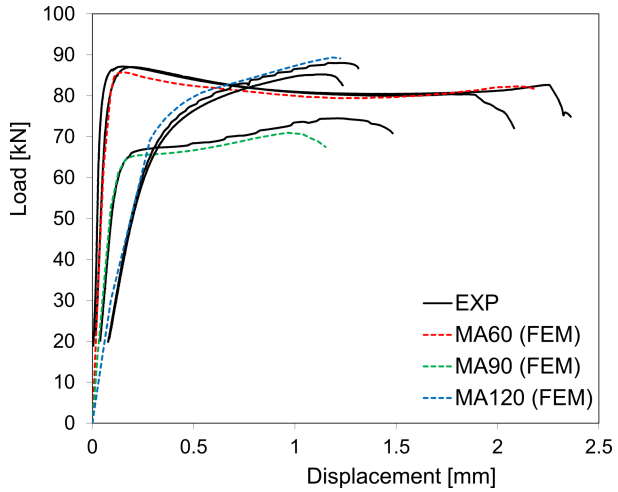


Figure 6.12: Comparison between experimental curves and numerical simulation of the multiaxial specimens (maraging AM) within distinct pressure angles.

been inversely estimated for the AM maraging steel, through the comparison between experimental and numerical results. A fracture energy density of G_f=10 mJ/mm^3 is proposed.

The load-displacement curves of figure 6.12 present the comparison between the experimental multiaxial tests and the constitutive modelling (plasticity and damage) for the AM maraging steel. Taking into account the significantly distinct load levels and fracture strains, a reasonably good agreement seems to be found with the suggested approach and results.

In sum, the slight differences in the flow stresses obtained by typical characterization tests (compression and tension) motivated the usage of a hybrid approach. This hybrid approach means the usage of flow stress data from tensile tests for incipient deformation, whereas from compression tests for larger deformation. The numerical simulation of the multiaxial fracture specimens was highly important for the validation of this hybrid approach (curves "a"), since a close match between the numerical and experimental deformed shapes and load-displacement curves was attained. That approach has, therefore, been selected for flow stress representation of the maraging steels. The satisfactory load-displacement failure prediction of the additively manufactured multiaxial specimens, enabled the identification of a damage law for that metallurgical condition. The much higher relative ductility and quasi-stable necking seem to have delayed fracture in the conventional specimens. Due to the lack of data for this metallurgical condition (CM), an identical damage evolution to the AM was adopted, however shifted (offset) towards a match with the corresponding tensile specimens data. For that, the d_1 parameter of the JC damage equation (refer to eq.2.55) was modified. Figure 6.13 shows the damage behaviour law of both AM and CM maraging steels, describing the used approach.

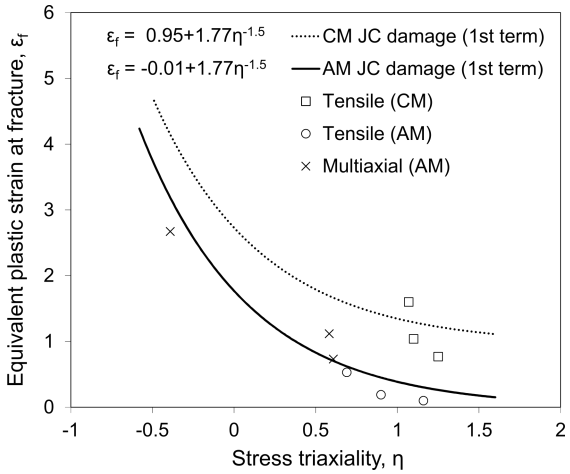


Figure 6.13: Suggested JC damage parameters for the AM and CM maraging steels modelling of fracture.

6.4. Viscous effect modelling

Numerically modelling of manufacturing processes is believed to be essential towards their analysis, improvement and optimization, even though it commonly poses a very demanding task, due to the associated multiphysics nature. In metal cutting, the exceptionally high strain and strain rate conditions impose an increased challenge, since knowing the material's plastic response under such extreme loading conditions usually means very difficult characterization procedures. The same problem extends to damage and friction definition, given that they are, as well, influenced by strain and strain rate. The current section aims at identifying a plastic model based on the experimental characterization tests for metal cutting simulation. As reviewed from literature, typical plasticity models used in metal cutting simulation, include the effect of strain hardening, viscoplasticity and temperature. As denoted through the multiaxial specimens simulation (section 6.3), the strain hardening of the maraging steel appears to be highly sensitive to geometrical softening (necking) which in this material seems to occur in a quasi-stable manner, up to final plastic instability and damage. Such effect is not accounted in compression due to the fact that for negative stress triaxialities void growth and nucleation is negligible. For that reason, the hardening behaviour identified in the multiaxial specimens simulation is believed to closely represent the materials behaviour in cutting conditions.

With regards to the viscoplastic behaviour of the maraging steel, the C parameter of the second term of Johnson Cook plasticity equation (eq. 6.4) was calibrated based on the compression tests, which were conducted for increasing levels of strain rate. It is important to note that, given the purpose on strain rate influence assessment, the compression curves were truncated up to a strain of 0.06. This was performed in an attempt of neglecting the complex metallurgical phenomena related to deformation-induced phase transformations that seem to be occurring for certain speed and temperature conditions on the compression behaviour of both AM and CM maraging steels, which may not be representative of metal cutting. The first step towards the identification of C parameter is the definition of the hardening curve that matches the compression tests. That was performed through the linearisation of the first term of JC equation, as shown in equation 6.4, which describes the materials response in quasi-static and room temperature conditions. Parameter A corresponds to the materials' yield strength. The slope of the linear regressions shown in figures 6.14 allows for the identification of n parameter, while B can be obtained by the interception in the yy axis.

$$\begin{aligned} \sigma &= A + B\varepsilon_p^n \\ ln(\sigma - A) &= lnB + nln\varepsilon_p \end{aligned} \tag{6.1}$$

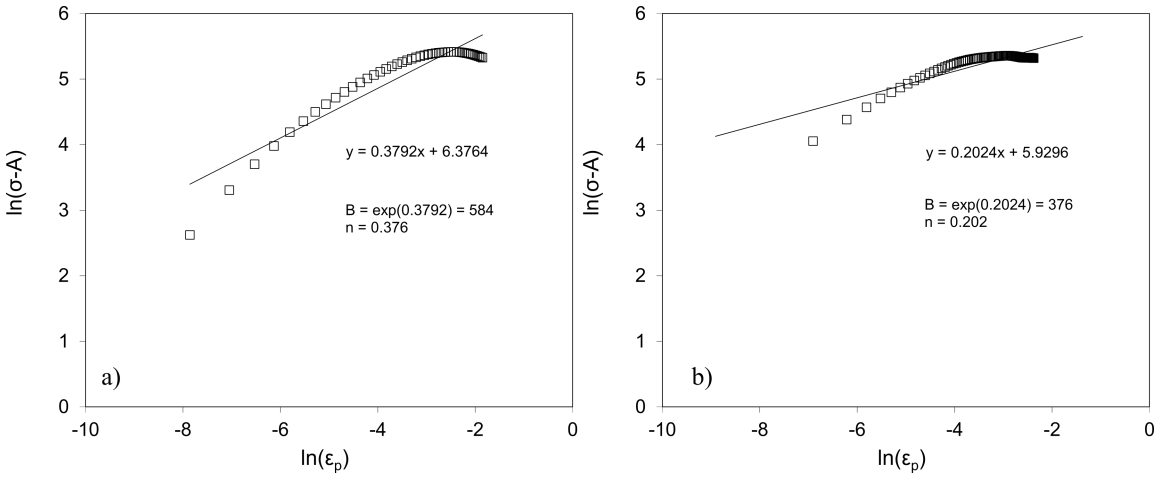


Figure 6.14: Identification of B and n parameters of the JC equation for the AM (a) and CM (b) maraging steels.

With regards to C parameter a similar approach was performed, including the second JC term of the equation, as shown in the manipulation of equation 6.2. The slope of the fitted linear regression in figure 6.15 enables the identification of the viscoplastic parameter C. As previously noticed in the analysis of compression test results, a higher strain rate influence is noticed on the additively manufactured maraging steel, which translates into a relatively higher C parameter. The fitted C parameter results are shown in figure 6.16 applied to the hardening obtained from compression tests. A reference strain rate, $\dot{\varepsilon_0}$, of 70 was employed in order to improve the popular poor predictability of JC material model in very high strain rates (Sima and Özel, 2010).

$$\begin{aligned} \sigma &= (A + B\varepsilon_p^n)\left[1 + Cln\frac{\dot{\varepsilon}}{\dot{\varepsilon_0}}\right] \\ \frac{\sigma}{(A + B\varepsilon_p^n)} &- 1 = Cln\frac{\dot{\varepsilon}}{\dot{\varepsilon_0}} \end{aligned} \tag{6.2}$$

Despite the some deviation (in very low strains) of the proposed high strain rate flow curves with the experimental, a global satisfactory approximation is achieved, employing a widely used model in literature for several materials. Moreover the slight mismatch (of experimental and modelled curves) may be connected with the challenging task that is the characterization in such extreme conditions. The suggested viscous term is coupled to the previously identified flow stress model (in section 6.3), enabling the cutting simulation.

Despite the very challenging characterization, it is well known that fracture onset is sensitive to strain rate. In this study, that effect has been inversely identified, based on literature values on the same material. High strain rate tensile tests (Fu et al., 2020b) and Charpy tests (Madhusudhan et al., 2018) are usually applied towards the identification of stain rate influence on fracture strain,

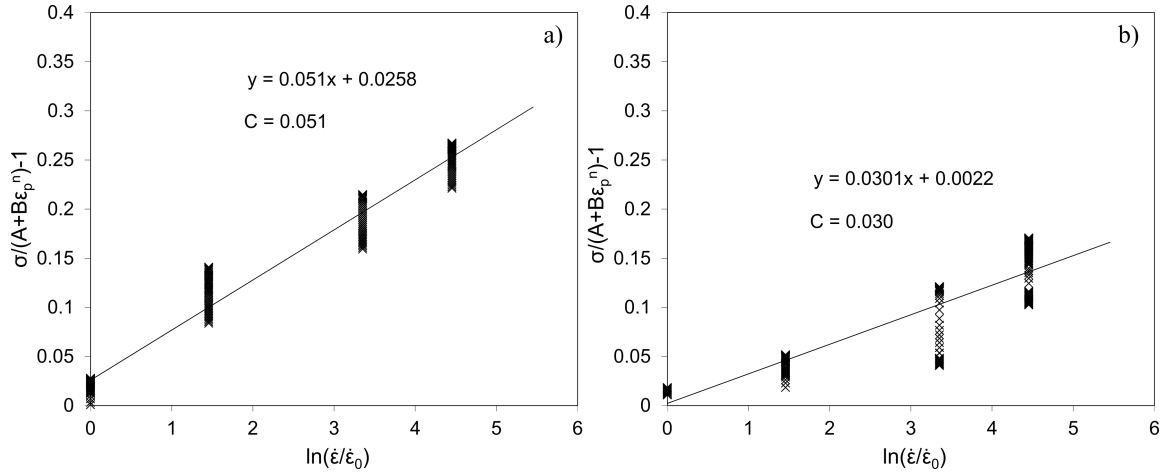


Figure 6.15: Identification of C parameters of JC equation for the AM (a) and CM (b) maraging steels.

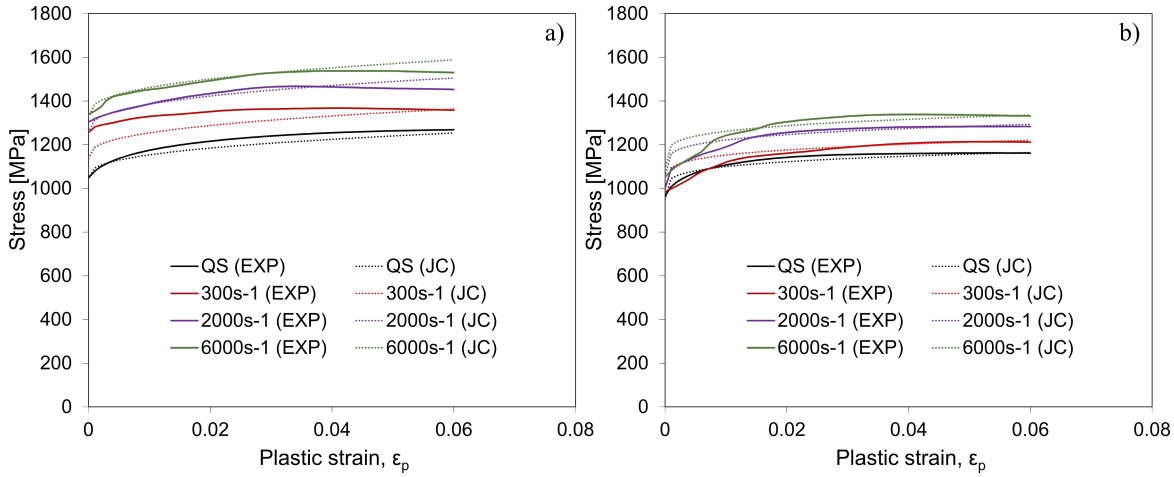


Figure 6.16: Viscoplastic flow stress curves, using the identified C parameter on the compression-based hardening curves of AM (a) and CM (b) maraging steels.

which is typically modelled through the d_4 parameter in the second term of damage JC equation (refer to eq. 2.55). An average value was considered (d_4=0.03) taking into account the range of literature estimation (0.014>d_4>0.05), for a reference strain rate, $\dot{\varepsilon_0}$, of 0.01.

Chapter 7. Metal cutting simulation

The current chapter focuses on the simulation of the cutting process of the AM 18Ni300 maraging steel. Firstly, as a validation of the built numerical model, the orthogonal cutting process is simulated using two distinct chip separation techniques. Chip morphology, shear angle, chip compression ration and specific cutting pressure were assessed, allowing for a benchmark of the two distinct chip separation approaches. The same material model was used in the simulation of an industrial machining operation, namely longitudinal turning, using a tool with chip-breaking geometry. A selection of the same experimentally used cutting parameters of section 5.3.2 was employed, enabling the validation of both numerical and material models in distinct operative conditions.

7.1. Orthogonal cutting simulation

The simulation of the orthogonal cutting problem can be seen as a way to validate the found material plasticity and damage laws in (relatively) closer conditions to industrial machining operations. With the plastic, fracture and friction behaviour fully depicted within the previous chapters, the current section focuses on the description of the built numerical orthogonal cutting model and the assessment of the suggested material models under varied (experimentally tested) cutting conditions. In the current study, a two-dimensional orthogonal cutting model was built in Abaqus CAE using a coupled temperature-displacement (explicit) formulation with a Lagrangian approach. Figure 7.1 illustrates the built numerical model. In order to minimize the high element distortion and eventual non-convergence, distinct aspects ratios were imposed to elements at the uncut chip thickness. Attributing a "pre-deformed" shape to the elements through its diagonal positioning allows for easier convergence of the model. A distinct mesh distribution was also defined, meaning a finer mesh at the uncut chip thickness with decreasing mesh density towards the bottom of the workpiece. Haddag et al. (2010) have focused on studying the impact of finite element formulation and mesh density in orthogonal cutting chip morphology simulation. The authors state that, despite not significantly affecting cutting force, a finer mesh contributes to an improved realistic depiction of chip morphology (at the cost of computing time). In addition, a gradual engagement of the tool was imposed with a chamfered geometry (45°) on the workpiece. Identical tool geometry to the experimental tests was employed in the numerical model, meaning that two rake angles (α_r=5° and α_r=12°) were

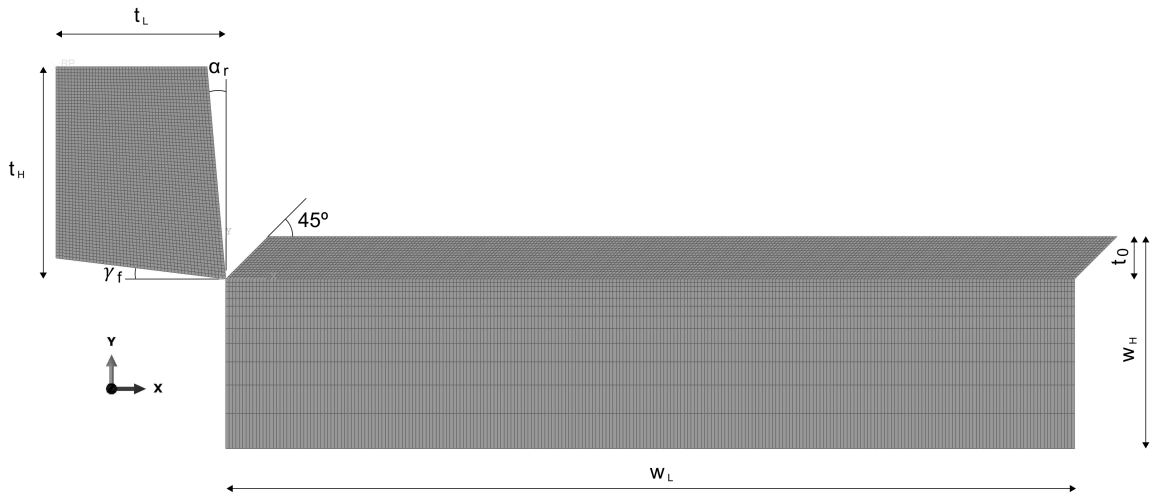


Figure 7.1: Workpiece geometry and parametrized dimensions.

Table 7.1: Parametrized workpiece, tool and mesh dimensions.

	t_H	t_L	w_H	w_L	element size
Dimension	$5t_0$	$4t_0$	$5t_0$	$20t_0$	$0.08t_0$

simulated with a fixed relief angle (γ_f=7°). Workpiece, tool and mesh sizes were scaled accordingly to the uncut chip thickness value. Parametrized dimensions are shown it table 7.1 in accordance with the nomenclature of figure 7.1. A theoretically sharp tool was considered in all tool-workpiece geometrical configurations. Four-node plane strain elements with reduced integration and enhanced hourglass control (CPE4RT) were employed. Tool was considered rigid whilst the workpiece was considered elasto-plastic. The corresponding identified material models were applied. All material properties are summarized in table 7.2. When it comes to boundary conditions, displacement and rotation of the nodes at the base of the workpiece were null (encastre). On the tool, note rotation was null for all degrees of freedom. Identically, displacement was also set to zero in yy direction and experimental cutting speed was imposed in the xx direction.

It is important to note that the identified plastic model was not calibrated in function of temperature. In fact, it is assumed that plasticity-generated heat is already accounted in the flow stress obtained by compression tests, meaning that thermal softening and visco-hardening are regarded as a coupled effect. Also important to highlight, is that most of the generated heat in the primary deformation zone flows to the chip (Shaw, 2005), meaning that at the workpiece and primary cutting zone, temperatures are not high enough to significantly influence material properties (Astakhov, 2006). In order to be able to visualize the temperature fields, it was numerically specified that a fraction of plastic work is converted into heat. Despite the far from understood (Zubelewicz, 2019), it is generally acknowledged that the fraction is approximately 0.9, which has been used in the built numerical model. Still regarding the plasticity model, an isotropic approach was adopted due to

Table 7.2: Material properties of AM 18Ni300 used in the built numerical model of orthogonal cutting.

Material properties	
Young's modulus [GPa]	E=190
Plastic model [MPa]	$\sigma = \Big[0.2\big[950(1+\varepsilon_p)^{-0.7}\big] + (1-0.2)\big[887.5 - 362.5(1-e^{-170\varepsilon_p})\big]\Big] \Big[1 + 0.05ln\frac{\dot{\varepsilon}}{\dot{\varepsilon_0}}\Big]$
Damage model	$\varepsilon_f = \big[-0.01 + 1.77\eta^{-1.5}\big]\big[1 + 0.03ln\frac{\dot{\varepsilon}}{\dot{\varepsilon_0}}\big]$
Fracture energy [mJ/mm^3]	$G_f = 10$
Friction	μ=0.3 (Coulomb)
Density [kg/m^3]	ρ=8.0
Conductivity [W m^{-1} C^{-1}]	λ = 0.0206T+15.4
Specific heat[J/kg^{-1} °C^{-1}]	c_p=0.374T+437.3
T. Expansion [C^{-1}]	α_{inst}=1.12E-3T-4.03E-3

the very little influence of build direction of the metal cutting behaviour of the maraging steel. In fact, as previously noticed, the influence of tool geometry revealed to be more significant. Relying on the assumption that adhesion is the prevailing friction mechanism, the identified friction values have been incorporated in the orthogonal cutting model through Coulomb's law, motivated by its simplicity and considering the general disagreement of friction modelling in the metal cutting scenario.

Chip separation has been applied through element deletion. When reaching the fracture strain that is determined by the damage model, elements are disregarded from the mesh. Moreover, their degradation was modelled using equation 2.58, taking into consideration energy consumption towards fracture occurrence. Failed elements are deleted from the mesh once the overall damage variable (D) reaches the value of 1. Despite mass loss, this method seemed the most appropriate for the assessment of the identified damage law. In order to promote computational efficiency, the mass of the entire model has been scaled. When used appropriately, this method can significantly

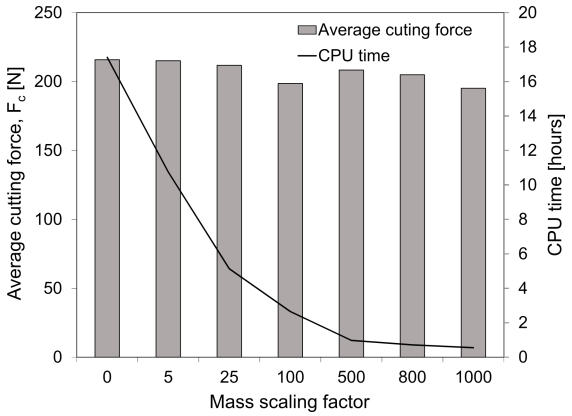


Figure 7.2: Mass scaling influence on average cutting load and CPU time on the orthogonal cutting model (t_0=0.1mm; L_c=0.5mm).

decrease simulation time without jeopardizing the degree of accuracy (Smith, 2009). Several mass scaling factors have been tested on the orthogonal cutting numerical model, for a cutting length, L_c of 0.5 mm. Figure 7.2 shows a small influence (<6%) of that parameter on the average cutting force. Thus, a value of 10^3 was used in the orthogonal cutting simulation. It is important to note that the considered interval for average calculation of the cutting force, F_c corresponds to steady state chip flow.

Figures 7.4 and 7.5 show chip formation and its evolution at four distinct cutting lengths for an uncut chip thickness of 0.1 mm and tool rake angles of 5° and 12°, respectively. Stress distribution (von Mises) is plotted which shows, as expected, maximum values at the primary deformation zone. Stress concentration is also developed at the secondary deformation zone, due to friction effect, which is coherent with analytical modelling literature. Moreover, with regards to the predicted strain rate, there seems to be coherence with literature, given its localization at the shear plane and ranging values of 10^4, as depicted in figure 7.3.

The simulated chip morphology is identical within same tool models, regardless of uncut chip thickness, for the (small) tested cutting lengths (L_c). Still, chip curvature radius shows some coherence with the experimental, for incipient (steady-state) cutting length. After a certain cutting length, the chip seems to contact the workpiece, shifting its curvature, which has not been the focus of the current models. Also noteworthy, is the slightly less pronounced chip curvature of figure 7.5d (α_r=12°) when compared to the one of figure 7.4d (α_r=5°), showing the same experimental trend. The accumulation of near-deleted elements is noticed in the obtained results, especially at the tool-chip interface. The reason for such element detachment is related to the adopted chip separation modelling methodology (the damage model is applied to the whole workpiece). Such effect is not noticed in orthogonal cutting models with a sacrificial layer, given that elements can only fail in the predicted line of chip separation. However, the arbitrary confinement of damage (which is known to be a critical aspect in FEM) to a sacrificial layer may misrepresent stress and strain fields distribution and result in poor predicting accuracy. Moreover, the application of a damage model that is global, allows for more appropriate fracture energy balance, given that other elements in the

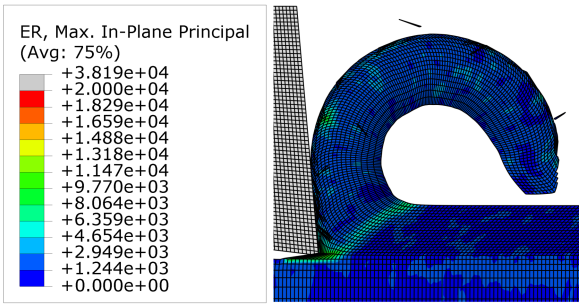


Figure 7.3: Strain rate field on the orthogonal cutting model for a t_0=0.1.

model (especially at the secondary deformation zone) may fail or be close to failing (D= almost 1). Remarkably, the images of tool rake face after successive orthogonal cutting tests (performed to evaluate tool robustness, refer to figure 4.22) show that significant material degradation may occur as material separates from the chip and sticks to the tool, which is coherent with the observed numerical damaged material, to a certain extent. One possible approach to improve the portrayal of material degradation would be to perform additional experimental testing, leading the material to failure in negative triaxialities. The goal would be to identify the cut-off value of negative triaxiality for which fracture ceases to occur. Bao and Wierzbicki (2005) has found that for AISI1045 steel, this lower bound limit is η=-1/3. However, that value does not seem to match with the fracture behaviour of the maraging steel, as demonstrated by the multiaxial damage tests, particularly in the 60° pressure angle configuration. In addition, the implementation of two distinct fracture energies (corresponding to mode I and mode II, as seen in figure 2.13) might significantly enhance element degradation in the critical regions of tool-chip interface and primary deformation zone.

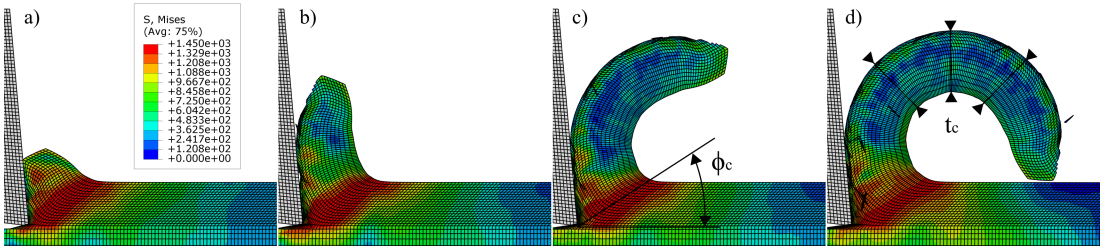


Figure 7.4: Orthogonal cutting chip formation and evolution for α_r=5°, t_0=0.1mm and cutting lengths of 0.15 (a), 0.4 (b), 0.8 (c) and 1.3 mm (d).

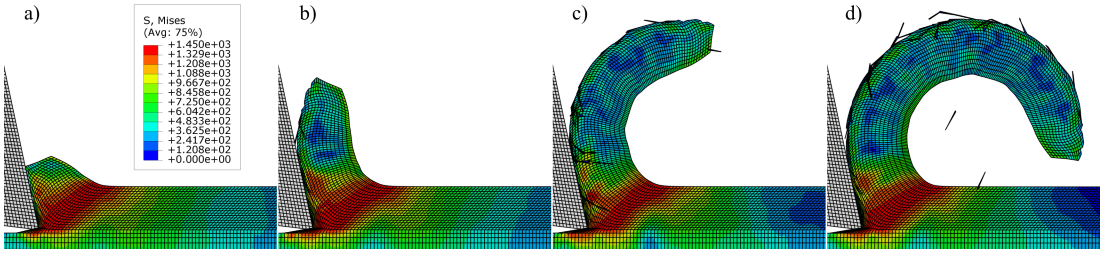


Figure 7.5: Orthogonal cutting chip formation and evolution for α_r=12°, t_0=0.1mm and cutting lengths of 0.15 (a), 0.4 (b), 0.8 (c) and 1.3 mm (d).

In order to be able to benchmark the developed model and the popular sacrificial layer model (Vaziri et al., 2011), the same amount of simulations were performed with damage confinement to a $0.03t_0$ thickness layer that is placed straight ahead of cutting tool edge. A mesh with two elements per thickness was defined for that sacrificial region, with the tool cutting edge aligned with the interception of those two elements. Moreover, the elements in that region were the only assigned with damage properties, in the model. Figures 7.6 and 7.7 show those results for a t_0 of 0.1 mm, for the two selected tool rake angles. A less pronounced chip curvature results from the application of a sacrificial element layer, meaning that when it comes to chip morphology, the application of the damage model to the whole workpiece may promote smaller chip thickness which result in more

pronounced curvature due to the smaller cross section submitted to chip bending. Nonetheless, the experimental trend of increasing chip curvature radius for increasing tool rake angle is correctly depicted by the sacrificial layer model, as derived from figures 7.6d and 7.7d.

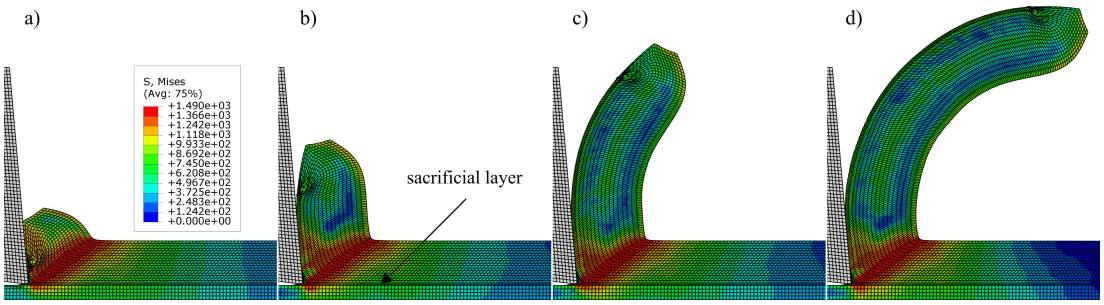


Figure 7.6: Orthogonal cutting chip formation and evolution (using sacrificial layer) for α_r=5°, t_0=0.1mm and cutting lengths of 0.15 (a), 0.4 (b), 0.8 (c) and 1.3 mm (d).

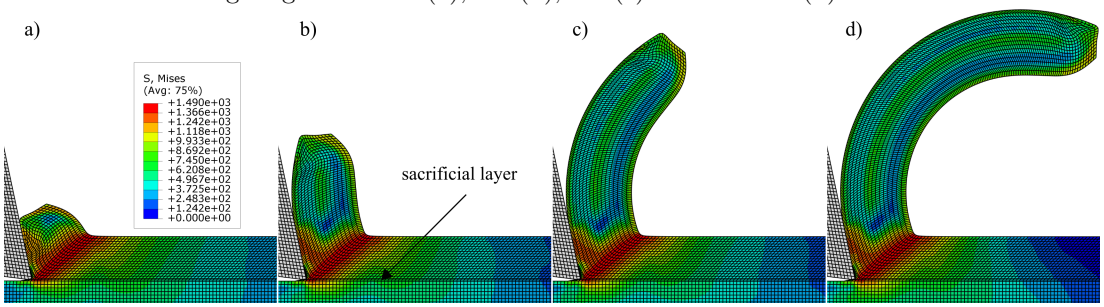


Figure 7.7: Orthogonal cutting chip formation and evolution (using sacrificial layer) for α_r=12°, t_0=0.1mm and cutting lengths of 0.15 (a), 0.4 (b), 0.8 (c) and 1.3 mm (d).

In order to compare the predicting performance of each model when it comes to shear angle and chip thickness, these values were measured for each conducted simulation as illustrated in figures 7.4c and 7.4d. The obtained results are compared within chip separation approaches and with equivalent experimental data in figure 7.8. With regards to chip compression ratio, r_c, (refer to figure 7.8a) it is highlighted that while none of the models is capable of its accurate prediction in the whole spectrum of tested uncut chip thicknesses. However, both numerical models seem to result in higher r_c when the 5° rake angle tool is employed, which is in accordance with the experimental results. In addition the physically-based orthogonal cutting model shows a similar r_c decreasing tendency with t_c increase. These results contrast with the ones obtained by the sacrificial layer model, which estimate a negligible variation (very slight increase) of chip compression ratio with t_0. When it comes to shear angle results (refer to figure 7.8b), it is found that the sacrificial layer method yields very constant results, regardless of r_c (and t_0). The method seems to accurately depict the average ϕ_c and r_c values. On the other hand, the physically-based chip separation method provides a precise estimation of the shear angle experimental trend, despite lacking accuracy. Also worth mentioning is the fact that continuous chip is simulated (unlike the experimentally observed lamellar/segmented), promoting very little variation of the shear angle with cutting length. Moreover, the constant friction conditions result in identical shear angle values, amongst the tested range of uncut chip thickness.

Such aspect is coherent with literature, since the majority of analytical models regarding shear angle prediction (refer to table 2.1) dependent simply on rake angle, α_r, and friction angle, β_f. The results emphasize the complexity in modelling of the metal cutting phenomenon, given that, concerning geometrical prediction of the chip and important orthogonal cutting parameters, both tested approaches present their advantages and disadvantages.

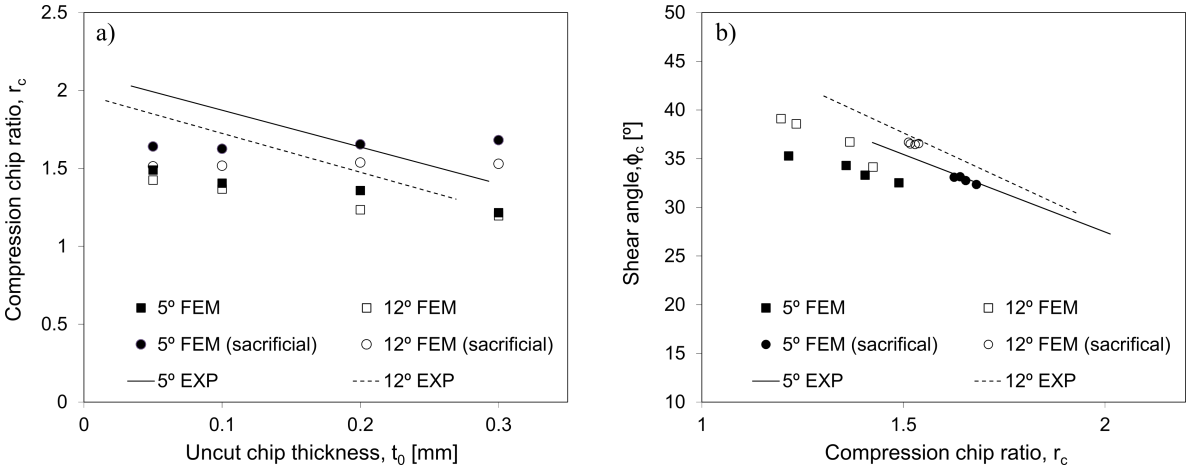


Figure 7.8: Comparison between experimental trends and numerical results of chip compression ratio, r_c (a) and shear angle, ϕ_c (b).

The study of cutting forces under the most varied machining conditions is a common approach towards cutting process improvement. It can be seen as a benchmarking parameter of cutting efficiency and cutting tool geometry suitability, especially in the development of novel geometries. Such data is typically obtained through extensive experimental testing. Numerical simulation can be highly advantageous in the virtual identification of characteristic cutting constants such as the specific cutting pressure, K_c, enabling extrapolation from the numerically validated trends and

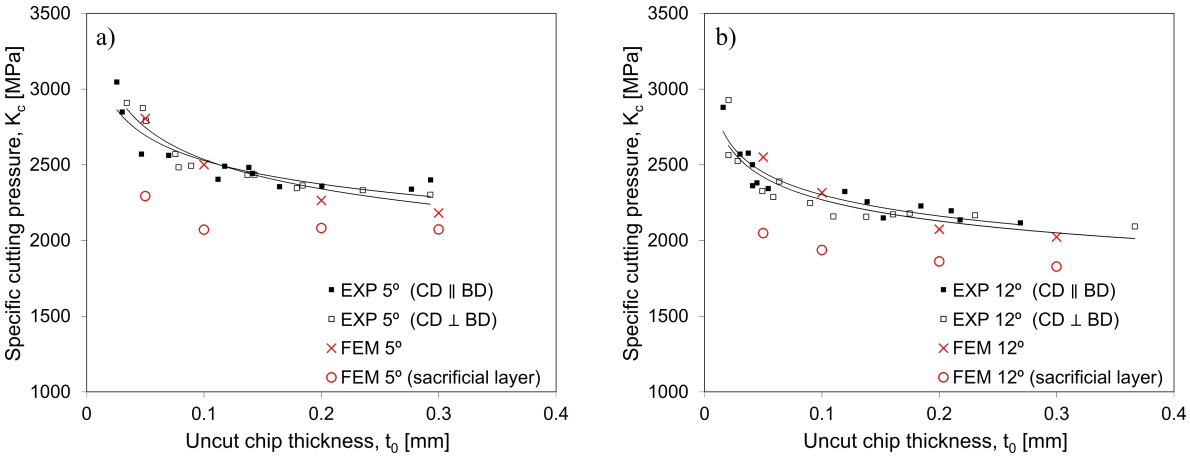


Figure 7.9: Comparison between experimental and numerical specific cutting pressure on the orthogonal cutting with a 5° (a) and 12° (b) rake angle, using the two described chip separation methods.

minimizing experimental machinability tests. Towards the assessment and validation of the built FEM models when it comes to load prediction, the experimental range of t_0 has been covered numerically for the comparison of specific cutting pressure. Figure 7.9 presents the numerical (using two distinct chip separation modelling techniques) and experimental K_c results for the additively manufactured maraging steel in function of the selected tool geometries. A significant discrepancy is noticed in the prediction of K_c depending on the chip separation criteria. Despite presenting a similar tendency to the experimental, the sacrificial layer criterion leads to an underestimation of K_c. The obtained results show that damage confinement to the predicted workpiece-chip parting line may be less representative of load scenario in the metal cutting phenomenon. Inversely, the satisfactory numerical estimation for a wide range of uncut chip thickness in two distinct tool geometries enables the validation of the identified material laws as well as the orthogonal cutting numerical model. An approximate maximum error of 4% from the experimental exponential trend has been calculated.

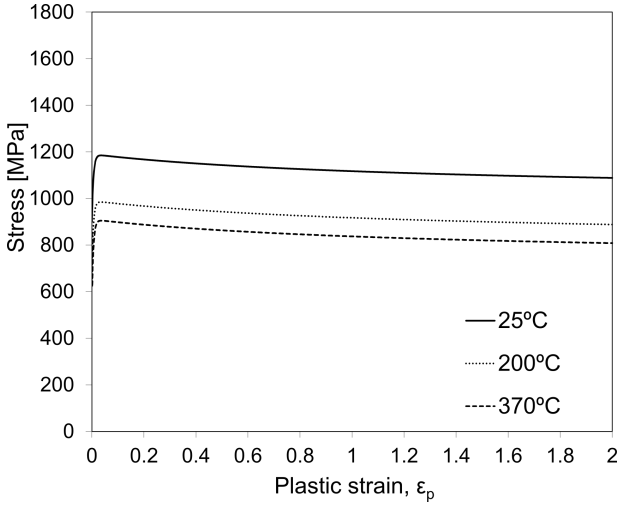


Figure 7.10: Temperature dependent flow curves used in the simulation of orthogonal cutting with thermal softening behaviour.

As a final remark regarding the simulation of chip morphology, it is relevant to mention that most plasticity models (and also some damage laws) found in literature are temperature sensitive. The thermal softening behaviour is typically modelled through expressions such as the third term of JC equation (eq. 2.42), which is often calibrated after isothermal characterization tests (usually compression tests). It is, however, important to note that the identification of visco-plastic behaviour also entails the raising temperature effects, meaning that in high speed compression tests the strain-hardening and thermal softening effect are coupled, due to adiabatic conditions. Thus, endowing the material behaviour with a thermal softening behaviour results in accounting twice for this effect. For a physically correct depiction of chip morphology, decoupling of these effects would have to be performed which further emphasize the complexity in capturing the chip formation phenomenon. Figure 7.11 illustrates lamellar/segmented chip prediction feasibility, in both

physical (figures 7.11a and 7.11c) and sacrificial (figures 7.11b and 7.11d) numerical approaches, with a temperature-sensitive material model. The thermal softening effect has been inversely identified based on the curves of figure 5.14a and coupled to the plastic model through the expression of the third term of JC equation, eq. 2.42, similarly to literature practice. The used temperature dependent flow curves are shown in figure 7.10. Both equivalent plastic strain (in figures 7.11a and7.11b) and temperature fields (in figures 7.11c and 7.11d) are plotted showing consistency with the expected strain and temperature values. The fact that the sacrificial layer model presents very (unrealistically) high strains and temperatures for highly deformed elements is associated with the absence of element deletion (apart from the ones at the sacrificial layer), meaning that those results should be neglected. Despite also being related to non-uniform microstructure and cutting vibration Klocke (2011), lamellar chip can also be assumed as a specific case of less severe adiabatic shear bands Toenshoff and Denkena (2013). The results of figure 7.11 show that the segmented/lamellar chip morphologies can be simulated from both damage (element deletion) and thermal softening (adiabatic shearing) perspectives.

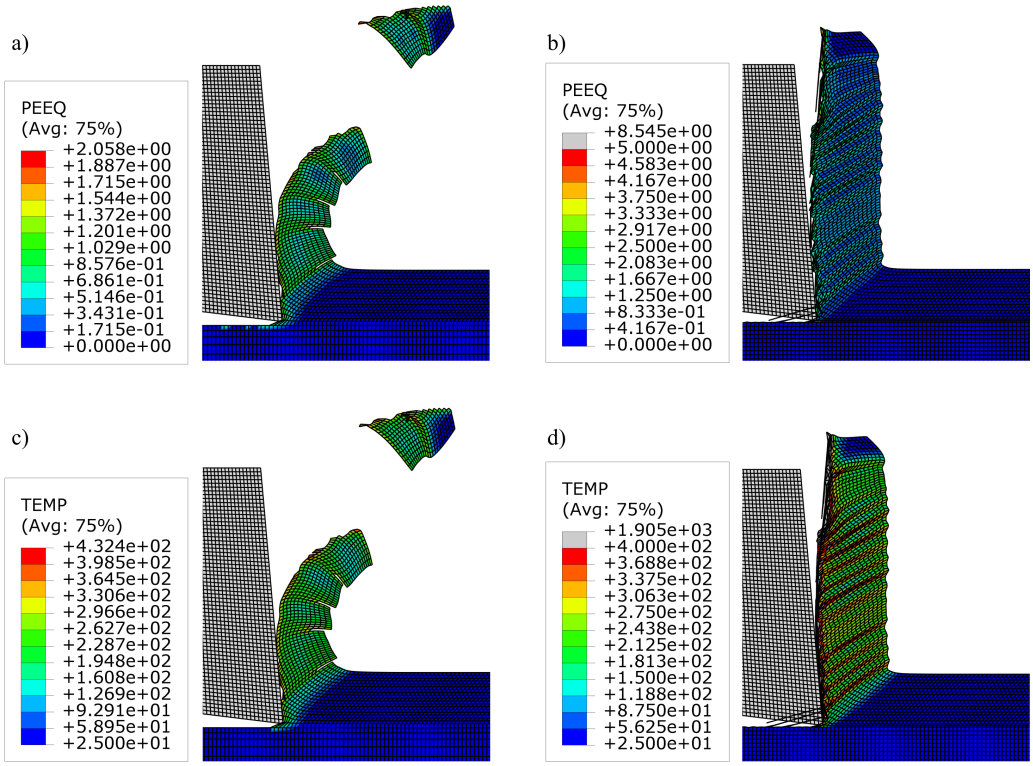


Figure 7.11: Equivalent plastic strain on the physical (a) and sacrificial (b) numerical approaches of the orthogonal cutting model; temperature field on the physical (a) and sacrificial (b) numerical approaches of the orthogonal cutting model.

7.2. Turning simulation

Despite providing valuable insight on metal cutting mechanics, material models validation and simplified kinematics, the orthogonal cutting operation does not accurately represent 3D industrial cutting processes with intricate tool geometries, such as the turning operation. In an attempt of bringing closer the industrial processes with the numerical simulation, longitudinal turning operations, described in section 5.3.2 (3D) were modelled in ABAQUS/Explicit. Figure 7.12b shows the tool and workpiece schematic configuration, illustrating the geometrical cutting parameters. It is important to note that, for kinematics simplification, and similarly to other models in literature (da Silva et al., 2017; Liu et al., 2019), the workpiece was defined as a rectangular extrusion with the contour of tool nose radius, focusing on a small portion (but steady-state representative) of the cutting process. The customized chip-breaking insert tool geometry (T-CB) was represented in the model through a rigid body. The workpiece was modelled with 8-node linear elements with reduced integration and hourglass control (C3D8R). In order to be able to apply two distinct structured mesh densities, the workpiece was divided in two regions, labelled as "core" and "envelope" of figure 7.12a. In order to ensure continuity between these two parts, a tie constraint was used, ensuring no relative motion between the nodes of each part. Chip separation is modelled through the application of the identified damage model to the whole workpiece. The usage of a sacrificial layer method as a chip separation criteria is more complex in 3D models (comparatively to 2D). With regards to the tool, a finer mesh density (unstructured) was defined around nose radius. In both tool and workpiece parts, finer meshes correspond to a 0.02 mm seed size, whilst 0.05 mm for coarser meshes. The workpiece base was encastred and degrees of freedom of the tool were null, except in z direction, allowing

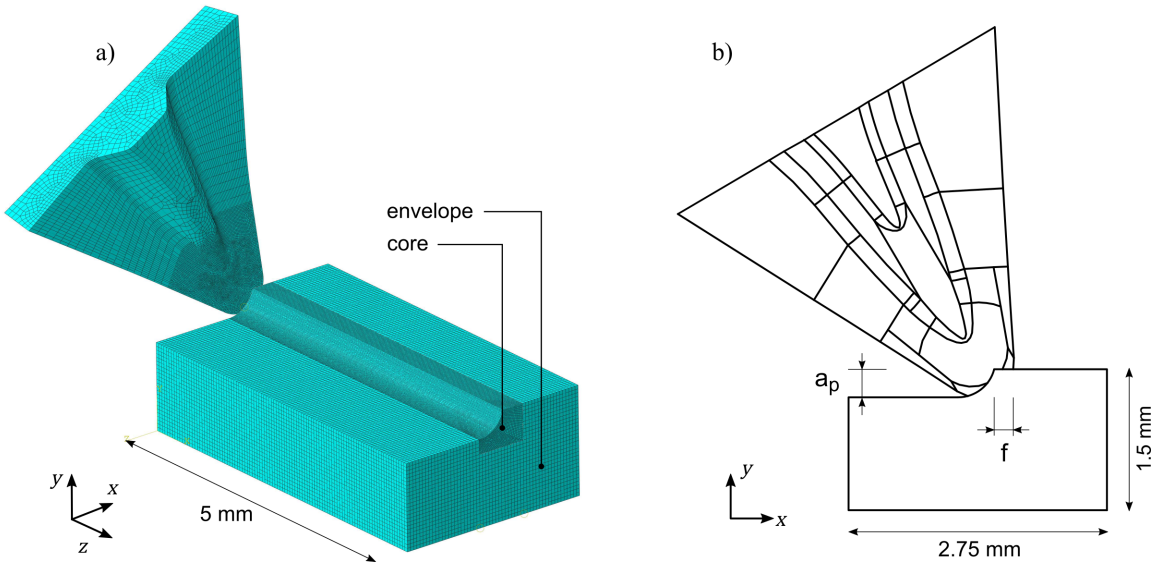


Figure 7.12: Schematic view of the longitudinal turning numerical model (a) and definition of geometrical cutting parameters (b).

for tool cutting speed definition which was the same as the maximum experimentally tested. With regards to material parameters, the same conditions as orthogonal cutting simulation were applied, which are fully described in table 7.2. However, due to the associated computational cost, an higher order of magnitude was selected in mass scaling definition (10000). Three distinct depths of cut a_p (0.5, 0.3 and 0.1 mm) were simulated for a fixed feed, $f = 0.2$ mm. The selection of such cutting parameters is related with the larger chip sections, comparatively to other experimentally tested configurations. The simulation of smaller chips is hindered by the very fine required meshes and associated computational cost. Figure 7.13 shows the final chip geometry for each simulated set of cutting parameters and a cutting length of 5 mm. A similar tendency to the experimental chip morphology shown in figure 5.47a is found. This means that for minimum depth of cut (a_p=0.1mm)

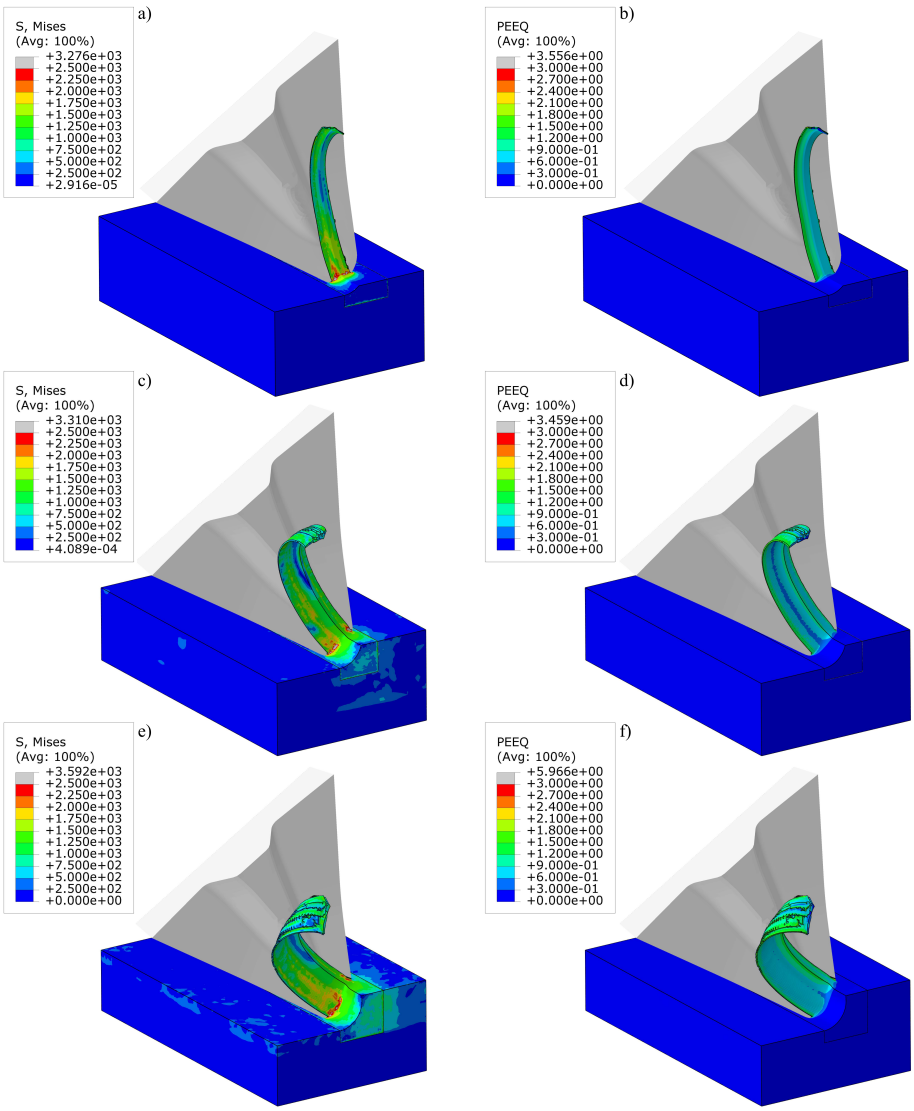


Figure 7.13: Chip geometry, von Mises stress (S) and equivalent plastic strain (PEEQ) for a_p=0.1 mm (a, b); for a_p=0.3 mm (c, d); for a_p=0.5 mm (e, f) and f=0.2 mm.

a ribbon-like chip morphology is developed, while for bigger chip sections curling seems to occur, promoting helical chip formation as the one being developed in the numerical model with a_p=0.5mm. With regards to principal cutting forces, the simulated results are compared with the experimental analogous conditions in figure 7.14a. A very satisfactory correlation between the experimental and numerical results is observed, showing the robustness of the identified material model towards cutting force prediction (in both 2D and 3D metal cutting scenarios). The good experimental-numerical correlation and successful simulation of the industrial turning process addresses the urgent need towards shifting from theoretical 2D models into more accurate and complex 3D simulations, stated by Rodríguez et al. (2020). It is, however important to highlight the significant computational cost of approximately 48 hours, using 10 multiple processors, for each simulation.

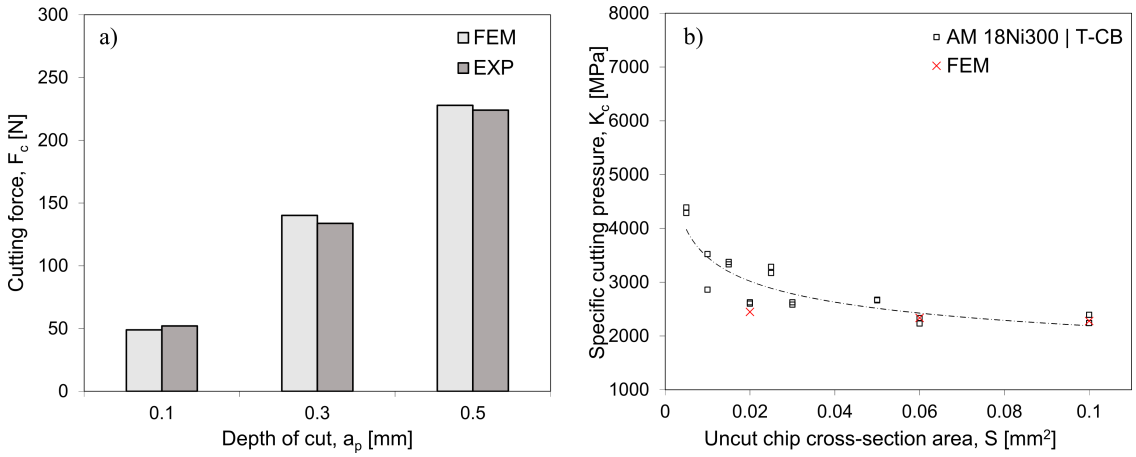


Figure 7.14: Comparison between experimental and numerical cutting force, F_c (a) and specific cutting pressure, K_c (b).

Chapter 8. Conclusions and future work

8.1. Conclusions

As one of the most recent trends of advanced manufacturing, AM clearly stands out due to promising features such as topological optimization, given the relative ease in attaining complex geometries. Its usage is, however, typically restricted to very few parts in an assembly and, in order to ensure its functionality, demanding geometrical tolerances should be fulfilled, which is commonly done through the traditional subtractive manufacturing processes such as machining. Therefore the machinability of AM metal is timely, including their constitutive modelling and cutting simulation. This chapter focuses on the main conclusions of each stage of the conducted research work. Conclusions will be presented in several sections, covering the major aspects of this research.

8.1.1. Materials characterization

- The average surface roughness of as-built additively manufactured samples is approximately one order of magnitude higher than the obtained through conventional subtractive manufacturing, namely finishing operations. Even though the AM process can be tuned in order to achieve excellent surface quality, the selected parameters would not be feasible time and cost-wise, given the relatively easier subtractive approach.

- Despite their distinct metallurgical condition, the thermal properties of additively manufactured alloys revealed to be identical to their conventional counterparts.

- Even though identical phase transition phenomenon are observed for both AM and CM 18Ni300 maraging steel, the distinct magnitudes of dilatometric curves slope variation indicate distinct austenite and martensite microstructural percentages, according to the metallurgical condition.

- The specially designed experimental apparatus that was built for high strain rate, high temperature (and the simultaneous effects) compression testing of engineering materials allowed for a successful characterization of the considered steels.

- The higher yield strength found for the AM alloys are in accordance with finer crystalline structures of these materials, relatively to the CM. Moreover, anisotropic behaviour was found for the AM steels, where the highest yield strength occurred for compression in perpendicular-to-build direction, explained by the higher grain boundary density in that loading path. Yield strength in build direction was averagely 10% lower.

- The strain-rate hardening behaviour of the 316L steel is very much in accordance with literature values, which allows for the validation of the adopted experimental methodology that concerns dynamic characterization of engineering materials, through compression tests. In this steel, an expected hardening is noticed for increasing test speed, resulting in an approximate increase of 15% on the mechanical strength of both AM and CM alloys, when comparing quasi-static with highest speed tested conditions ($6000s^{-1}$).

- Strain-rate hardening has a more pronounced effect on the AM 18Ni300 steel, when compared to the conventional counterpart. Yield strength increases 20% when comparing quasi-static to high strain rate conditions ($6000s^{-1}$), on the AM maraging steel. This increase is roughly 15% in the conventional material.

- The mechanical strength of maraging steel in high strain rate conditions shows sudden softening from strains >0.1 followed by hardening from strains >0.8. Despite occurring for both metallurgical conditions, the softening seems to be more pronounced for the conventional 18Ni300. This effect is compatible with the intermetallic precipitation and phase transformations identified in the dilatometric tests. A viable explanation for such pronounced softening is, as shown by the cross-sections of compression tests, the occurrence of localized adiabatic shear flow. With regards to the hardening it is possible that intermetallic precipitation and austenite reversion (through TRIP) significantly increased the mechanical strength of the maraging steels in both metallurgical conditions.

- The isothermal compression tests revealed a typical thermal softening of both metallurgical conditions of maraging steel. However, compression tests in simultaneous high temperature and dynamic conditions show that the mechanical strength can escalate to roughly 2GPa for both AM and CM maraging steels. The high initial temperatures seems to trigger intermetallic precipitation and TRIP effect with increased significance and surpassing the thermal softening effect.

- Tensile tests have shown a higher ductility of the CM maraging steel, with regards to the AM. Negligible tensile-compression asymmetry (strength-differential effect) is found for the maraging steel in both metallurgical conditions, which is coherent with literature regarding identically manufactured maraging steel. In contrast, a significant amount of diffuse necking

seems to occur in both AM and CM maraging steels which accounts for incipient geometrical softening in tensile conditions.

- The multiaxial fracture tests have confirmed the higher mechanical strength of AM metallurgical condition as well as the increased ductility of the conventional maraging steel. In addition the diffuse necking tendency allied to the high ductility of the latter material have precluded its fracture characterization, revealing the inadequacy of the selected novel geometries towards fracture strain identification, on materials with high strength-ductility ratios.

8.1.2. Tribological characterization

- Ring compression tests proved to be an excellent method towards friction assessment in identical conditions to the material characterization compression tests. The combination of this experimental technique with numerical modelling enables the estimation of materials' frictionless flow stress for high strains, strain rate and temperature conditions.
- The friction coefficient between the tool and additively manufactured workpiece material ranges within 0.1 and 0.25 for the tested conditions of temperature, strain rate and without lubrication (dry). Slightly larger friction coefficient was measured for the conventionally manufactured material, ranging from 0.1 to 0.35. The obtained friction values correspond to the main friction mechanism (adhesion), given the highly controlled roughness conditions of the contacting pair, minimizing mechanical interlocking and plastic deformation effects.
- Higher temperatures seem to promote higher coefficient of friction and the same trend is observed for strain rate. The obtained results suggest further development of friction constitutive modelling (including temperature and strain rate effects) towards a more accurate representation of the metal cutting phenomenon, throughout finite element simulation.

8.1.3. Orthogonal cutting tests

- Showing the same tendency as the mechanical strength inferred from compression tests, the additively manufactured maraging steel shows a slightly higher cutting load relatively to its conventional counterpart (approximately 9%). Also, within the additively maraging steel, cutting that was performed in perpendicular-to-build direction resulted in slightly higher cutting load (approximately 7%). Nonetheless, tool geometry (more specifically rake angle) has a bigger influence on cutting load than cutting orientation or metallurgical condition, given that cutting force decreases averagely 11% when switching from 5° to 12° rake angle.
- Concerning the specific cutting pressure values, the tool rake angle had the major role. Specific cutting pressure values tend to plateau value around 2000-2500 MPa, which is consistent with

similar alloys. Size effects on specific cutting pressures were observed for the smaller uncut chips thicknesses. Serrated chips were observed mostly for the highest tested chip thicknesses which is typical of these materials. The computed friction coefficients were always above the von Mises theoretical limit, which despite showing coherence with literature, reveals the difficulty in friction definition on metal cutting. Therefore, the computed values should be regarded as apparent values and not true ones. The analytical cutting models towards friction estimation relies on the narrow assumption of a load pair at the tool-chip interface which, neglecting important tool edge roundness, such as ploughing effects, or even the tool-workpiece interface friction (tertiary zone). As regards the experimental shear angle evaluations, the inadequacy of the Merchant equation is demonstrated, when compared to the geometrical definition of shear angle, which shows a strong correlation with the chip compression ratio.

- Besides the strength increase of AM maraging steel, its machinability is not significantly affected. Nevertheless, the possibility of generating serrated chips (for $t_0 \gtrapprox 0.3$ mm) may endanger the surface finish, which is critical in post-processing operations.

8.1.4. Machinability tests

- A slight tendency for higher cutting loads in the AM materials can be observed, which is an outcome of their higher mechanical strength as noted in the compression tests. Nonetheless, the observed differences in the cutting loads are not as pronounced as the ones observed in the mechanical characterization tests, mostly due to the distinct stress triaxiality and lode angle in the primary deformation zone, promoted by the oblique-chip formation and nose radius effect. A notorious tool influence is noticed on cutting loads. Despite the suitability of both inserts towards finishing operations, the T-CB insert allows for a better performance due to its improved chip breaker geometry capable of more efficient chip control and significantly lower cutting loads.

- Even though the observed higher mechanical behaviour of the additively manufactured steels, no substantial differences in specific cutting pressure were noticed in processing AM and CM materials, meaning that no additional energy requirements are required for machining the additively manufactured tested steels. Nevertheless if one focuses the attention into the high chips cross-sections, the specific cutting pressures are consistent with the flow stresses of the materials for high strain values, meaning that the saturated K_C values are always slightly larger for both additively manufactured alloys, when compared to their corresponding counterparts. The usage of chip breaker geometry inserts yields lower specific cutting pressure, thus representing an energy-wise more favourable scenario in the processing of both AM and

CM materials. In addition, coherence between the specific cutting pressures identified through turning and orthogonal cutting is verified, especially within the most similar (analogous) tool geometries (T-FLAT and α_r=5).

- Although lower forces were registered when using tool insert with chip-breaking groove (T-CB), when it comes to chip morphology, no clear improvement was observed, meaning that chips segmented almost equally for both insert tools, regardless of their rake surface geometry. On the other hand, when using a flat cutting tool insert (T-FLAT) helical shaped chips were generated, in contrast with conical shaped, for the T-CB tool, which is due to the distinct associated chip flow.

- The formation of segmented chips is almost exclusive of depths of cut equal to 0.5 mm and feed rates of 0.2mm/rev, when considering the 18Ni300, and even for such conditions, chips were occasionally long. The obtained chips of 316L were favourable (e.g. segmented) for a wider range of cutting conditions, in the range of highest feeds and depths of cut. The lower heat conduction of 316L when compared with 18Ni300 seems to have promoted a higher segmentation of the chips for that material. Despite the serrated chip formation in both, deeper valleys are noticed in the 316L, revealing high cutting instabilities.

- The surface roughness of the machined samples has considerably improved, when compared with the as-built AM surfaces. The initial higher roughness of 316L AM parts did not have an influence on the post-processed samples, and minimum values lower than 0.5 μm of R_a were attained for both materials, using insert tools with chip-breaking grooves (T-CB).

- Surface analysis using Scanning Electron Microscopy (SEM) showed the occurrence of built-up edge on both tools, which induced rake surface wear, exposing the substrate material (WC). Nevertheless, short-term cutting tests were conducted to ensure that insert geometry and tribological condition remain constant during experiments. It is, however, important to highlight the presumably short tool life and the challenge that finishing operations represent.

8.1.5. Constitutive modelling

- The influence of friction on the identified flow stress is not negligible and (for non-interrupted tests) its significance is enhanced with increasing strain. The obtention of frictionless flow stress is of vital importance towards a correct representation of the material's flow behaviour.

- The usage of both tensile and compression tests for the depiction of flow stress comes as a promising hybrid characterization approach, where tensile loading is seen as more appropriate for initial yield characterization and compression for higher strain values.

- Even though they are labelled as 'multiaxial fracture' specimens, these tests provided very important insight on material's plasticity and flow stress inverse identification. Given the flaws of typical mechanical characterization methodology (say for example friction in compression tests and plastic instability in tensile test) the multiaxial specimens allowed a crucial benchmark of the suggested plastic law, directed towards the numerical simulation of metal cutting.

- The combination of the Swift power law hardening for portrayal of initial yield and Voce saturation for consequent higher strains accurately depicted the constitutive behaviour of maraging steel for distinct pressure conditions in the plastic deformation of the multiaxial fracture specimens. Despite the "apparent" pressure dependency (strength-differential effect) of the maraging steel, identified in a preliminary stress analysis, it has been verified that isotropic hardening assumption is plausible.

- The suitability of the tested notched geometries (multiaxial and tensile) in materials that are prone to very incipient diffuse necking is questionable when the goal is fracture characterization, given that the expected state of stress can be compromised. Unforeseen high transversal deformation capability led to difficulties in monitoring strain fields using 2D digital image correlation. Despite seemingly incapable of capturing the highly heterogeneous strain fields developed in the numerical simulation of multiaxial specimens, digital image correlation provided important qualitative validation of the material plasticity model through the comparison of the experimental and simulated deformed shapes.

- The multiaxial fracture tests have revealed to be very useful for calibration the constitutive flow stress behaviour of the materials for more representative stress states typical of cutting operations (plane strain and combined shear - tension/compression conditions). These tests are a useful complement to the conventional compression and tensile tests which show some recognized limitations. They are also valuable for damage onset definition despite requiring a proper design to avoid large deformations that could led to stress states less interesting. The capability of the tests for evaluation of fracture energies is limited since it does not corresponds to a truly fracture test, since a significant of energy will precede the crack initiation.

- Despite the significant deviation from the expected (intermediate) range of stress triaxialities, the identified damage onset model and its evolution were able to satisfactorily portray the fracture behaviour of the additively manufactured maraging steel.

8.1.6. Numerical simulation

- The build material model is able to predict the specific cutting pressure of orthogonal cutting operations for distinct uncut chip thickness and rake angles, using a physical numerical approach. The slightly less pronounced curvature of the chips formed with a 12° tool rake angle is also simulated.

- Despite the inadequacy of the sacrificial model towards load prediction, it can rather satisfactorily predict average shear angle and compression chip ratio vales, whereas the physical model depicts only the correct tendency and slightly underestimates those values, suggesting that, due to the complexity of metal cutting, specific models should be developed towards specific variables estimation/prediction. For instance, the prediction of residual stresses demands the usage of ultra-fine meshes and the absence of element deletion. The need for developing specific modelling solutions according to the intended estimated variables is further emphasized/illustrated by the numerical simulation of segmented chip morphology when a temperature sensitive model is applied.

- The suitability of the identified material model is confirmed in the three dimensional simulation of the longitudinal turning process, where a good match between the experimental and numerical cutting force and, thus, specific cutting pressure is achieved. Moreover, a similar tendency of chip curling is noticed.

- Despite the very high computational cost, especially in three-dimensional models, the numerical simulation of machining operations is a very promising technique towards the prediction/estimation of important cutting data, namely specific cutting pressure. Moreover, there is a necessity of developing the numerical model according to the intended output.

8.2. Future work

The challenging task and increased complexity of machining operations characterization and its modelling is currently not fully understood among researchers Melkote et al. (2017), which, on its own, poses a significant amount of further research. Given the (relatively) limited amount of time of PhD studies, and envisioning a continuation of metal cutting research, a set of ideas is listed not only towards further development of the presented techniques but also to a wider understanding of the metal cutting phenomenon:

- The quantification of the austenite and martensite phases percentage (through X-ray diffraction, for instance) according to metallurgical condition of 18Ni300 maraging steel will allow a better understanding of their microstructural condition. In fact, through interrupted compression tests (for different increasing strain levels), it is possible to track the occurrence of microstructural changes in function of strain, taking into account the effects of temperature and strain rate. Microhardness measurements may, as well, be advantageous due to their relative simplicity and possibility in phase identification. This technique can be readily performed on the cross-sectioned compression samples of figures 5.15, 5.16 and 5.18, further confirming the proposed explanations to the atypical strain-hardening identified in the compression tests (TRIP, intermetallic precipitation). Moreover, conducting interrupted compression tests in similar temperature and speed conditions may allow to more accurately identify the onset of adiabatic shearing, which is coherent with a more appropriate identification of strain rate influence on fracture strain, allowing for the evolution from phenomenological modelling toward micromechanics-based approaches.

- The usage of DIC-levelling approaches, in which the FEA data are processed through the same DIC engine as the experimental DIC date allows for the mitigation of apparent strain errors, through minimization of inconsistencies between FEA and DIC, namely the strain calculation algorithm, spatial resolution and data filtering Lava et al. (2020). The fact that such procedure seems to realistically simulate experimental heterogeneous deformations at various load steps (Lava et al., 2009), which may bring a new light on the digital image correlation results.

- The high ductility and geometrical softening of the maraging steel contributes to the non-preservation of the multiaxial fracture specimens geometry, resulting in a big deviation from the intended state-of-stress conditions at fracture. The development of fracture characterization setups that do not dependent on geometrical specimen configuration should be regarded as a more interesting option for the considered material and allow explicit definition of fracture properties.

- In order to avoid excessive element deletion promoted by the extreme contact pressures between the tool rake face and the chip underside, the definition of a cut-off stress triaxiality value for which there is absence of element damage (deletion) may significantly enhance chip morphology prediction, given that its section area is more accurately simulated.

- In further work, aiming at the portrayal of chip segmentation through numerical modelling, a decoupling of the temperature and mechanical effects is necessary. Numerical simulation of the compression tests may be an important tool for the identification of an uncoupled thermal softening parameter.

- Despite very challenging, equivalent fracture strain characterization in high temperature and strain rate conditions might be necessary towards a direct identification of damage models. Such tests should also be conducted for distinct states of stress. In addition, the influence of temperature and strain rate on fracture toughness (for both modes I and II) should be inspected, given the seemingly simplistic approach of a literature commonly adopted constant value, in metal cutting.

Bibliography

H. F. Abed and Z. G. Voyiadjis. A consistent modified Zerilli-Armstrong flow stress model for BCC and FCC metals for elevated temperatures. *Acta Mechanica*, 175(1):1–18, 2005.

Y. M. Abushawashi. *Modeling of metal cutting as purposeful fracture of work material (PhD Thesis)*. 2013. ISBN 1303542315.

O. B. Adetoro and P. H. Wen. Prediction of mechanistic cutting force coefficients using ALE formulation. *The International Journal of Advanced Manufacturing Technology*, 46(1-4):79–90, 2010.

M. Agmell, A. Ahadi, and J.-E. Ståhl. The link between plasticity parameters and process parameters in orthogonal cutting. *Procedia CIRP*, 8:224–229, 2013.

U. Ali, R. Esmaeilizadeh, F. Ahmed, D. Sarker, W. Muhammad, A. Keshavarzkermani, Y. Mahmoodkhani, E. Marzbanrad, and E. Toyserkani. Identification and characterization of spatter particles and their effect on surface roughness, density and mechanical response of 17-4 PH stainless steel laser powder-bed fusion parts. *Materials Science and Engineering: A*, 756:98–107, 2019.

Y. Altintas. *Manufacturing Automation: Metal Cutting Mechanics, Machine Tool Vibrations, and CNC Design*. Cambridge University Press, 2012.

P. J. Arrazola and T. Özel. Investigations on the effects of friction modeling in finite element simulation of machining. *International Journal of Mechanical Sciences*, 52(1):31–42, 2010.

P. J. Arrazola, T. Özel, D. Umbrello, M. Davies, and I. S. Jawahir. Recent advances in modelling of metal machining processes. *CIRP Annals-Manufacturing Technology*, 62(2):695–718, 2013.

P. J. Arrazola, A. Kortabarria, A. Madariaga, J. A. Esnaola, E. Fernandez, C. Cappellini, D. Ulutan, and T. Özel. On the machining induced residual stresses in IN718 nickel-based alloy: Experiments and predictions with finite element simulation. *Simulation Modelling Practice and Theory*, 41:87–103, 2014.

ASM International. *ASM Handbook Volume 8: Mechanical Testing and Evaluation*. ASM International, 2000.

V. P. Astakhov. *Metal Cutting Mechanics*. CRC press, 1998. ISBN 9781466571778.

V. P. Astakhov. *Tribology of metal cutting*. Elsevier, 2006.

V. P. Astakhov. Tribology of cutting tools. In *Tribology in Manufacturing Technology*, pages 1–66. Springer, 2012.

V. P. Astakhov and J. Outeiro. Importance of Temperature in Metal Cutting and Its Proper Measurement/Modeling BT - Measurement in Machining and Tribology. pages 1–47. Springer International Publishing, Cham, 2019.

V. P. Astakhov and J. C. Outeiro. Metal Cutting Mechanics, Finite Element Modelling. In *Machining: Fundamentals and Recent Advances*, pages 1–27. Springer London, London, 2008.

V. P. Astakhov and X. Xiao. A methodology for practical cutting force evaluation based on the energy spent on the cutting system. *Machining Science and Technology*, 12(3):325–347, 2008.

ASTM-A276. *Standard Specification for Stainless Steel Bars for Shapes*. ASTM International, West Conshohocken, PA, 2017.

ASTM-A370. *Standard Test Methods and Definitions for Mechanical Testing of Steel Products*. ASTM International, West Conshohocken, PA, 2020.

A. G. Atkins. Modelling metal cutting using modern ductile fracture mechanics: quantitative explanations for some longstanding problems. *International Journal of Mechanical Sciences*, 45(2):373–396, 2003.

Y. Bai and T. Wierzbicki. A new model of metal plasticity and fracture with pressure and Lode dependence. *International Journal of Plasticity*, 24:1071–1096, 2008.

Y. Bai, A. Chaudhari, and H. Wang. Investigation on the microstructure and machinability of ASTM A131 steel manufactured by directed energy deposition. *Journal of Materials Processing Technology*, 276:116410, 2020.

P. Bajaj, J. Wright, I. Todd, and E. A. Jägle. Predictive process parameter selection for Selective Laser Melting Manufacturing: Applications to high thermal conductivity alloys. *Additive Manufacturing*, 27:246–258, 2019.

P. Bajaj, A. Hariharan, A. Kini, P. Kürnsteiner, D. Raabe, and E. A. Jägle. Steels in additive manufacturing: A review of their microstructure and properties. *Materials Science and Engineering: A*, 772:138633, 2020.

Y. Bao and T. Wierzbicki. On fracture locus in the equivalent strain and stress triaxiality space. *International Journal of Mechanical Sciences*, 46(1):81–98, 2004.

Y. Bao and T. Wierzbicki. On the cut-off value of negative triaxiality for fracture. *Engineering Fracture Mechanics*, 72(7):1049–1069, 2005.

F. Bartolomeu, M. Buciumeanu, E. Pinto, N. Alves, O. Carvalho, F. S. Silva, and G. Miranda. 316L stainless steel mechanical and tribological behavior—A comparison between selective laser melting, hot pressing and conventional casting. *Additive Manufacturing*, 16:81–89, 2017.

U. S. Bertoli, A. J. Wolfer, M. J. Matthews, J.-P. R. Delplanque, and J. M. Schoenung. On the limitations of volumetric energy density as a design parameter for selective laser melting. *Materials & Design*, 113:331–340, 2017.

R. Bertolini, L. Lizzul, S. Bruschi, and A. Ghiotti. On the surface integrity of Electron Beam Melted Ti6Al4V after machining. *Procedia CIRP*, 82:326–331, 2019.

T. Bhardwaj and M. Shukla. Effect of laser scanning strategies on texture, physical and mechanical properties of laser sintered maraging steel. *Materials Science and Engineering: A*, 734:102–109, 2018.

J. I. Bluhm and R. J. Morrissey. Fracture in a tensile specimen. Technical report, 1966.

P. W. Bridgman. *Studies in Large Plastic Flow and Fracture*. McGraw-Hill, New York, 1952.

S. Buchkremer, B. Wu, D. Lung, S. Münstermann, F. Klocke, and W. Bleck. FE-simulation of machining processes with a new material model. *Journal of Materials Processing Technology*, 214(3):599–611, 2014.

E. Budak, Y. Altintas, and E. J. A. Armarego. Prediction of milling force coefficients from orthogonal cutting data. *Journal of Manufacturing Science and Engineering*, 118(2):216–224, 1996. ISSN 1087-1357.

A. Calleja, G. Urbikain, H. González, I. Cerrillo, R. Polvorosa, and A. Lamikiz. Inconel®718 superalloy machinability evaluation after laser cladding additive manufacturing process. *The International Journal of Advanced Manufacturing Technology*, 97(5):2873–2885, 2018.

I. Campbell, O. Diegel, J. Kowen, and T. Wohlers. Wohlers report 2018: 3D printing and additive manufacturing state of the industry: annual worldwide progress report. Wohlers Associates. Technical report, 2018.

L. N. Carter, X. Wang, N. Read, R. Khan, M. Aristizabal, K. Essa, and M. M. Attallah. Process optimisation of selective laser melting using energy density model for nickel based superalloys. *Materials Science and Technology*, 32(7):657–661, 2016.

R. Casati, J. N. Lemke, A. Tuissi, and M. Vedani. Aging behaviour and mechanical performance of 18-Ni 300 steel processed by selective laser melting. *Metals*, 6(9):218, 2016.

K. V. A. Chakravarthi, N. Koundinya, S. V. S. N. Murty, and B. N. Rao. Microstructure, properties and hot workability of M300 grade maraging steel. *Defence technology*, 14(1):51–58, 2018.

B. T. Chao. The significance of the thermal number in metal machining. *Trans. ASME*, 75:109–120, 1953.

W. Cheng, J. Outeiro, J.-P. Costes, R. M'Saoubi, H. Karaouni, and V. Astakhov. A constitutive model for Ti6Al4V considering the state of stress and strain rate effects. *Mechanics of Materials*, 137:103103, 2019a.

W. Cheng, J. Outeiro, J.-P. Costes, R. M'Saoubi, H. Karaouni, S. Dietrich, B. Marcon, and P. Rosa. Optimization-based procedure for the determination of the constitutive model coefficients used in machining simulations. *Procedia CIRP*, 82:374–378, 2019b.

T. H. C. Childs. Friction modelling in metal cutting. *Wear*, 260(3):310–318, 2006.

T. H. C. Childs. Revisiting flow stress modelling for simulating chip formation of carbon and low alloy steels. *Procedia CIRP*, 82:26–31, 2019.

T. H. C. Childs and K. Maekawa. Computer-aided simulation and experimental studies of chip flow and tool wear in the turning of low alloy steels by cemented carbide tools. *Wear*, 139(2):235–250, 1990.

L. Chong, S. Ramakrishna, and S. Singh. A review of digital manufacturing-based hybrid additive manufacturing processes. *The International Journal of Advanced Manufacturing Technology*, 95(5-8):2281–2300, 2018.

H. Choo, K.-L. Sham, J. Bohling, A. Ngo, X. Xiao, Y. Ren, P. J. Depond, M. J. Matthews, and E. Garlea. Effect of laser power on defect, texture, and microstructure of a laser powder bed fusion processed 316L stainless steel. *Materials & Design*, 164:107534, 2019.

P. Church, M. Reynolds, P. Gould, R. Oakley, N. Harrison, D. Williamson, C. Braithwaite, and N. Taylor. Tensile properties of AM maraging steel. In *EPJ Web of Conferences*, volume 183, page 1058. EDP Sciences, 2018.

J. D. Cinnamon, A. N. Palazotto, N. S. Brar, Z. Kennan, and D. Bajaj. Johnson-Cook Strength Model Constants for VascoMax 300 and 1080 Steels. In *AIP Conference Proceedings*, volume 845, pages 709–712. American Institute of Physics, 2006.

M. G. Cockcroft and D. J. Latham. Ductility and the workability of metals. *J Inst Metals*, 96(1):33–39, 1968.

J. Coelho. *Tribological characterization of the additively manufactured 18Ni300 maraging steel (MSc Thesis)*. IST, Lisbon, 2021.

F. F. Conde, J. D. Escobar, J. P. Oliveira, A. L. Jardini, W. W. Bose Filho, and J. A. Avila. Austenite reversion kinetics and stability during tempering of an additively manufactured maraging 300 steel. *Additive Manufacturing*, 29:100804, 2019.

A. Couto. *Machinability studies of conventional and AM 18Ni300 maraging steels (MSc Thesis)*. FEUP, Porto, 2019.

V. A. M. Cristino, P. A. R. Rosa, and P. A. F. Martins. Cutting under active and inert gas shields: A contribution to the mechanics of chip flow. *International Journal of Machine Tools and Manufacture*, 50(10):892–900, 2010.

E. Cyr, A. Lloyd, and M. Mohammadi. Tension-compression asymmetry of additively manufactured Maraging steel. *Journal of Manufacturing Processes*, 35:289–294, 2018.

T. F. da Silva, R. Soares, A. Jesus, P. Rosa, and A. Reis. Simulation Studies of Turning of Aluminium Cast Alloy Using PCD Tools. *Procedia CIRP*, 58:555–560, 2017.

M. Daoud, W. Jomaa, J. F. Chatelain, and A. Bouzid. A machining-based methodology to identify material constitutive law for finite element simulation. *The International Journal of Advanced Manufacturing Technology*, 77 (9-12):2019–2033, 2015.

J. P. Davim. Application of Merchant theory in machining particulate metal matrix composites. *Materials & Design*, 28(10):2684–2687, 2007.

L. G. de Carvalho, M. S. Andrade, R. L. Plaut, F. M. Souza, and A. F. Padilha. A dilatometric study of the phase transformations in 300 and 350 maraging steels during continuous heating rates. *Materials Research*, 16(4): 740–744, 2013.

T. DebRoy, H. L. Wei, J. S. Zuback, T. Mukherjee, J. W. Elmer, J. O. Milewski, A. M. Beese, A. Wilson-Heid, A. De, and W. Zhang. Additive manufacturing of metallic components – Process, structure and properties. *Progress in Materials Science*, 92:112–224, 2018.

A. G. Demir and B. Previtali. Investigation of remelting and preheating in SLM of 18Ni300 maraging steel as corrective and preventive measures for porosity reduction. *The International Journal of Advanced Manufacturing Technology*, 93(5-8):2697–2709, 2017.

A. Devotta, T. Beno, R. Löf, and E. Espes. Quantitative characterization of chip morphology using computed tomography in orthogonal turning process. *Procedia CIRP*, 33:299–304, 2015.

DIN8589. *Manufacturing Processes Chip Removal–Part 0: General; Classification, Subdivision, Terms and Definitions*. Deutsches Institut Fur Normung EV, 2003.

T. dos Santos, J. C. Outeiro, R. Rossi, and P. Rosa. A New Methodology for Evaluation of Mechanical Properties of Materials at Very High Rates of Loading. *Procedia CIRP*, 58:481–486, 2017.

D. C. Drucker and W. Prager. Soil mechanics and plastic analysis or limit design. *Quarterly of applied mathematics*, 10(2):157–165, 1952.

F. Ducobu, E. Rivière-Lorphèvre, and E. Filippi. Application of the Coupled Eulerian-Lagrangian (CEL) method to the modeling of orthogonal cutting. *European Journal of Mechanics-A/Solids*, 59:58–66, 2016.

D. Dudzinski and A. Molinari. A modelling of cutting for viscoplastic materials. *International Journal of Mechanical Sciences*, 39(4):369–389, 1997.

J. L. Endrino, G. S. Fox-Rabinovich, and C. Gey. Hard AlTiN, AlCrN PVD coatings for machining of austenitic stainless steel. *Surface and Coatings Technology*, 200(24):6840–6845, 2006.

J. M. Flynn, A. Shokrani, S. T. Newman, and V. Dhokia. Hybrid additive and subtractive machine tools – Research and industrial developments. *International Journal of Machine Tools and Manufacture*, 101:79–101, 2016.

P. Follansbee and U. Kocks. A constitutive description of the deformation of copper based on the use of the mechanical threshold stress as an internal state variable. *Acta Metallurgica*, 36(1):81–93, 1988.

A. Fortunato, A. Lulaj, S. Melkote, E. Liverani, A. Ascari, and D. Umbrello. Milling of maraging steel components produced by selective laser melting. *The International Journal of Advanced Manufacturing Technology*, 94(5): 1895–1902, 2018.

J. C. Fox, S. P. Moylan, and B. M. Lane. Effect of process parameters on the surface roughness of overhanging structures in laser powder bed fusion additive manufacturing. *Procedia Cirp*, 45:131–134, 2016.

W. E. Frazier. Metal Additive Manufacturing: A Review. *Journal of Materials Engineering and Performance*, 23(6): 1917–1928, 2014.

H. Fu, X. Wang, L. Xie, X. Hu, U. Umer, A. U. Rehman, M. H. Abidi, and A. E. Ragab. Dynamic behaviors and microstructure evolution of Iron–nickel based ultra-high strength steel by SHPB testing. *Metals*, 10(1):62, 2020a.

H. Fu, L. Xie, X. Wang, X. Hu, and F. Gao. Fracture mechanism and model of 18Ni maraging steel. *Materials Science and Technology*, 36(7):894–898, 2020b.

S. Gain, T. E. F. Silva, A. M. P. Jesus, A. Cavaleiro, P. A. R. Rosa, and A. Reis. Mechanical characterization of the AlSi9Cu3 cast alloy under distinct stress states and thermal conditions. *Engineering Fracture Mechanics*, 216: 106499, 2019.

A. Gebhardt, F. Schmidt, J. Hötter, W. Sokalla, and P. Sokalla. Additive manufacturing by selective laser melting the realizer desktop machine and its application for the dental industry. *Physics Procedia*, 5:543–549, 2010.

H. Gong, K. Rafi, H. Gu, T. Starr, and B. Stucker. Analysis of defect generation in Ti–6Al–4V parts made using powder bed fusion additive manufacturing processes. *Additive Manufacturing*, 1:87–98, 2014.

M. P. Groover. *Fundamentals of Modern Manufacturing: Materials, Processes, and Systems*. John Wiley & Sons, 2010. ISBN 9780470467008.

W. Grzesik. Experimental investigation of the influence of adhesion on the frictional conditions in the cutting process. *Tribology international*, 32(1):15–23, 1999.

W. Grzesik and P. Nieslony. Prediction of friction and heat flow in machining incorporating thermophysical properties of the coating–chip interface. *Wear*, 256(1-2):108–117, 2004.

J. S. Gunasekera, J. Havranek, and M. H. Littlejohn. The effect of specimen size on stress-strain behavior in compression. *Journal of Engineering Materials and Technology*, 104(4):274–279, 1982.

M. Günay, E. Aslan, I. Korkut, and U. Şeker. Investigation of the effect of rake angle on main cutting force. *International Journal of Machine Tools and Manufacture*, 44(9):953–959, 2004.

P. Guo, B. Zou, C. Huang, and H. Gao. Study on microstructure, mechanical properties and machinability of efficiently additive manufactured AISI 316L stainless steel by high-power direct laser deposition. *Journal of Materials Processing Technology*, 240:12–22, 2017.

B. Haddag, S. Atlati, M. Nouari, and M. Znasni. Finite element formulation effect in three-dimensional modeling of a chip formation during machining. *International Journal of Material Forming*, 3(1):527–530, 2010.

N. Haghdadi, M. Laleh, M. Moyle, and S. Primig. Additive manufacturing of steels: a review of achievements and challenges. *Journal of Materials Science*, 56:64–107, 2021.

R. S. Hahn. On the temperature developed at the shear plane in the metalcutting process. *Journal of Applied Mechanics-Transactions of the ASME*, 18(3):323, 1951.

E. O. Hall. The deformation and ageing of mild steel: III discussion of results. *Proceedings of the Physical Society. Section B*, 64(9):747, 1951.

D. Herzog, V. Seyda, E. Wycisk, and C. Emmelmann. Additive manufacturing of metals. *Acta Materialia*, 117: 371–392, 2016.

A. Hillerborg, M. Modéer, and P.-E. Petersson. Analysis of crack formation and crack growth in concrete by means of fracture mechanics and finite elements. *Cement and Concrete Research*, 6(6):773–781, 1976.

J. M. Huang and J. T. Black. An Evaluation of Chip Separation Criteria for the FEM Simulation of Machining. *Journal of Manufacturing Science and Engineering*, 118(4):545–554, 1996.

H. Hucks. *Plastizitätsmechanische Grundlagen und Kenngrößen der Zerspanung*. Rheinisch-Westfälische Technische Hochschule, Aachen, 1951.

I. Hutchings and P. Shipway. *Tribology: friction and wear of engineering materials*. Butterworth-Heinemann, 2017.

J.-K. Hwang. Revealing the small post-necking elongation in twinning-induced plasticity steels. *Journal of Materials Science*, 55(19):8285–8302, 2020.

ISO/ASTM52910-17. *Additive manufacturing — Design — Requirements, guidelines and recommendations*. West Conshohocken, PA, 2017.

K. Iwata, K. Osakada, and Y. Terasaka. Process Modeling of Orthogonal Cutting by the Rigid-Plastic Finite Element Method. *Journal of Engineering Materials and Technology*, 106(2):132–138, 1984.

E. A. Jägle, P.-P. Choi, J. Van Humbeeck, and D. Raabe. Precipitation and austenite reversion behavior of a maraging steel produced by selective laser melting. *Journal of Materials Research*, 29(17):2072–2079, 2014.

E. A. Jägle, Z. Sheng, P. Kürnsteiner, S. Ocylok, A. Weisheit, and D. Raabe. Comparison of maraging steel micro-and nanostructure produced conventionally and by laser additive manufacturing. *Materials*, 10(1):8, 2017.

J. M. Jeon, J. M. Park, J.-H. Yu, J. G. Kim, Y. Seong, S. H. Park, and H. S. Kim. Effects of microstructure and internal defects on mechanical anisotropy and asymmetry of selective laser-melted 316L austenitic stainless steel. *Materials Science and Engineering: Part A*, 763:138152, 2019.

G. R. Johnson and W. H. Cook. Fracture characteristics of three metals subjected to various strains, strain rates, temperatures and pressures. *Engineering Fracture Mechanics*, 21(1):31–48, 1985.

J. B. Jones. Repurposing mainstream CNC machine tools for laser-based additive manufacturing. In *Proc.SPIE Laser 3D Manufacturing III*, volume 9738, 2016.

M. Kamal and G. Rizza. *Design for metal additive manufacturing for aerospace applications*. Elsevier, 2019.

R. Kannan and P. Nandwana. Insights into the Transformation-Induced Plasticity (TRIP) Effect in Ti-Free Grade 300 Maraging Steel Manufactured by Laser Powder Bed Fusion (LPBF). *The Journal of The Minerals, Metals & Materials Society*, pages 1–9, 2020.

R. Kapoor, L. Kumar, and I. S. Batra. A dilatometric study of the continuous heating transformations in 18wt.% Ni maraging steel of grade 350. *Materials Science and Engineering: Part A*, 352(1-2):318–324, 2003.

Y. Kaynak and O. Kitay. The effect of post-processing operations on surface characteristics of 316L stainless steel produced by selective laser melting. *Additive Manufacturing*, 26:84–93, 2019.

P. M. Kelly and J. Nutting. The martensite transformation in carbon steels. *Proceedings of the Royal Society of London. Series A. Mathematical and Physical Sciences*, 259(1296):45–58, 1961.

K. Kempen. *Expanding the materials palette for Selective Laser Melting of metals (PhD Thesis)*. Katholieke Universiteit Leuven, 2015.

K. Kempen, E. Yasa, L. Thijs, J. P. Kruth, and J. Van Humbeeck. Microstructure and mechanical properties of Selective Laser Melted 18Ni-300 steel. *Physics Procedia*, 12:255–263, 2011.

K. Kempen, B. Vrancken, S. Buls, L. Thijs, J. Van Humbeeck, and J.-P. Kruth. Selective laser melting of crack-free high density M2 high speed steel parts by baseplate preheating. *Journal of Manufacturing Science and Engineering*, 136(6), 2014.

D. P. Kendall. The effect of strain rate and temperature on yielding in steels. *Journal of Basic Engineering*, 94(1): 207–212, 1972.

S. Khairallah. Spatter reduction laser scanning strategy in selective laser melting, 2019.

S. A. Khairallah, A. T. Anderson, A. Rubenchik, and W. E. King. Laser powder-bed fusion additive manufacturing: Physics of complex melt flow and formation mechanisms of pores, spatter, and denudation zones. *Acta Materialia*, 108:36–45, 2016.

F. H. Kim, S. P. Moylan, T. Q. Phan, and E. J. Garboczi. Investigation of the Effect of Artificial Internal Defects on the Tensile Behavior of Laser Powder Bed Fusion 17–4 Stainless Steel Samples: Simultaneous Tensile Testing and X-Ray Computed Tomography. *Experimental Mechanics*, 60(7):987–1004, 2020.

H.-G. Kim, J.-H. Sim, and H.-J. Kweon. Performance evaluation of chip breaker utilizing neural network. *Journal of Materials Processing Technology*, 209(2):647–656, 2009.

W. E. King, H. D. Barth, V. M. Castillo, G. F. Gallegos, J. W. Gibbs, D. E. Hahn, C. Kamath, and A. M. Rubenchik. Observation of keyhole-mode laser melting in laser powder-bed fusion additive manufacturing. *Journal of Materials Processing Technology*, 214(12):2915–2925, 2014.

F. Klocke. *Manufacturing Processes, 1, Cutting*. Springer, 2011.

F. Klocke, D. Lung, and H. Puls. FEM-Modelling of the thermal workpiece deformation in dry turning. *Procedia CIRP*, 8:240–245, 2013.

T. J. Kneen, C. Barrett, G. P. Manogharan, P. R. Carlson, J. Dimon, and B. P. Conner. Mechanical behaviour and high strain rate deformation of stainless steel 316L processed by selective laser melting. *International Journal of Rapid Manufacturing*, 9(1):84–103, 2020.

Y. Kok, X. P. Tan, P. Wang, M. L. S. Nai, N. H. Loh, E. Liu, and S. B. Tor. Anisotropy and heterogeneity of microstructure and mechanical properties in metal additive manufacturing: A critical review. *Materials & Design*, 139:565–586, 2018.

R. Komanduri and Z. B. Hou. A review of the experimental techniques for the measurement of heat and temperatures generated in some manufacturing processes and tribology. *Tribology International*, 34(10):653–682, 2001.

S. Kou. *Welding metallurgy*. WILEY, 2003.

M. Król, P. Snopiński, and A. Czech. The phase transitions in selective laser-melted 18-NI (300-grade) maraging steel. *Journal of Thermal Analysis and Calorimetry*, 142:1011–1018, 2020.

L. J. Kumar and C. G. K. Nair. *Current trends of additive manufacturing in the aerospace industry*. Springer, Singapore, 2017.

F. H. Lang and N. Kenyon. *Welding of maraging steels*. Welding Research Council New York, 1971.

P. Lava, S. Cooreman, S. Coppieters, M. De Strycker, and D. Debruyne. Assessment of measuring errors in DIC using deformation fields generated by plastic FEA. *Optics and Lasers in Engineering*, 47(7):747–753, 2009.

P. Lava, E. M. C. Jones, L. Wittevrongel, and F. Pierron. Validation of finite-element models using full-field experimental data: Levelling finite-element analysis data through a digital image correlation engine. *Strain*, 56(4): e12350, 2020. ISSN 0039-2103.

K. Q. Le, C. Tang, and C. H. Wong. A study on the influence of scanning strategies on the levelness of the melt track in selective laser melting process of stainless steel powder. *The Journal of The Minerals, Metals & Materials Society*, 70(10):2082–2087, 2018.

T. C. Leça, T. E. F. Silva, A. M. P. de Jesus, R. L. Neto, J. L. Alves, and J. P. Pereira. Influence of multiple scan fields on the processing of 316L stainless steel using laser powder bed fusion. *Proceedings of the Institution of Mechanical Engineers, Part L: Journal of Materials: Design and Applications*, 235(1):19–41, 2020.

E. H. Lee and B. W. Shaffer. The theory of plasticity applied to a problem of machining. *Journal of Applied Mechanics*, 18(4):405–413, 1951.

W.-S. Lee and C.-C. Chiu. Deformation and fracture behavior of 316L sintered stainless steel under various strain rate and relative sintered density conditions. *Metallurgical and Materials Transactions A*, 37(12):3685–3696, 2006.

J. J. Lewandowski and M. Seifi. Metal Additive Manufacturing: A Review of Mechanical Properties. *Annual Review of Materials Research*, 46:151–186, 2016.

P. Li, C. R. Siviour, and N. Petrinic. The effect of strain rate, specimen geometry and lubrication on responses of aluminium AA2024 in uniaxial compression experiments. *Experimental mechanics*, 49(4):587–593, 2009.

X. Li, C. C. Roth, T. Tancogne-Dejean, and D. Mohr. Rate-and temperature-dependent plasticity of additively manufactured stainless steel 316L: Characterization, modeling and application to crushing of shell-lattices. *International Journal of Impact Engineering*, 145:103671, 2020.

G. Liu, C. Huang, R. Su, T. Özel, Y. Liu, and L. Xu. 3D FEM simulation of the turning process of stainless steel 17-4PH with differently texturized cutting tools. *International Journal of Mechanical Sciences*, 155:417–429, 2019.

J. Liu, Y. Bai, and C. Xu. Evaluation of Ductile Fracture Models in Finite Element Simulation of Metal Cutting Processes. *Journal of Manufacturing Science and Engineering*, 136(1), 2013.

L. Liu, Q. Ding, Y. Zhong, J. Zou, J. Wu, Y.-L. Chiu, J. Li, Z. Zhang, Q. Yu, and Z. Shen. Dislocation network in additive manufactured steel breaks strength–ductility trade-off. *Materials Today*, 21(4):354–361, 2018.

S. Lou, X. Jiang, W. Sun, W. Zeng, L. Pagani, and P. J. Scott. Characterisation methods for powder bed fusion processed surface topography. *Precision Engineering*, 57:1–15, 2019.

M. Lowther, S. Louth, A. Davey, A. Hussain, P. Ginestra, L. Carter, N. Eisenstein, L. Grover, and S. Cox. Clinical, industrial, and research perspectives on powder bed fusion additively manufactured metal implants. *Additive Manufacturing*, 28:565–584, 2019.

P. Ludwik. *Elemente der technologischen Mechanik*. Springer, 1909.

T. Mabrouki, F. Girardin, M. Asad, and J.-F. Rigal. Numerical and experimental study of dry cutting for an aeronautic aluminium alloy (A2024-T351). *International Journal of Machine Tools and Manufacture*, 48(11):1187–1197, 2008.

T. Mabrouki, C. Courbon, Y. Zhang, J. Rech, D. Nélias, M. Asad, H. Hamdi, S. Belhadi, and F. Salvatore. Some insights on the modelling of chip formation and its morphology during metal cutting operations. *Comptes Rendus Mécanique*, 344(4–5):335–354, 2016.

D. Madhusudhan, S. Chand, S. Ganesh, and U. Saibhargavi. Modeling and simulation of Charpy impact test of maraging steel 300 using Abaqus. *IOP Conference Series: Materials Science and Engineering*, 330(1):012013, 2018.

K. Maekawa, T. Shirakashi, and E. Usui. Flow stress of low carbon steel at high temperature and strain rate. ii: flow stress under variable temperature and variable strain rate. *Bulletin of the Japan Society of Precision Engineering*, 17(3):167–172, 1983.

F. H. Marbury. *Characterization of SLM printed 316L stainless steel and investigation of microlattice geometry (Senior Project Report)*. California Polytechnic State University, 2017.

A. P. Markopoulos. *Finite element method in machining processes*. Springer Science & Business Media, 2012.

A. P. Markopoulos, N. E. Karkalos, N. M. Vaxevanidis, and D. E. Manolakos. Friction in Orthogonal Cutting Finite Elements Models with Large Negative Rake Angle. *Tribology in Industry*, 38(2), 2016.

F. Martín, M. J. Martín, L. Sevilla, and M. A. Sebastián. The Ring Compression Test: Analysis of Dimensions and Canonical Geometry. *Procedia Engineering*, 132:326–333, 2015.

Marvac. DATA SHEET MARVAC ^{TM} 300 VIM-VAR. Technical report, Latrobe Specialty Steel Co., Latrobe PA, USA, 2009. URL https://customer.cartech.com/assets/documents/datasheets/Marvac{_}300.pdf.

A. A. Mazhar, E. A. Khokhar, and A. Q. Khan. Effect of strain rate on tensile deformation and fracture behaviour of 18% Ni 300 maraging steel sheet. *Materials science and technology*, 4(6):535–539, 1988.

M. Mazur, M. Leary, M. McMillan, J. Elambasseril, and M. Brandt. SLM additive manufacture of H13 tool steel with conformal cooling and structural lattices. *Rapid Prototyping Journal*, 22(3):504–518, 2016.

F. A. McClintock. A Criterion for Ductile Fracture by the Growth of Holes. *Journal of Applied Mechanics*, 35(2): 363, 1968.

S. N. Melkote, W. Grzesik, J. Outeiro, J. Rech, V. Schulze, H. Attia, P.-J. Arrazola, R. M'Saoubi, and C. Saldana. Advances in material and friction data for modelling of metal machining. *Cirp Annals*, 66(2):731–754, 2017.

L. Meng, W. Zhang, D. Quan, G. Shi, L. Tang, Y. Hou, P. Breitkopf, J. Zhu, and T. Gao. From Topology Optimization Design to Additive Manufacturing: Today's Success and Tomorrow's Roadmap. *Archives of Computational Methods in Engineering*, 27:805–830, 2020.

P. Mercelis and J. Kruth. Residual stresses in selective laser sintering and selective laser melting. *Rapid Prototyping Journal*, 12(5):254–265, 2006.

H. E.-M. Merchant and H. Ernst. Chip formation, friction and high quality machined surfaces. *Surface Treatment of Metals*, 29:299–378, 1941.

Metal AM. Milacron's DME partners with Linear to introduce conformal cooling to product range, 2017. URL https://www.metal-am.com/milacrons-dme-partners-linear-introduce-conformal-cooling-product-range.

MIL-S-46850D. *Steel: Bar, Plate, Sheet, Strip, Forgings and Extrusions - 18 percent Ni Alloy Maraging 200 KSI, 250 KSI and 300 KSI.* US Military Standards, 1986.

J. Minguella-Canela, S. Morales Planas, D. los Santos-López, and M. Antonia. SLM Manufacturing Redesign of Cooling Inserts for High Production Steel Moulds and Benchmarking with Other Industrial Additive Manufacturing Strategies. *Materials*, 13(21):4843, 2020.

Mitsubishi. Mitsubishi Materials C009B. Cutting tools general catalogue 2020-2021 (Technical Catalogue). Technical report, 2020.

K. Monkova, I. Zetkova, L. Kučerová, M. Zetek, P. Monka, and M. Daňa. Study of 3D printing direction and effects of heat treatment on mechanical properties of MS1 maraging steel. *Archive of Applied Mechanics*, 89(5):791–804, 2019.

K. P. Monroy Vazquez, C. Giardini, and E. Ceretti. Cutting Force Modeling. In L. Laperrière and G. Reinhart, editors, *CIRP Encyclopedia of Production Engineering*, pages 315–329. Springer Berlin Heidelberg, Berlin, Heidelberg, 2014. ISBN 978-3-642-20617-7.

F. Montevecchi, N. Grossi, H. Takagi, A. Scippa, H. Sasahara, and G. Campatelli. Cutting Forces Analysis in Additive Manufactured AISI H13 Alloy. *Procedia CIRP*, 46:476–479, 2016.

R. M'Saoubi and H. Chandrasekaran. Innovative methods for the investigation of tool-chip adhesion and layer formation during machining. *CIRP annals*, 54(1):59–62, 2005.

T. Mukherjee, H. L. Wei, A. De, and T. DebRoy. Heat and fluid flow in additive manufacturing–Part II: Powder bed fusion of stainless steel, and titanium, nickel and aluminum base alloys. *Computational Materials Science*, 150: 369–380, 2018.

L. E. Murr, S. M. Gaytan, D. A. Ramirez, E. Martinez, J. Hernandez, K. N. Amato, P. W. Shindo, F. R. Medina, and R. B. Wicker. Metal fabrication by additive manufacturing using laser and electron beam melting technologies. *Journal of Materials Science & Technology*, 28(1):1–14, 2012.

K. Okushima and K. Hitomi. An Analysis of the Mechanism of Orthogonal Cutting and Its Application to Discontinuous Chip Formation. *Journal of Engineering for Industry*, 83(4):545–555, 1961.

A. R. Oliveira, A. L. Jardini, and E. G. Del Conte. Effects of cutting parameters on roughness and residual stress of maraging steel specimens produced by additive manufacturing. *The International Journal of Advanced Manufacturing Technology*, 111(9):2449–2459, 2020.

J. C. Outeiro, J.-P. Costes, and J. R. Kornmeier. Cyclic variation of residual stress induced by tool vibration in machining operations. *Procedia CIRP*, 8:493–497, 2013.

P. L. B. Oxley. A strain-hardening solution for the "shear angle" in orthogonal metal cutting. *International Journal of Mechanical Sciences*, 3(1-2):68–79, 1961.

T. Özel and T. Altan. Determination of workpiece flow stress and friction at the chip–tool contact for high-speed cutting. *International Journal of Machine Tools and Manufacture*, 40(1):133–152, 2000.

W. B. Palmer and P. L. B. Oxley. Mechanics of orthogonal machining. *Proceedings of the Institution of Mechanical Engineers*, 173(1):623–654, 1959.

L. Parry, I. A. Ashcroft, and R. D. Wildman. Understanding the effect of laser scan strategy on residual stress in selective laser melting through thermo-mechanical simulation. *Additive Manufacturing*, 12:1–15, 2016.

L. A. Parry. *Investigation of residual stress in selective laser melting*. PhD thesis, University of Nottingham, 2018.

A. E. Patterson, S. L. Messimer, and P. A. Farrington. Overhanging features and the SLM/DMLS residual stresses problem: Review and future research need. *Technologies*, 5(2):15, 2017.

E. V. Pereloma, A. A. Gazder, and I. B. Timokhina. Retained austenite: Transformation-induced plasticity. *Faculty of Engineering and Information Sciences - Papers: Part A (University of Wollongong)*, 6578, 2016.

H. Pérez, A. Vizán, J. C. Hernandez, and M. Guzmán. Estimation of cutting forces in micromilling through the determination of specific cutting pressures. *Journal of Materials Processing Technology*, 190(1-3):18–22, 2007.

V. Piispanen. Lastunmuodostumisen teoriaa. *Teknillinen aikakauslehti*, 27(9):315–322, 1937.

I. Polyzois. *Finite Element Modeling of the Behavior of Armor Materials Under High Strain Rates and Large Strains (MSc Thesis)*. 2010.

K. G. Prashanth and J. Eckert. Formation of metastable cellular microstructures in selective laser melted alloys. *Journal of Alloys and Compounds*, 707:27–34, 2017.

J. M. R. Prieto, J. M. Carbonell, J. C. Cante, J. Oliver, and P. Jonsen. Generation of segmental chips in metal cutting modeled with the PFEM. *Computational mechanics*, 61(6):639–655, 2018.

H. Puls, F. Klocke, and D. Lung. Experimental investigation on friction under metal cutting conditions. *Wear*, 310 (1-2):63–71, 2014.

D. Raabe, D. Ponge, O. Dmitrieva, and B. Sander. Nanoprecipitate-hardened 1.5 GPa steels with unexpected high ductility. *Scripta Materialia*, 60(12):1141–1144, 2009.

H. K. Rafi, D. Pal, N. Patil, T. L. Starr, and B. E. Stucker. Microstructure and Mechanical Behavior of 17-4 Precipitation Hardenable Steel Processed by Selective Laser Melting. *Journal of Materials Engineering and Performance*, 23(12):4421–4428, 2014.

K. P. Rao and K. Sivaram. A review of ring-compression testing and applicability of the calibration curves. *Journal of Materials Processing Technology*, 37(1-4):295–318, 1993.

B. Redwood, F. Schffer, and B. Garret. *The 3D Printing Handbook: Technologies, Design and Applications*. 3D Hubs, 1st edition, 2017.

J. Rice and D. Tracey. On the ductile enlargement of voids in triaxial stress fields. *Journal of the Mechanics and Physics of Solids*, 17(3):201–217, 1969.

J. Risse. *Additive manufacturing of nickel-base superalloy IN718LC by laser powder bed fusion (PhD Thesis)*. Michigan Technological University, 2019.

A. M. Roach, B. C. White, A. Garland, B. H. Jared, J. D. Carroll, and B. L. Boyce. Size-dependent stochastic tensile properties in additively manufactured 316L stainless steel. *Additive Manufacturing*, 32:101090, 2020.

J. M. Rodríguez, J. M. Carbonell, and P. Jonsén. Numerical Methods for the Modelling of Chip Formation. *Archives of Computational Methods in Engineering*, 27(2):387–412, 2020.

P. Rosa, O. Kolednik, P. Martins, and A. Atkins. The transient beginning to machining and the transition to steady-state cutting. *International Journal of Machine Tools and Manufacture*, 47(12-13):1904–1915, 2007a.

P. A. Rosa, R. M. O. Baptista, J. M. C. Rodrigues, and P. A. F. Martins. An investigation on the external inversion of thin-walled tubes using a die. *International journal of plasticity*, 20(10):1931–1946, 2004.

P. A. R. Rosa, P. A. F. Martins, and A. G. Atkins. Revisiting the fundamentals of metal cutting by means of finite elements and ductile fracture mechanics. *International Journal of Machine Tools and Manufacture*, 47(3–4): 607–617, 2007b.

P. A. R. Rosa, A. V. L. Gregorio, and J. P. Davim. The role of oxygen in orthogonal machining of metals. In *Measurement in Machining and Tribology*, pages 49–88. Springer, 2019.

A. Röttger, J. Boes, W. Theisen, M. Thiele, C. Esen, A. Edelmann, and R. Hellmann. Microstructure and mechanical properties of 316L austenitic stainless steel processed by different SLM devices. *The International Journal of Advanced Manufacturing Technology*, 108:769–783, 2020.

T. Sakaki, K. Sugimoto, and O. Miyagawa. Strain Hardening and Uniform Elongation of 1700MPa Grade Maraging Steel. *Transactions of the Iron and Steel Institute of Japan*, 26(3):219–227, 1986.

D. Samantaray, S. Mandal, and A. K. Bhaduri. A comparative study on Johnson Cook, modified Zerilli–Armstrong and Arrhenius-type constitutive models to predict elevated temperature flow behaviour in modified 9Cr–1Mo steel. *Computational materials science*, 47(2):568–576, 2009.

W. J. Sames, F. A. List, S. Pannala, R. R. Dehoff, and S. S. Babu. The metallurgy and processing science of metal additive manufacturing. *International Materials Reviews*, 61(5):315–360, 2016.

T. Sata. Friction process on cutting tool and cutting mechanism. *Proceedings of the Fourth Japan National Congress for Applied Mechanics*, 1954.

T. Sata and H. Yoshikawa. A new expression for the shear angle in metal cutting. *Proceedings of International Production Engineering Research Conference (ASME)*, pages 18–25, 1963.

E. Schmidova, P. Hojka, B. Culek, F. Klejch, and M. Schmid. Dynamic Strength and Anisotropy of Dmls Manufactured Maraging Steel. *Communications-Scientific letters of the University of Zilina*, 21(3):35–39, 2019.

M. Schmidt and K. Rohrbach. Heat treating of maraging steels. *ASM International, ASM Handbook.*, 4:219–228, 1991.

G. S. Sekhon and J. L. Chenot. Numerical simulation of continuous chip formation during non-steady orthogonal cutting. *Engineering computations*, 10(1):31–48, 1993.

S. L. Semiatin and J. J. Jonas. *Formability and workability of metals: plastic instability and flow localization*. ASM International (OH), 1984.

S. Shamsdini, M. H. Ghoncheh, M. Sanjari, H. Pirgazi, B. S. Amirkhiz, L. Kestens, and M. Mohammadi. Plastic deformation throughout strain-induced phase transformation in additively manufactured maraging steels. *Materials & Design*, 198:109289, 2021. ISSN 0264-1275.

M. C. Shaw. The size effect in metal cutting. *Sadhana*, 28(5):875–896, 2003.

M. C. Shaw. *Metal Cutting Principles*. Oxford University Press, 2005.

M. C. Shaw, N. H. Cook, and I. Finnie. The shear-angle relationship in metal cutting. *Trans. ASME*, 75(2):273, 1953.

T. Shirakashi and E. Usui. Friction characteristics on tool face in metal machining. *Journal of the Japan Society of Precision Engineering*, 39(9):966–971, 1973.

C. M. A. Silva, P. A. R. Rosa, and P. A. F. Martins. Electromagnetic Cam Driven Compression Testing Equipment. *Experimental Mechanics*, 52(8):1211–1222, 2012.

T. Silva. *Numerical Simulation of Metal Cutting Processes Based on DEFORM software*. Msc thesis, Porto, 2016.

M. Sima and T. Özel. Modified material constitutive models for serrated chip formation simulations and experimental validation in machining of titanium alloy Ti–6Al–4V. *International Journal of Machine Tools and Manufacture*, 50(11):943–960, 2010.

J. A. Slotwinski, E. J. Garboczi, and K. M. Hebenstreit. Porosity Measurements and Analysis for Metal Additive Manufacturing Process Control. *Journal of Research of the National Institute of Standards and Technology*, 119: 494, 2014.

M. Smith. ABAQUS/Standard User's Manual, Version 6.9, 2009.

R. Soares. *Estudos de Maquinabilidade da Liga AlSi9Cu3 Recorrendo a Ferramentas PCD com Quebra-Aparas (MSc Thesis)*. FEUP, 2016.

H. Sofuoglu and J. Rasty. On the measurement of friction coefficient utilizing the ring compression test. *Tribology International*, 32(6):327–335, 1999.

B. Song, P. E. Wakeland, and M. Furnish. Dynamic tensile characterization of Vascomax® maraging C250 and C300 alloys. *Journal of Dynamic Behavior of Materials*, 1(2):153–161, 2015.

A. B. Spierings, M. Schneider, and R. Eggenberger. Comparison of density measurement techniques for additive manufactured metallic parts. *Rapid Prototyping Journal*, 17(5):380–386, 2011.

W. A. Spitzig, R. J. Sober, and O. Richmond. The effect of hydrostatic pressure on the deformation behavior of maraging and HY-80 steels and its implications for plasticity theory. *Metallurgical Transactions A*, 7(11):1703–1710, 1976.

G. V. Stabler. The fundamental geometry of cutting tools. *Proceedings of the Institution of Mechanical Engineers*, 165(1):14–26, 1951.

G. Stepan, Z. Dombovari, and J. Munoa. Identification of cutting force characteristics based on chatter experiments. *Cirp Annals*, 60(1):113–116, 2011.

G. Struzikiewicz, W. Zębala, A. Matras, M. Machno, Ł. Ślusarczyk, S. Hichert, and F. Laufer. Turning research of additive laser molten stainless steel 316L obtained by 3D printing. *Materials*, 12(1):182, 2019.

J. A. Stull, M. A. Hill, T. J. Lienert, J. Tokash, K. R. Bohn, and D. E. Hooks. Corrosion characteristics of laser-engineered net shaping additively-manufactured 316L stainless steel. *The Journal of The Minerals, Metals & Materials Society*, 70(11):2677–2683, 2018. ISSN 1047-4838.

K. Sun, W. Peng, B. Wei, L. Yang, and L. Fang. Friction and wear characteristics of 18Ni (300) maraging steel under high-speed dry sliding conditions. *Materials*, 13(7):1485, 2020.

A. Svoboda, D. Wedberg, and L.-E. Lindgren. Simulation of metal cutting using a physically based plasticity model. *Modelling and Simulation in Materials Science and Engineering*, 18(7):75005, 2010.

H. W. Swift. Plastic instability under plane stress, Journal of the Mechanics and Physics of Solids. 1952.

N. Takata, R. Nishida, A. Suzuki, M. Kobashi, and M. Kato. Crystallographic features of microstructure in maraging steel fabricated by selective laser melting. *Metals*, 8(6):440, 2018.

C. Tan, K. Zhou, W. Ma, P. Zhang, M. Liu, and T. Kuang. Microstructural evolution, nanoprecipitation behavior and mechanical properties of selective laser melted high-performance grade 300 maraging steel. *Materials & Design*, 134:23–34, 2017.

C. Tan, K. Zhou, M. Kuang, W. Ma, and T. Kuang. Microstructural characterization and properties of selective laser melted maraging steel with different build directions. *Science and Technology of Advanced Materials*, 19(1): 746–758, 2018.

M. Tang, P. C. Pistorius, and J. L. Beuth. Prediction of lack-of-fusion porosity for powder bed fusion. *Additive Manufacturing*, 14:39–48, 2017.

N. Taniguchi. *The art of nanotechnology [Lecture]*. 1993.

N. E. Taylor, D. M. Williamson, C. H. Braithwaite, and S. J. Ward. Tensile Hopkinson Bar Analysis of Additively Manufactured Maraging Steel. In *Dynamic Behavior of Materials, Volume 1*, pages 111–114. Springer, 2020.

H. K. Toenshoff and B. Denkena. *Basics of Cutting and Abrasive Processes*. Lecture Notes in Production Engineering. Springer Berlin Heidelberg, Berlin, Heidelberg, 2013.

H. K. Tönshoff and B. Denkena. Surface and Subsurface Properties. In *Basics of Cutting and Abrasive Processes*, pages 349–370. Springer, 2013.

C. Turk, H. Zunko, C. Aumayr, H. Leitner, and M. Kapp. Advances in Maraging Steels for Additive Manufacturing. *BHM Berg-und Hüttenmännische Monatshefte*, 164(3):112–116, 2019.

E. Uhlmann, S. Henze, R. Gerstenberger, K. Brömmelhoff, W. Reimers, T. Fischer, and N. Schell. An extended shear angle model derived from in situ strain measurements during orthogonal cutting. *Production engineering*, 7(4): 401–408, 2013.

D. Umbrello, S. Rizzuti, J. C. Outeiro, R. Shivpuri, and R. M'Saoubi. Hardness-based flow stress for numerical simulation of hard machining AISI H13 tool steel. *Journal of Materials Processing Technology*, 199(1-3):64–73, 2008.

E. Van der Aa. *Finite element modelling of temperature profiles, distortions and residual stresses due to tig welding (MSc Thesis)*. Delft University of Technology, 2002.

V. Varghese, K. Akhil, M. R. Ramesh, and D. Chakradhar. Investigation on the performance of AlCrN and AlTiN coated cemented carbide inserts during end milling of maraging steel under dry, wet and cryogenic environments. *Journal of Manufacturing Processes*, 43:136–144, 2019.

M. R. Vaziri, M. Salimi, and M. Mashayekhi. Evaluation of chip formation simulation models for material separation in the presence of damage models. *Simulation Modelling Practice and Theory*, 19(2):718–733, 2011.

E. Voce. The relationship between stress and strain for homogeneous deformations. *J Inst Metals*, (74):537–562, 1948.

Voestalpine. Product description: BOHLER W720 VMR, 2021. URL https://www.bohler-edelstahl.com/en/products/w720-vmr/.

B. Wang, Z. Liu, G. Su, and X. Ai. Brittle removal mechanism of ductile materials with ultrahigh-speed machining. *Journal of Manufacturing Science and Engineering*, 137(6), 2015.

L. Wang, Q. S. Wei, Y. S. Shi, J. H. Liu, and W. T. He. Experimental investigation into the single-track of selective laser melting of IN625. *Advanced Materials Research*, 233:2844–2848, 2011.

X. Wang, S. Xu, S. Zhou, W. Xu, M. Leary, P. Choong, M. Qian, M. Brandt, and Y. M. Xie. Topological design and additive manufacturing of porous metals for bone scaffolds and orthopaedic implants: A review. *Biomaterials*, 83: 127–141, 2016.

X. Wang, H. Li, K. Chandrashekhara, S. A. Rummel, S. Lekakh, D. C. Van Aken, and R. J. O'Malley. Inverse finite element modeling of the barreling effect on experimental stress-strain curve for high temperature steel compression test. *Journal of Materials Processing Technology*, 243:465–473, 2017.

Y. M. Wang, T. Voisin, J. T. McKeown, J. Ye, N. P. Calta, Z. Li, Z. Zeng, Y. Zhang, W. Chen, and T. T. Roehling. Additively manufactured hierarchical stainless steels with high strength and ductility. *Nature materials*, 17(1): 63–71, 2018.

D. Wedberg, A. Svoboda, and L.-E. Lindgren. Modelling high strain rate phenomena in metal cutting simulation. *Modelling and Simulation in Materials Science and Engineering*, 20(8):85006, 2012.

T. Wierzbicki, Y. Bao, Y.-W. Lee, and Y. Bai. Calibration and evaluation of seven fracture models. *International Journal of Mechanical Sciences*, 47(4-5):719–743, 2005.

M. L. Wilkins. Mechanics of penetration and perforation. *International Journal of Engineering Science*, 16(11): 793–807, 1978.

M. L. Wilkins, R. D. Streit, and J. E. Reaugh. Cumulative-strain-damage model of ductile fracture: simulation and prediction of engineering fracture tests. Technical report, United States, 1980.

A. E. Wilson-Heid, S. Qin, and A. M. Beese. Multiaxial plasticity and fracture behavior of stainless steel 316L by laser powder bed fusion: Experiments and computational modeling. *Acta Materialia*, 199:578–592, 2020.

A. S. Wu, D. W. Brown, M. Kumar, G. F. Gallegos, and W. E. King. An experimental investigation into additive manufacturing-induced residual stresses in 316L stainless steel. *Metallurgical and Materials Transactions A*, 45 (13):6260–6270, 2014.

H. Wu and S. To. Serrated chip formation and their adiabatic analysis by using the constitutive model of titanium alloy in high speed cutting. *Journal of alloys and compounds*, 629:368–373, 2015.

P. Wüst, A. Edelmann, and R. Hellmann. Areal surface roughness optimization of maraging steel parts produced by hybrid additive manufacturing. *Materials*, 13(2):418, 2020.

M. Xia, D. Gu, G. Yu, D. Dai, H. Chen, and Q. Shi. Influence of hatch spacing on heat and mass transfer, thermodynamics and laser processability during additive manufacturing of Inconel 718 alloy. *International Journal of Machine Tools and Manufacture*, 109:147–157, 2016.

A. Yadollahi, N. Shamsaei, S. M. Thompson, and D. W. Seely. Effects of process time interval and heat treatment on the mechanical and microstructural properties of direct laser deposited 316L stainless steel. *Materials Science and Engineering: Part A*, 644:171–183, 2015.

A. Yaghi, S. Ayvar-Soberanis, S. Moturu, R. Bilkhu, and S. Afazov. Design against distortion for additive manufacturing. *Additive Manufacturing*, 27:224–235, 2019.

M. Yakout, M. A. Elbestawi, S. C. Veldhuis, and S. Nangle-Smith. Influence of thermal properties on residual stresses in SLM of aerospace alloys. *Rapid Prototyping Journal*, 2020.

L. Yang, K. V. Patel, K. Jarosz, and T. Özel. Surface integrity induced in machining additively fabricated nickel alloy Inconel 625. *Procedia CIRP*, 87:351–354, 2020.

X. Yang and C. R. Liu. A new stress-based model of friction behavior in machining and its significant impact on residual stresses computed by finite element method. *International Journal of Mechanical Sciences*, 44(4):703–723, 2002.

Y. Yang, Y. Zhu, M. M. Khonsari, and H. Yang. Wear anisotropy of selective laser melted 316L stainless steel. *Wear*, 428:376–386, 2019.

C. Y. Yap, C. K. Chua, Z. L. Dong, Z. H. Liu, D. Q. Zhang, L. E. Loh, and S. L. Sing. Review of selective laser melting: Materials and applications. *Applied Physics Reviews*, 2(4):041101, 2015.

E. Yasa, K. Kempen, J. Kruth, L. Thijs, and J. Van Humbeeck. Microstructure and mechanical properties of maraging steel 300 after selective laser melting. *Solid Freeform Fabrication Symposium Proceedings*, pages 383–396, 2010.

S. Yin, C. Chen, X. Yan, X. Feng, R. Jenkins, P. O'Reilly, M. Liu, H. Li, and R. Lupoi. The influence of aging temperature and aging time on the mechanical and tribological properties of selective laser melted maraging 18Ni-300 steel. *Additive Manufacturing*, 22:592–600, 2018.

M. J. Yokota and G. Y. Lai. Toughness of Lath Versus Plate Martensites. *Metallurgical Transactions A*, 6(A): 1832–1835, 1974.

H. Yu, J. Yang, J. Yin, Z. Wang, and X. Zeng. Comparison on mechanical anisotropies of selective laser melted Ti-6Al-4V alloy and 304 stainless steel. *Materials Science and Engineering: Part A*, 695:92–100, 2017.

C. Zener and J. H. Hollomon. Effect of strain rate upon plastic flow of steel. *Journal of Applied physics*, 15(1):22–32, 1944.

M. Zenou and L. Grainger. Additive manufacturing of metallic materials. In *Additive Manufacturing*, pages 53–103. Elsevier, 2018.

F. J. Zerilli and R. W. Armstrong. Dislocation-mechanics-based constitutive relations for material dynamics calculations. *Journal of Applied Physics*, 61(5):1816–1825, 1987.

M. Zetterberg. *A critical overview of machining simulations in ABAQUS (MSc Thesis)*. KTH ROYAL INSTITUTE OF TECHNOLOGY, 2014.

D. Zhang, X.-M. Zhang, W.-J. Xu, and H. Ding. Stress field analysis in orthogonal cutting process using digital image correlation technique. *Journal of Manufacturing Science and Engineering*, 139(3), 2017a.

D. Zhang, X.-M. Zhang, G.-C. Nie, Z.-Y. Yang, and H. Ding. Characterization of material strain and thermal softening effects in the cutting process. *International Journal of Machine Tools and Manufacture*, 160:103672, 2021.

M. Zhang, C.-N. Sun, X. Zhang, P. C. Goh, J. Wei, D. Hardacre, and H. Li. Fatigue and fracture behaviour of laser powder bed fusion stainless steel 316L: Influence of processing parameters. *Materials Science and Engineering: A*, 703:251–261, 2017b.

X. Zhang, J. Zhang, and W. Zhao. A new method for cutting force prediction in peripheral milling of complex curved surface. *The International Journal of Advanced Manufacturing Technology*, 86(1):117–128, 2016.

Y. Zhong, L. Liu, J. Zou, X. Li, D. Cui, and Z. Shen. Oxide dispersion strengthened stainless steel 316L with superior strength and ductility by selective laser melting. *Journal of Materials Science & Technology*, 42:97–105, 2020.

F. Zhou. A new analytical tool-chip friction model in dry cutting. *The International Journal of Advanced Manufacturing Technology*, 70(1-4):309–319, 2014.

M. Zimmermann, D. Müller, B. Kirsch, S. Greco, and J. C. Aurich. Analysis of the machinability when milling AlSi10Mg additively manufactured via laser-based powder bed fusion. *The International Journal of Advanced Manufacturing Technology*, 112(3):989–1005, 2021.

N. N. Zorev. Results of work in the field of the mechanics of the metal cutting process. *Proc Inst Mech Eng*, 255, 1958.

N. N. Zorev. Inter-relationship between shear processes occurring along tool face and shear plane in metal cutting. *International research in production engineering*, 49:143–152, 1963.

N. N. Zorev. *Metal cutting mechanics*. Pergamon Press, 1966.

A. Zubelewicz. Century-long Taylor-Quinney interpretation of plasticity-induced heating reexamined. *Scientific Reports*, 9(1):9088, 2019.